KU LEUVEN
Group Biomedical Sciences
Faculty of Medicine
Department of Imaging and Pathology
Medical Physics and Quality Assessment

CUSTOMIZED MONTE CARLO MODELLING FOR PAEDIATRIC PATIENT DOSIMETRY IN DENTAL AND MAXILLOFACIAL CONE BEAM COMPUTED TOMOGRAPHY IMAGING

Andreas STRATIS

Promoter: Prof. Dr. Ir. Hilde Bosmans
Co-Promoters: Prof. Dr. Reinhilde Jacobs, Prof. Dr. Ria Bogaerts

Doctoral thesis in Biomedical Sciences
Leuven, 2018

Contents

LIST OF ABBREVIATIONS 5

General Introduction 7

I1. 2D and 3D imaging in dental and maxillofacial radiology 7

I2. Dental and maxillofacial Cone Beam Computed tomography 8

I3. Patient radiation dose and risk concepts 9

I4. Radiation dose in dental and maxillofacial radiology 11

I5. Radiation dose metrics and dose monitoring 13

I6. Monte Carlo simulations and voxel phantoms 15

I7. Thesis objectives and structure 17

CHAPTER 1 21

Monte Carlo simulation framework for dental Cone Beam Computed Tomography 21

1.1 Introduction 22

1.2 Methods and Materials 22

1.2.1 Monte Carlo framework customization 22

1.2.2 Monte Carlo framework calibration 24

1.2.3 Validation 25

1.2.3.1 Validation in water and PMMA phantoms 26

1.2.3.2 Validation in anthropomorphic phantoms. 27

1.3 Results 27

1.4 Discussion 29

1.5 Conclusions 30

1.6 APPLICATION 1: Investigating the influence of the elemental composition of x-ray tube added filtration on patient dose 30

1.6.1 Methods and Materials 30

1.6.2 Results 32

1.6.3 Discussion and Conclusions 33

1.7 APPLICATION 2: Investigating the impact of the shape of x-ray tube added filtration on patient dose 34

1.7.1 Methods and Materials 34

1.7.2 Results 36

1.7.3 Discussion and Conclusions 36

1.8 APPLICATION 3: Investigating the impact of Tube Current Modulation on patient dose in dental CBCT scanners 36

1.8.1 Methods and Materials 37

1.8.1.1 Study I. TCM vs fixed current acquisitions 38

1.8.1.2 Study II. Are dose calculations reliable if the TCM is not simulated? 39

1.8.1.3 Study III. Preprogrammed TCM ('Safebeam') vs attenuation-based TCM 39

1.8.2 Results 42
1.8.2.1 Results of Study I. TCM vs fixed current acquisitions 42
1.8.2.2 Results of Study II. Are dose calculations reliable if the TCM is not simulated? 43
1.8.2.3 Results of Study III. Preprogrammed TCM ('Safebeam') vs attenuation-based TCM 43
1.8.3 Discussion and Conclusions 46
CHAPTER 2 50
Development of a paediatric head and neck voxel model database for MC dose studies 50
2.1 Introduction 51
2.2 Methods and Materials 52
2.2.1 Selection of MDCT image datasets 52
2.2.2 Segmentation procedure 53
2.2.3 Matching with reference values 54
2.3 Results 55
2.4 Discussion 59
2.5 Conclusions 60
2.6 APPENDIX 1: Applying corrections to voxel models to establish an horizontal Frankfort plane 61
2.6.1 Methods and Materials 61
2.6.2 Results 64
2.6.3 Discussion and Conclusions 67
2.7 APPENDIX 2: Are organ doses age and/or gender – dependent? 68
2.7.1 Methods and Materials 68
2.7.2 Results 69
2.7.3 Discussion and Conclusions 69
CHAPTER 3 71
Indication-based radiation dose and risk assessment 71
3.1 Introduction 72
3.2 Methods and Materials 73
3.2.1 Voxel models and investigated protocols 73
3.2.2 Organ dose, E and LAR calculations 76
3.3 Results 77
3.4 Discussion 84
3.5 Conclusions 87
3.6 Roadmap for accurate dose assessment 87
3.6.1 Methods and Materials 88
3.6.2 Results 89
3.6.3 Conclusions 90
3.7 Appendix 92

CHAPTER 4 111
Radiation dose metrics for dental and maxillofacial CBCT dose monitoring: the CTDI concept 111
4.1 Introduction 112
4.2 Methods and Materials 115
4.2.1 Investigation of the applicability of $CTDI_{w,IEC2.0}$, $CTDI_{w,IEC3.0}$ and $CTDI_{w,IEC3.1}$ method for different scanners, technical specifications and investigated clinical protocols 115
4.2.2 Implementation of the IEC methods through voxel modeling 117
4.2.3 Calculation of $CTDI_{w,IEC3.1}$ for every FOV and scanner involved in the study and proposal of conversion factors 119
4.3 Results 119
4.3.1 Investigation of the applicability of $CTDI_{w,IEC2.0}$, $CTDI_{w,IEC3.0}$ and $CTDI_{w,IEC3.1}$ methods for different scanners, technical specifications and investigated clinical protocols 119
4.3.2 Calculation of $CTDI_{w,IEC3.1}$ for every FOV and scanner involved in the study and proposal of conversion factors 124
4.4 Discussion 125
CHAPTER 5 130
General Discussion and Conclusions 130
BIBLIOGRAPHY 137
SUMMARY 145
SAMENVATTING 146
ACKNOWLEDGMENT 147
DISCLOSURE OF CONFLICT OF INTEREST 150
CURRICULUM VITAE 151

LIST OF ABBREVIATIONS

2D	Two-dimensional
3D	Three-dimensional
Al	Aluminum
ALARA	As Low As Reasonably Achievable
CAD	Computer Aided Design
CBCT	Cone Beam Computed Tomography
CLI	Central Lower Incisor
CT	Computed Tomography
CTDI	Computed Tomography Dose Index
CTDIw	Weighted Computed tomography index
Cu	Copper
CUI	Central Upper Incisor
CV	Coefficient of Variance
DAP	Dose Area Product
DCS	Differential Cross Section
DDREF	Dose and Dose Rate Effectiveness Factor
E	Effective dose
ESD	Entrance Surface Dose
ESM	Equivalent Source Model
FOV	Field of View
FPD	Flat Panel Detector
Gy	Gray
µGy	micro Gray
H_T	Tissue equivalent dose
HVL	Half Value Layer
IAEA	International Atomic Energy Agency
IC	Ion chamber
ICRP	International Commission on Radiological Protection
IEC	International Electrotechnical Commission
IR	Iterative Reconstruction
keV	kilo electon volt
kVp	kilovolt peak
LAR	Life Attributable Risk
LET	Linear Energy Transfer
LJ	Lower Jaw
LNT	Linear No-Threshold Hypothesis
mAs	milli ampere second product
MC	Monte Carlo
MDCT	Multi Detector Computed Tomography
NURBS	Non Uniform Rational Basis Spline
PACS	Picture Archiving and Communication System
PDF	Probability Distribution Function
PL	Lower premolar
PMMA	Polymethyl Methacrylate
PU	Upper premolar
QA	Quality Assurance
QC	Quality Control

RBE	Relative Biological Effectiveness
RBM	Red Bone Marrow
SAD	Source to Axis of rotation Distance
SDD	Source to Detector Distance
SI	International System of Units
SPR	Scatter to primary ratio
SSCT	Single Slice Computed Tomography
Sv	Sievert
TCM	Tube Current Modulation
TLD	Thermoluminescent dosemeter
ULJ	Upper / Lower Jaw
w_R	Radiation quality weighting factor
w_T	Tissue radiosensitivity weighting factor

General Introduction

I1. 2D and 3D imaging in dental and maxillofacial radiology

The history of radiography in dentistry begins shortly after the discovery of x-rays by Prof. Wilhelm Roengten in 1895. The first dental radiograph ever was made by F. Otto Walkhoff, a dentist from Braunschweig, Germany, who obtained an image of his own crowns of the mandibular and maxillary teeth, just fourteen days after the announcement of the discovery of x-rays (Langland et al. 1995). In 1913 Dr. William Coolidge developed the first x-ray tube with a tungsten (W) anode and a few years later in 1920 he designed a small reproducible x-ray unit for dental radiography, considered to be the precursor of the modern dental x-ray modalities.

Intraoral x-ray units (figure I1, upper and bottom left images) are the most common radiography modalities in dental clinics. The designation is due to the acquisition technique where the imaging system (film, phosphor or digital sensor) is placed inside the mouth cavity and a circular or rectangular collimated beam exposes the film from outside the head of the patient. Depending on the acquisition technique, an intraoral radiograph shows different aspects of the teeth. A bitewing exposure shows a tooth from its crown to the level of the supporting bone and allows dentists to detect interproximal decay, early periodontal disease, recurrent decay under restorations and the fit of metallic fillings or crowns. A periapical exposure shows the entire tooth from the crown to beyond the root and is performed to visualize the tooth and the surrounding bone in their entirety, hence being essentially important in endodontics and oral surgery. Occlusal views are obtained to examine the skeletal or pathologic anatomy of the entire floor of the mouth (mandibular view) or the palate (maxillary view).

Extraoral x-ray imaging refers to two-dimensional (2D) panoramic and cephalometric radiographs where the detector is placed outside the head of the patient (figure I1, upper and bottom middle images). In panoramic units the paired x-ray tube – detector system rotates around the head while the x-rays are narrowly collimated to form a slit-shaped radiation beam which is directed to the dental arc at each projection of the rotation. The resulting 2D image displays the entire denture (upper and lower jaw) and enables dentists to examine both the emerged and the emerging teeth along with the jaw bones and any adjacent structure. A cephalometric radiograph is a lateral 2D image of the craniofacial region. It is mainly used for treatment planning purposes in surgery and in orthodontics. In most cases, panoramic and cephalometric modalities are combined in a single unit, making use of the same x-ray tube, yet different detector systems, being held with different arms. Once the radiographer specifies the acquisition mode, the x-ray tube aligns to either the panoramic or the cephalometric imaging system.

Intraoral and extraoral radiographs suffer from tissue superpositioning issues as any other 2D imaging modality, hindering the accuracy of the diagnostic outcome. Advances in technology include 3D Computed Tomography (CT) scanners capable of reconstructing the scanned volume into multiple slices in axial, sagittal, coronal and even oblique planes. Dental and maxillofacial radiology and surgery exploited the advances in CT technology which contributed to precise diagnosis and to surgical treatment planning. In the early 2000s, the first dedicated dental Cone Beam CT (CBCT) scanners were introduced (Figure I1, upper and bottom right) as an emerging technology which is considered nowadays an indispensable imaging tool in endodontics, periodontics, orthodontics and implantology (Scarfe et al. 2006, De Vos et al. 2009, Miracle et al. 2009a, Mah et al. 2010).

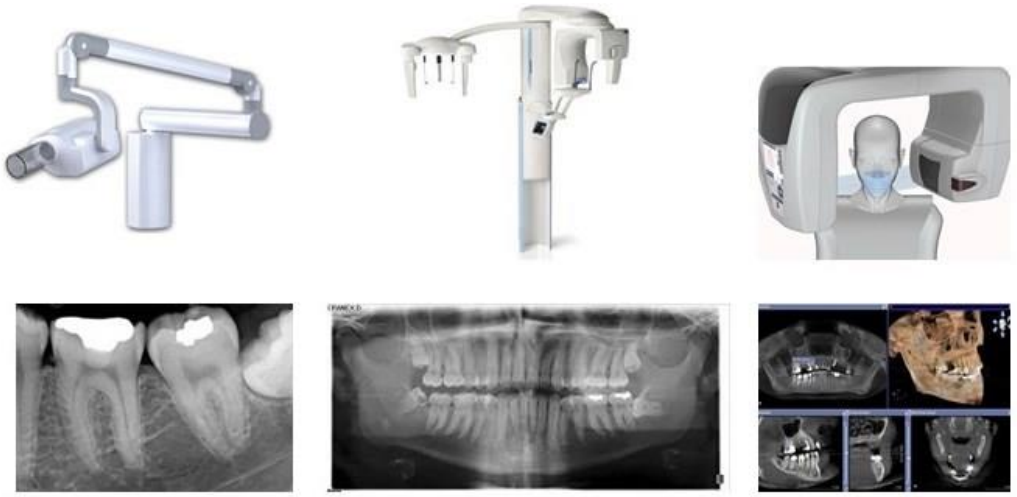

Figure I1. X-ray modalities in dental and maxillofacial radiology. Upper left image shows an intraoral unit (https://www.dentaltix.com/en/csn-industrie/max70hf-dc-intraoral-x-ray) and the respective radiograph (bottom left image). The upper middle image shows a panoramic 2D modality (http://www.planmeca.com/na/Imaging/3D-imaging/Planmeca-ProMax-3D/) and the respective 2D image (bottom middle). The upper right image shows the geometry of a dental CBCT scanner (https://www.studiobsmiles.com/cone-beam-ct-3d-imaging.html) and the resulting 3D image dataset (bottom right)

I2. Dental and maxillofacial Cone Beam Computed tomography

The first clinical CT scanner was installed at the Atkinson – Morley Hospital in Wimbledon, UK, in 1971 by EMI (Goldman 2007). The undoubted clinical value created an enormous interest and CT technology has subsequently remarkably evolved over the years. However, the basic principles of CT imaging have never been changed. In a CT scanner the patient is laying on a table with the head on a supportive apparatus. A paired x-ray source – detector system rotates around the patient, exposing the scanning volume of interest from different angles, i.e. projections (Figure I2, A). The table either remains stationary during rotation and moves prior to a subsequent rotation which irradiates the adjacent volume (axial or sequential or step and shoot mode), or it continuously moves during the rotation of the x-ray source – detector until the entire volume of interest is imaged. The combined table translation and x-ray source – detector system rotation creates in this way a helical path of the system relative to the patient (helical or spiral mode). In both modes, the imaging system detects the x-rays which are traversing the scanning volume at each projection and a dedicated software resolves its attenuating properties. These physical quantities are saved as a stack of 2D images and represent the 3D anatomy. This mathematical process is called reconstruction.

As the x-ray beam is always confined to the dimensions of the detector array, MDCT scanners use fan shapes due to the relatively small width along the longitudinal axis in comparison to the dimensions in the transaxial planes. The evolution in detector technology increased the number of CT detector rows and hence the number of slices that can be captured simultaneously in one rotation. CT scanning has seen the evolution from Single Slice CT (SSCT) scanners to Multidetector CT (MDCT). The first 16-slice scanner presented in 2002 (Flohr et al 2002a, 2002b) was employing such a broad detector that the radiation beam didn't have a fan shape anymore but was a wide beam with cone beam characteristics. Since then, scanners capable of acquiring more than 16 slices simultaneously per rotation have been considered as wide cone beam MDCT scanners.

At about the same period in time, the first commercial CBCT scanners dedicated for dental and maxillofacial applications were introduced in the market. Their main difference over cone beam MDCTs was the implementation of large flat panel detectors (FPDs) (Figure I2, B), enabling them to capture

large scanning volumes in a single rotation of the x-ray source-detector system around the patient. In CBCTs, a conical beam is directed towards the patient at each projection. The beam width covers a relatively large volume along the longitudinal direction at each projection. However, the axial dimensions of the radiation field are rather limited to a restricted length which, in most cases, is smaller compared to the circumference of the head. As the system rotates around the patient, a cylindrical Field of View (FOV) around the geometrical centre of rotation is captured (Figure I3). The cylindrical FOVs are usually reported as the product of the diameter times the height of the scanned volume and expressed in cm^2 (diameter x height). Depending on the scanned volume, FOVs are categorized into small (for single tooth imaging), medium (for jaw, sinus, cleft and temporal bone imaging) and large (face and skull imaging). They can be reconstructed in small isotropic volume elements, i.e. voxels which give rise to fully isotropic images, i.e. of identical resolution in the 3D space, providing superior spatial resolution compared to anisotropic MDCT images. CBCT achieve this quality mainly due to the small physical dimensions of the FPD pixel elements (Scarfe et al. 2008, Yu et al. 2010). The large conical radiation fields and especially their large z-coverage allows x-ray scatter to be generated from the entire volume of the coverage resulting in a poor low contrast resolution which impedes the differentiation of soft tissues which are close in density. Furthermore, dental CBCTs are equipped with large Flat Panel Detectors (FPDs) which do not have septa or antiscatter grids to deal with increased scatter. The scatter to primary ratio (SPR) is around 3 in large FOV CBCTs compared to up to 0.8 in cone beam MDCTs where the collimated x-ray beam is restricted to a thinner z-coverage allowing scatter to be generated only from a small volume (Endo et al 2006, Miracle and Mukherji 2009b, Kim et al 2012). However, it is the ability of CBCTs to provide very sharp images of the high contrast structures in the head (bony structures) which made them popular in the dental and maxillofacial radiology society.

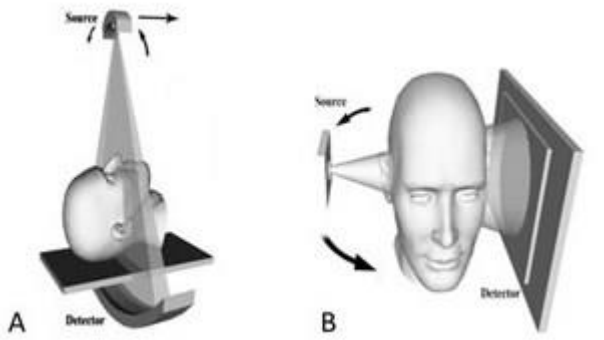

Figure I2. SSCT/MDCT (A) and CBCT (B) acquisition geometry (Miracle and Mukherji 2009b); the figure is for illustration purposes to show the conical shape of the beam and not the exact collimation; the real beam cross section in CBCT systems has a rectangular rather than a circular shape.

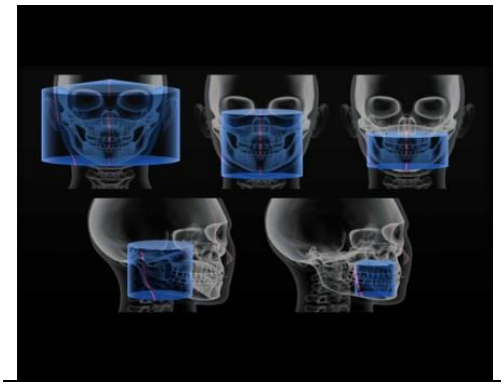

Figure I3. Scanning volumes – FOVs in dental CBCT imaging (Puthenpurayil et al. 2015)

I3. Patient radiation dose and risk concepts

In medical x-ray examinations, millions of photons pass through the body and they are either attenuated, depositing their energy in several organs or tissues, or they cross the body and strike the detector, contributing to image formation. The absorbed energy per unit mass of an organ or tissue is called absorbed dose and is measured using the unit Gray (Gy) according to the International System of Units (SI). X-rays are ionizing, causing damage to the molecules in the tissue, and in particular also to chromosomes and DNA. DNA repair mechanisms most often restore the damage, yet there is a

possibility that a chromosome can be mutated and this may ultimately lead to cancer or other radiation induced damage. The lower the absorbed dose, the lower is the risk to develop a cancer. Due to the fact that there is no threshold dose above which a cancer would certainly develop, they are called stochastic. At high dose levels, it is that the so called deterministic effects will definitely develop, above a certain threshold dose level. Examples are skin erythema, necrosis or epilation, radiation induced cataract, sterility, nausea, radiation sickness, fetal effects. Dose levels in dental and maxillofacial radiology are very low, however, and should not give rise to these deterministic effects (Edwards and Lloyd 1998).

The absorbed organ dose value (Gy) as such is not capable of quantifying the detriment and the radiation risk as it does not take into account the biological effectiveness of the radiation and the radiosensitivity of different organs or tissues. The detriment that a certain amount of absorbed dose may cause to a tissue depends on the type of radiation. Photons have a low linear energy transfer (LET) coefficient: in human tissue, they induce ionizations to atoms that are spaced far away from each other, compared to high LET neutrons or alpha particles. To express the relative biological effectiveness (RBE) of certain types of radiation, the International Commission on Radiological Protection (ICRP) assigned to each type of radiation a specific weighting factor (w_R). For photons, this radiation strength weighting factor w_R is equal to one (ICRP, 2003). The product of absorbed dose and radiation strength weighting factor (w_R) gives rise to tissue equivalent dose, HT, the SI unit of which is called Sievert (Sv). For x-rays, absorbed dose and tissue equivalent dose are numerically equal since for photons w_R is unity. Furthermore, biological aspects such as cell division rate, cell metabolic rate, cell nutrition and their differentiation in specialized and non-specialized cells influence their radiosensitivity and hence they make some organs more tolerant to radiation compared to other ones. ICRP classified the organs in the body according to their radiosensitivity by assigning to each of them a tissue radiosensitivity weighting factor (w_T) (ICRP 2007) (table I1).

Table I1. Tissue radiosensitivity weighting factors (w_T) (ICRP 2007)

Tissue	w_T	$\sum w_T$
Bone-marrow (red), Colon, Lung, Stomach, Breast, Remainder Tissues* (Nominal w_T applied to the average dose to 14 tissues)	**0.12**	0.72
Gonads	**0.08**	0.08
Bladder, Oesophagus, Liver, Thyroid	**0.04**	0.16
Bone surface, Brain, Salivary glands, Skin	**0.01**	0.04

* Remainder Tissues (14 in total): Adrenals, Extrathoracic (ET) region, Gall bladder, Heart, Kidneys, Lymphatic nodes, Muscle, Oral mucosa, Pancreas, Prostate, Small intestine, Spleen, Thymus, Uterus/cervix.

To quantify the total detriment from an exposure to radiation, each tissue equivalent dose (H_T) should be multiplied with the respective w_T. The sum of the radiosensitivity-weighted tissue equivalent doses gives rise to the effective dose (E) which is also measured in Sv (equation I1):

$E = \sum w_T H_T$ (eq. I1)

Despite the fact that E is a universally accepted term which has been used since its introduction by ICRP in 1970s, it exhibits several drawbacks which provoke criticism by the scientific community (Martin 2007, 2008, Brenner 2008). The tissue radiosensitivity weighting factors on which the calculation of E is based, represent a committee-determined subjective balance of different stochastic cancer endpoints, and change every decade or so, as different groups of experts that make up the committee may have different scientific views (ICRP 1977, 1991, 2007). Most importantly, the weighting factors are considered to be age- and sex-averaged and hence, E is independent of gender and age at exposure while epidemiology data analysis reveals very different age-at-exposure dependencies for different cancer sites (National Research Council of the National Academies, 2006).

Therefore, it must not be forgotten that E applies to a reference patient and provides an average estimation of risk between males and females over a population of all ages. It should intrinsically not be used for person specific dosimetry.

To overcome the limitations of E, the National Research Council of Academies proposed the Life Attributable Risk (LAR) for more accurate risk estimations in the BEIR VII phase 2 report (National Research Council of the National Academies, 2006). The LAR is an organ-based radiation risk estimation. Epidemiology data has been extensively analyzed for males and females separately, for different ages at exposure and for different cancer sites for two different endpoints: cancer incidence and cancer mortality. For each gender, age at exposure and organ (cancer site), the number of cases per 100,000 persons for the two endpoints has been calculated for an organ dose of 0.1 Gy. The organ LAR is then calculated for a certain organ dose value. The whole body LAR is obtained by summing up the individual organ LARs. The LAR for all cancer sites apart from leukemia was based on the Linear-No-Threshold (LNT) hypothesis which assumes a linear no threshold relationship between radiation risk and radiation dose regardless of the level of exposure (Figure I4). However, based on epidemiology data, for each cancer site and for practical dose levels, described as 'low', a dose and dose rate effectiveness factor (DDREF) of 1.5 was introduced to adjust (reduce) the dose-risk relationship. Such a factor coverts the LNT model to a Linear-quadratic or biphasic model without essentially abandoning the LNT hypothesis (Calabrese and O'Connor 2014). For leukemia, a linear quadratic model was employed since such a curve fitted the data significantly better than the linear model.

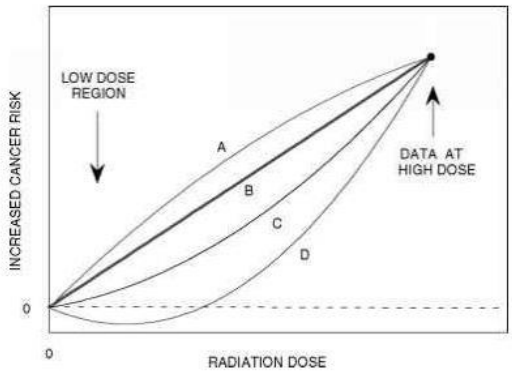

Figure I4. Models for extrapolating the radiation risk to low dose levels; (A) supralinear, (B) linear, (C) linear-quadratic, (D) hormesis (https://www.briangwilliams.us/nuclear-energy-3/the-shape-of-the-doseresponse-curve-alternative-models.html)

I4. Radiation dose in dental and maxillofacial radiology

In most countries, intraoral and extraoral 2D dental exposures account for more than 30% of medical exposures, yet their contribution to the annual collective dose (population dose) from all x-ray procedures, is rather limited (Tanner et al 2000, Hart and Wall 2002, Hart et al 2002, Hart et al 2010, EC 2014). In intraoral and panoramic radiography, the radiation field is restricted to a very small region in the denture where most of the photons are absorbed by non-radiosensitive structures. Furthermore, the radiosensitive organs which are exposed to scatter radiation have a low radiosensitivity weighting factor of about 0.01 (i.e. bone surface, skin, brain and salivary glands; oral mucosa, extra-thoracic tissue, muscles, lymph nodes belong to remainder tissues, each having a w_T of about 0.01). Furthermore, radiosensitive organs like oesophagus and thyroid gland which have a w_T of 0.04 (table I1) receive negligible dose from scatter x-rays. The Red Bone Marrow (RBM) is the most sensitive, irradiated organ, yet the percentage of its total mass in the head and neck region is very small and therefore the absorbed dose (to its total mass) is very low. For intraoral systems the reported

effective doses in literature are in the order of 1-5 μSv per exposure (Looe et al 2008, Ludlow et al 2008a, White and Pharoah 2009, Granlund et al 2016) while cephalometric acquisitions deliver equivalent doses (Visser et al 2001, Gijbels et al 2004). For panoramic exposures, the reported effective doses range from 3 to 75 μSv (Okano and Sur 2010, Lee et al 2013, Granlund et al 2016).

The introduction of CBCTs in early 2000 gave a new perspective in dental and maxillofacial radiology. Being the only alternative solution for 3D imaging beyond MDCTs, CBCTs became an imaging tool with a widespread range of applications not only due to image quality reasons but also due to their low cost, small size, and limited medico-legal requirements (Pauwels et al 2015a). CBCT imaging gradually replaced dental MDCT and 2D panoramic acquisitions without always presenting a sound evidence for the added value in terms of the diagnostic outcome for certain dental applications. Organization bodies and scientific groups have worked over the last years towards developing a justification frame and setting basic principles on the use of CBCTs in dental and maxillofacial radiology (Horner et al 2009, HPA 2010, SEDENTEXCT 2011, Jacobs 2011, 2014, American Dental Association Council on Scientific Affairs 2012, European Commission 2012). However, the extensive use of CBCTs has not been the only reason to raise concerns on radiation protection; The radiation dose is not insignificant.

While the dose to a patient can be lower compared to dental MDCT exposures, it is 2-27 times higher compared to 2D panoramic acquisitions (Table I2). Besides, and as it can also be derived from table I2, there is an overlapping region in CBCT and MDCT doses. Advances in MDCT technology such as Tube Current Modulation (TCM), Iterative Reconstruction (IR), Adaptive Collimation and more sensitive detectors, have contributed to the establishment of low dose MDCT clinical protocols which provide good image quality datasets with very low doses, e.g. for implant and surgery planning (180 μSv, Loubele et al 2005) and temporal bone imaging (280 μSv, Stratis et al 2017a). A recent meta-analysis of published data showed that adult effective doses in dental CBCT imaging range from 5-622 μSv for small FOVs (7-521 μSv for children), 9-560 μSv for medium FOVs (13-769 μSv for children) and 46-1073 μSv for large FOVs (also 13-769 μSv for children) (Ludlow et al 2015). While the abovementioned figures show that doses can either reach intraoral and extraoral (low dose) or MDCT (high dose) levels, most remarkable is the reported range. Pauwels et al (2012a) have reported a 19-fold dose range for 14 CBCT models, Ludlow et al (2008b) a 16-fold range for 7 CBCT models and Rottke et al (2013) a 23-fold range for 10 CBCT models.

Scanner-specific, radiographer-related and dosimetry-related parameters are responsible for this variability in doses. Scanners operate in different ways and with different exposure parameters. There are models which carry out full (360°) rotations while others fulfill half (180°) or even partial acquisitions. The x-ray beam shape is symmetrical in some models, i.e. the radiation field is equally split among the central x-ray, or asymmetrical, both in the sagittal/coronal and in the axial plane, in some others. The operating voltage ranges between 70-110 kV giving rise to the use of different energy spectra. Along with the voltage, it is also the filtration of the x-ray tube has an impact on the beam energy. Different filter combinations of Copper (Cu) and Aluminum (Al) have been applied by vendors and different filter shapes have been used; flat filters are mostly applied, yet beam-shaping / bow-tie filters are also employed, aiming to provide a uniform x-ray intensity all over the detector. TCM is another technical specification which aims to decrease doses. However, this is a high-end technical advancement which has not yet been greatly adopted by CBCT vendors. Radiographer – related parameters correspond to the options provided to personnel to carry out exposures. If these settings are either not optimized or not properly used, doses on good hardware systems could be much higher than needed. It must be said that optimization of exposures, to adhere the ALARA principle (radiation doses As Low As Reasonably Achievable), is a complex procedure which requires indication-oriented and age-specific adjustments of exposures based on image quality and dose assessment (Oenning et al 2017). The wide range of doses witnesses that optimization in CBCT is in a very preliminary stage.

Finally, dosimetry-related parameters may have an impact on the wide range of reported doses. There is a huge amount of organ dose and effective dose assessment studies in literature. However, most of

them have been performed with Thermoluminescent dosimeters (TLDs) mounted into anthropomorphic phantoms. TLD dosimetry, however, exhibits several limitations in CBCT imaging. Most importantly, currently available anthropomorphic phantoms do not represent the realistic anatomy of a patient, since radiosensitive organs like salivary glands, oral mucosa, ET tissue, oesophagus, etc. are not present. The delineation of these tissues depends on the experience of the user in human anatomy and hence dose results become very subjective. Furthermore, the organ dose assessment is performed in a rather limited region of each organ, where the holes to mount the TLDs are found. In conjunction with the fact that CBCTs present steep dose gradient and axial inhomogeneity (Pauwels et al 2012b), the partial irradiation of a part of the TLDs which are supposed to account for the entire organ, makes the results questionable. Furthermore, all the tissues are given the same density and the bone structures are not realistic.

Paediatric dosimetry, not only in dental CBCT imaging but also in medical exposures in general, is challenging. Apart from scanner-related factors which have an impact on radiation dose, the latter is also patient-dependent. In particular, organ dose is dependent on the fraction of the organ which is directly exposed to the primary radiation field; for a given FOV size, the larger the fraction, the higher the organ dose. While there is a limited variability in adult organ sizes and masses, with established reference values as a consequence, this is not the case for paediatric populations where organ sizes show a rapid increase with age (ICRP 2002). Furthermore, due to smaller physical size, radiosensitive organs in children, like brain and thyroid in case of dental CBCT acquisitions, are closer to the primary field and hence, they receive higher exposure from scatter x-rays. This is also related to a major limitation of CBCT scanners. To the best of our knowledge there is not any commercially available CBCT scanner with manual collimation. The FOVs are fixed in size, and therefore, the beam cannot be manually collimated to restrict the radiation field to a specific anatomical region, leading to patient overexposure. Besides, paediatric patients are at increased radiation risk due to the longer life expectancy and due to biological reasons such as cellular growth, associated with organ development, which makes organs much more radiosensitive. Therefore, paediatric populations cannot be represented by a reference anthropomorphic phantom which covers the entire paediatric age range, as is the case with adults. Dosimetric studies on paediatric dental CBCT dosimetry are rather limited (Theodorakou et al 2012, Al Najjar et al 2013, Pauwels et al 2014). All of them have been carried out with TLDs mounted on two 5- and 10- years old anthropomorphic phantoms or on adult phantoms with doses extrapolated to paediatric ages, and have pointed out the increased risk of children, and the need for more extensive paediatric dosimetry studies that will contribute to the optimization of exposures.

Table I2. Doses as a multiple of the dose from a panoramic acquisition (Holroyd and Gulson 2009)

Examination	Dose as a multiple of the dose from a typical panoramic exam
Panoramic	1
Small Field of View CBCT	2-27
Large Field of View CBCT	3-45
CT scan (dental program)	22-88

I5. Radiation dose metrics and dose monitoring

Organ dose and radiation risk assessment requires either time-consuming measurements in very specialized physical human-like phantoms (TLD dosimetry) or special high-end software tools and voxel models, i.e. Monte Carlo (MC dosimetry). For Quality Control (QC)- Quality Assurance (QA) assessment and dose monitoring purposes, neither of these two methods is appropriate. Alternatively, well

established dose metrics which quantify the radiation output of an x-ray tube can be used for x-ray tube output monitoring; comparison and optimization purposes have been proposed.

In CBCT imaging, the most popular dose metrics are the Dose Area Product (DAP) and the Computed Tomography Dose Index (CTDI). DAP (eq. I2) is given by the product of the air kerma in air at any distance from the x-ray tube multiplied by the area of the radiation field at the same distance. As the air kerma follows the Inverse Square Law, i.e. the output is inversely proportional to the square of the distance from the x-ray tube while the area is proportional to the square of the distance, the DAP remains constant any point from the source.

$$DAP = Dose\ (mGy)\ x\ irradiated\ area\ (cm^2) \quad (eqI2)$$

However, the use of DAP in CBCT imaging presents several practical limitations. Its assessment following the traditional methodology with a dosemeter (to measure the central air kerma) and a film to specify the irradiated field area is not applicable for scanners which employ bow-tie filters, because the measured DAP value is hugely overestimated. A square-shaped ion chamber (DAP meter) may also be used. In such case, the DAP meter must follow the rotation of the paired x-ray tube-detector system and shall be placed as close as possible to the tube such that the entire radiation field strikes the DAP meter. This requirement makes the verification of displayed DAP values by a medical physicist difficult if there is no access to the x-ray tube and the detector, e.g. systems having a MDCT structure where the tube and the detector are enclosed in a gantry. Finally, the DAP cannot give an answer to dose comparisons requests against MDCT exposures.

The Computed Tomography Dose Index (CTDI) was first introduced by Shope et al (1981). It aimed to quantify the total dose accumulated by a cylindrical phantom from a single rotation of a fan shaped X-ray CT beam. The introduction of the 10 cm long pencil ion chamber (IC) some years later enabled the measurement of CTDI, as its active volume could encompass the primary and the scattered radiation from a narrow, fan-shaped CT beam. CTDI became a standard method for measuring and comparing the radiation output, initially for single-slice CT scanner technology on which the technique was developed and later for MDCT. For state-of-the-art cone beam MDCT scanners and for CBCTs, the use of CTDI gets problematic, since the beam width can be much larger compared to the active volume of the pencil-like ion chamber (10cm) which is routinely used for dose assessment is CT imaging. To this end, the International Electrotechnical Commission (IEC) and the International Atomic Energy Agency (IAEA) have proposed a new methodology which will be discussed in Chapter 3, to account for the large beam widths and the long scatter tails of the x-ray beams, especially when phantom measurements are to be obtained (IEC 2010, IAEA 2011).

The SEDENTEXCT consortium has suggested a CTDI-like two tier approach for CBCT dose estimation (SEDENTEXCT 2011, Pauwels et al 2012b). The method requires a special Polymethyl Methacrylate (PMMA) phantom for dose measurements and a point dose farmer-type ion chamber. The PMMA phantom shall provide measuring points along the axis of the phantom and in the periphery. For central acquisitions, i.e. for those where the centre of the head coincides with the centre of rotation, they suggest weighted CTDI (CTDIw)-like index, with the only difference being the equal weighting (1/2) between the dose at the centre and the average dose in the periphery of the phantom. For off-center acquisitions, i.e. where the center of rotation, and hence the center of the FOV, does not coincide with the center of the head (as is the case in most small and medium FOV protocols), they suggest to re-position the phantom from the center accordingly, to measure the dose in several points along the front-back axis, and to take a simple average of the measured dose values. The method may simulate clinical cases, yet has not been validated against the average dose in the scan plane and requires dedicated equipment which is not readily available in a radiology medical physics department.

Finally, the American Association of Physicists in Medicine (AAPM) has proposed the central cumulative dose at the centre of the beam profile, f(0), as a candidate dose metric for MDCT systems and for protocols without any table translation (AAPM 111 report) (2010). The method requires dose assessment with a farmer-type ion chamber positioned at the midline of a very long (at least 40 cm)

PMMA phantom. Although the method may be valid for MDCT stationary acquisitions, e.g. perfusion scans, the dental CBCTs present several specifications which question the applicability. CBCTs present complex in-plane (off-set scans, discussed later in chapter 1) and longitudinal (divergent) radiation fields which differ a lot from the rectangular and symmetrical MDCT radiation field profiles. Furthermore, the acquisitions are not always associated with full rotations like in MDCTs. Finally, a 40 cm long phantom, apart from not being commercially available, is also difficult to physically position in a CBCT scanner with a panoramic-like orientation.

I6. Monte Carlo simulations and voxel phantoms

MC simulation is a statistical sampling technique that has been successfully applied to a vast number of scientific problems (Eckhardt 1987) and relies on repetitive random sampling of probability distributions (Fishman 1995). In medical physics, the MC technique is most popular in simulating radiation transport of particles in matter (Andreo 1991, Rogers 2006). When a certain particle penetrates matter, it undergoes multiple interactions by which energy is transferred to matter, and secondary particles are generated. The secondary particles give rise to extra interactions and this procedure goes on until secondary particles deposit all their energy in the medium or until they get out of the medium. In MC simulations, the history of the initial particle and of the cascade of secondary particles is tracked.

In a MC context, each particle, either the primary or any secondary, is initially considered to move freely inside a medium until an interaction event takes place where the particle loses energy, changes direction and produces new secondary particles. To simulate the history of the primary particle and its cascade, the interaction model shall be defined; this is a set of equations, described by the so-called Differential Cross Sections (DCS) for each different type of interaction of a particle in a medium. The DCSs determine the Probability Distribution Functions (PDFs) of random variables which characterize the path, i.e. the free path between successive events, the type of interaction that takes place and the energy loss and angular deflection in a particular interaction event. Once the PDFs have been defined, histories of primary particles are generated randomly and both these and their secondary particles are tracked until all particles are absorbed or leave the geometry of interest (Kawrakow et al 2009, Salvat 2015).

A full MC simulation consists of four different, yet interrelated parts: (1) the cross section data for all the processes being considered in the simulation, (2) the algorithms used for the particle transport, (3) the methods used to specify the geometry of the problem and to determine the physical quantities of interest, and (4) the analysis of the information obtained during the simulation (Rogers and Bielajew 1990). MC codes have been in development for over half a century and their newest versions are nowadays used in several applications in diagnostic radiology, nuclear medicine and radiotherapy, e.g. EGSnrc (Kawrakow et al 2009), MCNP (Brown 2003), GEANT (Agostinelli et al 2003) and PENELOPE (Salvat et al 2003). The use of MC techniques has vastly increased due to the complexity of radiation transport in matter which makes analytic solutions intractable, and the rapid increase in speed and decrease in cost of data processing.

To carry out dosimetry studies via MC, apart from the physics which determines the transport of radiation, software models that mimic patient anatomy are required. During recent years, computational phantoms evolved from a stylized form, based on quadratic mathematical equations, to designs of organs in the body and more anatomically realistic voxel models, due to the availability of more powerful computers and tomographic imaging. These phantoms, being compatible to most Monte Carlo transport codes, have been extensively used in several dose studies; from internal and external experimental particle dosimetry in health physics to dose studies in medical imaging, nuclear medicine and radiotherapy.

The first mathematical-stylized phantoms were reported in the 1960s (Fisher and Snyder 1966, Fisher and Snyder 1967). They developed computational anthropomorphic phantoms using shapes such as elliptical cylinders and cones to mimic different regions of the body; only the head and neck, the trunk including the arms and the legs were defined. The stylized phantoms evolved over the years to more realistic ones that were adopted by International bodies for dosimetric purposes, e.g. the hermaphrodite MIRD-5 phantom (Snyder et al 1969, ICRP 1975) (figure I5). The MIRD-5 phantom was later advanced to a pair of gender-specific models known as the ADAM and EVA (Kramer et al 1982), was scaled down to paediatric ones (Cristy and Eckerman 1987) and was used as a reference for the development of several others (Chen et al 2004, Park et al 2006, Hirata et al 2008, Kim et al 2010).

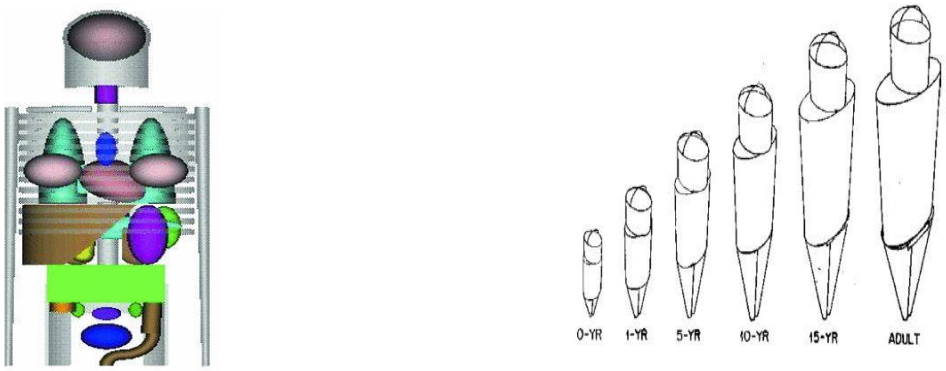

Figure I5. The evolution in computational phantoms; right image: external views of age-specific phantoms (Cristy and Eckerman 1987)

Despite the fact that dose assessment with those phantoms provided reasonable estimates, more sophisticated phantoms that could more accurately model individual organs in the body were required for more accurate dose calculations. The advent of tomographic imaging gave rise to the so-called voxel models. Based on 3D image datasets, each organ in the body is segmented either on a slice-by-slice basis or by thresholding the grey values of the tomographic images to a certain range which corresponds to specific tissues. As the resolution of the 3D imaging technology was evolving so the resulting voxel models were also advancing. Since early 1980s until today, a large number of voxel models have been developed based on Computed Tomography (CT), Magnetic Resonance (MRI) imaging and/or cross sectional photographic imaging (Bozkurt et al 2000, Xu et al 2010, 2014). Xu et al (2014) reported a total number of 84 voxel models in 2014. International bodies adopted the new technology, presenting a pair of reference, adult, gender-specific voxel models in 2009 (ICRP 2009) (Figure I6). The term voxel phantoms results from the finest picture element in the 3D tomographic data, i.e. a volume pixel (voxel), based on which the phantom is designed.

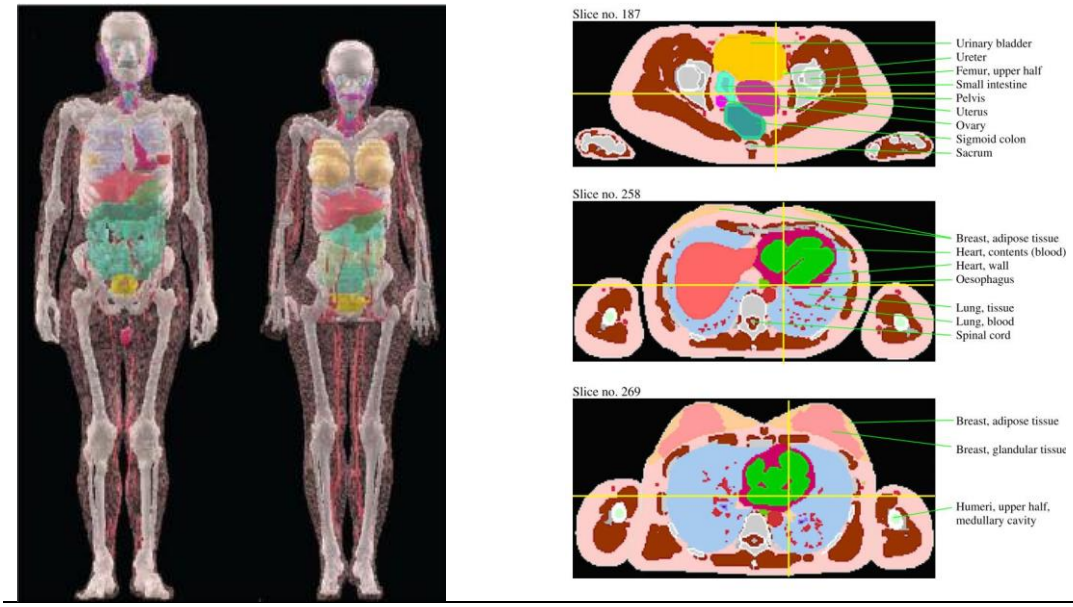

Figure I6. ICRP adult reference male (left) and female (right) voxel models and their internal structure.

Modern Computed Aided Design (CAD) software systems have resulted in more advanced hybrid phantoms where the voxel model can be tuned to specific situations while preserving its realism such as to smooth the internal structure and the contour of the organs. Non Uniform Rational Basis Spline NURBS hybrid phantoms are such an example where the voxel phantom anatomy is exported as a polygon mesh in which the organs are represented by triangular surfaces. These phantoms can be more flexible, yet they are not compatible with most MC simulation frameworks which require a voxel phantom format.

I7. Thesis objectives and structure

This research project focuses on paediatric dosimetry in dental and maxillofacial CBCT imaging via MC simulations. The project aims to fill the gaps of the current research on paediatric dose assessment by developing dedicated software solutions that conventional dosimetry with anthropomorphic phantoms and TLDs fails to provide. This is accomplished by employing a Monte Carlo (MC) framework and the work-out of a unique database of paediatric voxel models. Advanced technical specifications only since recently available on some dental CBCT systems, like bow-tie filtration and tube current modulation (TCM), are investigated towards their impact on paediatric dosimetry. A thorough age and gender-specific simulation study is performed to assess organ doses and the associated radiation-induced risk for the most frequently applied clinical protocols. Radiation risk is quantified via E and the age and gender dependent LAR. Finally, the use of CTDI-based metrics in CBCT imaging are investigated and protocol, age and gender specific conversion factors from CTDI to Effective dose and LAR are proposed. The study is divided into four chapters.

Chapter 1 presents the customization, calibration and validation of the MC dosimetry platform. It is based on a hybrid simulation framework which had been developed in KU Leuven and has been extensively used for dosimetric studies in 3D imaging (Zhang et al 2011, 2013a, Lopez-Rendon et al 2014, 2017a, Woussen et al 2016). The simulation code has been modified and further advanced into a flexible dose simulation tool, which can be easily customized and adjusted to different scanner models. The motivation to modify the code was mainly to overcome the limitation of getting information regarding the shape and the composition of the added bow-tie filtration which many vendors employ in their systems and which they consider proprietary data. The entire chain from MC

customization (i.e. implementation of technical and geometric specifications) to calibration (i.e. production of MC dose to absolute dose conversion factors) and validation (i.e. test of the reliability of the MC tool) for five different models is presented. Chapter 1 investigates also the impact of different filter compositions and shapes and the influence of TCM on the dose. The work has been presented in the following papers and presentations:

Stratis A, Zhang G, Lopez-Rendon X, Jacobs R, Bogaerts R, Bosmans H. 2016a Customization of a Monte Carlo dosimetry tool for dental Cone Beam CT systems. Radiat Prot Dosim 169 (1-4): 378-385
Stratis A, Zhang G, Jacobs R, Bogaerts R and Bosmans H. Should Dental CBCT Devices be Equipped with Cu-filters? A Monte Carlo Organ Dose Comparison Study (Radiological Society of North America, RSNA 2015, oral presentation)
Stratis A., Zhang G., Awouters J., Jacobs R., Bogaerts R., Bosmans H. Patient – specific organ dose assessment in a dental cone beam CT scanner with tube current modulation, (European Congress of Radiology, ECR 2016, DOI link: (http://dx.doi.org/10.1594/ecr2016/C-1145)
Stratis A., Zhang G., Awouters J., Jacobs R., Bogaerts R., Bosmans H. Does rotational tube current modulation have a significant impact on organ doses in dental CBCT to impose its implementation in dose calculating software tools? (Radiological Society of North America, RSNA 2016, oral presentation)
Stratis A., Zhang G., Jacobs R, Bogaerts R, Bosmans H. Preprogrammed Tube Current Modulation vs Attenuation-based Tube Current Modulation vs fixed current acquisitions: which technique delivers the lowest doses in dental CBCT scanners? Radiological Society of North America, RSNA 2017, poster presentation
Paper to be submitted: Stratis A., Zhang G., Jacobs R., Bogaerts R., Bosmans H, 'The influence of Tube Current Modulation on organ doses in dental and maxillofacial CBCT imaging: Theoretical and clinical Tube Current Modulation Schemes'

Chapter 2 presents the development of a database consisting of seventeen paediatric male and female head voxel models from 3 to 14 years old. It describes the entire voxelization procedure; from the selection of the 3D image datasets from the Picture Archiving and Communicating System (PACS) of the hospital (Universiteit Ziekenhuis Leuven, UZ Leuven, BE) to the formation of the appropriate MC-oriented text file. Only full head MDCT acquisitions, from the crown of the head up to at least the C5 spinal segment were retrieved. Image datasets with severe artefacts that could hinder organ segmentation were rejected, along with those datasets of patients with severe trauma injuries. The work also describes the procedure of adjusting organ masses to reference values (ICRP 2002, 2009) such that each specific model can be considered a reference for the associated age and gender category. Each model consists of twenty-two organs, segmented in a manual or semi-automatic way. This chapter also deals with a software-technical correction which has been employed to all voxel models of the database. Voxel phantoms are most frequently based on MDCT image data sets and they preserve patient MDCT acquisition geometry; in case of head voxel models, the head support which MDCT scanners are equipped with, introduces an inclination to the head and hence to the head voxel model. In dental Cone Beam CT (CBCT) imaging, patients are always positioned in such a way that the Frankfort line is horizontal, implying that there is no head inclination. A procedure to adjust the orientation is proposed and a study to investigate the impact of head inclination on organ doses in dental CBCT is carried out. The work has been presented in the following papers and presentations:

Stratis A., Zhang G., Jacobs R, Bogaerts R, Bosmans H. 2016b Rotating and translating anthropomorphic head voxel models to establish an horizontal Frankfort plane for dental CBCT Monte Carlo simulations: a dose comparison study. Phys Med Biol. 61(24): N681-N696.
Stratis A., Touyz N, Zhang G., Jacobs R, Bogaerts R, Bosmans H and DIMITRA project partners 2017b Br J Radiol. 90 (1078):20170051. doi: 10.1259/bjr.20170051. Epub 2017 Jul 27

Touyz N, Stratis A, Zhang G, Jacobs R, Bogaerts R, Bosmans H 2016 Creation of a Paediatric Head Voxel Model Database for Dosimetric Applications (1st European Congress of Medical Physics, ECMP 2016, O165, oral presentation)

Chapter 3 presents an extensive dose assessment study which involves more than 1000 simulations. Each of the seventeen voxel models has been applied to each scanner-specific MC framework and organ doses have been calculated for different clinical cases, i.e. single tooth imaging (central upper and lower incisor, upper and lower premolar), upper-lower jaw, lower jaw, cleft palate, maxillofacial complex, sinus, face and skull imaging. For the NewTom 5G, organ doses were also calculated for unilateral and bilateral temporal bone imaging. A statistical analysis was carried out to investigate the dose – age relationship for every different clinical case. The radiation induced risk was calculated both via E and incidence LAR. To simplify LAR estimate, a software tool requiring gender, age-at-exposure and organ dose as an input was developed. The current study aims to provide a roadmap towards clinical, patient-based protocol optimization. Chapter 3 has been presented in the following papers and presentations:

Stratis A, Zhang G, Lopez-Rendon X, Politis C, Hermans R, Jacobs R et al 2017a Two examples of indication specific radiation dose calculations in dental CBCT and Multidetector CBCT scanners Phys Med 41 71-77

EzEldeen M, Stratis A, Coucke W, Codari M and Jacobs R 2017 As Low Dose As Sufficient Quality: Optimization of Cone-Beam Computed Tomography Scanning Protocol for Tooth Autotransplantation Planning and Follow-up in Children J Endod 43 (2) 210-7

Oenning AC, Jacobs R, Pauwels R, Stratis A, Hedesiu M, Salmon B 2017 Cone-Beam CT in paediatric dentistry: DIMITRA project position statement Pediatr Radiol 48 (3) 308-316

Marcu M, Hedesiu M, Salmon B, Pauwels R, Stratis A, Oenning ACC et al 2018 Estimation of the radiation dose for pediatric CBCT indications: a prospective study on Promax 3D Int J Paediatr Dent (accepted for publication), doi: 10.1111/ipd.12355

Stratis A., Zhang G., Jacobs R., Bogaerts R. Bosmans, 'A clinical-based, age and gender –oriented, multiscanner dose assessment study in dental and maxillofacial CBCT imaging' (in preparation)

Stratis A., EzEldeen M, Zhang G., Jacobs R, Bogaerts R, Bosmans H. A Monte Carlo dosimetry comparison study of two different paediatric protocols for teeth autotranspantation planning and follow up. Radiological Society of North America, RSNA 2015, oral presentation

Stratis A., Zhang G., Jacobs R., Bogaerts R. Bosmans H. A Monte Carlo study on the effect of the orbital bone to the radiation dose delivered to the eye lens. Proc. SPIE 9412, Medical Imaging 2015: Physics of Medical Imaging, 941231 (18 March 2015); doi: http://proceedings.spiedigitallibrary.org/proceedings.aspx?articleid=2210185

Stratis A., Lopez-Rendon X., Zhang G., Jacobs R, Bogaerts R, Bosmans H. Organ dose and radiation risk assessment for orthognathic patients in large FOV dental CBCT and head MSCT imaging. Radiological Society of North America, RSNA 2016, oral presentation

Stratis A., Zhang G., Jacobs R, Bogaerts R, Politis C, Shaheen E, Bosmans H. Head CBCT vs Head MSCT imaging; comparing organ doses and radiation risks for a cohort of orthognathic patients. 1st European Congress of Medical Physics, ECMP 2016, oral presentation

Stratis A., Zhang G., EzEldeen M., Jacobs R, Bogaerts R, Bosmans H and the Dimitra consortium. Age-dependent organ dose calculations in dental CBCT imaging for a cohort of cleft palate patients. European Congress of Dentomaxillofacial Radiology, June 2016, Cardiff, WAL, poster presentation

Stratis A., Zhang G., Jacobs R., Bogaerts R. Bosmans H. Patient specific paediatric dose assessment in dental Cone Beam Computed Tomography via Monte Carlo calculations. PiDRL, European Diagnostic Reference Levels for Paediatric Imaging, 2015, Oral presentation

A Stratis, G Zhang, R Jacobs, R Bogaerts and H Bosmans, Customization of a Monte Carlo dosimetry tool for dental Cone Beam CT systems. Optimisation in X-ray and Molecular Imaging 2015, Fourth Malmö Conference on Medical Imaging, 2015, oral presentation
Stratis A., Zhang G., Jacobs R., Bogaerts R., Bosmans H. The influence of the orbital bone density on the eye-lens dose in dental CBCT, European Congress of Radiology, European Society of Radiology (ECR), Vienna, Austria, oral presentation, (SS 7 13), B-0680 (Best on site scientific presentation, Physics in Radiology, Innovations in CT technology).
Stratis A., Zhang G., Jacobs R., Bogaerts R., Bosmans H. Patient-specific approach of CBCT imaging in children: custom-made Monte Carlo simulations, 2nd EADMFR junior meeting, 2015, oral presentation

Chapter 4 investigates the role and relevance of CTDI-based metrics in dental and maxillofacial scanners. It examines whether the unique technical and geometric specifications like large beam widths along the longitudinal axis, restricted – small in-plane axial FOVs, offset-asymmetrical beam shapes, and partial and half rotations have an impact on the applicability of CTDI. Considering that CTDI is an established method for conventional MDCT scanners where the x-ray tube-detector rotation is accompanied by table translation (either in a simultaneous (helical) or in a step-and-shoot (axial) mode), it discusses the applicability and the connotation of such a metric in stationary systems like CBCTs. All the existing IEC- proposed CTDI versions were tested against the total accumulated dose (infinite CTDI), to investigate which one preserves a constant measuring efficiency over the entire range of beam widths. It further explores the axial dose distributions in a standard head PMMA phantom to study whether the average dose in the scan region can be retrieved from CTDI measurements and whether the weighting 1/3 and 2/3 factors in the weighted CTDI formula (for central and periphery dose measurements respectively) are still relevant. In conjunction with organ dose and radiation risk assessment study in chapter 3, CTDI to effective dose and LAR conversion factors are suggested along with a roadmap for assessing CTDI to organ dose conversion factors. Chapter 4 was presented in the following papers and presentations:

Stratis A., Zhang G., Jacobs R., Bogaerts R., Bosmans H The relevance and role of CTDI-based metrics for dental Cone Beam CT scanners: a Monte Carlo investigation (to be submitted)
Stratis A., Zhang G., Jacobs R., Bogaerts R., Bosmans H. Employing CTDI to dental CBCT scanners – A Monte Carlo study, “Belgian Hospital Physicist Association”, Annual meeting, 2016, oral presentation

CHAPTER 1

Monte Carlo simulation framework for dental Cone Beam Computed Tomography

1.1 Introduction

There are two ways to estimate the radiation induced risk from medical exposures: to apply conversion factors to dose metrics, e.g. DAP or CTDI to effective dose conversion factors created from organ dose estimates for a generic patient, or to directly measure or estimate organ doses and quantify a total body risk (*E or LAR*). While universal conversion factors have not yet been reported for dental CBCT equipment and a commonly accepted dose metric has not yet been proposed by the scientific community, the organ-based risk estimation is always a robust methodology. The conventional way of assessing doses via TLDs and anthropomorphic phantoms has already been discussed. Alternatively, MC dosimetry is a software approach, involving the simulation of particles and their interaction with matter.

In a previous study, a hybrid MC framework, developed in our group, capable of simulating the entire dental CBCT imaging chain from x-ray production to image formation, was described (Zhang et al 2011, 2013a). The framework was built in EGSnrc code and was employing the phase space concept; the x-ray tube was explicitly simulated in full detail and the output was saved in phase space data files which can then be applied subsequently to simulate specific radiation fields (Kawrakow et al 2009, Rogers et al 2011). To accurately simulate the x-ray source and the filtration of the x-ray tube without having access to manufacturer proprietary data, we modified the MC framework and adapted the code to start from equivalent source models (ESM) which characterize the output and the filtration of the source based on real measurements (Turner et al 2009). Customization refers to the production of scanner and protocol-specific simulation frameworks which account for the technical and geometric specifications of each system; the energy spectrum and the total x-ray tube filtration along the radiation field, the in-plane and longitudinal beam shape, the rotation angle and the beam-on and beam-off angles, the acquisition geometry (symmetrical or offset), the collimation at each FOV and the implementation of TCM. In a next step, a calibration procedure is needed to relate the MC calculated doses which are normally provided in μGy per number of simulation histories (μGy/#hist) to absolute dose values (μGy or μGy/mAs). Finally, the MC scanner-specific frameworks were validated against real measurements to test their reliability for dosimetric studies. The aim of the study was to customize the code for five different scanner models, i.e. for Promax 3D Max (Planmeca, FI), Accuitomo 170 (Morita, JP), CS 9300 (Carestream, USA), NewTom 5G (QR S.R.L, IT) and NewTom VGi-evo (QR S.R.L, IT). With these customized frameworks, five more studies were then conducted and are presented in this chapter. The first two studies investigated the influence of x-ray tube filter material composition and the impact of bow-tie filtration on doses. Three more studies were conducted to test the effect of TCM on doses. Apart from drawing conclusions about the influence of such dose reduction systems (TCM) on dose, the studies aimed to investigate the necessity to include TCM curves in MC framework for accurate dose assessment.

1.2 Methods and Materials

1.2.1 Monte Carlo framework customization

The MC framework was developed in EGSnrc code and has three individual components: source modelling, angular projection modelling and dose tracking. The x-ray source modelling is based on the equivalent source model concept (ESM); this method has been introduced to obviate the need for obtaining proprietary data which are required for the accurate simulation of the x-ray tube. The ESM includes the energy spectrum of the x-ray beam and weighting factors which reflect the attenuation of the x-rays when they cross the filter from different paths. As the operating voltage (kVp) is the only practically changeable exposure parameter which may influence the energy spectrum (the inherent and added filtration are fixed), ESMs were produced for each scanner but only for those specific kVp

energies which the clinical protocols are performed with. A calibrated farmer ion chamber (IC) (FC65-G, SN:1698, IBA Dosimetry, Schwarzenbruck, Germany) was used to measure the Half Value Layer (HVL) at the operating voltage of each scanner. Subsequently, a dedicated Matlab (version 7.12.0.635, R2011a, MathWorks Inc) software tool, SPEKTR (Siewerdsen et al 2004), which generates energy spectra for user-specified filter combinations, was used. Through an iterative procedure where the measured HVL was checked against SPEKTR provided HVL values for different filter combinations, the energy spectrum of each scanner, and hence of each ESM, was the one that resulted from the best HVL match. Air kerma measurements along the anode-cathode axis of each scanner were also carried out to assess total x-ray tube filtration along the radiation field. All the measurements were performed in service mode with the x-ray tube – detector system held in a fixed position. For these filtration-related air kerma measurements, the IC was positioned as close as possible to the detector to increase the distance along the anode-cathode axis which corresponds to two different filter points – x-ray path lengths (figure 1.1). The ratio of the air kerma at each point to that at the central point provides the extra attenuation of the filter. For each x-ray energy of the polychromatic spectrum (in 1 keV steps), the attenuation is defined at each different ray-path and inserted into the code in terms of weighting factors allocated in dedicated look up tables. This method has been employed for both bowtie and non-bowtie filtrations.

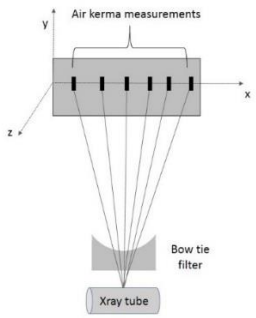

Figure 1.1 The IC is positioned against the detector and air kerma measurements corresponding to different path lengths through the bow-tie filter are obtained

Each ESM is part of the corresponding scanner-specific input file. The input files also incorporate the geometric specifications of each system which are required for accurate projection modelling: the source-to-axis of rotation distance (SAD), the size of the field of view (FOV), the x-ray tube angular intervals, the x-ray beam shape, the total rotation angle and the Beam-ON and Beam-OFF angles. The input files also consider whether the acquisition geometry is symmetrical or offset. In a symmetrical acquisition geometry, the centre of the in-plane (axial) radiation field strikes the centre of the detector (Figure 1.2 left image). In an asymmetrical geometry, the detector is offset positioned with respect to the radiation field (figure 1.2 right image) and at each projection only half of the FOV is scanned. Normally, offset techniques are carried out under full rotation acquisitions such that the entire FOV is irradiated during the rotation, allowing to properly reconstruct the images. In the context of the MC framework, the offset geometry is defined by the lower bounds of the radiation with respect to the centre of rotation.

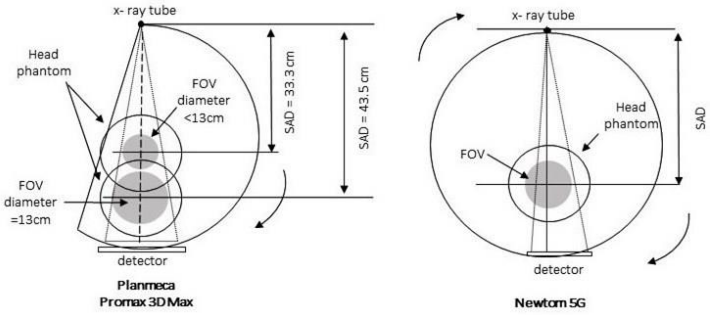

Figure 1.2 left: Planmeca Promax 3D Max employs a symmetrical beam and a 210° rotation (except for the largest FOV). There is also a change in the SAD according to the diameter of the FOV. Right: Newtom 5G employs an offset beam and a full rotation (except for the smallest FOVs)

Finally, for scanners equipped with tube current modulation (TCM) systems, the input file contains the features of the (patient-specific) TCM curve. A TCM scheme is implemented to the code in terms of projection-specific weighting factors to the dose integral and are specified by the ratio of the mA value at each simulated projection to the average mA value over the entire scan.
The dose tracking part is performed with a history-by-history statistical estimator; each simulated particle is tracked until it exits the geometry of interest or reaches the predefined cut-off energies, set at 10 keV for photons and 520 keV for electrons (9 keV of kinetic energy). The particle transport simulation is carried out with spin effects, electron impact ionization, bound Compton scattering, radiative Compton corrections, atomic relaxations and Rayleigh scattering all turned on. NRC Bremsstrahlung cross sections and the XCOM photon cross sections were employed. Target simulation uncertainty on the dose is set to 99.7% confidence intervals (Sempau et al 2001, Walters et al 2012).
Table 1.1 illustrates the technical specifications of each scanner that participated in the study.

Table 1.1 Technical specifications of dental CBCT scanners in the study

Scanner	Operating voltage (kV)	Bowtie filter	Rotation angle (°)	TCM	Cu filter	Offset acquisition
Promax 3D Max (Planmeca, FI)	96 (1)	No	210/360 (3)	No	Yes	No (5)
Accuitomo 170 (Morita, JP)	90 (1)	Yes	180/360 (4)	No	No	No
CS 9300 (Carestream, USA)	70-90 (2)	Yes	200/360 (3)	No	Yes	No
NewTom 5G (QR S.R.L, IT)	110	No	360	Yes	No	Yes
NewTom VGi-evo (QR S.R.L, IT)	110	No	360	Yes	No	Yes

(1) The operating voltage can be altered by the user, yet the preset clinical protocols are carried out with the tube voltages indicated in the table. (2) Depending on the FOV, the operation mode and the size of the patient, the voltage varies from 70-90 kV. (3) In Promax 3D Max, for every clinical FOV apart from the largest one for skull imaging (23x16 cm² and 23x26 cm²) the scanner employs a partial rotation (210°); for skull protocols the rotation is 360°. In CS9300, the rotation angle is 200° apart from the largest 17x13 cm² FOV. (4) Accuitomo 170 provides half and full rotation options for every FOV, yet only FOVs with 360° are applied in the clinic. (5) For every clinical FOV, apart from the largest one for skull imaging (23x16 cm² and 23x26 cm²), the in-plane radiation field is symmetrical.

1.2.2 Monte Carlo framework calibration

In MC simulations the calculated dose value is always proportional to the number of simulation histories. To get absolute dose values, the MC framework has to be calibrated, i.e. to get a conversion factors that relate the simulated dose values (μGy/# hist.) to real dose values (μGy/mAs). To this end,

each different protocol-FOV for each scanner had to undergo a calibration procedure which was carried out in three steps. For each different FOV, the farmer-type IC was positioned at the SAD, with the active volume being parallel to the center of rotation and with the center of the active volume coinciding with the center of the FOV. An exposure was made and the normalized to mAs air kerma $K_{air,meas.}$ was estimated (μGy/mAs). The farmer-type IC had been recently calibrated such that the measured current from the ionization of the air in the active volume of the IC provided the dose at a point in the air.

A voxel model (figure 1.3) of the active volume was designed and the exact acquisition geometry of each protocol and FOV, was modelled. The active volume, although not necessary, was explicitly simulated, to reduce the simulation time; The graphite cap increases the photon fluence in the air volume of the IC and reduces the number of simulated histories required to provide an acceptable simulation uncertainty. Simulations were performed at 1° angular projection steps with $1*10^9$ histories per projection. The simulated air kerma, $K_{air,sim.}$ was assessed and normalized to the total number of histories (μGy/# hist.).

Protocol-specific calibration factors were obtained from the ratio of the measured to simulated air kerma (equation 1.1). The resulting calibration factors are provided in units of (histories/mAs).

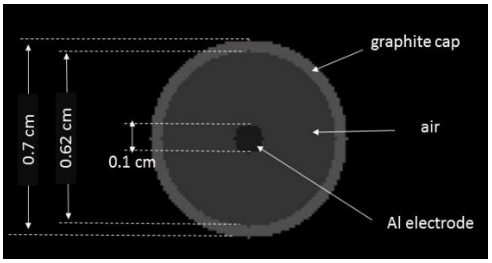

Figure 1.3 Cross section of the active volume of the farmer IC voxel model

$$f_{MC} = \frac{K_{air,meas.}}{K_{air,sim.}} \left[\frac{histories}{mAs}\right] \quad (1.1)$$

Table 1.2 Calibrated protocol FOVs at each scanner

Scanner	FOV (cm²) (diameter x height)
Promax 3D Max (Planmeca, FI)	4.2x4.8, 5x5.5, 8.5x4.8, 8.5x7.5, 8.5x11, 10x5.5, 10x9, 10x13, 11x5, 11x7.5, 11x11, 11x13, 13x5.5, 13x9, 13x13, 13x16, 23x16, 23x26
Accuitomo 170 (Morita, JP)	4x4, 6x6, 8x8, 10x5, 10x10, 14x5, 14x10, 17x12
CS 9300 (Carestream, USA)	5x5, 8x8, 10x5, 10x10, 17x6, 17x11, 17x13.5
NewTom 5G (QR S.R.L, IT)	6x6, 8x8, 12x8, 15x5, 15x12, 18x16
NewTom VGi-evo (QR S.R.L, IT)	5x5, 8x5, 8x8, 10x5, 10x10, 12x8, 15x5, 15x12, 16x16, 24x19

1.2.3 Validation

This section deals with the reliability of the MC code for dose assessment studies. The MC framework was validated against dose measurements performed in a water phantom, in a PMMA phantom in case of NewTom 5G and against TLD measurements in a pediatric anthropomorphic phantom to test its performance when the beam passes through inhomogeneous media.

1.2.3.1 Validation in water and PMMA phantoms

To validate the framework for Promax 3D Max, Accuitomo 170 and CS 9300, a cylindrical hollow phantom, 15.2 cm in diameter and 25 cm high with 0.3 cm PMMA wall thickness was filled with water. For every protocol FOV of each scanner (table 1.2) the water proof IC which had also been used in the calibration procedure, was positioned at seven different locations in the scanned volume. Figure 1.4a demonstrates the different positions of the IC in the case of a 10x9 cm² protocol in Promax 3D Max (positions A-G). An exposure was made for each different IC position and a set of seven dose-in-water measurements, normalized to mAs, were determined for each FOV (in mGy/mAs). As the water phantom does not have fixed positions for dose measurements (as it is the case in PMMA phantoms), the exact coordinates of the IC were derived from the images after exposure. A voxel model of the water phantom was designed and the water voxels which lay in the same positions (A-G) were specified for each different case. The MC dose at each position was obtained from the dose to these water voxels (mGy/#hist.) and converted to mGy/mAs after applying the calibration factor of the corresponding protocol.

In NewTom 5G the hollow water phantom was not applicable due to the CT-like-orientation of the scanner (patient lying on a table). The most reliable method for validating the code was via CTDI measurements. The adjusted version of CTDIw to deal with large beam widths, $CTDI_{w,IEC3.0}$ (IEC, 2009), where dose is divided by the minimum value of the typical pencil IC (10cm) and the beam width, was applied. $CTDI_{w,IEC3.0}$ was measured for each different protocol with a pencil IC (DCT10, RTI Electronics, Molndal, SE) in a standard head CTDI phantom. CTDI-based metrics are further discussed in chapter 4. The IC was subsequently voxelized along with the CTDI phantom (figure 1.4b and 1.4c) to reproduce the exact geometry and calculate the MC-based CTDI values.

To validate the framework for NewTom VGi-evo which uses a TCM technique, a cylindrical phantom with an elliptical cross section was designed (figure 1.4d), 3D printed and filled with water, in order to force the generator of the scanner to induce the current modulation. The farmer-type IC was placed again at seven different positions (A-G) within the scanned volume and the same validation approach that was followed for every scanner, except for NewTom 5G, was implemented.

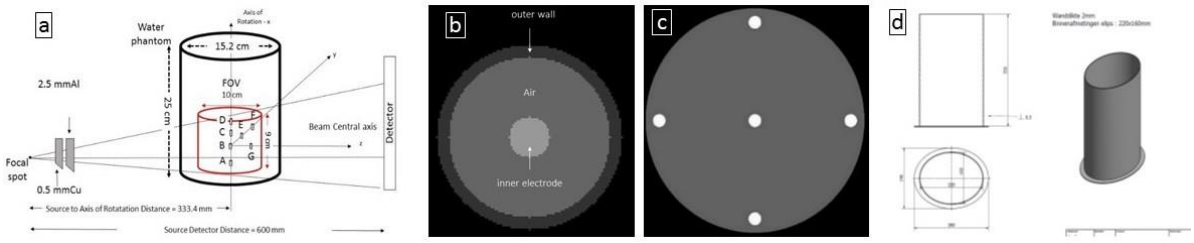

Figure 1.4 a. IC positions in the water phantom, b. cross section of the pencil IC voxel model, c. cross section of the standard head CTDI phantom, c. hollow phantom for validating a system with TCM

In all cases, simulations were carried out with $20*10^6$ histories per projection at 1° angular interval steps. The validity of the framework for each different case was tested as the percent difference (%Δ) between the MC-calculated and the measured dose values. Considering the measured values as reference ones, the percent difference was calculated based on equation 1.2.

$$\%\,\Delta = (Dose_{sim.} - Dose_{meas.})/\,Dose_{meas.} \quad (1.2)$$

1.2.3.2 Validation in anthropomorphic phantoms.

The water and the PMMA phantoms are homogeneous and the x-rays do not pass through different materials. To check the MC framework in a more clinically relevant situation, it was tested against TLD measurements in an anthropomorphic model. To this end, an anthropomorphic 5 years old pediatric phantom (ATOM 705, CIRS, USA) was employed.

The phantom is sectioned in 25 mm slices along the longitudinal axis providing optimized TLD locations specific to 22 inner organs. For the purpose of the study only the head and neck region was used. The phantom was initially scanned in a MDCT scanner to get the image dataset that would enable its voxelization. The TLDs (TLD-100 chips, LiF:Mg,Ti) (Harshaw Thermo Fisher Scientific Inc, Waltham, USA) were calibrated using a ^{90}Sr source, that had been calibrated using an ionization chamber with a calibration factor traceable to a Secondary Standard Dosimetry Laboratory (SSDL, Gent, Belgium). The total uncertainty associated with the TLDs was 8% (1SD). A TLD selection process was performed by exposing them repeatedly under identical exposure parameters in a conventional x-ray tube and by discarding those exhibiting a read-out value varying more than 3%. TLDs were loaded in specific locations, namely holes for estimating the dose to the brain, the thyroid and the cranium in the Promax 3D Max for a cleft (10 x 5 cm^2) and for an upper/lower jaw (10 x 9 cm^2) protocol (both at 96kV, 75.6 mAs) and in the NewTom VGi-evo for a standard resolution 8x8 cm^2 Upper/Lower Jaw protocol (110kV, 17.4 mAs with TCM). We also calculated the dose to the eyes by positioning TLDs on the exterior surface of the phantom. A couple of unexposed TLDs was used to estimate the background dose. The read out was performed by a Harshaw 6600 reader, 24 hours after exposure. The doses to the above-mentioned organs were calculated as the average value of the TLDs in the corresponding organ-specific locations. Subsequently, a voxel model of the ATOM phantom was designed and MC simulations were carried out with $20*10^6$ histories per projection at 1° angular interval steps. The doses to all the holes were determined and the MC-based organ doses were obtained. The % Δ was also used (equation 1.2) to assess the reliability of the code. Figure 1.5 shows the exterior of the ATOM 5 anthropomorphic phantom, one of its cross sections in the head region and the voxelized counterpart.

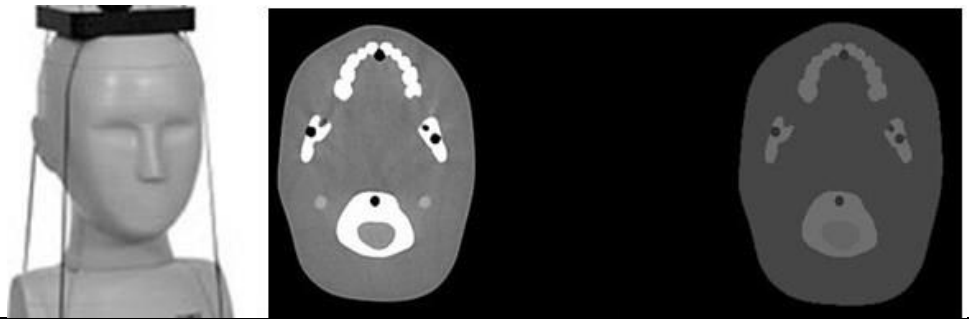

Figure 1.5 The exterior of the ATOM 5 phantom (left), a cross section in the head region (middle) and its voxelized counterpart

1.3 Results

Two types of dose meters were used in the study; the farmer (IBA Dosimetry, Schwarzenbruck, DE) and the pencil IC (RTI Electronics, Molndal, SE). IBA provides an uncertainty of 2.5% for air kerma measurements, and 4.6% for dose in water measurements, while the uncertainty of the pencil IC is 3% both for CTDI in air and in PMMA measurements according to RTI. All the above-mentioned uncertainty values correspond to a 95% confidence interval. The simulation statistical uncertainty which is determined by the number of transported histories per projection, has been obtained using k=3, denoting a confidence interval of 99.7%. For a number of 10^9 histories per projection in calibration

simulations, the Coefficient of Variance (% CV) of the average air-kerma-in-air simulation was 1.5%. In validation simulations, $20*10^6$ histories were applied per projection resulting in an average simulation uncertainty smaller than 2 % in all cases. Therefore, the overall uncertainty for dose calculations, including the uncertainty due to the relatively flat energy dependence of the chambers in the small energy range of the spectra in the study, was considered about 6%.

Table 1.3 presents the measured HVL values at the operating voltage of each scanner and the resulting energy spectra (Figure 1.6) which were obtained via the SPEKTR tool and were used to produce the scanner-specific ESMs. The ratios of the output at each measurement point to the output at the centre provided the extra attenuation of the filter at each respective directional beam angle ϕ through an iterative procedure where the extra filtration relative to the central filter thickness that reduces the output to the measured value (as determined from the output ratio) was specified. Figure 1.7 presents the relative filter thickness - pathlength of an x-ray photon at each directional angle ϕ through the filter, to the central pathlength.

Table 1.3 Measured HVL at the operating voltage of each CBCT scanner

Scanner	kV	HVL (mmAl)
Promax 3D Max (Planmeca, FI)	96	9.05
Accuitomo 170 (Morita, JP)	90	4.21
CS 9300 (Carestream, USA)	80	5.64
	85	5.95
NewTom 5G (QR S.R.L, IT)	110	4.75
NewTom VGi-evo (QR S.R.L, IT)	110	8.43

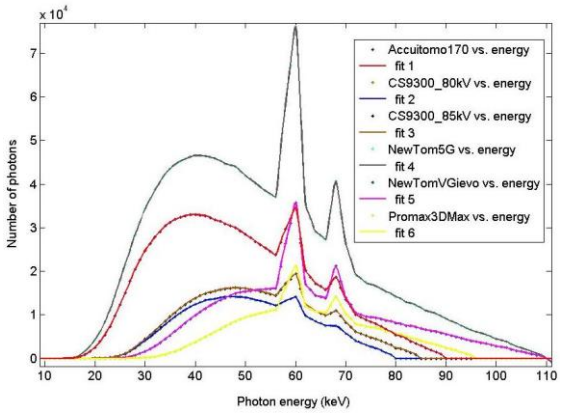

Figure 1.6 The energy spectra of the scanners in the study at their specific operating voltage

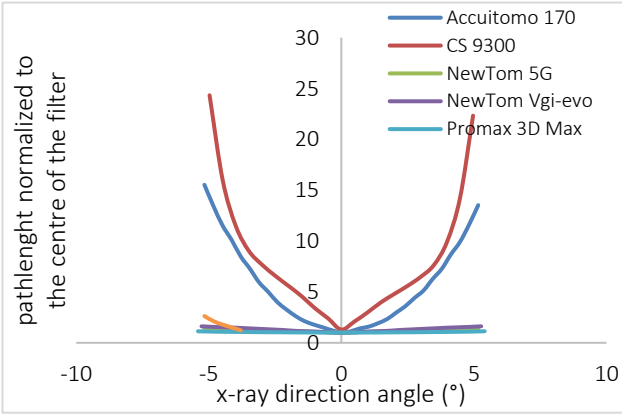

Figure 1.7 The relative filter thickness – pathlength of photons for different x-ray angles

For Promax 3D Max, Accuitomo 170, CS 9300, and NewTom VGi-evo the MC code was validated against dose in water measurements at 7 different IC positions (A-G, figure 1.4a) for every protocol in table 1.2. The % Δ between measured and simulated dose values was subsequently calculated. The validation procedure involved a total of 301 simulations (43 protocols in total, 7 IC positions). Table 1.4 presents the maximum % Δ value, the FOV and the position of the IC within the FOV for which the maximum % Δ was observed for each scanner. For NewTom 5G, the MC framework was validated via $CTDI_{w,IEC3.0}$. Table 1.5 presents the measured and the simulated values and their % Δ. Table 1.6 presents the results of the TLD-based validation procedure. The TLD and simulated doses to the brain, the eyes, the thyroid and the cranium and their % Δ are displayed.

Table 1.4 Maximum validation values indicated as %Δ difference between measured with IC and MC calculated values for each scanner and the respective IC position

Scanner	Promax 3D Max	Accuitomo 170	CS 9300	NewTom VGi-evo
FOV (cm²)	13 x 16	14 x 10	17 x 13.5	15 x 12
IC position	D	A	A	D
Max % Δ	4.6	-3.1	3.6	-5.9

Table 1.5. Validating NewTom 5G via $CTDI_{w,IEC3.0}$

FOV (cm²) (diameter x height)	Monte Carlo $CTDI_{w,IEC3.0}$ (mGy/mAs)	Measured $CTDI_{w,IEC3.0}$ (mGy/mAs)	% Δ
6 x 6	0.123	0.116	5.7
15 x 5	0.202	0.195	3.5
15 x 12	0.215	0.212	1.4
18 x 16	0.225	0.228	-1.3

Table 1.6. MC validation against TLD measurements

Organs	Promax 3D Max 10 x 9 cm²			Promax 3D Max 10 x 5 cm²			NewTom VGi-evo 8 x 8 cm²		
	TLD (mGy)	MC (mGy)	% Δ	TLD (mGy)	MC (mGy)	% Δ	TLD (mGy)	MC (mGy)	% Δ
Brain	0.52	0.50	-2.6	0.49	0.47	-5.6	0.33	0.31	-6.1
Eyes	1.82	2.03	12.0	1.67	1.94	16.1	0.99	1.09	10.1
Thyroid	5.32	5.13	-3.6	5.04	4.87	-3.3	0.78	0.74	-5.1
Cranium	1.17	1.11	-4.6	1.13	1.09	-4.9	0.89	0.92	3.4

1.4 Discussion

In present study, an EGSnrc-based MC framework was customized, calibrated and validated for five different scanners. The simulation of the x-ray source is based on ESMs, and hence, the code is flexible and easily adjustable to any scanner since only physical measurements are required as an input. Protocol-specific calibration factors were produced and validated in homogeneous (water/PMMA) and inhomogeneous media (anthropomorphic phantom). The energy spectra illustrated in figure 1.6 are totally different from each other, and this is a reason for the wide range of doses observed in CBCT imaging. Figure 1.7 displays the total filtration through which x-rays pass before exposing a patient at each scanner. Most scanners employ flat filters, apart from Accuitomo 170 and CS 9300 which have a bow-tie-like, beam-shaping filter. The air kerma measurements for the filter description inherently account for the heel effect which is included in the weighting factors employed to the code. This is the reason why the filtration curves slightly deviate from symmetry along the anode-cathode axis (this can be more easily observed in case of Accuitomo 170 and CS 9300 curves, fig 1.7).

The validation results in homogeneous media are presented in tables 1.5 and 1.6. The maximum % Δ between measured and simulated values was -5.9% in the case of the 15 x 12 cm² FOV in NewTom VGi-evo. Negative % Δ denote higher measured values while positive ones correspond to higher simulated ones. Table 1.4 also reveals that the highest % Δ corresponded to positions A and D. Positions A and D were always found close to the edges of the FOV (figure 1.4a). The reason why the highest % Δ were observed in those positions lies in the implementation of the ESM to the code. As mentioned, the total

filter description was based on air kerma measurements along the x-axis (figure 1.1) and hence, the filtration of the x-ray tube was only centrally characterized (along the corresponding filter x-axis). All the points of the filter along the y-axis passing through a given point in the x-axis (x,yi) were considered to have equal thickness. This means that the code does not take into account any slight differences in the path length of a photon which crosses the filter centrally versus diagonally at an upward or downward trajectory.

Table 1.6 presents the validation measurements against TLDs in an anthropomorphic 5 years-old phantom. The highest % Δ was observed in the dose to the eyes. This is due to the fact that TLDs were positioned externally on the surface of the phantom, while the MC dose was specified in the dedicated internal holes. The % Δ for the rest organs was ranging between -4.6% (cranium) and -2.6% (brain) for the 10x9 cm^2 and between -5.6% (brain) and -3.3% (thyroid) for the 10x5 cm^2 FOVs in Promax 3D Max and between -6.1% (brain) and 3.4% (cranium) in NewTom VGi-evo.

The reported in literature %Δ values between measured and simulated doses range between 1.3 and 1.8% (Khatonabadi et al 2012) and -4.8 to 2.2% (Li et al. 2011). Long et al (2013) reported average differences of 3.5% and 3.9% for the head and body CTDI phantom while Salvadó (2015) reported percentage errors within a range of ±8% for a cone beam CT.

1.5 Conclusions

An EGSnrc-based MC dosimetry tool was customized for 5 scanners, i.e. for Promax 3D Max (Planmeca, FI), Accuitomo 170 (Morita, JP), CS 9300 (Carestream, USA), NewTom 5G (QR S.R.L, IT) and NewTom VGi-evo (QR S.R.L, IT). The code takes into account geometric and technical specifications of each scanner. It was calibrated to enable absolute dose assessment and validated both in homogenous media against IC measurements and in anthropomorphic models against TLD measurements. The validation results clarify its reliability for accurate dose estimations.

1.6 APPLICATION 1: Investigating the influence of the elemental composition of x-ray tube added filtration on patient dose

It is a common technique in radiography to filter the energy spectrum with added Cu filtration in the x-ray tube to reduce the soft, low energy photons which do not contribute to image but increase the dose as they are mainly absorbed by the patient. The use of Cu filters, apart from reducing the entrance surface dose (ESD) and the skin dose, has been reported to present advantages regarding both image quality and cost (Koedooder et al 1986, Shrimpton et al 1988, Nicholoson et al 1995, Wandl-Vergesslich 2000). In the dental CBCT market, there are a few CBCT scanners which already employ Cu filters. The purpose of the study was twofold: to investigate the influence of Cu filtration on patient dose in dental CBCT imaging and to examine whether the exact composition of the filtration is required for accurate MC dose calculation.

1.6.1 Methods and Materials

The study was based on a scanner with an existing Cu filtration. Promax 3D Max has an added filtration in the tube of 0.5 mm Cu plus 2.5 mm Al which, along with the inherent filtration and any other source of filtration, produces an x-ray beam of 9.05 mmAl HVL. From these data, it follows that the inherent (and other) filtration is equivalent to 4.04 mmAl. This is the extra filtration which is required as a supplement to the nominal added filtration to result in the measured HVL value (9.05 mmAl). We designed theoretical ESMs for different filter combinations following the procedure in figure 1.8. The

equivalent energy spectrum of the ESM was defined immediately after the added filtration at point A. With the use of Spektr tool in Matlab, energy spectra for different Cu and Al configurations were designed; 6 spectra for filtrations of 0 mmCu + 2.5 mmAl to 0.5 mmCu + 2.5 mmAl in 0.1 mmCu steps and 3 spectra from 0 mmCu + 2.5 mmAl to 0 mmCu + 10 mmAl in 2.5 mmAl steps. All the energy spectra defined at point A had to pass through the initially determined extra 4.04 mmAl.

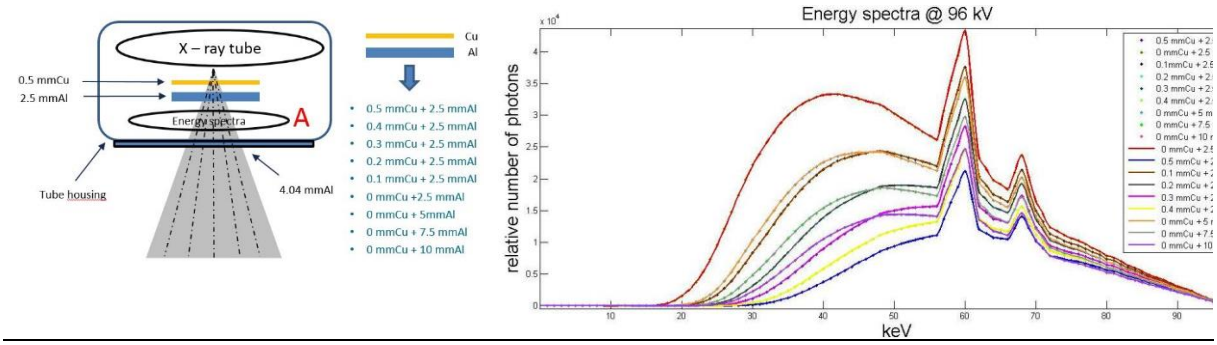

Figure 1.8 Producing different energy spectra for different Cu and Al configurations. All spectra are defined at point A

Each of the above-mentioned spectra has a different HVL value and a different output implying that in a clinical case each of them requires a different tube load (mAs) to provide the same amount of energy to the detector. A simple experiment via ray tracing was therefore set up to specify a compensation factor Cf , which reflects the relative number of photons for each spectrum that provides the same amount of energy to the detector. The procedure is displayed in figure 1.9: for each spectrum the output I_o at the tube exit was calculated with Spektr tool. Each spectrum was subsequently directed towards a 15 cm cube of water and the output I_1 at the at the exit level of the beam was determined. The output at this level (Part IV, figure 1.9) serves also as an input to the detector. For a given required dose to the detector D_{det}, the compensation factor is given by the following equation 1.3:

$$C_f = (D_{det}/I_1) * (I_0/I_1) \quad \text{(eq. 1.3)}$$

The first ratio (D_{det}/I_1) specifies the number of photons for each beam, required to provide a certain amount of dose D_{det} to the detector. The second ratio (I_0/I_1) is to estimate the number of required photons back at the x-ray tube level for the given absorption of the phantom.Each C_f (of each spectrum) was normalized to the C_f of the basic spectrum (0.5 mmCu + 2.5 mmAl), i.e. the C_f of the basic spectrum was considered to be equal to one.

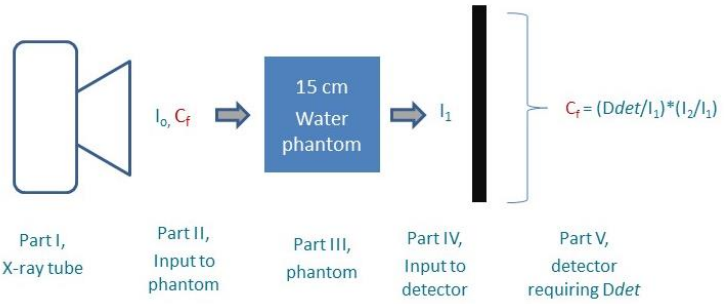

Figure 1.9. Experimental set up to determine the compensation factors Cf

Each energy spectrum was directed towards the anthropomorphic adult male Zubal voxel model (Zubal et al 1994) and organ doses were calculated for a typical 13 x 9 cm² upper-lower jaw protocol (figure 1.10). We only used the 56 slices of the model which correspond to the head and neck region. The in-

plane number of voxels is 512 x 512 with a resolution of 0.5 mm while the longitudinal resolution is 5mm. As the thyroid was not segmented, we further designed two ellipsoids along the trachea to enable thyroidal dose estimations. Tissue compositions and densities were obtained from ICRP 2009.
To compensate for the different mAs which are required such that each spectrum delivers the same amount of energy to the detector, the MC calculated doses were multiplied by the spectrum-specific compensation factor C_f (eq 1.4):
Organ dose = MC dose *C_f (eq. 1.4)
A number of 10^7 histories per projection at 1° angular steps were simulated with the same physics-related simulation parameters mentioned in 1.2.1; since it was not feasible to calibrate the framework for each spectrum, i.e. to obtain calibration factors f_{MC} as that would require access and intervention to the x-ray tube to alter the filtration, only the MC calculated organ dose values for a total number of $2.1*10^9$ are presented.

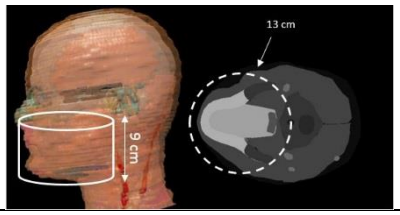

Figure 1.10 The anthropomorphic Zubal adult male voxel model and the FOV position in the head

1.6.2 Results

Table 1.7 presents the different filter configurations, their HVL values and the respective compensation factors.

Table 1.7 Filter combinations that were used in the study, their HVL and C_f compensation factors

Filtration		Spectrum number # (ID)	HVL (mmAl) at 96 kV	C_f
0 mmCu + 2.5 mmAl	+ 4.04 mmAl	Spec 1	6.10	1.43
0.1 mmCu + 2.5 mmAl	+ 4.04 mmAl	Spec 2	7.03	1.26
0.2 mmCu + 2.5 mmAl	+ 4.04 mmAl	Spec 3	7.72	1.16
0.3 mmCu + 2.5 mmAl	+ 4.04 mmAl	Spec 4	8.24	1.09
0.4 mmCu + 2.5 mmAl	+ 4.04 mmAl	Spec 5	8.67	1.04
0.5 mmCu + 2.5 mmAl	+ 4.04 mmAl	Spec 6	9.05	1.00
0 mmCu + 5 mmAl	+ 4.04 mmAl	Spec 7	6.76	1.33
0 mmCu + 7.5 mmAl	+ 4.04 mmAl	Spec 8	7.29	1.22
0 mmCu + 10 mmAl	+ 4.04 mmAl	Spec 9	7.75	1.16

Figure 1.11 presents the results of the study. Organ doses were assessed for skin, eye lenses, salivary glands, thyroid, brain, oral mucosa, oesophagus, extra thoracic tissue (ET) and muscles. The graphs present the simulated dose values versus the HVL of the beam. The points in blue correspond to non-Cu filtrations (Spec 1, 7, 8 and 9) whereas the red ones denote Cu-filtrated spectra (Spec 2, 3, 4, 5 and 6).

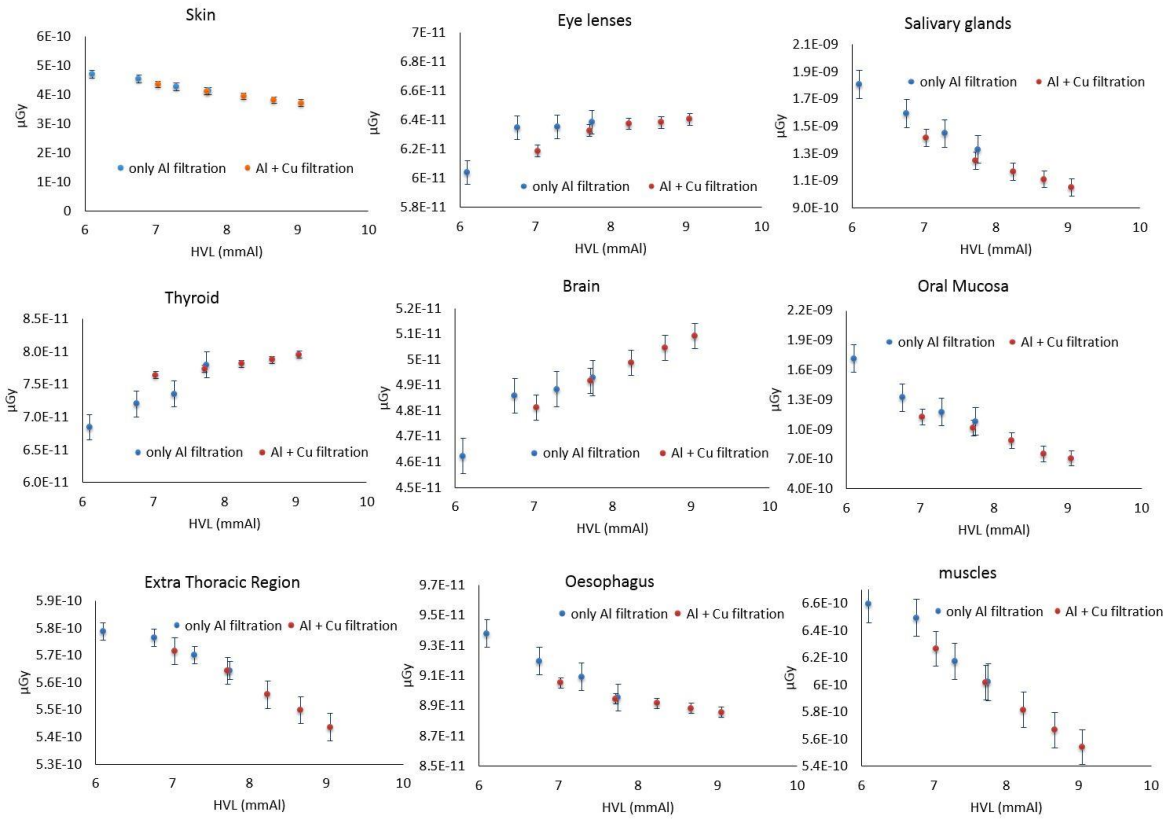

Figure 1.11 MC calculated organ doses for different filter combinations

1.6.3 Discussion and Conclusions

In present study the influence of Cu filtration in the x-ray beam was investigated. Organ doses were calculated by directing each beam towards the Zubal anthropomorphic voxel model for a 13x9 cm² FOV. Figure 1.11 shows that there is a clear decrease in the dose to the skin as the HVL increases. The lowest skin dose is observed for the highest HVL beam (Spec 6) which is the real one employed by Planmeca in the Promax 3D Max (0.5 mmCu + 2.5 mmAl). Salivary glands, oral mucosa, ET, oesophagus and muscles follow the same dose pattern. Comparing the highest HVL beam (Spec 6, 0.5 mmCu + 2.5 mmAl) to the lowest one (Spec 1, 0 mmCu + 2.5 mmAl), there is a 26% dose reduction to skin, 71% dose reduction to salivary glands, a 145% dose reduction to oral mucosa, a 20 % dose decrease in the dose to muscles and a 5% drop for the dose to ET and oesophagus. On the contrary, there is an increasing dose trend with HVL for the thyroid, brain and the lenses of the eye. Comparing again Spec 6 to Spec 1, there is a 14% increase in the dose to thyroid, a 10% to brain and 6% to eye lenses.

It shall be noted that the impressive dose reduction to oral mucosa can be attributed to the voxel model itself rather than to the influence of the filtration. This is due to the fact that oral mucosa, which should have been the mucous outline of the entire mouth cavity, was considered to be a layer adjacent to teeth (figure 1.12). In such a segmentation, oral mucosa surrounds a very high attenuating region (teeth), is very influenced by the stopping power of the teeth, and when the beam has a larger low energy content (Spec 1 vs Spec 6) the dose to oral mucosa increases considerably.

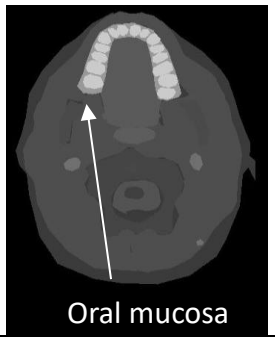

Figure 1.12 The grey region surrounding teeth is considered as oral mucosa in the Zubal phantom

As the beam filtration (and the HVL) increases, the mean energy of the beam also increases and the x-ray photons become more penetrating. This has a double influence on the dose. For those organ-tissues which are in the primary radiation field there is a dose reduction (skin, salivary glands, muscles, oral mucosa, ET and oesophagus) as a higher number of photons escape without being absorbed, and therefore deposit a lower amount of energy in the tissue, and a larger amount of photons reach the detector. The organs which are outside the primary field (eye lenses, thyroid and brain) are only exposed to scatter. The higher energy beams produce more scatter and therefore the dose to these organs increases with HVL. However, the high decrease in the dose to the organs in the primary field counteracts the slight increase to those organs outside the radiation field.
In conclusion, Cu filtration is beneficial for the dose to the patient. The exact composition of the added x-ray tube filtration is required for accurate MC dose simulations.

1.7 APPLICATION 2: Investigating the impact of the shape of x-ray tube added filtration on patient dose

Beam shaping filters, i.e. the so-called bowtie filters, are widely applied in MDCT imaging to modify the spatial distribution of the emitted x-rays. While the exact morphology is proprietary information, the filter has a thickness that increases towards the edges (figure 1.1). As a result, bowtie filters modulate the axial beam profile by increasing the photon fluence at the centre and reducing the beam intensity towards the periphery; this is to compensate for the higher central absorption of the beam at the centre of the object or patient (longer path length) compared to the periphery. By means of the bowtie filter a more uniform photon fluence, with unchanged local contrasts, is obtained at the detector (Tack and Gevenois 2007, Buzug 2008). This allows to cope with the limited dynamic range of the detector, or, in other words, the detector can be tuned for a smaller dose level range. Furthermore, bowtie filters provide a more uniform spectrum to the detector which enables a better calibration of the resultant Hounsfield Units. In dental CBCT imaging, bowtie filters are also being introduced by vendors. The presented axial beam profiles (figure 1.7) testify that Accuitomo 170 and CS 9300 employ such beam shaping filters. The purpose of this study was to evaluate the influence of such filters on radiation dose and to check whether detailed data of the filter thickness is required for accurate MC dose assessment studies.

1.7.1 Methods and Materials

This study was performed with data of the Accuitomo 170 scanner. According to its ESM assessment (described in section 1.3), the central thickness of the total-beam shaping filter was found to be 2.5 mmAl, which along with the inherent filtration produces an x-ray beam of 4.21 mmAl HVL at 90kV

(table 1.3). The ESM that served as an input to the MC code was characterized by producing an equivalent energy spectrum that has been filtered by a 2mmAl beam and that has to pass next through an extra bow tie filter with a central thickness of 0.5 mm and with increasing thickness towards the edges as the air kerma measurements for the filter description indicated (figure 1.13). As the beam crosses the bowtie shaped part (part B) of the filter, the axial attenuating profile becomes that of figure 1.7.

To compare bow-tie vs flat filtration, a theoretical flat filter, 0.5 mm thick, was designed to replace the bowtie part (B). The equivalent spectrum had to pass through the designed flat filter before exposing a patient. The path length through the designed flat filter for different photon angles θi was calculated based on a simple mathematical equation (eq 1.5):

$$x_i(mm) = 0.5/\cos\partial_i \text{ (eq. 1.5)}$$

For each path length (in $\partial_i = 1°$ angular steps), the absorption for each photon energy of the equivalent energy spectrum was calculated. The mathematical formula (eq. 1.5) is not capable of taking heel effect into account. The deviation from symmetry, which is due to heel effect that is present regardless of the filter shape, was calculated for the path length curve of Accuitomo 170 (fig 1.7). Therefore, at each path length x_i an extra contribution, equal to the deviation from symmetry in fig 1.7, was added to compensate for the heel effect. The x-ray absorption through the flat filter (plus the heel effect contribution) for each photon energy of the equivalent spectrum was calculated and employed to the code via weighting factors. In both cases, the central thickness of the filter is equal and so is the HVL of the two beams. As the calibration measurements take place centrally (chapter 1.2.2) the calibration factor for the bow-tie and the flat filter case would be identical.

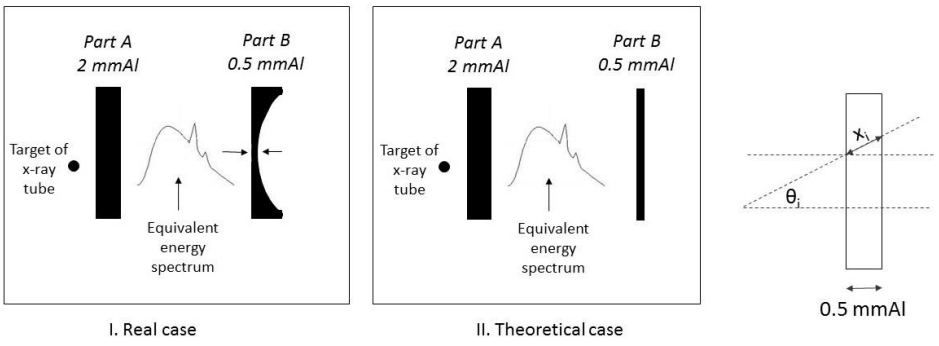

Figure 1.13 left image: The equivalent source model is established after a 2 mmAl flat filter and passes through a bowtie of 0.5 cm central thickness – real case scenario. Middle: Instead of passing through the bowtie, the beam passes through a theoretical 0.5 cm flat filter – theoretical scenario. Right: For each x-ray angle ∂_i, the ray path xi through the flattening filter is calculated.

Both ESMs were directed towards the standard female anthropomorphic voxel model (ICRP, 2009) and organ doses were calculated for a typical 10x10 cm², standard resolution (90 kV, 5 mA, 17.5 sec) full rotation upper-lower jaw protocol. Only 59 out of 346 slices of the voxel model, from slightly below the neck region up to the crown of the head, were used in the study. The in-plane resolution of the voxel model was 1.775 mm while the z-axis resolution was 4.84 mm. A total $3.6*10^9$ histories were simulated for a full rotation acquisition in 1° angular intervals under the same physics-related simulation parameters as those mentioned in 1.2.1.

1.7.2 Results

Table 1.8 summarizes the results of the study, in terms of absorbed doses to radiosensitive organs. The average statistical simulation uncertainty in terms of % CV for the number of simulation histories was less than 0.1%.

Table 1.8 Organ dose comparison between bowtie and flat filtration

Organs	Flat filter	Bowtie filter	% decrease
	Absorbed organ doses (μGy)		
ET	5002	4146	-17%
Oral mucosa	7067	6326	-10%
Brain	189	167	-11%
Eye lens	542	460	-15%
Lungs	3.2	2.8	-12%
Lymphatic nodes	283	237	-16%
Muscles	116	97	-16%
Oesophagus	298	249	-16%
Salivary glands	5075	4206	-17%
Skin	158	126	-21%
Thymus	20	17	-12%
Thyroid	566	492	-13%
RBM	128	109	-15%
Bone Surface	594	505	-15%

1.7.3 Discussion and Conclusions

In this study the influence of a beam shaping filtration on organ doses was examined. The investigated exam was a typical 10x10 cm² standard resolution protocol for an adult female patient undertaken in Accuitomo 170 with and without bowtie filtration. The analysis showed that the use of bowtie filtration reduces the dose to all radiosensitive organs by 15% on average (maximum decrease 21% for skin dose, minimum 10% for oral mucosa). As expected, the skin was the tissue which benefits most from the bowtie as the reduced photon fluence towards the edges of the axial FOV (diameter) results in less skin exposure at each projection. The lowest decrease in the dose to oral mucosa can be attributed to the fact that oral mucosa is centrally positioned in the FOV, and therefore the influence of the bowtie is not as pronounced as it is towards the edges of the axial FOV. Present study is in line with another study investigating the influence of bowtie in a Scanora 3D system (Soredex, FI): dose reductions with bowtie were reported (compared to a flat filter) which from 8.7% at the centre to 53.8% at the periphery of a 16cm cylindrical water phantom (Zhang et al 2013b). These organ dose reductions indicate that detailed simulation of bowtie filtration is required for accurate dose calculations.

1.8 APPLICATION 3: Investigating the impact of Tube Current Modulation on patient dose in dental CBCT scanners

When the use of MDCT scanners rapidly increased in the beginning of this century, there was an unquestionable need to optimize the exposures. To this end, CT manufacturers gradually began to equip their scanners with systems that were able to adjust the exposure factors according to the attenuation characteristics of the patient and the scanning volume. These so-called Tube Current Modulation (TCM) or Automatic Exposure Control (AEC) systems adjust the tube current either along

the z-axis of the patient (longitudinal TCM), or at each projection (x-y or angular or rotational TCM), or they simultaneously combine both mA adaptation methods (3D TCM) (McCollough et al 2006). The TCM systems are based on different specification criteria; some manufacturers aim to provide uniform noise across the scanning volume whereas some others aim to provide lower noise for smaller patients (Li et al 2014). TCMs were mainly employed in body scans, yet recently, their use has been extended to head acquisitions (AAPM 2015, 2016).

Contrary to MDCTs where most of the state-of-the art scanners are nowadays equipped with TCM systems, in dental CBCTs this technology has not been widely employed yet. In most cases, the tube current is fixed during rotation and the mAs are predefined for each operation mode; higher resolution mode acquisitions are carried out with higher x-ray tube load. In dental CBCT scanners the paired x-ray tube – detector systems perform one rotation around the head of a patient, apart from large field of view (FOV) imaging, i.e. full head CBCT protocols, where some systems carry out two consecutive rotations and use a stitching technique to image the entire scanning volume. Therefore, the appropriate type of a modulation system dedicated for CBCT scanners would be a rotational TCM. Most rotational TCM systems in MDCTs nowadays are attenuation-based, requiring on-line feedback for the attenuation properties of the scanning volume to modulate the current accordingly. This approach requires fast electronic circuits and powerful generators which are not available in most CBCT scanners. However, as it was the case in the first rotational TCM approach in GE scanners (General Electric (GE) Healthcare Technologies, Waukesha, WI), i.e. the Smart Scan, the current modulation could be pre-programmed, following a predetermined mathematical function during rotation (McCollough et al 2006). Such a pre-programmed approach is not purely patient-specific and attenuation-based, yet it does not require sophisticated electronic circuits and is more easily implemented in systems with lower generator capacities. Two review articles by Pauwels et al (2015b) and Kiljunen et al (2015) reported that there was no CBCT scanner equipped with a TCM system at the time of the publication. Meanwhile, TCM systems gradually began to be employed in dental CBCT scanners. NewTom VGi-evo introduced the Safe Beam technology as an approach to modulate the current. Every exposure in this scanner is carried out under a preprogrammed TCM scheme.

A MC study based on the TCM scheme of NewTom VGi-evo was conducted with a threefold aim: (1) to assess the influence of the preprogrammed TCM (‘Safebeam’) on organ doses; (2) to compare ‘Safebeam’ with a theoretical attenuation-based TCM scheme; (3) to investigate whether reliable MC dose calculations can still be carried out when data regarding the TCM scheme, which is considered proprietary, is not available.

1.8.1 Methods and Materials

NewTom VGi-evo has the typical dental CBCT orientation, i.e. the patient is sitting on a chair during the exposure. Every protocol is carried out at 110 kV with the x-ray tube-detector system performing one full rotation around its centre of rotation. Like any scanner equipped with TCM systems, the modulation curve is based on pre-scan projection radiographs. In the case of NewTom VGi-evo, an anterior-posterior AP prescan acquisition, where the beam crosses the most attenuating part of the head, and a lateral (LAT) one, through the least attenuating volume, are carried out. These two radiographs define a maximum mA value for the AP projection and a minimum mA for the LAT one (figure 1.14). Subsequently, a mathematical formula takes into account these two mA values and predefines the mA value at each projection. The mathematical formula is considered proprietary data and no details are available. However, for the purpose of this study, the manufacturer provided the mA values per projection for the protocols under investigation.

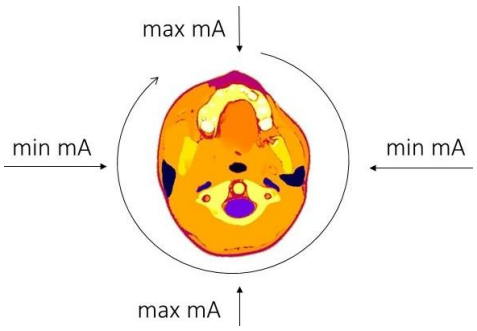

Figure 1.14 The mA per projection changes from a maximum AP mA to a minimum LAT mA value, based on a mathematical formula (proprietary data of QR S.R.L., Verona, IT)

1.8.1.1 Study I. TCM vs fixed current acquisitions

To investigate the impact of TCM on organ doses, a comparison study between TCM-driven protocols and fixed current (mA) acquisitions was carried out. Five pediatric patients that had already been scanned in NewTom VGi-evo with TCM were extracted from the PACS database of the hospital. The acquisition parameters are displayed in table 1.9.

Table 1.9 Acquisition parameters of the 5 patients participated in the NewTom VGi-evo TCM evaluation study

Patient #	Age	FOV (cm^2)	Clinical indication	Mode*	I LAT (mA)	I AP (mA)	Exposure time (sec)	Total mAs
1	7	8x5	Cleft palate	Standard	3	9	1.8	9.3
2	7	5x5	Upper Incisors	High Res	5	10	4.3	31.6
3	8	5x5	Upper Incisors	Standard	3	12	1.8	11.8
4	12	10x5	Cleft palate	Standard	4	13	1.8	15.4
5	12	16x16	face	Standard	3	6	1.8	8.1

*All exposures are performed at 110 kV

As NewTom VGi-evo does not operate in a fixed-current mode, it was considered that the most attenuating AP projection of the prescan radiograph would define the required mA that results in an acceptable, noise-free image quality. In other words, in real case TCM protocols, the current at each projection modulates between I LAT (min mA) and I AP (max mA), while in a fixed-mA protocol, the current would always be equal to I AP. The current is delivered in a pulsed mode with pulse time being equal to the total exposure time divided by 360 pulses per rotations. Therefore, for TCM protocols, the total mAs per rotation is given by equation 1.6

$$mAs_{tot,TCM} = \sum_i \left[(mA)_i * s_i\right] \quad \text{(eq. 1.6)}$$

where i refers to each projection, $(mA)_i$ to the current at each projection and $s_i$to the pulse time. For fixed current acquisitions, the total mAs per rotation is given by eq. 1.7

$$mAs_{tot,fixed} = I_{AP}\,(mA) * total\ exposure\ time\ (sec) \quad \text{(eq. 1.7)}$$

In this study, we used total exposure time as provided in table 1.9. Table 1.10 presents the total mAs for TCM-based and fixed mA acquisitions.

Table 1.10 X-ray tube exposure parameters for TCM and fixed current acquisitions

Patient #	ITCM (mA)	$mAs_{tot,TCM}$	Ifixed (mA)	$mAs_{tot,fixed}$
1	3-9	9.3	9	16.2
2	5-10	31.6	10	43
3	3-12	11.8	12	21.6
4	4-13	15.4	13	23.4
5	3-6	8.1	6	10.8

For the purpose of this study, three voxel models of 7 (Guozhi), 8 (Peter) and 12 years old (Mike) were designed (figure 1.15). More details on the voxelization procedure, the specifications of each model, the segmented organs and the full voxel model database are provided in the following chapter 2.

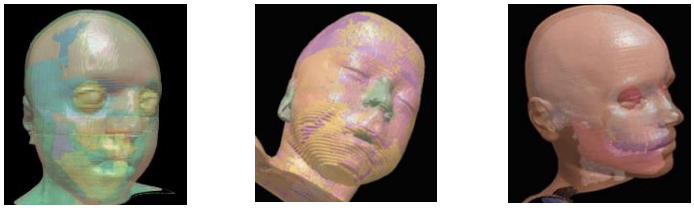

Figure 1.15 Guozhi, Peter and Mike voxel models

1.8.1.2 Study II. Are dose calculations reliable if the TCM is not simulated?

As already mentioned, the mathematical formula which provides $(mA)_i$ is proprietary data, and it was only for the purpose of this study that data became available. Therefore, it was necessary to investigate whether MC dose calculations can still be reliable without any data on the modulation curve.
In the DICOM header of each protocol, the total mAs after exposure is recorded. This is the $mAs_{tot,TCM}$ that equation 1.6 provides, yet without any info on the current modulation $(mA)_i$. The total mAs per rotation was included in the last column of table 1.9. Present study runs MC calculations for (1) a fully characterized TCM curve and for (2) fixed tube current, and compares organ doses for the same x-ray tube load (mAs). In the previous paragraph, the fixed protocol uses the maximal mA, in order to study the dose reduction potential of TCM. Here we compare to the full information to using the averaged TCM curve, to investigate the necessity of having all TCM input.

1.8.1.3 Study III. Preprogrammed TCM ('Safebeam') vs attenuation-based TCM

In this third study we investigated the case of a 12 years old male patient who underwent an 8x8 cm² (diameter x height of the cylindrical FOV) upper/lower jaw protocol, a 5x5 cm² lower premolar and a 5x5cm² upper premolar acquisition. The centre of the FOV in the 8x8cm² protocol is longitudinally positioned between the upper and the lower and axially around the centre of the mouth cavity and hence along the midline of the head. On the other hand, in 5x5 cm² acquisitions, the centre of the FOV is axially offset to the midline, i.e. around the premolars (figure 1.16). This asymmetrical position may influence the operation of the TCM, especially in preprogrammed TCM systems. Based on the two prescan-defined AP and LAT mA values which are illustrated in table 1.11, the x-ray tube current values at each projection were calculated based on the proprietary preprogrammed mathematical formula which was provided by the manufacturer.

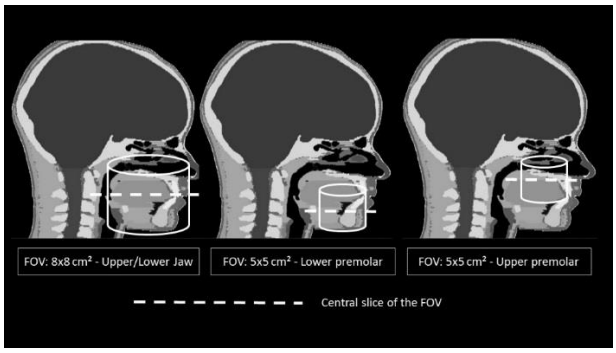

Figure 1.16 The FOV position in the mouth cavity for the three investigated FOVs. The dashed line indicates the central slice of the scanning volume

Table 1.11 Protocol exposure factors

Protocol	8x8 cm² (upper / lower jaw)	5x5 cm² (lower premolar)	5x5 cm² (upper premolar)
Operation mode*	Normal / Regular	High Resolution	Normal / Regular
AP mA	7.5	13	5.6
LAT mA	3.7	6	3
Total scan time/rotation	1.8	4.32	1.8
Total mAs/rotation	9.76	41.34	7.71
*All exposures are performed at 110 kV			

The 'Safebeam' TCM program that NewTom VGi-evo employs is not a fully patient-specific modulation technique. The extreme mA values may be specified according to individual patient anatomic details as they are based on the AP and LAT prescan acquisitions, yet the TCM scheme itself is based on a preprogrammed mathematical formula which is fixed. A fully patient-specific modulation curve would modulate the current according to the attenuation that the x-ray beam undergoes at each projection, i.e. attenuation-based modulation curve.

Keat (2005) showed in a previous study that in MDCT scanners the logarithm of the tube current (mA) increases linearly with phantom diameter. Based on this result, Li et al (2014) developed theoretical TCM schemes in different modulation strengths for thorax and abdomen-pelvis CT exposures for a female cardiac-torso (XCAT) phantom to investigate their impact on patient dose. We adopted the same methodology to assess attenuation-based TCM schemes for the three investigated protocols and we subsequently employed each theoretical attenuation-based scheme in the NewTom VGi-evo scanner.

In the case of a CT scanner the effective mAs (mAs/pitch) at each projection angle θ is given by the following equation

$$eff\ mAs_{\theta} = eff\ mAs_{ref}\left(\frac{A_{\theta}}{A_{ref}}\right)^{a} \quad \text{(eq. 1.7)}$$

where Aθ is the attenuation of the beam at each projection-gantry angle θ, Aref is a reference attenuation, mAsref is the corresponding reference exposure value and α indicates the modulation strength. Since in dental CBCTs the scanner performs only one rotation, we reformatted the previous equation to

$$mA_{\theta} = mA_{ref}\left(\frac{A_{\theta}}{A_{ref}}\right)^{a} \quad \text{(eq. 1.8)}$$

as the pitch is an irrelevant term for dental CBCT exposures and the pulse time at each projection is constant. In eq. 1.8 mA_{θ} corresponds to the x-ray tube current at each projection and mA_{ref} to the current for a reference attenuation. A modulation strength of $\alpha = 0$ implies no modulation, i.e. the mA per projection is fixed. When the modulation strength is equal to $\alpha = 1$, the noise is constant in all

projection whereas α = 0.5 has been shown to provide the minimum noise at a given dose level (Gies et al 1999, Li et al 2014).
The attenuation values in equation 1.8 were calculated via raytracing using the 'fanbeam' function in Matlab (version 7.12.0.635, R2011a, MathWorks Inc). This function considers the central pixel of the DICOM image as the centre of rotation. However, in our case the centre of rotation should coincide with the anatomy of interest, i.e. the centre of the mouth cavity for the 8x8cm² protocol, the upper premolar tooth for the 5x5 cm² upper premolar protocol and the lower premolar tooth for the 5x5 cm² lower premolar protocol. The central slices which corresponded to the centre of the FOV along the longitudinal z-axis were extracted and were further processed (dashed lines in figure 1.16) such that their central pixel coincides with the anatomy of interest. It shall be noted that the DICOM images that were used for raytracing were the ones which were used to voxelize the models, i.e. head and neck MDCT images (further discussion in chapter 2).
Figure 1.17 illustrates the processing of the central image in the case of the 8x8 cm² protocol. The 512x512 pixel dimensions of the original images were not sufficient to reposition the head. Therefore, we first converted each image from 512x512 to 1024x1024 pixels (figure 1.17, middle image) and we subsequently applied geometric, axial translation corrections to bring the centre of the clinical volume at the centre of the image (figure 1.17, right image).

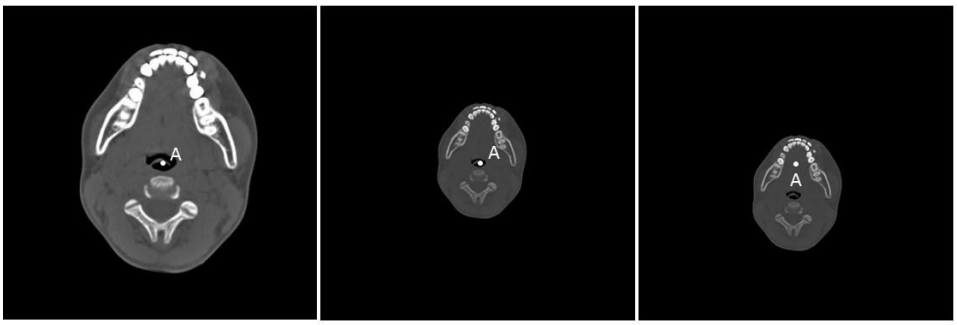

Figure 1.17. Point A corresponds to the central pixel; on the left the initial central 512 x 512 central image is shown; in the middle, the same image is illustrated after having been converted to 1024x1024; geometric offset corrections were applied to get the centre of the mouth cavity at the centre of the image (right image)

To calculate the attenuation per projection via raytracing we created a linear attenuation coefficient (μ) map of each central CT slice by converting the Hounsfield Units (HU) of each voxel to μ values, based on the HU definition formula and the μ_w and μ_{air} values for the Newtom VGI-evo energy spectrum. The raytracing was carried out for 360 projections in 1° steps. We only tracked the central 12 rays of the raytracing at each projection which form a radiation beam of 1.5x1.5 mm² (vertical x axial) at the centre of the detector. The vertical dimension of the beam (1.5 mm) is deduced by applying the geometric magnification factor of the scanner to the 1mm thick central image, while the transverse one is extracted by multiplying the number of the tracked rays (12) with the detector pixel size. The average attenuation of the 12 rays per projection was calculated to specify the A_θ values in equation 3.
The reference attenuation A_{ref} and the associated mA_{ref} which are required to calculate the mA_θ at each projection were obtained for each case from the respective AP prescan exposure conditions (table 1). The reason why we considered the AP projection as the reference one is that the AP exposure determines the maximum mA value of the preprogrammed modulation scheme in NewTom VGi-evo scanner. The beam crosses the most attenuating projection and hence, it defines the noise level in the

final image. This means that in the absence of a TCM scheme, the AP mA value would have been the one that would provide the desired noise level in the final image.
We designed theoretical attenuation-based modulation curves for each investigated protocol for modulation strength values from α = 0 to α = 1, in 0.25 modulation strength steps. To ensure that the system is capable of managing the variations in the mA values between successive projections, we fitted a Savitzky-Golay filter to each modulation curve before implementing them to our framework. In such a way, any abrupt changes in the mA modulation curve were smoothed out.
While the total mAs for each protocol, for the 'Safebeam' TCM technique is recorded in the DICOM header after exposure (also based on eq. 1.6, table 1.11), the total mAs for the theoretical attenuation-based protocols is calculated via the following equation 1.9:

$$mAs_{tot,TCM,AB} = \sum_i \left[(mA_\theta)_i * s_i\right] \text{ (eq 1.9)}$$

where i corresponds to each projection, mA_θ is the derived from the equation 1.8 attenuation-based current per projection and s_i the pulse time.
In all studies each TCM was applied in terms of weighting factors to the dose integral of each simulated projection. Each modulation scheme was simulated with 5 million histories per projection, corresponding to a total number of 1.8 billion histories for the 360 simulated projections in 1° steps under the same physics-related simulation parameters as those mentioned in 1.2.1. This number of simulation histories provided very low Coefficient of Variance values (%) in organ dose calculations, resulting in estimated dose uncertainties less than 0.1% for every simulated organ.

1.8.2 Results

1.8.2.1 Results of Study I. TCM vs fixed current acquisitions

In table 1.12 absorbed organ doses (μGy) for TCM and fixed current acquisitions are presented for each patient in the study.

Table 1.12 Calculated absorbed organ dose values (TCM vs fixed, study 1)

	Patient # 1		Patient # 2		Patient # 3		Patient # 4		Patient # 5	
Organ	TCM	fixed	TCM	fixed	TCM	fixed	TCM	fixed	TCM	fixed
	Absorbed organ doses (μGy)									
Brain	145	226	155	185	53	85	172	269	1386	2390
Skin	62	108	117	155	42	76	65	110	168	275
Oesophagus	47	80	67	75	28	39	35	52	66	107
Eye lens	161	283	350	488	95	177	172	337	2647	3728
Muscle	47	80	75	90	34	53	42	61	105	138
ET	581	1019	662	727	225	344	259	383	1009	1507
Thyroid	71	119	292	324	90	140	36	51	96	137
Salivary glands	1472	2793	1654	2132	531	934	1503	3011	2466	5170
Oral mucosa	2169	3792	5040	6915	1551	2846	2016	3944	1813	2765
RBM	50	82	106	130	35	61	59	107	116	233
Bone surface	233	382	508	620	165	286	275	500	540	1082
Lymph nodes	66	120	197	242	54	87	87	130	189	245
% organ dose decrease with TCM (Average all organs)	-41.7%		-18.3%		-39.6%		-39.5%		-37.1%	

1.8.2.2 Results of Study II. Are dose calculations reliable if the TCM is not simulated?

Table 1.13 presents the results of the second study where absorbed organ doses, obtained with TCM acquisitions, are compared to those obtained with fixed current exposures under the same tube load (mAs).

Table 1.13 Calculated absorbed organ dose values (TCM vs fixed, study 2)

	Patient # 1		Patient # 2		Patient # 3		Patient # 4		Patient # 5	
Organ	TCM	fixed	TCM	fixed	TCM	fixed	TCM	fixed	TCM	fixed
	Absorbed organ doses (μGy)									
Brain	145	132	155	142	53	48	172	165	1386	1395
Skin	62	63	117	120	42	43	65	64	168	167
Oesophagus	47	47	67	59	28	22	35	33	66	66
Eye lens	161	163	350	376	95	100	172	174	2647	2657
Muscle	47	46	75	70	34	31	42	39	105	107
ET	581	591	662	562	225	194	259	270	1009	1019
Thyroid	71	71	292	253	90	80	36	35	96	96
Salivary glands	1472	1617	1654	1645	531	529	1503	1563	2466	2490
Oral mucosa	2169	2197	5040	5333	1551	1611	2016	2071	1813	1821
RBM	50	48	106	100	35	34	59	53	116	116
Bone surface	233	246	508	481	165	148	275	281	540	543
Lymph nodes	66	62	197	187	54	53	87	78	189	188
% organ dose change (Average all organs)	0.2%		5.4%		6.8%		2.6%		-0.4%	

1.8.2.3 Results of Study III. Preprogrammed TCM ('Safebeam') vs attenuation-based TCM

Figure 1.18 illustrates the attenuation profiles of the patient for the investigated protocols as calculated with the raytracing. The x-axis represents the projection angle with 0° corresponding to the AP projection and 90° to the lateral one. The y-axis represents the raytracing-based calculated attenuation A_θ values per projection. Table 1.14 demonstrates the reference A_{ref} and mA_{ref} values. It is important to mention that the high mA_{ref} value of the lower premolar protocol is due to the fact that the scan was carried out in high resolution mode compared to the other two protocols which were Normal resolution ones. The attenuation values in figure 1.18 and the reference values in table 1.14 were used to calculate the TCM schemes based on equation 1.8. Figure 1.19 illustrates the smoothed TCM schemes for each FOV.

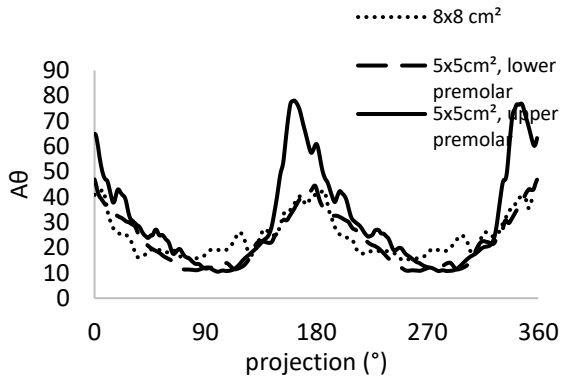

Figure 1.18. Attenuation profile of the patient for the three different FOV - protocols

Table 1.14. Attenuation and x-ray tube current reference values

Protocol	A_{ref}	mA_{ref}
8x8 cm²	40.8	7.5
5x5 cm² / lower premolar	46.9	13
5x5 cm² / upper premolar	64.9	5.6

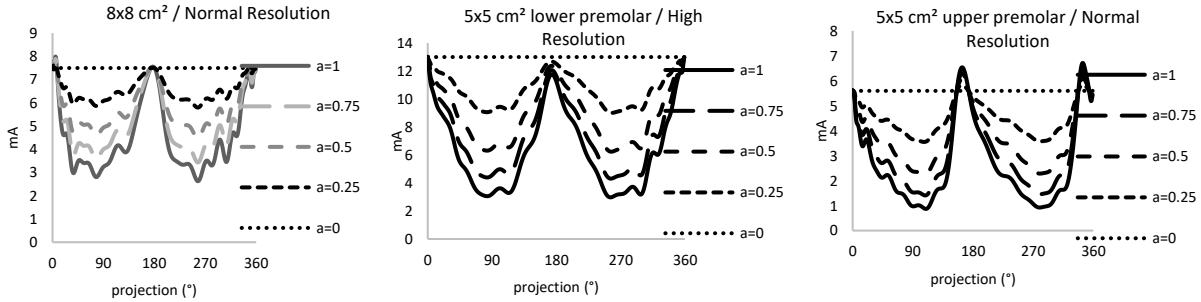

Figure 1.19. TCM schemes (mA_θ vs projection angle) or the 8x8 cm² protocol for different modulation strengths

Based on the above mA_θ values per projection and per modulation strength, each TCM curve was designed and employed to the code in terms of weighting factors, and organ doses were calculated for a total $mAs_{tot,TCM,AB}$ value for each case (eq. 1.9). The $mAs_{tot,TCM,AB}$ for each protocol and modulation strength are presented in table 1.15.

Table 1.15 X-ray tube load (mAs) for attenuation-based TCM exposures (for each protocol and modulation strength) and for 'Safebeam'

α	Safebeam	0	0.25	0.5	0.75	1
8x8 cm² / Normal Resolution						
mAs	9.8	13.5	11.8	10.3	9.1	8.1
5x5 cm² lower premolar / High Resolution						
mAs	41.3	56.2	46	38.2	32.1	27.3
5x5 cm² upper premolar / Normal Resolution						
mAs	7.7	10.1	8.1	6.6	5.6	4.8

Tables 1.16 – 1.18 present the calculated absorbed organ dose values for each case.

Table 1.16. Absorbed organ doses for Safebeam and for attenuation based TCM schemes of different modulation strengths for the 8x8 cm² FOV Normal Resolution protocol

TCM	Safebeam	α = 0	α = 0.25	α = 0.5	α = 0.75	α = 1
Organs	Absorbed dose (μGy)					
Brain	86	112	98	88	79	70
Skin	66	88	77	67	59	53
Oesophagus	59	73	65	57	51	45
Eye lens	159	220	190	166	146	128
Muscle	47	60	54	47	41	38
ET	274	371	322	281	247	218
Thyroid	193	244	216	191	170	155
Salivary glands	1131	1573	1353	1169	1015	885
Oral mucosa	1581	2179	1885	1641	1438	1267
RBM	57	71	63	57	50	47
Bone surface	262	332	295	262	237	214
Lymph nodes	106	137	119	106	92	83

Table 1.17. Absorbed organ doses for Safebeam for attenuation based TCM schemes of different modulation strengths for the 5x5 cm² FOV lower premolar High Resolution protocol

TCM	Safebeam	α = 0	α = 0.25	α = 0.5	α = 0.75	α = 1
Organs	Absorbed dose (μGy)					
Brain	96	126	106	89	76	66
Skin	105	144	117	98	83	73
Oesophagus	94	116	100	86	74	64
Eye lens	124	172	140	116	96	82
Muscle	62	78	66	56	48	43
ET	667	871	727	614	522	450
Thyroid	187	252	207	173	144	124
Salivary glands	2204	3100	2511	2058	1707	1435
Oral mucosa	4043	5878	4694	3798	3115	2590
RBM	76	93	78	68	59	53
Bone surface	353	438	375	324	283	249
Lymph nodes	174	232	193	155	136	117

Table 1.18. Absorbed organ doses for Safebeam and for attenuation based TCM schemes of different modulation strengths for the 5x5 cm² FOV upper premolar Normal Resolution protocol

TCM	Safebeam	α = 0	α = 0.25	α = 0.5	α = 0.75	α = 1
Organs	Absorbed dose (μGy)					
Brain	18	22	19	16	14	13
Skin	22	29	23	19	16	13
Oesophagus	17	17	17	17	11	11
Eye lens	32	43	34	26	22	18
Muscle	15	19	16	14	13	11
ET	190	227	194	169	154	138
Thyroid	45	55	45	40	30	30
Salivary glands	242	308	245	198	162	135
Oral mucosa	873	1194	927	737	600	500
RBM	21	28	22	20	16	15

Bone surface	96	121	99	84	72	64
Lymph nodes	32	40	32	32	24	24

1.8.3 Discussion and Conclusions

Section 1.8 is dedicated to dose-related matters concerning the use of TCM in dental CBCT imaging. In a first study, a clinically employed TCM-system, the 'Safebeam' of NewTom VGi-evo, was tested against fixed-current-acquisitions, for image quality reasons set at the highest mA value of the TCM scan, for five different clinical protocols aiming to clarify and quantify radiation dose reductions with TCM. The results of this study in table 1.12 showed that there was a considerable organ dose reduction in all cases when protocols were performed with TCM. In the first case of a 7 year old male patient who underwent a cleft 8x5 cm² standard resolution exam, TCM resulted in an average organ dose reduction of 42%. The highest % dose decrease was for salivary glands (-47.3%, 1472 μGy with TCM vs 2793 μGy w/o TCM) while the lowest dose reduction was for brain (-36%, 145 μGy with TCM vs 226 μGy w/o TCM). Lower dose savings were observed in the second case of a 7 years old male who underwent an upper incisor 5x5 cm² High Resolution protocol. The average organ dose reduction was about 18% with the highest being for eye lenses (-28.3%, 350 μGy with TCM vs 488 μGy w/o TCM) and the lowest for ET tissue (-9%, 662 μGy with TCM vs 727 μGy w/o TCM). A 40% average organ dose reduction was noticed in the case of an 8 years old male having undergone a standard 5x5 cm² upper incisor protocol. The highest dose reduction was again for eye lenses (-46%) while the lowest for oesophagus (-28 %). The same average dose reduction (-40%) was also observed in the case of a 10x5 cm² standard resolution cleft protocol to a 12 years old male patient. The maximum dose reduction was for salivary glands (-50%). Finally, in the case of the large-FOV face protocol, an average 37% organ dose reduction was observed. Overall, TCM leads to considerable organ dose reductions. It shall be mentioned that the study was based on the assumption that in a fixed current mode the scanner would operate with the tube current value which would provide an acceptable, noise-free, image; as the AP is the highest attenuating projection which defines the overall noise level, the AP current value, as specified by the scannogram in a real scan, was selected to be the fixed current value in a hypothetical fixed –current operation mode.

A more careful look into table 1.12 shows that the most highly irradiated organ for small and medium size FOVs is oral mucosa. Being segmented as the outline of the mouth cavity, oral mucosa is always in the primary field and is constantly irradiated throughout rotation. Salivary glands are also highly irradiated, yet the largest gland, i.e. the parotid, is not always totally included in the primary radiation field, and hence the dose is lower compared to oral mucosa. On the contrary, in the large 16x16 cm² face protocol where the parotid is inside the primary field and is also subject to increased scatter radiation due to large field size, salivary glands receive the highest absorbed dose. In this case, a huge increase in the dose to brain and to the lenses of the eye is also observed. This is due to the fact that the lenses are in the primary field and given the size of the 12 years old patient's head, brain is also almost totally exposed to primary photons. The complex anatomy of the head and its influence on dose distributions do not allow to draw conclusions on organ dose reductions and their position in the head. Considerable dose reductions were observed for organs which are totally, partially, or not at all covered by the primary beam. As an example, thyroid and brain which are mainly exposed to scatter (brain is only exposed to primary photons in the face protocol), demonstrated substantial dose reductions in all cases.

The second study compared organ doses between TCM and fixed mA schemes for the same total x-ray tube load settings (mAs). The objective of the study was to investigate whether MC dose calculations can still be reliable without simulating the TCM curve. The results in table 1.13 reveal that the average organ dose difference in all cases is within the range of the MC simulation uncertainty (~6%, section 1.4). This means that when it comes to the total energy that is deposited within the scanned volume,

there is not any statistically significant difference that imposes the implementation of TCM for MC dose assessment. However, the low average organ dose % difference is also attributed to the fact that the non-application of the TCM curve has opposing results in individual organ doses. More specifically, in the first case (cleft palate, 7 years old), the implementation of TCM increases the dose to the brain by 10% while the dose to salivary glands decreases by the same amount. While a 10% difference can still be considered acceptable, a 17% increase is observed in the dose to ET (Patient #2) and an almost 28% increase in the dose to oesophagus (Patient #3). There is not any noticeable difference in organ doses between TCM and fixed technique (for the same mAs settings) for patients #4 and #5. Overall, the implementation of the TCM curve can be skipped when there is no available data. However, care shall be taken in cases where accurate dose calculations to individual organs are required. Lopez et al (2017b) reached the same conclusion investigating the necessity of rotational (x-y) TCM curve implementation to MC frameworks for accurate dose calculations in chest MDCT examinations. They suggested that accurate organ dose calculations (with a 10% tolerance) can be achieved when info of the z-modulation (i.e. the mAs per rotation) is provided in a 3D TCM modulation scheme. At the introduction of a new CBCT modality with TCM, at least one scientific study should be performed with full knowledge of the TCM scheme, to allow its justification.

The aim of the third study was to investigate the 'Safebeam' TCM scheme of NewTom VGi-evo, a preprogrammed TCM technique based on a fixed mathematical formula, and to compare with theoretical attenuation-based TCM schemes derived with raytracing. Raytracing was centered around the clinical volume of interest for each clinical protocol, i.e. the centre of the mouth cavity for the 8x8 cm² and the upper and lower premolars for the 5x5 cm² FOVs and hence, the attenuation profiles (figure 1.18) were not symmetrical (as it would have been the case if the center of rotation was the centre of the head). The attenuation profiles also revealed that the maximum and minimum attenuation projections deviated slightly from 0° (AP projection) and 90° (LAT projection) respectively. This was more pronounced in the upper molar 5x5 cm² protocol where there was a noticeable phase shift from 0° and 90°. The maximum attenuation in projections just before the AP (but not the AP) were due to the longest ray path of the beam along the denture and the upper part of the spine compared to the AP projection which resulted in a higher Aϕ value compared to A0 (figure 1.20). In the same context, the minimum attenuation was observed slightly after the lateral projection (Aθ < A90). Even if this was a patient-specific outcome considering that patient anatomy may influence the above-mentioned remark, this case reveals that it is not always the AP projection which defines the maximum attenuation, and hence, the noise level of the image is mistakenly defined by the AP projection in systems which consider the AP as the most attenuating projection.

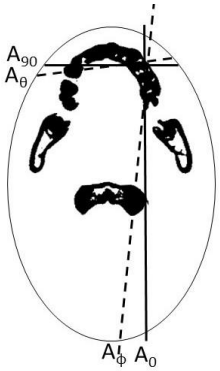

Figure 1.20. The ray paths in the AP and LAT projections (solid lines) and in the least and most attenuating ones (dashed lines) in the case of the 5x5cm² upper premolar FOV

Figure 1.19 presents the attenuation-based TCM curves for different modulation strengths. Given that for the majority of the projections in all cases the ratio A_θ/A_{ref} was < 1, the stronger modulation strength (α=1) resulted in lower mA values and hence, in lower overall exposure to the patient. In projections where the A_θ/A_{ref} was >1, the mA increased with the modulation strength, yet this was observed in only a few projections out of the 360 involved in a full rotation, i.e. in 5x5 cm² upper premolar protocol (figure 7) where the peak mA values surpassed the reference mA value. For these cases we verified with the company that the generator is powerful enough to operate properly.

The dose results of the study are presented in the tables 1.16-1.18. The organs which received the highest doses were the oral mucosa and the salivary glands. These are the only radiosensitive organs which are entirely or partially irradiated by the primary beam and which are totally included in the voxel model. RBM, bone surface, muscles, oesophagus and skin were partially irradiated; their mass fraction in the scanned volume was very small compared to their distribution in the entire body and therefore the doses were low. The rest of the organs (thyroid, brain and the eye lenses) were outside the field and they were only exposed to scatter radiation.

In all cases, organ doses decrease with increasing modulation strength with the lowest doses being observed for a=1 which provides constant noise in all projections and the highest ones for a=0 which denotes no modulation at all (Li et al 2014). Comparing attenuation-based TCM vs fixed current schemes, there was an average dose decrease of 12% for a=0.25 and 39% for a=1 in the case of the 8x8 cm² protocol. The largest decrease was observed in the dose to salivary glands (14% and 44% respectively for a=0.25 and a=1). In the case of the 5x5 cm² lower premolar protocol the average dose decrease with a=0.25 was 17% and 49% with a=1. The largest dose decrease was observed in oral mucosa (20% and 56% respectively for a=0.25 and a=1). In the case of the upper premolar protocol, the average dose reduction was 21% with a=0.25 and 46% with a=1, with oral mucosa showing again the largest dose decrease. The preprogrammed TCM scheme which is employed by the manufacturer resulted in an average dose decrease of 23% in the case of the 8x8 cm² protocol (max decrease = 28% for salivary glands), in 24% decrease in the 5x5 cm² lower protocol (max decrease = 31% for oral mucosa) and 20% in the 5x5 cm² upper premolar FOV (max decrease = 27% for oral mucosa).

When the centre of the FOV was positioned centrally, i.e. along the midline of the mouth cavity as in the case of the 8x8 cm² FOV, the preprogrammed TCM scheme resulted in organ dose values close to attenuation-based TCM ones of α=0.5. This was not any more the case when the FOV had an off-center- offset position. For the 5x5 cm² lower premolar protocol, the preprogrammed TCM organ dose values were laying between those obtained with α=0.25 and α=0.5 whereas for the upper premolar protocol they were very close to α=0.25. Therefore, there is a clear influence of the position of the FOV on the dose response of the preprogrammed TCM system. This can be partly explained by the nature of the preprogrammed schemes. They may be based on the prescan acquisition exposures which define the limiting mA values of the real scan, yet the mathematical formula which provides the mA per projection can never identify and account for the position of the FOV inside the head. The nature of most preprogrammed schemes is such that the they always consider the centre of the head as the centre of the scanning volume. The inability of the preprogrammed TCM scheme to detect the centre of rotation may also have an influence on image quality. Since it is impossible for any mathematical formula to consider an offset position of the FOV, the system will falsely provide lower mA values to what is required for the highest attenuating projections and higher exposures for the lower attenuating ones.

Attenuation-based TCM systems are more faithful towards patient-specific optimization of exposures. However, they require more sophisticated and powerful generators which are currently not available or they are very expensive for dental CBCT scanners. The use of preprogrammed TCM schemes offers

an alternative solution which, as proved in this study, can considerably reduce the dose to patients compared to fixed current techniques which are currently used in most scanners.

CHAPTER 2

Development of a paediatric head and neck voxel model database for MC dose studies

2.1 Introduction

Anthropomorphic phantoms which mimic the anatomical features of human body have always been useful in all scientific fields where radiation exposures are involved. Either in a physical or in a computational form, these phantoms, as also called 'models', have been employed to optimize exposures, to calculate organ doses and to subsequently estimate the radiation induced risk. The use of thermoluminescent dosimeters (TLDs), positioned in organ-specific locations within the phantoms, has been a traditional dosimetry method in medical imaging for many years. However, this approach is expensive and time consuming as it requires the proper equipment (dosimeters and phantoms representing the population of the study) and the application of a large number of TLDs to perform trustful measurements. Furthermore, since the TLD placement at each organ occurs in the dedicated dosimetry holes which occupy a small region and not the entire organ, extrapolation from these punctual measurements to organ doses is difficult. In practice, the doses to radiosensitive organs like salivary glands, oral mucosa and extra thoracic tissues (ETs) are in most cases calculated from the dose to surrogate or substitute organs. Moreover, the paediatric physical phantoms which are available nowadays, represent specific age categories (newborns, 5 and 10 years old), and hence they don't represent the entire paediatric population since they do not adhere to the rapid changes in organ shape, mass and size which take place in early childhood. Monte Carlo (MC) dose simulation studies with the use of computational phantoms is a software alternative approach for organ dose calculations, and the method adopted in present manuscript.

In the first generation of computational phantoms mathematical equations were employed to describe and mimic human anatomy: elliptical cylinders for trunk and arms, circular cones for legs and feet, a cylinder followed by an elliptical cylinder to represent neck and head, ellipsoids for breast (figure I5). Advances in medical imaging technology and the advent of 3D imaging resulted in the development of more sophisticated and more realistic voxel phantoms. Over the last fifty years, an exponential growth of computational phantom research in radiation protection, imaging and radiotherapy has been realized (Xu 2014).

Among the voxel phantoms and at the moment of the launch of present project there were only a few candidates for paediatric applications of head and neck MC dose studies (Caon et al 1999, Nipper et al 2002, Lee et al 2003, 2005, Smans et al 2008, Christ et al 2010, Gosselin et al 2014) and we therefore decided to build our own models. There is an intrinsic difficulty in building paediatric voxel models. It starts with the difficulty to retrieve whole body or whole head and neck paediatric CT scans of sufficient quality (scans from PET-CT or SPECT-CT and taken for attenuation correction, would typically not be of a sufficient level). The voxelization procedure consists of concrete steps-tasks. However, paediatric voxel models differ between each other: in gender and age; in the design methodology as most of them are based on paediatric image datasets, yet in some cases they may emanate from adult models deformation (Nagaoka et al 2008); even in the number of segmented tissues and organs. The shortcoming of non-segmented organs/tissues in a model is usually circumvented in dose studies by specifying and estimating the dose to substitute organs, i.e. the tongue has been reported as a surrogate for the salivary gland (Zhang et al 2013a); the absence of oral mucosa has been encountered by splitting the weighting factor to the rest remainder organs (Zhang et al 2013a): blood vessels, muscles alone or in combination with residual tissue have been used as surrogate for lymph nodes (Ferrari et al 2005, Lee et al 2007, Petoussi-Hens et al 2012); pharynx and larynx for the extra thoracic region (Tian et al 2014). Furthermore, most of these models are not publicly available and have been developed to fulfill the research purposes of individual groups.

As a consequence, pediatric dosimetry in dental CBCT is challenging. On one hand there is a lack of appropriate pediatric phantoms for dose assessment studies as most of them, either physical or computational, are not detailed in terms of segmented organs. Furthermore, organ doses, especially in dental CBCT imaging, are age-dependent, i.e. the smaller the size the higher the irradiated fraction by a given radiation field size (and hence the higher the dose) and hence, pediatric population cannot be represented by one average model. A database of age and gender-specific head and neck models is required. The aim of this study was to develop a head and neck voxel model database, for both male and females, that covers the entire age range of the paediatric population.
Dedicated (complete full head and neck) models cannot be based on dental CBCT image datasets due to the restricted size of most FOVs. Critical radiosensitive organs, such as the thyroid which is one of the most radiation-sensitive organs in the head and neck region (Pauwels et al 2012a, Ludlow et al 2015), are usually not included in dental CBCT image datasets, yet their dose assessment is essential since they may receive high dose due to scatter. Furthermore, CBCT images lack the required low contrast resolution which would enable accurate organ segmentation. Therefore, we decided for the design of voxel models based on MDCT datasets rather than CBCT ones.
There is however a challenge when MDCT-based voxel models are used in dental CBCT MC dose studies: voxel phantoms retain all geometric characteristics of the initial MDCT scan. Due to the head support accessory which is mounted on a MDCT scanner, the head of a patient is slightly inclined to the front. This inclination is preserved throughout the voxelization procedure and the resulting voxel model appears with its Frankfort plane tilted to the front. As in dental CBCT scans the Frankfort plane is always horizontal, a method to correct for the inclination and to establish an horizontal Frankfort plane in the models is also presented in this chapter. A MC dose assessment study is also conducted to examine organ dose differences between males and females of the same age.

2.2 Methods and Materials

Seventeen head and neck MDCT image datasets were retrieved from the Picture Archiving and Communicating System (PACS) of our hospital and used for voxel model creation. Twenty two organs were segmented in each dataset. The same voxelization procedure was followed for each model. The segmented organ masses were compared to the respective age and gender specific ICRP reference mass value. To do so, interpolation algorithms were applied to ICRP 89 (2002) reference mass values to extract reference values for each age and gender category; the segmented masses were subsequently adapted to the reference ones. Adjustments were made such that segmented and reference mass values coincide within a tolerance of 10%. This was to correct for any segmentation errors and to ultimately create age and gender reference models. The voxelization procedure was based on the training course from the 2nd EURADOS (European Radiation Dosimetry Group) school on voxel phantom development and implementation for radiation physics calculations.

2.2.1 Selection of MDCT image datasets

Each image dataset had to strictly meet several requirements to get eligible for voxelisation. A first prerequisite was that the scanned volume should have been imaged in one sequence to guarantee uniform z-resolution across the image volume. When the volume is scanned in more than one sequence, i.e. as it is often the case in head MDCT imaging (two sequences for head base and cerebellum), the slice thickness (z-collimation) which defines the z-resolution of the resulting voxel model is different. Apart from ending up in a voxel model with a non-uniform z-resolution, there is also a potential risk that anatomical regions in the stitching region of the two sequences overlap.

Only full head CT acquisitions, from the crown of the head up to at least the C5 spinal segment, were scored eligible. This was to ensure that the thyroid would at least be partially included in the voxel models. Furthermore, image datasets with severe artefacts and those of patients with severe trauma injuries or distortions in the face were rejected.
For each qualified dataset, the occipitofrontal circumference was measured. This was to check whether the circumference of each model was in accordance with the respective reference values for each age category: only those heads whose circumference was calculated to be within the 3th and 97th percentile of the reference circumference values were qualified (Rollins et al 2010). The circumference was estimated by calculating the area of the head at the respective image plane in ImageJ (version 1.48 x Java 1.6, National Institutes of Health, USA) and by subsequently assessing an effective diameter and an effective circular circumference.

2.2.2 Segmentation procedure

Each MDCT image dataset was uploaded to ImageJ to create a corresponding initial image tiff file. The image stack was at first cleaned to get rid of any non-anatomy related features, such as the table of the scanner in the Field of View (FOV). A whole head mask was created by converting the stack of images to 8-bit binary ones. The skin was obtained as a one-voxel thick outline of the mask. Air cavities,the sinuses, bone-skeletal mixture, mandible and teeth were all segmented in a semiautomatic way by thresholding the grey values of these organs. Blood (arteries), brain, cartilage, connective tissue, oesophagus, eyes, eye lenses, fat, muscle, extra-thoracic tissue (ET), spinal cord, tongue, trachea, thyroid, salivary glands and oral mucosa were segmented manually by delineating each organ on an image by image basis. The extra-thoracic tissue was segmented as the outline of the pharynx and the larynx, whereas the oral mucosa was considered to be the outline of the mouth cavity. The spongiosa and the cortical bone were segmented as a uniform skeletal mixture. The resolution of most CT scanners nowadays is not adequate to allow for the segmentation of the medullary cavities where the red bone marrow (RBM) resides. Therefore, RBM was not segmented and was not included in the voxel models, yet the dose to RBM can be calculated in an indirect way, as mentioned in the following paragraphs. A particular grey value and identification number was given to every voxel of the same organ. The organs were added one by one to build the voxel model. After each organ had been segmented, any unsegmented regions which have not been attributed to any organ, were named residual tissue. Figure 2.1 illustrates the segmentation process in a specific slice of the 12 year old female model.

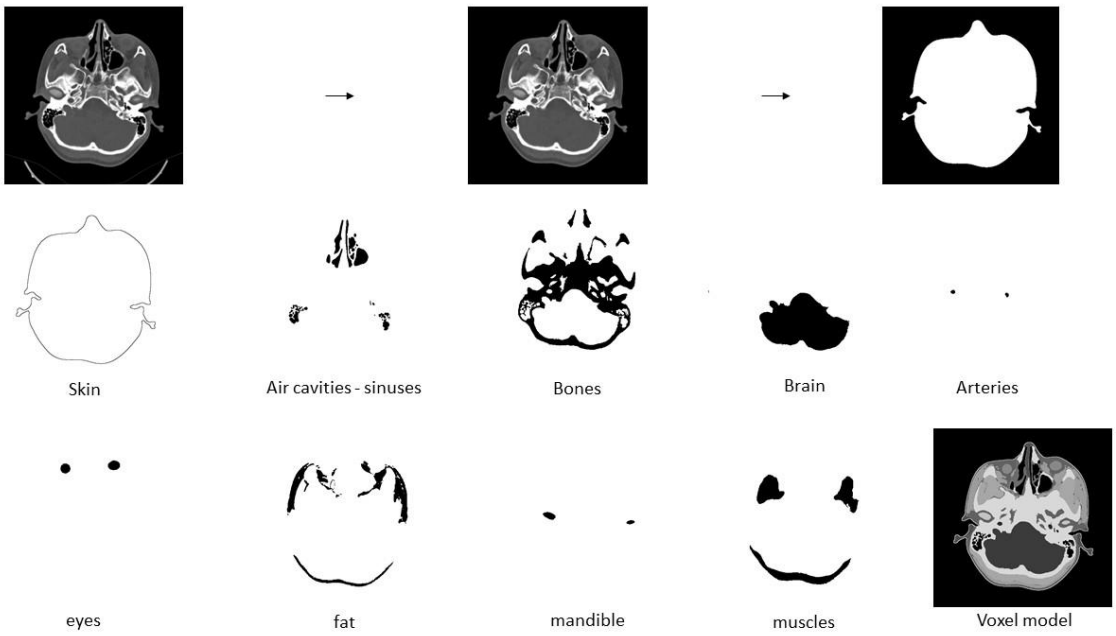

Figure 2.1 Segmentation procedure, upper row: the initial image (left) gets rid of non-anatomical features (middle) and a whole mask is created. Middle row: organs segmented one by one. Bottom row: When organ segmentation is over, each organ is given a different ID (grey value) and they are superimposed to the whole mask to create the voxel model

2.2.3 Matching with reference values

Each segmented organ mass was calculated by multiplying the number of segmented voxels by the voxel volume and the respective organ density obtained from ICRP publication 110 (2009). The segmented masses were compared to reference mass values published in ICRP publication 89 (2002) to investigate the magnitude of deviations from reference values. Due to the fact that the reference values are only available for newborns, 5, 10,15 years old and adults, a shape preserving algorithm was fitted to ICRP values in Matlab (version 7.12.0.635, R2011a, MathWorks Inc) to extract reference data for the entire paediatric age range. For those organs entirely located in the head region such as brain, eyes, eye lenses, salivary glands, teeth and tongue, the number of voxels was adjusted by adding to or removing voxels from the periphery of the segmented organ until the segmented mass matches the corresponding value within ±10 %. For oral mucosa, we only tried to keep an increasing mass pattern with increasing age, as reference values do not exist. For organs partially found in the head, the ratio of the segmented organ/tissue mass in the head to the respective total organ mass in the body was calculated. The skin segmented surface was calculated by multiplying the surface area of each voxel, i.e. the product of the in-plane and the z-voxel size, with the number of the segmented skin voxels. The ratio of the segmented to the total skin surface was calculated. The total skin surface of a human of the respective age and gender was calculated based on a formula described by Haycock et al (1978). The formula requires reference weight and height values which were obtained by the World Health Organization (WHO 2007).

2.3 Results

Eight image datasets of males, aged from three to twelve years old, and nine datasets of females, aged from two months to fourteen years old, fulfilled the requirements to undergo the voxelization procedure. Table 2.1 lists the characteristics of each dataset. These characteristics are preserved throughout the voxelization procedure and hence they can also be considered as the specifications of the resulting voxel models. The in-plane resolution corresponds to the x-y voxel size of the CT scanner and the z-resolution to the distance between two consecutive reconstructed images. Specific names were given to each model. Figures 2.2 and 2.3 depict the head circumference of the head voxel models embedded to specific growth curves. In all voxel models, the head circumference lies between the 3th and 97th percentile.

Table 2.1. Specifications of the voxel models

Voxel model	Gender	Age (years)	In-plane resolution (mm)	z-resolution (mm)	x, y number of voxels	Number of slices	Head circumference (cm)
John	Males	3	0.41	1.9	512	92	47.9
Dejan		5	0.22	2.75	1024	60	50.5
Joris		6	0.49	1.95	512	108	52.1
Guozhi		7	0.21	3	1024	64	51.4
Peter		8	0.62	0.7	512	330	51.3
Benjamin		9	0.43	0.6	512	370	50.8
Andrew		10	0.49	0.6	512	342	53.7
Mike		12	0.49	2	512	126	52.3
Lina	Females	2 months	0.33	2	512	77	37.2
Demi		5	0.41	0.6	512	355	49.2
Viktoria		6	0.43	2	512	113	49.3
Xoch		8	0.49	3	512	76	52.2
Louisa		10	0.45	0.7	512	305	50.2
Hilde		11	0.43	2	512	99	53.9
Vivian		12	0.41	1	512	230	51.8
Irene		13	0.45	0.6	512	367	53.2
Georgia		14	0.49	2.05	512	113	55.8

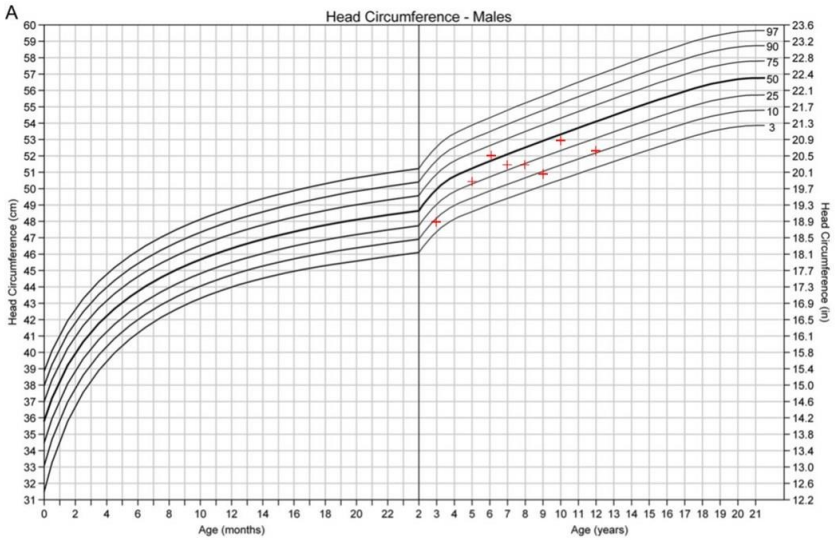

Figure 2.2 Head circumference of the male paediatric head voxel models (red dots) shown on the reference curve (background diagram from Rollins et al 2010)

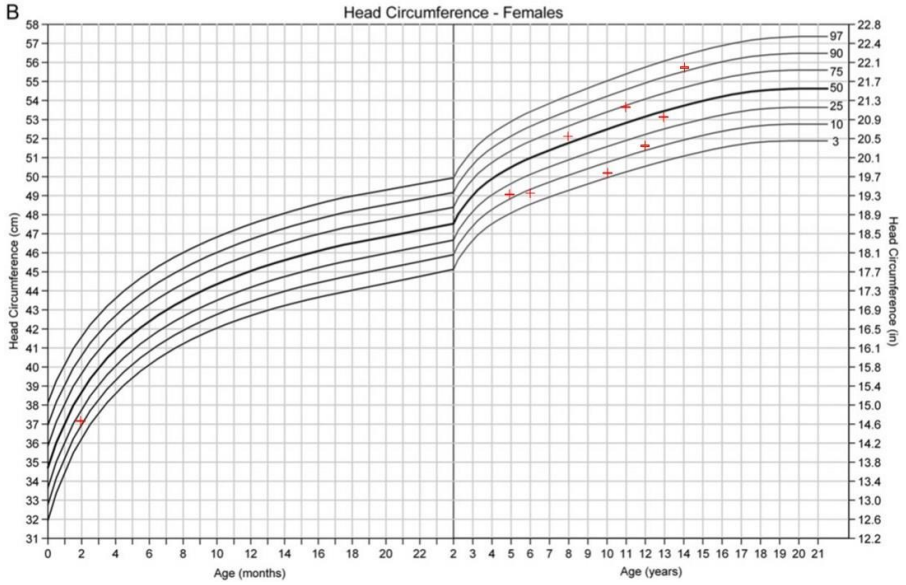

Figure 2.3 Head circumference of the female paediatric head voxel models (red dots), shown on the reference curve (background diagram from Rollins et al 2010)

Table 2.2 presents the mass values of the segmented organs. Next to each organ, the respective reference mass value, as extracted by fitting an interpolation algorithm to ICRP reference values, is also listed along with the percentage difference between them (%Δ). Table 2.3 depicts the segmented mass values of the organs which are partially located in the head along with the respective segmented fraction to the total mass of the organ in the entire body. Some organs are not radiosensitive according to ICRP 103, but they have been segmented anyway and are included in our voxel models (table 2.4). The extracted reference values correspond to the set year + sixth months, as this was thought to be closest to the real age. As an example, for the 9 year old model the reference values were calculated for 9.5 years. Figure 2.4 displays the 3D contour of four of our voxel models.

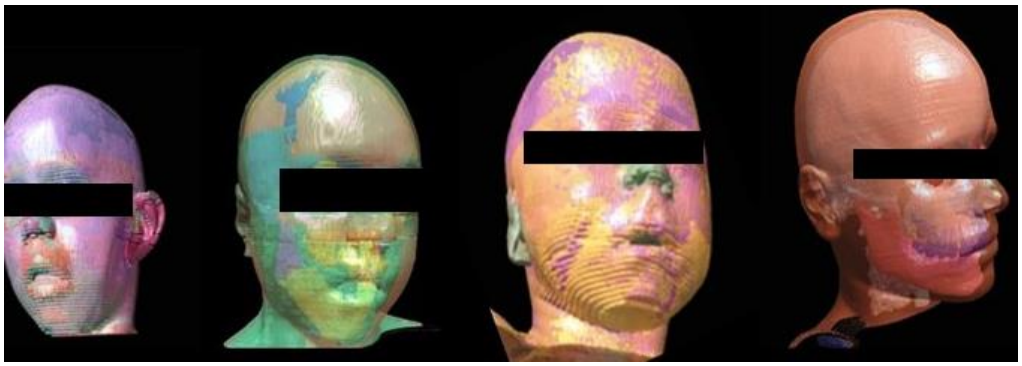

Figure 2.4 From the left to the right: Dejan, Guozhi, Xoch and Vivian.

voxel model	gender	age	brain			eyes			eye lenses			oral mucosa
			segmented mass (gr)	reference mass (gr)	%Δ	segmented mass (gr)	reference mass (gr)	%Δ	segmented mass (gr)	reference mass (gr)	%Δ	segmented mass (gr)
John	MALES	3	1139	1242	-8.3	9.2	9.9	-6.7	0.31	/	/	14.6
Dejan		5	1353	1324	2.2	10.8	11.2	-3.6	0.3	/	/	16.2
Joris		6	1465	1350	8.5	10.7	11.4	-6.2	0.35	/	/	11.6
Guozhi		7	1503	1370	9.7	10.5	11.6	-9.5	0.33	/	/	14.6
Peter		8	1464	1385	5.7	10.7	11.7	-8.5	0.3	/	/	19.4
Benjamin		9	1527	1396	9.4	12.4	11.9	4.4	0.37	/	/	16.3
Andrew		10	1396	1403	-0.5	13.1	12.1	8.3	0.3	/	/	24
Mike		12	1494	1410	6.0	13.2	12.4	6.3	0.36	/	/	18
Lina	FEMALES	2months	640	590	8.5	6.6	6.3	4.3	0.13	0.13	-1.5	7.3
Demi		5	1264	1187	6.5	12.2	11.2	8.9	0.31	/	/	12
Viktoria		6	1306	1196	9.2	11.4	11.4	-0.5	0.27	/	/	12.9
Xoch		8	1325	1208	9.7	11.2	11.7	-4.0	0.34	/	/	16.9
Louisa		10	1330	1227	8.4	12.3	12.1	1.8	0.37	/	/	18.6
Hilde		11	1329	1245	6.7	13.4	12.3	8.9	0.3	/	/	18
Vivian		12	1215	1267	-4.1	13.3	12.4	7.3	0.35	/	/	19.1
Irene		13	1214	1276	-4.9	13.4	12.4	8.4	0.35	/	/	14.2
Georgia		14	1410	1298	8.6	13.7	12.9	5.8	0.37	0.4	-7.5	19.1

voxel model	gender	age	salivary glands			Teeth			Tongue			mandible
			segmented mass (gr)	reference mass (gr)	%Δ	segmented mass (gr)	reference mass (gr)	%Δ	segmented mass (gr)	reference mass (gr)	%Δ	segmented mass (gr)
John	MALES	3	28.3	31.3	-9.5	10.7	11.4	-6.0	16.6	16	3.8	34.2
Dejan		5	35.7	35.1	1.7	18	16.4	9.6	21.8	20.2	7.7	58.2
Joris		6	34.2	36.9	-7.5	18.5	19.3	-4.1	20.5	22.5	-9.1	44.7
Guozhi		7	36.5	38.6	-5.3	24.5	22.3	9.7	27	24.9	8.2	45
Peter		8	37.2	40.6	-8.3	23	25.4	-9.6	25.2	27.5	-8.2	24.1
Benjamin		9	39.4	42.7	-7.7	26.2	28.5	-8.0	28.4	30.4	-6.6	40.8
Andrew		10	46.1	45.6	1.1	28.9	31.5	-8.2	37	33.8	9.6	36.6
Mike		12	50.6	54.8	-7.7	38.5	38.1	1.2	38.7	42.7	-9.4	66
Lina	FEMALES	2months	12.5	12.7	-1.8	2.3	2.1	7.6	6.4	5.8	9.7	9.6
Demi		5	32.5	35.1	-7.4	14.9	16.4	-9.2	22.1	20.2	9.6	33.8
Viktoria		6	38.8	36.9	5.2	20.1	19.8	1.5	20.5	22.6	-9.2	32
Xoch		8	36.8	40.6	-9.3	28.3	26.5	6.6	27.8	27.6	0.5	47.7
Louisa		10	40.3	44	-8.4	32.2	30.7	4.8	31.3	33.8	-7.3	38
Hilde		11	52.6	49.6	6.0	34.9	31.8	9.6	39.5	38	3.9	51.5
Vivian		12	55.8	54.5	2.4	35.8	32.9	8.8	38.9	42.4	-8.3	48.8
Irene		13	49.4	54.5	-9.4	36.2	33.5	8.1	38.5	42.7	-9.8	50
Georgia		14	58.9	63.6	-7.4	38.3	35.5	7.9	51.4	48.9	5.0	66

Table 2.2 Segmented mass values of organs which are entirely present in the head; the respective reference values were extracted by fitting a shape preserving interpolation algorithm to ICRP 89 reference mass values that are available for specific age categories; the percentage difference between the mass values is also listed

voxel model	gender	age	skin surface (cm²)	segmented fraction	oesophagus mass (gr)	segmented fraction	muscles mass (gr)	segmented fraction	Extra Thoracic surface (cm²)	segmented fraction	Thyroid mass (gr)	segmented fraction
John	MALES	3	943	0.14	1.0	0.15	295	0.08	134	0.86	0.6	0.24
Dejan		5	1011	0.13	1.7	0.16	313	0.06	103	0.52	0.6	0.18
Joris		6	1253	0.15	2.7	0.22	462	0.07	90	0.39	1.0	0.21
Guozhi		7	1202	0.13	1.8	0.13	430	0.06	90	0.38	0.8	0.15
Peter		8	1295	0.2	1.6	0.11	539	0.06	121	0.49	0.7	0.11
Benjamin		9	1359	0.13	2.7	0.16	548	0.06	126	0.46	1.0	0.14
Andrew		10	1291	0.12	1.8	0.09	452	0.04	105	0.36	0.7	0.09
Mike		12	1518	0.12	5.4	0.23	655	0.04	104	0.30	1.8	0.19
Lina	FEMALES	2months	720	0.24	0.6	0.19	225	0.20	12	0.20	0.4	0.24
Demi		5	1301	0.17	1.5	0.14	455	0.08	104	0.52	0.6	0.17
Viktoria		6	1249	0.15	3.5	0.29	496	0.07	117	0.52	1.5	0.33
Xoch		8	1327	0.14	2.1	0.14	395	0.05	111	0.40	1.0	0.15
Louisa		10	1347	0.12	2.0	0.11	491	0.04	134	0.46	0.9	0.11
Hilde		11	1249	0.10	2.2	0.10	592	0.05	146	0.46	1.0	0.11
Vivian		12	1312	0.10	2.8	0.12	574	0.04	138	0.41	1.6	0.14
Irene		13	1232	0.09	2.3	0.09	461	0.03	121	0.35	1.4	0.13
Georgia		14	1459	0.10	2.2	0.08	653	0.04	136	0.38	2.2	0.20

Table 2.3 Mass values of organs which are partially present in the head and neck region and their segmented fraction

voxel model	gender	age	Air cavities (gr)	Blood (gr)	Bone (gr)	Cartilage (gr)	Connective tissue (gr)	Fat (gr)	Spinal cord (gr)	Trachea (gr)	Residual tissue (gr)
John	MALES	3	0.02	12.7	411	32.8	218	169	16.1	3.2	25.9
Dejan		5	0.05	16.1	629	9.9	437	155	14.3	3.1	1.4
Joris		6	0.02	22.1	897	44	309	272	19	3.6	0.0
Guozhi		7	0.04	15.3	654	13.5	550	203	20.5	3.1	19.3
Peter		8	0.03	29.1	956	12.5	213	170	23.3	1.9	10.4
Benjamin		9	0.04	35	852	21.4	594	142	43.5	1.7	10.6
Andrew		10	0.06	29	801	23.8	681	367	21	1.9	16.0
Mike		12	0.07	40	768	23.4	770	263	41.8	3.1	6.4
Lina	FEMALES	2months	0.005	3.6	164	7.3	76	171	7.7	0.9	3.3
Demi		5	0.03	27.8	702	11.9	508	264	14.8	3.1	5.2
Viktoria		6	0.06	16.8	784	11	604	188	18.8	3.6	7.7
Xoch		8	0.06	22.4	952	19.7	779	140	28.3	2.6	3.2
Louisa		10	0.06	30.3	813	21	899	160	37.7	2.3	6.1
Hilde		11	0.05	35.6	784	21.1	738	125	30	2	5.3
Vivian		12	0.06	39.2	802	23.4	772	213	31.1	2.2	3.9
Irene		13	0.06	41.2	614	20.5	442	313	29.2	2.3	3.9
Georgia		14	0.07	29.5	793	26.1	868	179	35.2	2.8	2.1

Table 2.4 Segmented mass values for the rest of the organs which are present in the voxel models

2.4 Discussion

The aim of this work was to develop a family of reference paediatric voxel models, dedicated for MC dosimetry simulation studies of head & neck and dental acquisitions. The motivation of this study was to approximate as accurately as possible the radiation organ doses and subsequently the radiation induced risk for paediatric patients undergoing diagnostic medical exposures, mainly in dental CBCT imaging. Seventeen voxel models were finally designed, covering the greater part of the paediatric age range for both genders.

There were intrinsic difficulties in retrieving image datasets, suitable to undergo the voxelisation procedure. First of all, paediatric head and neck CT imaging is a rare examination; it is considered a high radiation risk diagnostic procedure and has been replaced, whenever this is feasible, by lower

radiation risk imaging techniques. Furthermore, there were a few datasets of severe trauma patients with broken jaw(s) that were rejected along with datasets with severe beam hardening and metal artefacts in the dental region. Since the ultimate target was to create a database of average-reference models, we decided to keep only those image datasets where the head circumference was within the reference age-specific circumference values.

Twenty two organs were segmented on an image by image basis. The masses were matched as closely as possible to mass reference values. The most corrections in terms of adjusting the number of voxels to get the proper mass values were applied to teeth. This was due to the fact that that teeth were initially segmented in a semi-automated thresholding way which was attributing extra voxels to teeth; due to the fact that teeth are high density structures, even a small number of extra voxels assigned as teeth leads to large deviations from the reference mass values. We adjusted the number of teeth voxels by assigning the inner outline of the teeth to the tongue which is usually in contact with the teeth. The oral mucosa was segmented as the outline of the mouth cavity, yet the parotid gland can also be used as a substitute organ to estimate the dose to oral mucosa. The segmented salivary glands include the parotid, the sublingual and the submandibular glands; all of them were given the same identification (ID) number. However, it is straightforward to assign different IDs to each of them such that the dose to each gland can be individually calculated.

The current resolution of CT images, even when obtained with the most recent state of the art MDCT scanners, poses limitations to the segmentation of specific tissues and organs in the head region. The in-plane (x,y) voxel size is too large compared to the thickness of the skin layer and to that of the extrathoracic (ET) tissue. The radiosensitive wall of the ET1 region (nasal vestibule) is a squamous epithelium layer which is 50μm thick; the wall of the ET2 region, i.e. the wall of posterior nasal passages, larynx, pharynx and mouth, has an average thickness of 65μm (mucous layer and stratified squamous epithelium) according to ICRP 89. By contrast, the lowest in-plane dimension of our images is 210μm . The skin was segmented as a one-voxel thick outline of the total head frame and the ET tissue as a one-voxel thick outline of the related tissues. Due to the relatively large voxel sizes, the segmented masses of the skin and the ET region are unavoidably overestimated. To extract the segmented fraction of these tissues, the segmented surface rather than the segmented mass was used.

The limited image resolution of CT images impedes also the segmentation of the RBM. It would be feasible in high resolution images to distinguish the spongy and the cortical parts of the segmented bones, however, it is impossible to segment the medullary cavities in the trabecular bone where RBM is present. Therefore, in order to follow the same segmentation strategy for each of our phantoms, we decided to segment the cortical bone and the spongiosa as a unified skeletal mixture and apply the well-established 3 factor approach to approximate the dose to the RBM (Kramer et al 1982, Lee et al 2006); the method, also called the Mass Energy Absorption Coefficient (MEAC) method, scales the energy deposited to the skeletal mixture by the ratio of the mass energy absorption coefficients of RBM to skeletal mixture (factor 1), by the RBM mass fraction in the skeletal mixture (factor 2) and by the King-Spiers dose enhancement factor (factor 3).

2.5 Conclusions

A family of paediatric head and neck voxel models, dedicated for MC dose studies, was developed. It consists of seventeen male and female models, each including 22 segmented organs. Each organ mass has been adjusted to reference values with a tolerance of 10% and hence it represents an age and gender-specific average model.

2.6 APPENDIX 1: Applying corrections to voxel models to establish an horizontal Frankfort plane

As already mentioned, the voxel model database, like most of the voxel models in literature, is based on MDCT image datasets. When a patient is laying on the table of a MDCT scanner to undergo a head exam, the head is positioned into a head support module which creates an inclination that is preserved to the final model. This drawback has already been pointed out in literature for the ICRP reference female voxel model, where a cephalometric analysis revealed that a rotation of 17° is necessary to bring the phantom to an alignment with the horizontal plane (figure 2.5) (Ludlow et al 2015).



Figure 2.5 The ICRP female voxel model needs to be rotated upwards by 17° to establish an horizontal Frankfort plane

However, for MC dose studies, merely applying rotation corrections does not solve the horizontality issue as it may lead to overestimating organ doses: If mere rotation corrections are applied, organs get even closer to the x-ray tube. They shall be accompanied by translation corrections, both towards the source-detector axis and the vertical axis. This is to ensure that the centre of the FOV coincides with the centre of the clinical volume of interest after rotation corrections have been applied.
The aim of this study is to describe a technique for applying the appropriate rotation and translation corrections to voxel phantoms and to calculate and compare organ doses delivered to the initially unrotated and the geometrically corrected voxel phantoms for common dental CBCT protocols in two different scanners.

2.6.1 Methods and Materials

Four voxel phantoms were included in the study: the ICRP reference adult female (ICRP AF) phantom and three in-house developed phantoms, i.e. Joris, Peter and Vivian. The initial version of the ICRP phantom was modified such that only the first 59 images out of the initial 346 images, from the crown of the head until the shoulder region, were used. The resulting head voxel volume consisted of 56 segmented organs, each with a different identification number (ID). To increase the simulation efficiency, some of these organs were merged together to finally obtain a head voxel model of 37 organs. To this end, any separately-segmented organ of the brain was given a unified ID and was considered to be part of the same organ, i.e. brain; the right and left parts of some organs were merged to one (lung, eyes, eye lenses, salivary glands. The elemental composition and the density of each organ were derived from ICRP 89 (ICRP 2002) and from Woodard and White (1986). The technical specifications of the ICRP female voxel model and the three in-house built models have already been presented in sections 1.7.1 and 2.3 respectively.
After loading each voxel model into Matlab, an algorithm was written to count the number of voxels corresponding to each segmented organ (base line) and used afterwards to investigate for potential organ overlaps during the rotation process. Since axial MDCT images constitute the basis upon which the voxel models were built, the resulting head models emerged as a stack of axial images. However,

the Frankfort line correction implies an upward lifting of the head, most appropriately illustrated as an upward rotation in the sagittal plane. To this end, a sagittal stack of images for each head model was composed from the original axial dataset.

The transformation of axial images to sagittal ones led the in-plane 2D image isotropic resolution to collapse. As indicated in phantom technical specifications (chapter 1.7.1 and table 2.1), the original voxel in-plane resolution is isotropic, i.e. the axial voxel (x, y) dimensions are equal, yet the third voxel z-dimension, determined by the slice thickness, is always different. The formation of sagittal images involves the transformation of (x, y, z) images to (z, x, y). The first two coordinates of the dataset indicate the in-plane coordinates and the third specifies the slice thickness direction. Since the x and z- voxel dimensions are always unequal the sagittal images appear to be stretched or squeezed when displayed. The latter fact posed a challenge towards accurately identifying the Frankfort line.

To overcome the latter shortcoming, each sagittal stack was resized such that the new in plane (z, x) voxel dimensions get equal. To avoid assigning organ ID numbers to anatomical regions which did not correspond to the respective organs during the resizing process and to avoid potential organ overlaps, the nearest-neighbor interpolation method was employed in Matlab. The central sagittal image of each stack was extracted and the Frankfort line for each voxel model was determined. To obtain the correction angle, the central sagittal image of each voxel phantom was rotated to various angles and each time the Frankfort line was being checked against horizontality. Once the correction angle had been defined, each entire sagittal stack was rotated on an image by image basis. To preserve the number of voxels of each organ, i.e. to uphold the number of voxels assigned with the same ID, and in order to preserve the size in the rotated image, the nearest-neighbor interpolation method and the cropping function in Matlab were employed. The final step included the conversion of the rotated sagittal stacks back to axial ones, such that they would be given a format suitable to the Monte Carlo (MC) platform which was used for the dose comparison study. To this end, the rotated sagittal stack was first resized to the original voxel dimensions and was afterwards converted to an axial one. The algorithm that was initially employed to count the number of organ voxels in the original unrotated phantoms was applied to the rotated versions. The organs whose number of voxels was slightly different between the original and the rotated versions were manually tracked on an image by image basis and minor adjustments were carried out such that the organ volume remained constant.

The abovementioned rotation corrections to establish an horizontal Frankfort plane should be accompanied with translation adjustments. When a voxel phantom is loaded into a MC platform, it is initially positioned with its volumetric centre at the Source to Axis of rotation distance SAD (figure 2.6, point A, upper image). Point A is still at the same position after rotation corrections have been applied. In a clinical dental CBCT case, the patient is positioned in such a way that the centre of the scanning volume of interest is placed as accurately as possible around the centre of rotation. The protocols that were examined in the study aimed to image the entire denture of paediatric patients. The original unrotated stacks were therefore shared with a paediatric dentist with the request to indicate the volume of interest and to define its central point (figure 2.6, point B, upper image, figure 2.7). Due to the fact that point B is the centre of the clinical volume of interest, in order to do MC dose calculations, the geometric adjustments would have to be applied to shift the centre of rotation from point A to point B. To get point A coincide with point B, a downward translation of point A, indicated by the yellow arrow in fig.2.6 (i.e. equivalent to an upward translation of the phantom towards point A), followed by a translation to the front (i.e. equivalent to a backward translation of the phantom), were required.

If identical translation adjustments were applied to the rotated phantoms, point A would not have reached point B, but would have attained point C (fig 2.6, lower image). In other words, translation corrections are required such that the imaging volume of interest does not shift to adjacent anatomical

regions after rotation. To image the same volume of interest, the rotated phantom should move a step back (i.e. further away from the x-ray tube) and a step down such that point C coincides with point B. To quantitatively assess the front-back translational corrections ycor, the geometry in figure 2.8 was considered. When rotating the phantom by a° (rotation correction), the line segments OB and OC can be regarded as radii of a circle whose centre is point O. The following mathematical formula was then applied:

$$y_{cor} = OB - y_c = OC - y_c = y_c * \frac{1-\cos a}{\cos a} \quad \text{(eq. 2.1)}$$

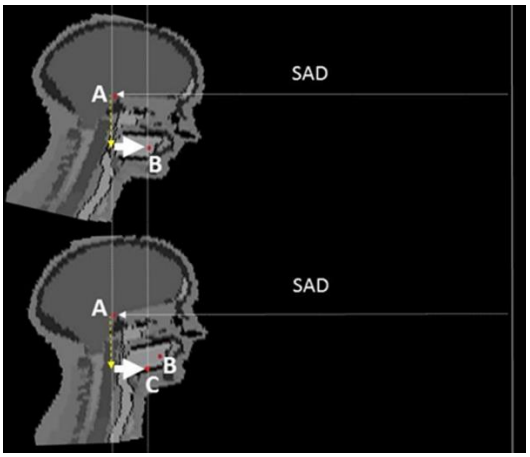

Figure 2.6 Point A is the centre of the anthropomorphic voxel volume; point B is the centre of the clinical volume of interest; point C is the shifted centre of the clinical volume to be exposed if translation corrections are not applied

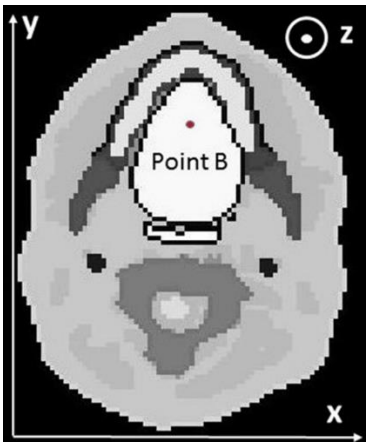

Figure 2.7 Example of the centre of the clinical volume of interest which is in all cases the entire denture. The image is an axial image of the ICRP adult female reference phantom.

To assess the vertical zcor correction, the following equation (2.2) was considered:

$$z_{cor} = y_c * \tan a \quad \text{(eq. 2.2)}$$

The line segment y_c in the rotated version is equal to the axial distance of point B in the original unrotated version (Fig.2).

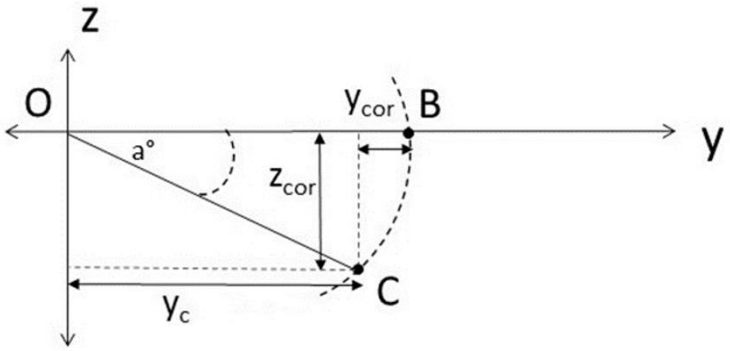

Figure 2.8 Translation corrections along the z and y axes that have to be applied after rotating the phantoms by an angle equal to a°.

The rotation and the translation corrections may have a counteracting influence on organ dose calculations. The former one may bring some organs closer to the x-ray tube implying an initial increase in the absorbed doses. However, the backward translation which is required to bring the FOV around

the clinical volume of interest gets the organs away from the tube. The aforementioned counteract does not imply that the final outcome is a zero effect; the rotation adjustment can partially bring in or out of the primary radiation field radiosensitive organs, influencing substantially the dose distribution and the absorbed organ doses.

Organ doses were calculated for a 10x9 cm² upper/lower jaw protocol (Normal Dose / Normal resolution, Medium Size operation mode for the adult ICRP and Normal Dose / Normal resolution, Small Size for the pediatric ones) in Promax 3D Max and for a standard resolution 8x8 cm² FOV in Accuitomo 170, prior to and after applying rotations. The exposure parameters are presented in table 2.5.

The dose to the bone marrow was calculated based on the mass energy absorption coefficient (MEAC) method, i.e. three factor scaling of the homogeneous skeletal mixture (Kramer et al 1982, Lee et al 2006). To extract the Red Bone Marrow (RBM) mass fraction in the head and to find the density of the skull, a method previously proposed by Kramer et al was applied (Kramer et al 2003). In all cases the skull density was found to be 1.83 gcm-3, corresponding to an RBM fraction of 0.1 in the skull skeletal mixture. The elemental composition of the bony mixture of such density was calculated based on a formula proposed by Zhou et al (2009). To calculate the dose to the bone surface the following equations were used (Ludlow et al 2008b):

Bone surface dose = RBM dose x bone/muscle mass energy coefficient ratio (MEACR) (eq. 2.3)

MEACR = -0.0618 x (2/3) kV peak + 6.9406 (eq. 2.4)

The dose to the lymph nodes was approximated based on a formula proposed by Tapiovaara et al (2008) which takes into account the absorbed dose to substitute organs. The remaining organ densities and the respective elemental compositions were obtained by ICRP 89 and by Woodward and White (1986). A total number of 1.05×10^9 histories for the 210° rotation angle in Promax 3D Max were simulated (5×10^6 histories per projection angle) to achieve a maximum Monte Carlo simulation uncertainty of 3% CV (Coefficient of Variation) in organ doses within an average simulation time of 20 hours.

Table 2.5 Exposure settings of the investigated protocols

Protocol	Scanner	Patient	FOV (cm^2)	kV	mAs
Teeth Std. Resolution	Accuitomo 170	All	8 x 8	90	87.5
3D Jaw ND/NR (Small)	Promax 3D Max	Pediatrics	10 x 9	96	67.2
3D Jaw ND/NR (Medium)	Promax 3D Max	Adult	10 x 9	96	85.4

2.6.2 Results

For each phantom, sagittal images were reproduced from the original axial datasets. The central sagittal image was used to guide the rotation correction (Fig. 2.9). The coordinates of the central point of the clinical volume of interest were then adjusted to the new voxel model geometry. Such an adjustment ensured that the clinical volume of interest is identical in both the original-unrotated and

the rotated voxel model cases and the dose comparison resembles a realistic case scenario. Table 2.6 illustrates the rotation and translation corrections for each phantom.

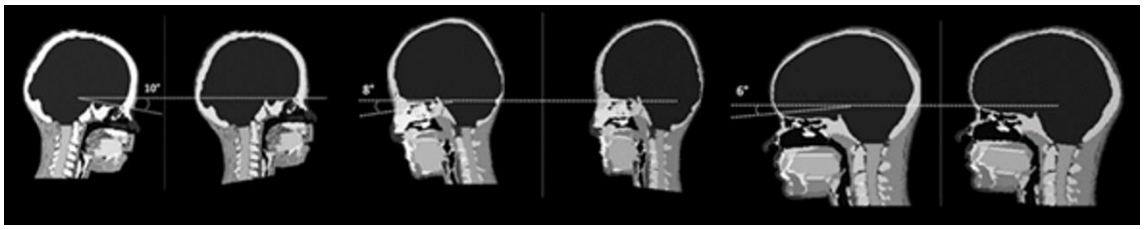

Figure 2.9. Defining an horizontal Frankfort line for the three in-built voxel models (Joris, Peter and Vivian from left to right)

Table 2.6. Corrections to be applied to each voxel model. The negative sign indicates the direction towards the centre of the coordinate system.

Phantom	Upward rotation angle, a(°)	Translation back, y_{cor} (cm)	Translation down, z_{cor} (cm)
ICRP reference female	17	-0.23	-1.55
5 years old male	10	-0.1	-1.11
8 years old male	8	-0.06	-0.85
12 years old female	6	-0.03	-0.51

Tables 2.7-2.10 present the calculated organ dose values in original (unrotated) and rotated voxel models.

Table 2.7 Organ doses (μGy) for original and rotated version for Joris

Organs	Accuitomo 170 Std Resolution 87.5 mAs 8x8 cm²		Promax 3D MAx ND / NR 67.2 mAs 10 x 9 cm²	
	original	rotated	original	rotated
Brain	173	307	236	283
Skin	318	312	358	359
Esophagus	361	355	604	638
Muscles	231	244	366	370
ET	1844	2567	3137	3324
Thyroid	842	689	1498	1395
Salivary glands	3633	4147	6490	6526
Oral mucosa	4421	4684	6304	6073
RBM	201	233	293	349
Bone surface	930	1079	1370	1632
Lymph nodes	318	366	777	798

Table 2.8 Organ doses (µGy) for original and rotated version for Peter

Organs	Accuitomo 170 Std Resolution 87.5 mAs 8x8 cm²		Promax 3D MAx ND / NR 67.2 mAs 10 x 9 cm²	
	original	rotated	original	rotated
Brain	156	251	195	328
Skin	268	289	288	302
Esophagus	305	371	572	688
Muscles	189	200	252	270
ET	1712	2072	2559	2486
Thyroid	696	620	1373	1165
Salivary glands	3334	3689	6011	6470
Oral mucosa	4000	3647	5988	5594
RBM	170	189	222	269
Bone surface	790	877	1031	1246
Lymph nodes	320	362	504	506

Table 2.9 Organ doses (µGy) for original and rotated version for Vivian

Organs	Accuitomo 170 Std Resolution 87.5 mAs 8x8 cm²		Promax 3D MAx ND / NR 67.2 mAs 10 x 9 cm²	
	original	rotated	original	rotated
Brain	130	167	165	165
Skin	216	215	240	244
Esophagus	235	196	461	404
Muscles	159	162	208	209
ET	1563	1801	2139	1989
Thyroid	569	407	965	859
Salivary glands	3135	3375	5374	5355
Oral mucosa	3529	3486	5298	5171
RBM	145	153	186	202
Bone surface	672	711	861	942
Lymph nodes	271	266	408	381

Table 2.10 Organ doses (μGy) for original and rotated version for the ICRP female voxel model

Organs	Accuitomo 170 Std Resolution 87.5 mAs 8x8 cm²		Promax 3D MAx ND / NR 85.4 mAs 10 x 9 cm²	
	original	rotated	original	rotated
Brain	56	86	122	190
Skin	86	90	168	180
Esophagus	88	51	296	161
Muscles	59	54	149	134
ET	614	558	1931	1791
Thyroid	199	159	763	569
Salivary glands	1335	1556	4260	4828
Oral mucosa	1489	1474	4152	3977
RBM	54	61	142	168
Bone surface	249	285	658	779
Lymph nodes	94	92	309	303

2.6.3 Discussion and Conclusions

This work demonstrates a methodology to rotate head voxel models to establish an horizontal Frankfort line and to position them properly around the centre of rotation. The motivation which triggered the application on two different CBCT systems was to investigate two scanners with different geometric and technical specifications. Accuitomo 170 performs a 360° rotation around the head resulting in a completely different dose distribution within the head compared to a 210° rotation in the Promax 3D Max scanner. Furthermore, in Promax 3D Max, the x-ray tube crosses the posterior part of the head avoiding the direct exposure of radiosensitive organs which are located in the anterior head and neck anatomic region. On the other hand, it gets closer to the skin due to shorter SAD compared to Accuitomo 170. Moreover, the two scanners differ in their inherent filtrations. Accuitomo employs a bowtie filter whereas Promax 3D Max implements a combination of flattening filters (Cu and Al). Therefore, their energy spectra at the operating voltages and their radiation field characteristics all over the FOV are also different. The two systems also exhibit different beam shape geometries: In Accuitomo 170 the beam is symmetrical (i.e. the radiation field is evenly distributed across its central axis), not only in the axial-transverse plane but also in the vertical-sagittal plane. On the other hand, in Promax 3D Max, the radiation field is more complex. It is symmetrical in the axial plane, whereas in the sagittal plane, the lower collimator jaw confines the lower part of the beam to a fixed length, allowing the upper collimation jaw to adjust the opening in order to meet the required height of the FOV at the SAD.

Tables 2.7-2.10 present the results of the calculated dose values. In all cases the thyroidal doses in the rotated voxel models were lower compared to the original ones (average -17.1% in all cases, maximum -29 % for Vivian in Accuitomo 170). This result implies that though the thyroid gets closer to the x-ray tube after rotation, the backward translation resulted in an overall dose reduction to the thyroid. On the other hand, increasing dose trends attributed to the applied corrections, i.e. higher than the MC overall uncertainty of ~6%, were noticed for the dose to the brain (46% on average), to RBM and bone

surface (14 % on average). Brain dose is due to scatter (for these investigated cases), either in rotated or the original models. The applied corrections, although they seem to shift brain backwards, they increase the part of the radiation field which goes beyond the mandibulae (which is a heavily attenuating structure), giving more scatter to the brain.
None of the rest organs presented a systematic dose response to the comparison of with or without Frankfort plane correction . The complex radiation fields, the different x-ray beam and scanner rotation geometries and the patient-specific anatomical details (shape, size and orientation of organs, location with respect to other organs) are at the origin of the a priori unpredictable response, not only across the phantom range, but also between different FOVs of the same model. These cases clarify the counteracting influence of the applied corrections on the dose; the upward rotation to establish the horizontal Frankfort plane increases the dose to most organs in the head and neck region as it brings them closer to the x-ray tube; the backward translation decreases the dose for the same reason, yet the downward translation may have both outcomes depending on the geometry and the position of the organ in the head. In addition, the reorientation of the head develops a different x-ray scatter pattern in the head which influences organ dosimetry.
This work didn't aim to compare doses between CBCT systems or organ doses delivered to different voxel models; its main purpose was to investigate whether the geometrical corrections which shall be applied to each individual voxel model such that it mimics a realistic patient positioning during dental CBCT exposures influences dosimetric calculations. Absorbed organ dose differences up to 45.6% were obtained in some cases when comparing the original and the rotated version of each individual model. This difference is considered substantial in MC dose studies; it may lead to large miscalculations in radiosensitive organ doses and to misinterpretation of the radiation induced risk. The corrections are protocol and model-specific. They depend on the position of the FOV inside the head and the anatomy of the patient-model. Therefore, they shall be determined for each individual case and applied to the model.

2.7 APPENDIX 2: Are organ doses age and/or gender – dependent?

In this section, a MC study is presented, aiming to clarify whether organ doses are age and/or gender –dependent. To this end, a cleft protocol was simulated in Promax 3D Max for both males and females of the same age; Dejan and Demi (5y.o), Peter and Xoch (8y.o), Mike and Vivian (12 y.o).

2.7.1 Methods and Materials

The investigated protocol in the study was a typical cleft 10 x 5.5 cm^2 (diameter x height) in Promax 3D Max. The most frequently used operation mode / exposure settings were applied; an ULD / NR (Ultra Low Dose / Normal Reconstruction) operation mode for a 'Small' Size patient which is carried out at 96 kV with 16 mAs and a reconstruction voxel size of 200 μm. The six abovementioned models were extracted from the database and protocol specific geometric corrections for the Frankfort plane were applied to each of them. The position of the cleft FOV inside the mouth cavity is demonstrated in figure 2.10.

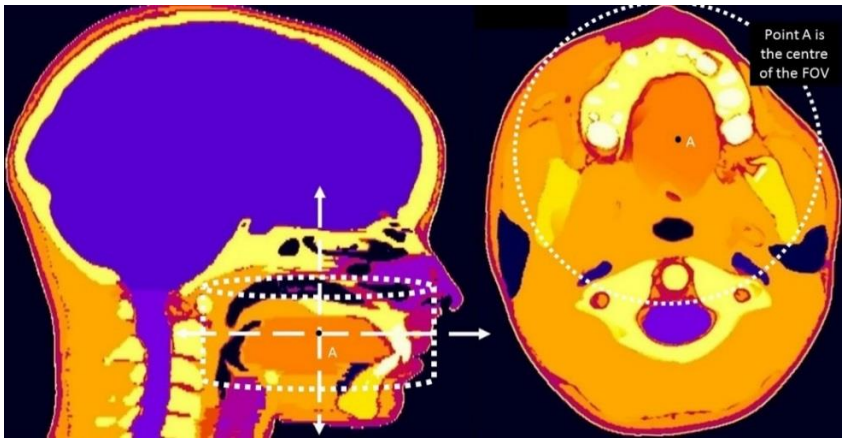

Figure 2.10 Cleft palate FOV positioning. The FOV is 5.5 cm in height and 10 cm in diameter. The centre of the FOV is positioned at the centre of the mouth cavity in the axial plane and on the level of the roots of the upper teeth along the vertical axis

2.7.2 Results

The results of the study are presented in table 2.11. The MC statistical simulation uncertainty was less than 1% in all cases and the overall statistical uncertainty ~6%. The presented dose values have been weighted to the total mass fraction of each organ in the body.

Table 2.11. Absorbed dose to radiosensitive organs under identical exposure cleft palate protocol conditions

Organs	Dejan 5y.o. Male	Demi 5y.o. Female	Peter 8y.o. Male	Xoch 8y.o. Female	Mike 12y.o. Male	Vivian 12y.o. Female
	Absorbed organ doses (μGy)					
Brain	31	34	26	28	21	20
Skin	56	58	40	43	27	30
Oesophagus	53	51	39	39	25	31
Eye lenses	273	309	216	217	124	159
Muscles	56	61	41	41	28	29
ET	696	786	592	588	387	370
Thyroid	239	282	198	192	112	111
Salivary glands	1341	1401	1072	999	654	650
Oral mucosa	1135	1355	836	844	604	647
RBM	49	52	38	40	28	28
bone surface	227	241	177	185	132	131
Lymph nodes	121	118	95	105	55	64

2.7.3 Discussion and Conclusions

The results showed that the average percentage difference in organ doses between pairs of the same age was, in all cases, within ±7 % between the two genders of the same age. These slight organ dose differences lie within the overall statistical uncertainty of the MC dose calculations. However,

noticeable differences were observed in some individual cases; a 17% lower dose to thyroid and oral mucosa were observed for Demi (vs Dejan). A 24% higher dose was also observed in the oesophageal dose of Vivian (vs Mike), yet the absolute dose values are very low. These differences are attributed to the anatomical particularities of each model.

When comparing different age categories in present study, there is a well-established organ dose decreasing pattern with age. On the other hand, comparing doses between genders of the same age, the dose response does not always follow a fixed pattern; Individual organs may receive either higher or lower doses.

There are many factors which contribute to this unstable dose response pattern; the size of the head where for a bigger head circumference and hence for a wider head, the skin surface comes slightly closer to the x-ray tube and therefore skin and muscles may receive higher doses; the segmented mass fractions that are not identical; the dose to the skin is dependent on the in-plane resolution of the voxel model (x-y dimension) and the voxel size of the segmented skin; the scatter distribution is different at each voxel model due to variations in head anatomy among the models. The results of the study suggest that age-specific voxel models are required to estimate organ doses in the head region. The two opposing gender models at each age category do not lead to large organ differences.

CHAPTER 3

Indication-based radiation dose and risk assessment

3.1 Introduction

Paediatric radiation dose assessment in dental and maxillofacial CBCT imaging is a complicated task which differs from any other modality in diagnostic radiology. From simple radiographic and mammography systems to more complicated MDCTs, all devices (of each modality) have similar technical specifications and acquisition geometries. Besides, well-established and documented guidelines, which suggest examination-specific exposure parameters, dictate the protocol selection process resulting in an organized radiation dose management.

This is not the case in dental and maxillofacial CBCT imaging. Scanners operate in different voltages (kV) (most frequently between 70 and 110 kV) and employ different filters not only in material composition and thickness but also in shape (flat vs beam shaping-bowties). This produces different energy spectra and x-ray tube outputs, each requiring different loads (mAs) to provide sufficient energy to the detector. Apart from energy spectra, different geometric characteristics exist among scanners. Acquisitions are realized in a full (360°), half (180°), or partial (180°-360°) rotation creating different in-patient dose distributions. The Source to Axis of Rotation Distance (SAD) and the magnification factor, i.e. the Source to detector distance (SDD) divided by the SAD, play a key role in patient dose as dose is inversely proportional to the square of the patient-x-ray source distance. Collimators may also impact dose in many ways; they define the size of the FOV and the shape of the beam. Neither the size nor the shape are similar for identical clinical cases among scanners. While FOVs can be categorized in Small, Medium and Large, dimensions for a specific clinical indication (diameter x height) are different among manufacturers. Furthermore, the longitudinal and the in-plane beam shape are also different. While the former influences the magnitude of the dose to organs beyond the actual anatomic site of interest, the in-plane beam is not always as in MSCT centered and covering the whole head. A symmetrical axial beam allows half or partial rotations to be carried out, while an offset one can only be performed in a full-rotation mode. Paediatric dose assessment is even more complicated. In paediatric ages the anatomy changes rapidly in size and shape. Each scanner offers a wide range of FOV sizes to allow the entire anatomy of interest to be imaged as it changes in size with age. Therefore, it is not only the fact that scanners offer different FOV options for identical clinical indications, but they also have different options for different age categories. Furthermore, each FOV size is offered in a wide range of exposure parameters (time or tube load-mAs) and reconstruction voxel sizes depending on the required image resolution level.

This chapter aims to deal with all the above-mentioned dosimetric issues and to provide an indication-based and scanner-specific radiation dose and risk guide for paediatric patients. We designed an extensive MC study consisting of about 700 simulations. Twelve voxel models of the database previously described in chapter 2, covering the entire paediatric age range, were used in the study. For each voxel model, organ doses were calculated for specific clinical indications in every scanner for which the MC framework has been customized. More specifically, MC simulations were carried out for four tooth imaging cases (Central Upper Incisors (CUI), Central Lower Incisors (CLI), Premolar Upper (PU) and lower (PL)), for Upper and Lower Jaw imaging (ULJ), for Lower Jaw (LJ) and cleft palate imaging, for sinus and dentomaxillofacial complex imaging and for face and skull imaging. For NewTom 5G, which is the only MDCT-like scanner with patients in supine position laying on a table, organ doses were also calculated for unilateral and bilateral temporal bone imaging. The choice of the FOV which was modelled for each clinical indication was based on the size of the patient head for each age category in full accordance with the selection of the FOV in clinical practice, i.e. smaller FOV sizes were used for upper/lower jaw imaging for 5 compared to 10 year old models to avoid over exposure of critical organs. The ultimate goal of the study was to investigate organ dose patterns with age.

Once organ doses had been calculated, the respective radiation risk was estimated for each case. The risk was assessed in two ways. At first, the traditionally used effective dose (E) was calculated using the ICRP publication 103 (2007) weighting factors. Even if E has been recently criticized by the scientific

community (Martin 2007, 2008, Brenner 2008), it is still used by medical teams to evaluate the potential detriment of an exposure. The E results were further analyzed to compute the detriment for cancer and hereditary effects such as to decode an incomprehensible figure (mSv) into a meaningful estimation (cases / 100,000). In a second step the Life Attributable Risk (LAR) incidence was calculated. The LAR incidence rather than mortality was selected to compare E-related detriment and LAR. This decision was founded by the A114 comment of the ICRP publication 103 (2007) where it is stated that the risk estimates provided in the publication are based on incidence data rather than mortality as they provide a more complete description of the cancer burden than do mortality data, particularly for cancers that have a high survival rate. In addition, cancer registry (incidence) diagnoses are more accurate and the time of diagnosis is more precise (ICRP 2007). To ease the LAR calculations an excel-based software tool was designed that requires the gender, the age at exposure and organ dose values as an input.

Organ dose, E and LAR calculations have all been normalized to mAs. The rational for such a decision was twofold. There are different operation modes for each FOV (low resolution, standard resolution, high resolution), each named differently by the manufacturer, i.e. Ultra-Low Dose, Low Dose, Standard Dose, Normal Dose, Echo, Regular, High Definition, High Resolution, Boost, R1, R2 etc). Therefore, in the context of this study, selecting one single operation mode from each scanner, even at the same resolution level, is not ideal. Absolute dose comparison between scanners shall be carried out after measurements have been performed to ensure similar image quality among comparable protocol related operation modes. As an example, an 'Ultra-Low dose – Normal Reconstruction' mode in one scanner, rather than the 'Normal dose – Normal reconstruction', is closer to the 'Standard resolution' mode of another scanner in terms of image quality. Therefore, it is not advised comparing the 'Normal Dose – Normal Resolution' mode of the former scanner against the 'Standard resolution' mode of the latter as naming may be rather similar, whereas denotations through benchmarking and dosimetric levels may vary extensively. Therefore, the results in this study are expressed in µGy/mAs and are applicable to every operation mode; the user can easily calculate an absolute dose value (µGy) by merely applying the mAs of the desired operation mode.

3.2 Methods and Materials

3.2.1 Voxel models and investigated protocols

Table 3.1 illustrates the voxel models which participated in the study. The models were picked such that they cover the entire paediatric age range from 5 to 14 years old. MC simulations were carried out for various clinical indications.

Table 3.1 The voxel models which participated in the study

# model	Name	Age	Gender
1	Demi	5	F
2	Dejan	5	M
3	Joris	6	M
4	Guozhi	7	M
5	Xoch	8	F
6	Peter	8	M
7	Benjamin	9	M
8	Louisa	10	F
9	Andrew	10	M
10	Vivian	12	F
11	Mike	12	M
12	Georgia	14	F

The selection of the simulated FOVs was not only age-dependent but was also based on morphometric measurements. For tooth imaging protocols, a single FOV was selected. For upper/lower jaw (ULJ) the selected FOV should encompass both jaws, i.e. it should have a diameter larger than the bigonial breadth, and a FOV height larger than the menton-subnasale length (figure 3.1). For lower jaw (LJ) and cleft protocols the bigonial breadth and the half menton-subnasale length (lower half for LJ and upper half for cleft) were used to specify the most appropriate FOV. For maxillofacial complex and sinus protocols, the diameter of the selected FOV should be larger than the bizygomatic breadth, while the height of the FOV should be larger than the menton-nasal root length (or at least from gnathion to glabella) in the former protocols and such that it covers the distance from the lower edge of the maxillary sinus to the top of the frontal sinus for the latter protocols. The facial FOVs were picked such that they cover most of the facial anatomy whereas the skull protocols should fit the entire head from menton to the crown of the head.

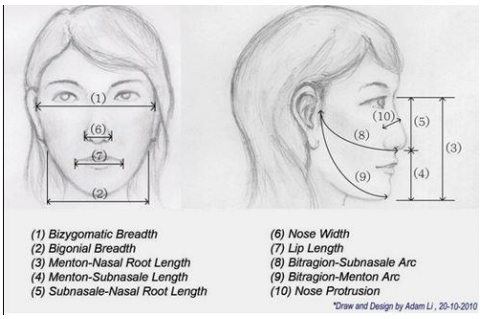

Figure 3.1 Facial morphometrics for FOV selection
(http://www.ouhk.edu.hk/~sctwww/computing/project/DisplayAdamLi.htm)

Tables 3.2 – 3.4 illustrate the simulated FOV per clinical Indication, voxel model and scanner. It must be pointed out that CBCT scanners do not have manual collimation, i.e. the FOVs at each scanner have fixed sizes. Therefore, the selection process aimed to determine the most appropriate FOV meeting the abovementioned size requirements.

Table 3.2 The selected SMALL FOVs for small tooth imaging

Protocols	Scanner	Voxel models	FOVs (diameter x height) (cm^2)
Central Upper Incisors (CUI) Central Lower Incisors (CLI) Premolar Lower (PL) premolar Upper (PU)	Promax 3D Max	All	5x5.5
	Accuitomo 170		6x6
	CS 9300*		5x5
	NewTom 5G**		6x6
	NewTom VGi evo**		5x5

*CS 9300 operates at 80kV for the above selected protocols
**Normal operation mode

Table 3.3 The selected MEDIUM FOVs (diameter x height – cm²)

Protocol	Scanner	Voxel models		
		5-6 years old	7-11 years old	12-15 years old
Lower Jaw (LJ)	Promax 3D Max	8.5 x 4.8	10 x 5.5	10 x 5.5
	Accuitomo 170	10 x 5	10 x 5	10 x 5
	CS 9300*	10 x 5	10 x 5	10 x 5
	NewTom 5G**	8 x 8	12 x 8	12 x 8
	NewTom VGi evo**	8 x 5	10 x 5	10 x 5
Cleft	Promax 3D Max	8.5 x 4.8	10 x 5.5	10 x 5.5
	Accuitomo 170	10 x 5	10 x 5	10 x 5
	CS 9300*	10 x 5	10 x 5	10 x 5
	NewTom 5G**	8 x 8	12 x 8	12 x 8
	NewTom VGi evo**	8 x 5	10 x 5	10 x 5
Upper/Lower Jaw (ULJ)	Promax 3D Max	8.5 x 7.5	10 x 9	10 x 9
	Accuitomo 170	8 x 8	10 x 10	10 x 10
	CS 9300*	8 x 8	10 x 10	10 x 10
	NewTom 5G**	8 x 8	12 x 8	12 x 8
	NewTom VGi evo**	8 x 8	10 x 10	10 x 10
Unilateral Temporal (UT)	Promax 3D Max	/	/	/
	Accuitomo 170	/	/	/
	CS 9300	/	/	/
	NewTom 5G**	8 x 8	8 x 8	8 x 8
	NewTom VGi evo**	/	/	/
Bilateral temporal (BT)	Promax 3D Max	/	/	/
	Accuitomo 170	/	/	/
	CS 9300	/	/	/
	NewTom 5G**	15 x 5	15 x 5	15 x 5
	NewTom VGi evo**	/	/	/

*CS 9300 operates at 85 kV for the above selected protocols
**Normal operation mode

Table 3.4 The selected LARGE FOVs (diameter x height – cm²)

Protocol	Scanner	Voxel models		
		5-6 years old	7-11 years old	12-15 years old
Maxillofacial Complex	Promax 3D Max	10 x 9	10 x 13	10 x 13
	Accuitomo 170	10 x 10	10 x 10	10 x 10
	CS 9300	10 x 10	10 x 10	10 x 10
	NewTom 5G**	12 x 8	12 x 8	12 x 8
	NewTom VGi evo**	10 x 10	10 x 10	10 x 10
Sinus	Promax 3D Max	10 x 9	10 x 13	10 x 13
	Accuitomo 170	10 x 10	10 x 10	10 x 10
	CS 9300	10 x 10	10 x 10	10 x 10
	NewTom 5G**	12 x 8	12 x 8	12 x 8
	NewTom VGi evo**	10 x 10	10 x 10	10 x 10
Face	Promax 3D Max	13 x 13	13 x 13	13 x 16
	Accuitomo 170	14 x 10	14 x 10	17 x 12
	CS 9300	17 x 11	17 x 11	17 x 13.5
	NewTom 5G**	15 x 12	15 x 12	18 x 16
	NewTom VGi evo**	15 x 12	15 x 12	16 x 16
Skull	Promax 3D Max	23 x 26	23 x 26	23 x 26
	Accuitomo 170	17 x 12	17 x 12	17 x 12

CS 9300	17 x 13.5	17 x 13.5	17 x 13.5
NewTom 5G**	18 x 16	18 x 16	18 x 16
NewTom VGi evo**	24 x 19	24 x 19	24 x 19

*CS 9300 operates at 85 kV for the above selected protocols
**Normal operation mode

3.2.2 Organ dose, E and LAR calculations

Organ doses were calculated for each tabulated protocol. As already mentioned, each FOV is clinically available in several operation modes. Dose-wise, the only difference between each operation mode is the total mAs / rotation. When a MC simulation is performed, organ dose values are provided in μGy/# hist. By multiplying that figure with the respective scanner and protocol-specific calibration factor fMC (# hist / mAs) (chapter 1), doses are converted to μGy/mAs. This is the final figure this study aims to present to make the results applicable to every operation mode, since doses are proportional to mAs. A simple further multiplication by the mAs of the operation mode of interest is sufficient to provide an absolute dose value.

Each individual organ dose is calculated as the sum of the energy which is deposited to a specific organ per projection. Promax 3D Max, Accuitomo 170 and CS 9300 operate with fixed mA at each projection and therefore, each projection is equally weighted, i.e. the x-ray output remains constant at each projection. NewTom 5G and VGi-evo on the other hand, employ a rotational, preprogrammed TCM based on a mathematical formula which takes into account the AP and LAT prescan mA values (chapter 1.8.1). For every investigated protocol, the AP and LAT prescan mA values were extracted from the PACS, and a TCM curve was subsequently designed by determining the mA at each projection (from the mathematical formula provided by the manufacturer). The average mA value during rotation was successively calculated, and each projection was given a weighting factor equal to the ratio of the formula-determined mA to the average mA value, i.e. the x-ray output is not constant at each projection. The weighting factors were employed to each final MC calculated organ dose integral after each projection. In order to simulate clinically relevant exposure settings, we tried to retrieve from PACS patients with similar anatomical characteristics as our voxel models, yet this was not feasible for small FOV protocols, since CBCTs only display a restricted region of the head around the anatomy of interest. When two or more patients of the same age and gender were found to have undergone the same exam, an average AP and LAT value was calculated, and thus, an average TCM curve was designed. This was accomplished for the most frequently applied small, medium, maxillofacial complex and sinus protocols. However, in some cases, it was just one exam that we managed to retrieve, implying that the designed TCM curve may not be an average one, but a patient-specific one applied to the respective average voxel model. This was the case for NewTom 5G face and skull protocols for ages < 12 years old and for VGI-evo for face and skull protocols (all ages).

Each case was simulated in 1° angular steps, that is 360 simulations per rotation for Accuitomo 170, NewTom 5G and VGi-evo scanners. For Promax 3D Max and CS 9300, 210 and 200 projections were simulated respectively apart from the largest FOV protocols (23x26 cm^2 and 17x19 cm^2 respectively), where 360 projections were also modelled as these acquisitions are carried out in a full rotational mode (table 1.1). Ten million histories per projection were simulated under the same physics related MC parameters mentioned in section 1.2.1. Once organ doses have been calculated, E was assessed for each case based on ICRP 103 (2007) weighting factors.

An excel-based software tool was also developed to ease the calculations of LAR. The tool was based on the BEIR VII report (National Research Council of the National Academies 2006). The report provides data on organ cancer incidence and mortality rates for certain cancer sites (organs), expressed in

number of cases per 100,000 persons exposed to a single organ dose of 0.1 Gy (Tables 12D-1 and 12D-2, p.311). Data are available for both males and females and for various ages-at-exposure (0-80 years old at 5 years steps). For both males and females, a shape preserving algorithm was fitted in Matlab (version 7.12.0.635, R2011a, MathWorks Inc) to LAR incidence and mortality rates to obtain data for intermediate ages (0-80 years old at 1 years steps).

From all radiosensitive organs present in the head and neck region, LAR data only exists for thyroid and leukemia (due to radiation dose to RBM). However, there is also data regarding the accumulated cancer incidence and mortality risk to all organs apart from those explicitly specified in tables 12D-1 and 12D-2 of the BEIR VII report, under the tab 'other'. Therefore, for each simulated case, In a first step, the LAR incidence for thyroid and RBM was calculated for the respective MC calculated absorbed dose values. The average organ dose to all organs but RBM and thyroid was subsequently calculated, and the LAR incidence for other organs was assessed. To obtain a total body LAR value, the sum of LAR incidence for thyroid, RBM and other organs was calculated.

A thorough analysis was carried out to investigate organ dose, E and LAR patterns with age. The analysis was performed in two stages. Initially, we investigated the feasibility to draw conclusions on organ dose patterns with age for each clinical case for all scanners participated in the study. In a second stage, a scanner-specific, rather than all-in-one, analysis was conducted. It shall be mentioned that for 5, 8, 10 and 12 years old models, the average organ doses and E of the two genders of the same age were calculated and used in the dose pattern investigation for each clinical case. However, for the LAR response pattern with age investigation, the individual calculations were used, as LAR is gender dependent.

3.3 Results

The number of simulated histories resulted in a MC simulation uncertainty of less than 0.5% in all radiosensitive organ doses (% CV). There was a poor correlation between global average organ dose values (for all scanners) with age for each clinical case (Pearson correlation coefficient range: -0.35 to 0.12). Furthermore, Standard deviations of average organ dose values were in most cases even higher than the absolute dose values, clarifying the totally different energy spectra, x-ray tube outputs among scanners, technical specifications and acquisition geometries among scanners. Therefore, a scanner-specific analysis was conducted. Analyzing each clinical case separately for each scanner, a very well-established organ dose decrease pattern with age was observed. The best fit option was in all cases a logarithmic curve between organ doses, E and LAR incidence vs age. Figures 3.2 – 3.6 present the organ dose values (μGy/mAs) vs age for each clinical case. We used a logarithmic scale for the organ dose axis to enable every organ to be illustrated in the figures.

Figure 3.2 Organ dose (µGy/mAs) vs age for the investigated clinical cases in Promax 3D Max.

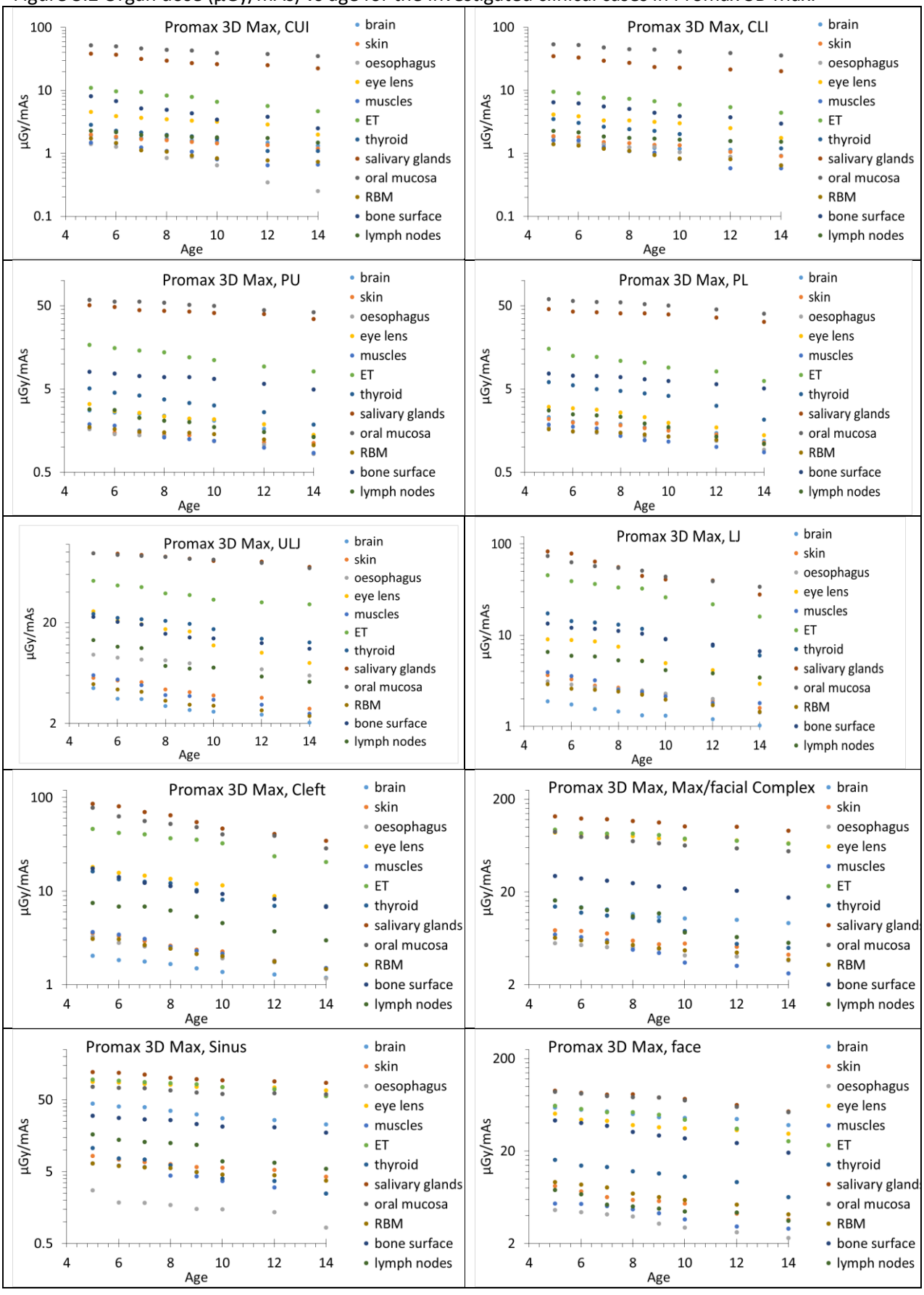

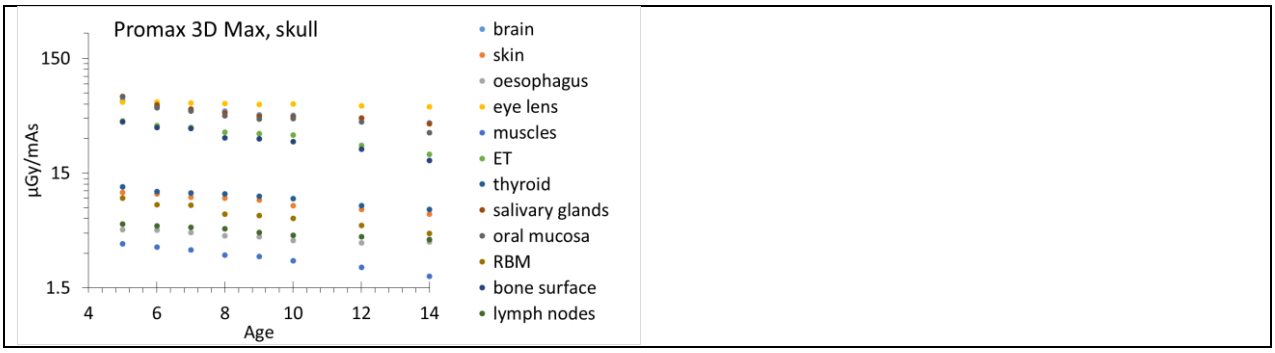

Figure 3.3 Organ dose (µGy/mAs) vs age for the investigated clinical cases in Accuitomo 170.

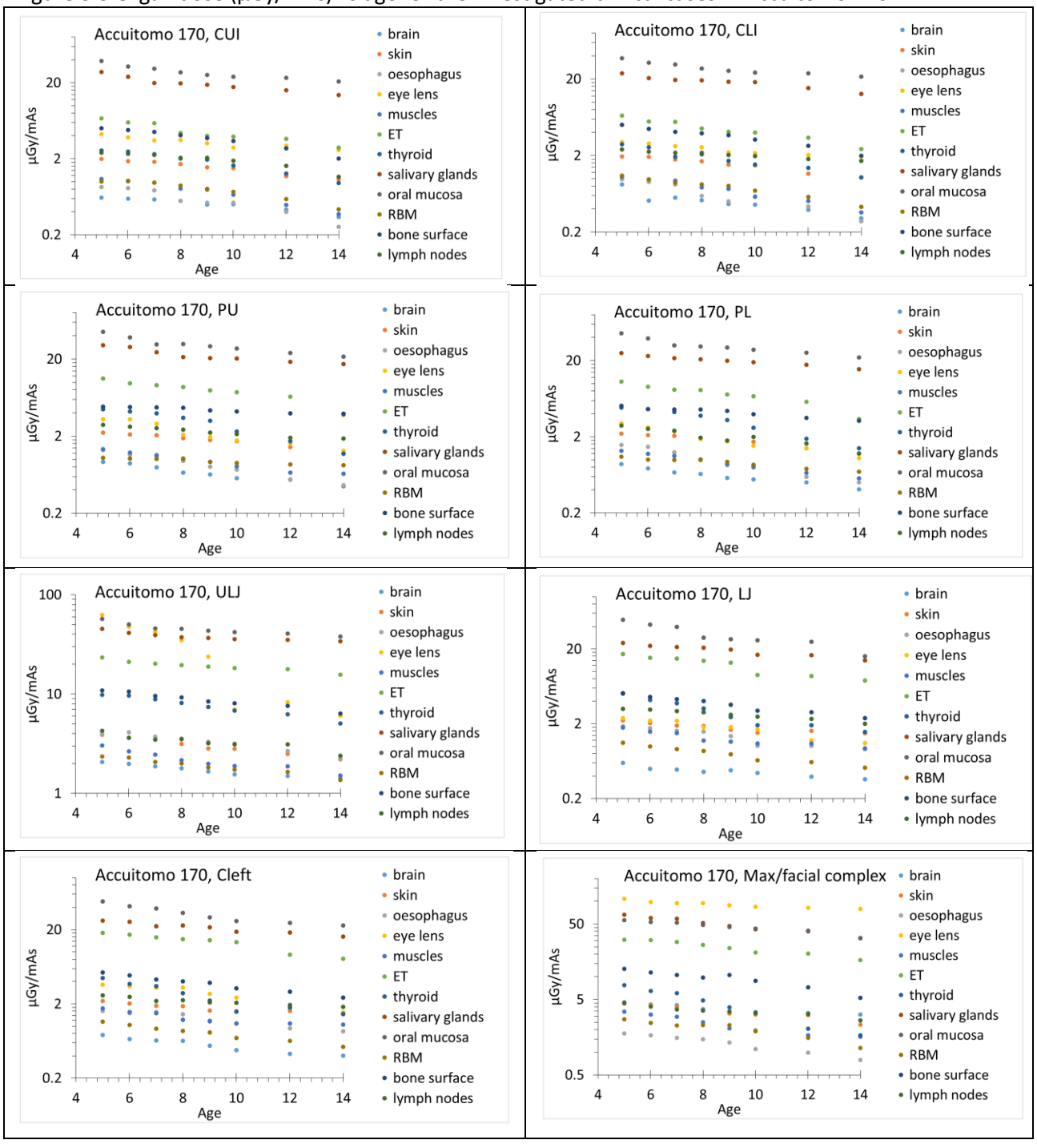

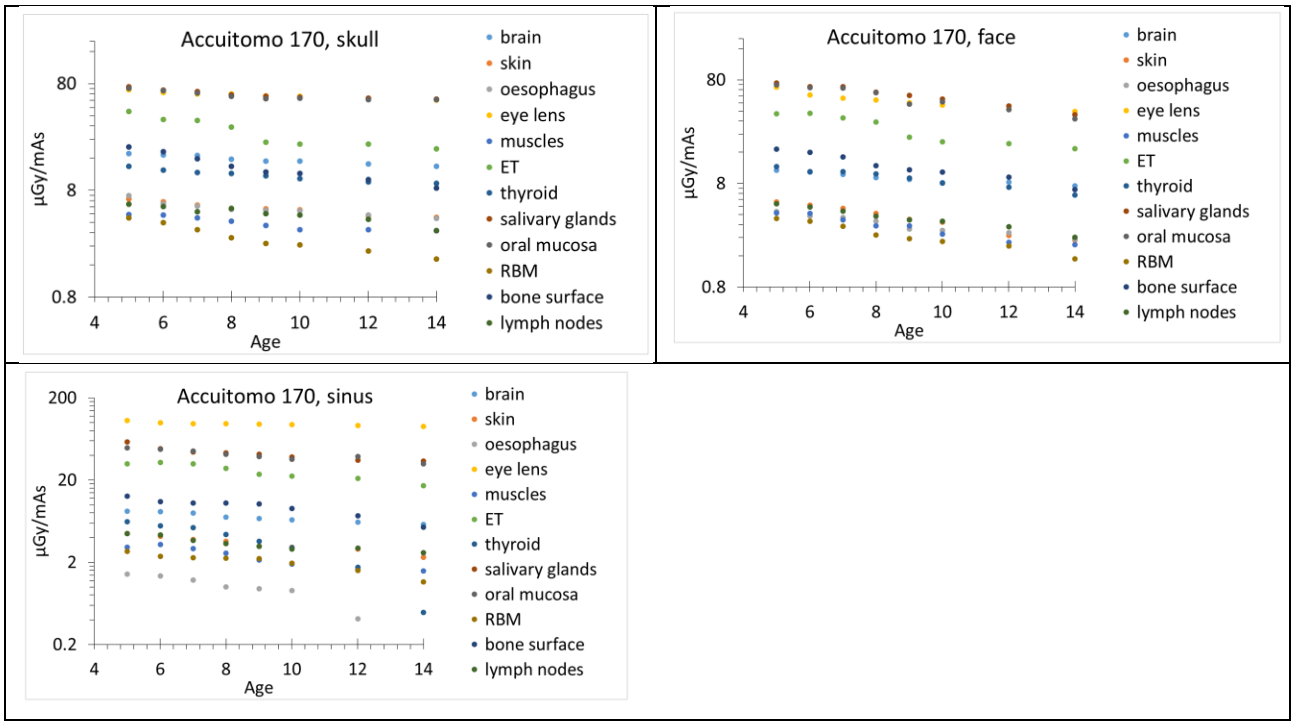

Figure 3.4 Organ dose (µGy/mAs) vs age for the investigated clinical cases in CS9300

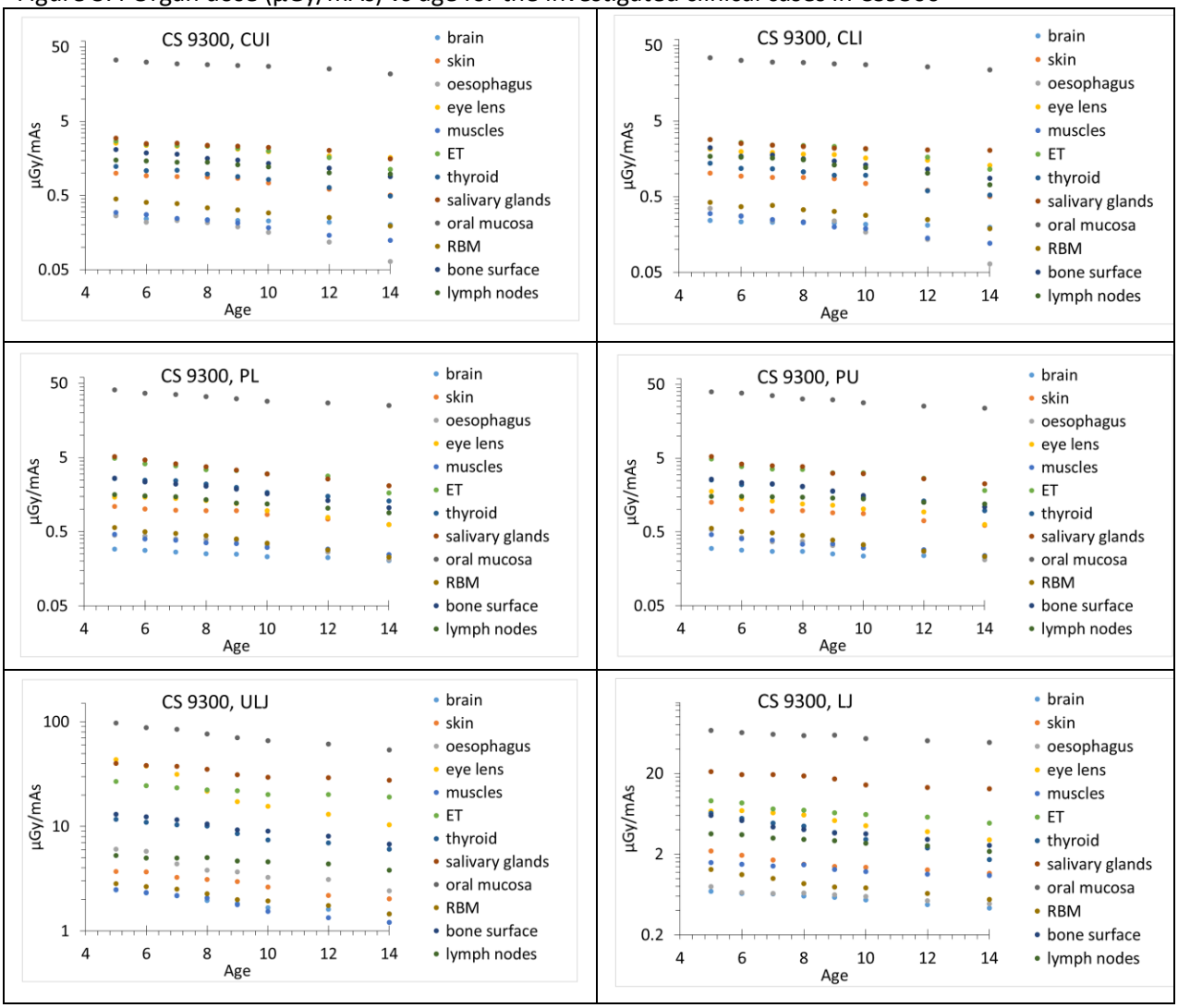

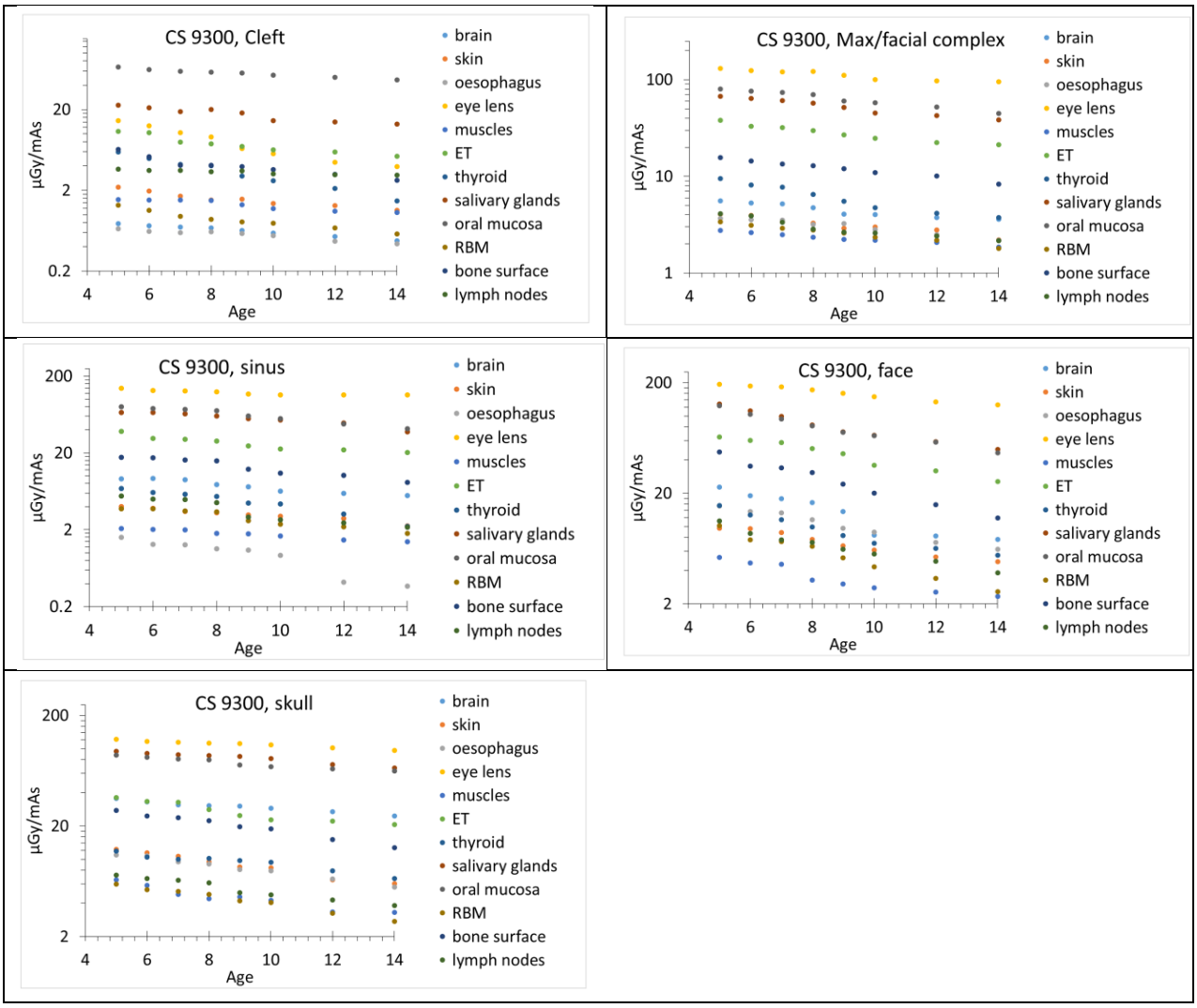

Figure 3.5 Organ dose (µGy/mAs) vs age for the investigated clinical cases in NewTom 5G

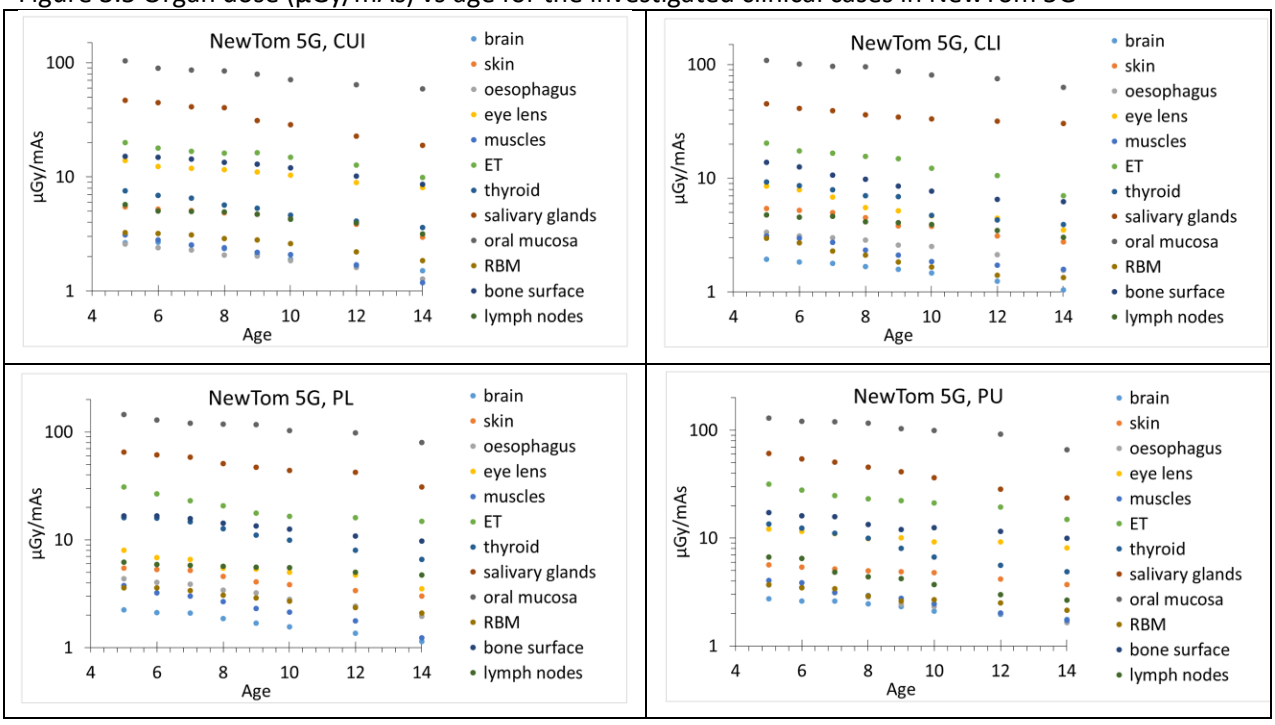

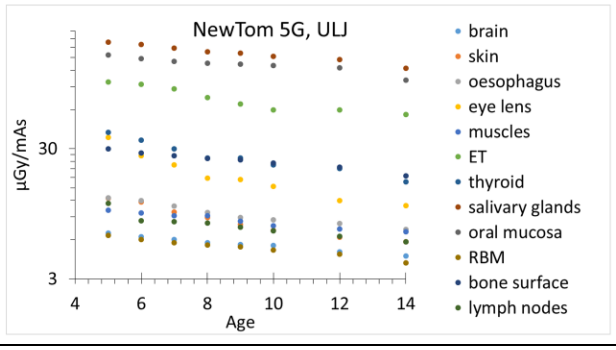
NewTom 5G, ULJ
µGy/mAs
30
3
4
6
8
10
12
14
Age
brain
skin
oesophagus
eye lens
muscles
ET
thyroid
salivary glands
oral mucosa
RBM
bone surface
lymph nodes

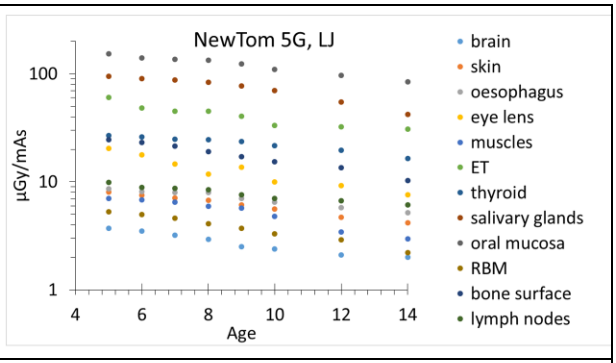
NewTom 5G, LJ
µGy/mAs
100
10
1
4
6
8
10
12
14
Age
brain
skin
oesophagus
eye lens
muscles
ET
thyroid
salivary glands
oral mucosa
RBM
bone surface
lymph nodes

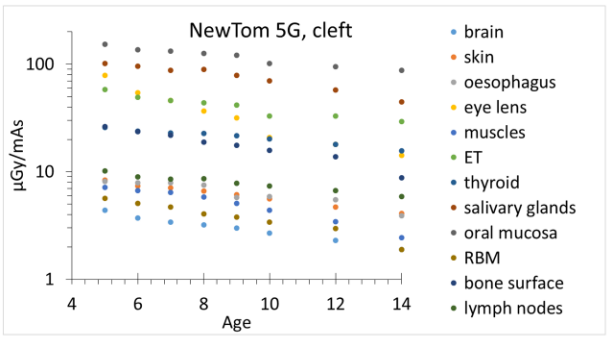
NewTom 5G, cleft
µGy/mAs
100
10
1
4
6
8
10
12
14
Age
brain
skin
oesophagus
eye lens
muscles
ET
thyroid
salivary glands
oral mucosa
RBM
bone surface
lymph nodes

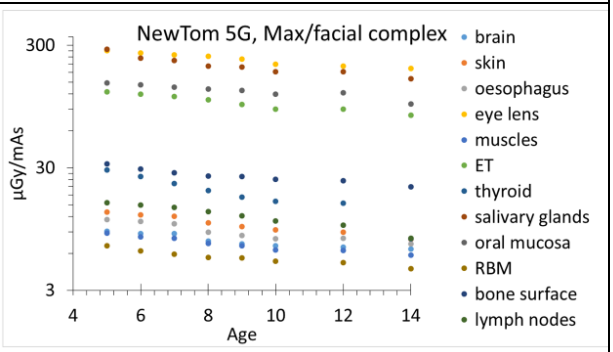
NewTom 5G, Max/facial complex
µGy/mAs
300
30
3
4
6
8
10
12
14
Age
brain
skin
oesophagus
eye lens
muscles
ET
thyroid
salivary glands
oral mucosa
RBM
bone surface
lymph nodes

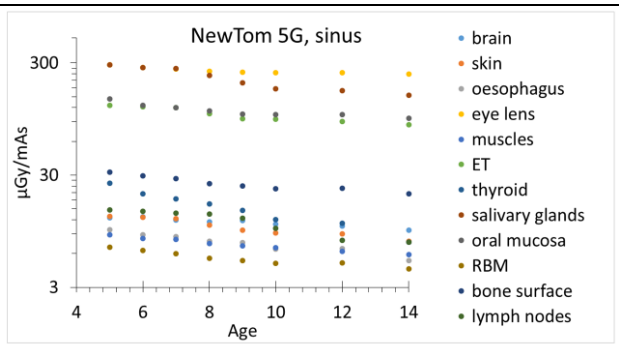
NewTom 5G, sinus
µGy/mAs
300
30
3
4
6
8
10
12
14
Age
brain
skin
oesophagus
eye lens
muscles
ET
thyroid
salivary glands
oral mucosa
RBM
bone surface
lymph nodes

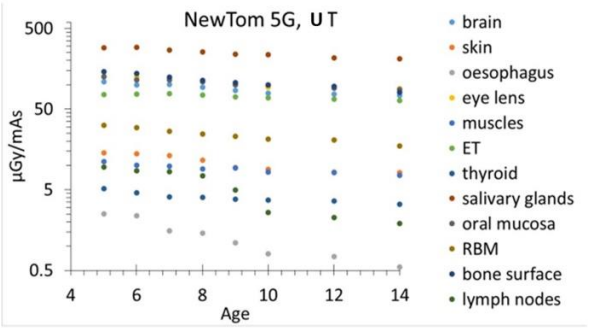
NewTom 5G, UT
µGy/mAs
500
50
5
0.5
4
6
8
10
12
14
Age
brain
skin
oesophagus
eye lens
muscles
ET
thyroid
salivary glands
oral mucosa
RBM
bone surface
lymph nodes

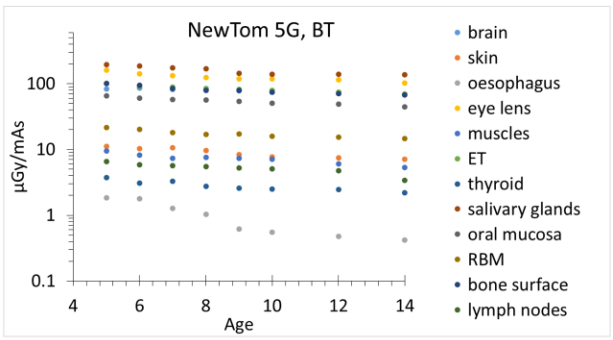
NewTom 5G, BT
µGy/mAs
100
10
1
0.1
4
6
8
10
12
14
Age
brain
skin
oesophagus
eye lens
muscles
ET
thyroid
salivary glands
oral mucosa
RBM
bone surface
lymph nodes

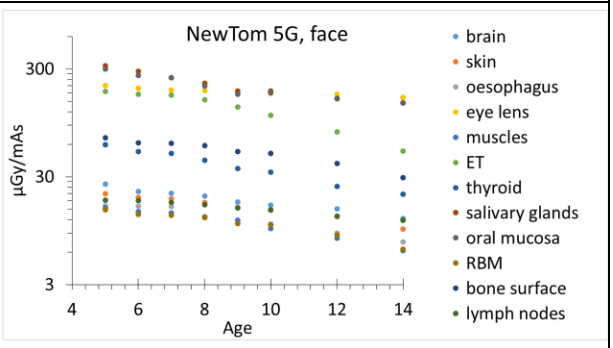
NewTom 5G, face
µGy/mAs
300
30
3
4
6
8
10
12
14
Age
brain
skin
oesophagus
eye lens
muscles
ET
thyroid
salivary glands
oral mucosa
RBM
bone surface
lymph nodes

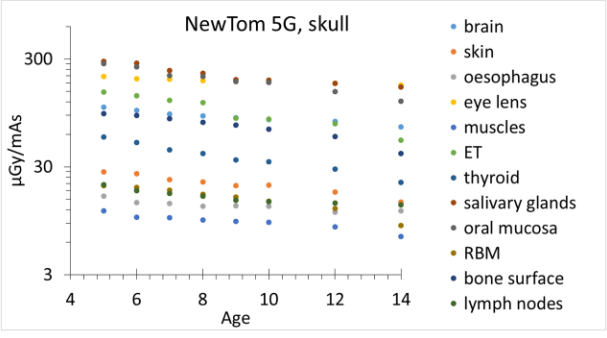
NewTom 5G, skull
µGy/mAs
300
30
3
4
6
8
10
12
14
Age
brain
skin
oesophagus
eye lens
muscles
ET
thyroid
salivary glands
oral mucosa
RBM
bone surface
lymph nodes

Figure 3.6 Organ dose (µGy/mAs) vs age for the investigated clinical cases in NewTom VGi-evo

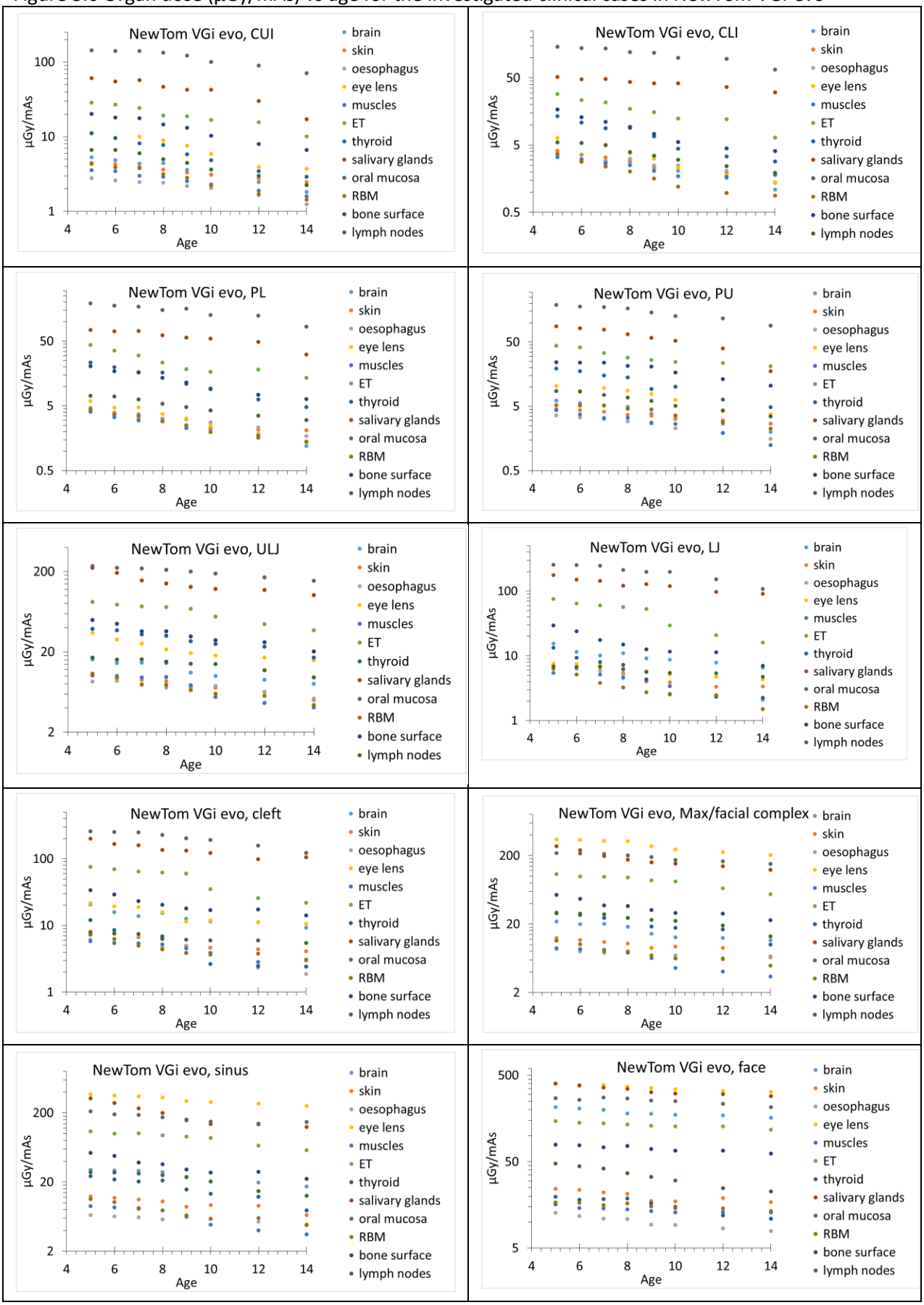

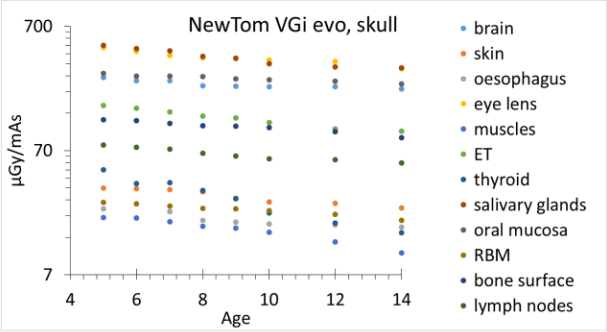

Organ doses, E and LAR incidence are all related to age via the following equation 3.1:

$y = a * \ln(x) + b$ (eq.3.1)

where y is the normalized absorbed organ dose value (µGy/mAs), the normalized E (µSv/mAs) and the normalized LAR incidence (cases/100,00/mAs) and x the age of the patient. The values of a and b are provided in the following tables for every organ, every clinical case and scanner.

In the appendix of this chapter (section 3.7), tables 3.5-3.17 present the scanner and protocol specific logarithmic formulas of organ dose, E and LAR incidence vs age, along with each coefficient of determination (R^2) and Pearson correlation coefficient (r).

3.4 Discussion

This was an extensive simulation study providing organ dose, effective dose and LAR incidence estimations for the most frequently applied clinical protocols in dental and maxillofacial imaging, for five different scanners and for the entire age range from 5 to 14 years old. While it is possible to extrapolate the dose values beyond the simulated paediatric age range, it remains to be investigated until which age it can be done. For each clinical case and scanner, the tables provide the a and b constants of equation 3.1 and enables organ dose, E and LAR incidence assessment for any requested paediatric age (x).

Figures 3.2-3.6 present the organ dose trends with age for each scanner and protocol. The y-axis which depicts the normalized organ dose (µGy/mAs) is always adjusted to a logarithmic scale in order to enable the dose trends of every organ to be displayed. The wide range of organ doses in each investigated case which necessitates the use of logarithmic scale is due to the position of each individual organ in the head with respect to the position of the FOV. For most small FOV acquisitions (CUI, CLI, PU and PL protocols), the highest irradiated radiosensitive organs are the oral mucosa, the salivary glands and the extra thoracic tissue (ET). In all aforementioned cases, oral mucosa, being always inside the primary field and thus constantly irradiated during rotation, receives a higher dose compared to salivary glands. This is due to the fact that the parotid gland which is the biggest salivary gland is not totally covered by the primary radiation field. Although the sublingual and submandibular are continuously exposed, the total energy received per unit mass of the salivary glands as a unit organ is still lower than the energy deposited to oral mucosa. Extra thoracic tissue (ET) dose is also high as the largest part of the pharynx and the larynx are inside the primary field (ET2 region), yet the ET1 region (outline of the nasal cavities) is still outside the field in small FOVs. The beam shape and the acquisition geometry determine the organs which receive the lowest dose at each scanner. In all small FOV cases, as expected, RBM, muscles, brain and esophagus receive the lowest doses among organs. This is due to the fact that organ doses have been weighted for their mass fractions and therefore, each dose value refers to the energy which was as been deposited to the entire organ in the body and not in the fraction of the organ present in the head and neck region. Although esophagus, RBM,

muscles may be partially in the primary field in some cases, their mass fraction in the irradiated region is very small compared to their total mass distributed all over the body.

For Medium FOV acquisitions (LJ, cleft, ULJ, maxillofacial complex, sinus plus MT and BT for NewTom 5G), salivary glands, oral mucosa and ET are still among the highest irradiated organs, yet there is a considerable dose increase to eye lenses, especially for the maxillofacial complex and sinus protocols. Although eye lenses are not associated with stochastic effects of radiation and thus, they are not included in the E and LAR estimations, their dose has been assessed as they are prone to radiation induced cataract. In all sinus and maxillofacial protocols eye lenses receive the highest dose, apart from the acquisitions with the Promax 3D Max. Promax 3D Max performs a 210° rotation where the x-ray tube starts from an anterolateral position, it crosses the head posteriorly, and stops at the opposite anterolateral position. With such an acquisition geometry, direct exposure of the eye lenses is prevented. However, the dose to the lenses are in all cases well below the limit of 0.5 Gy for radiation induced cataract (ICRP 2007, 2012). On the other hand, brain, RBM, muscle and oesophagus receive the lowest doses in LJ, cleft and ULJ protocols. However, in maxillofacial complex and sinus protocols, the dose to brain increases considerably, as it is partially covered by the radiation field. In temporal bone imaging, the dose to bone surface increases considerably as the FOV is positioned around the temporal bone. In MT protocols (on the NewTom 5G), bone surface is the second most highly irradiated tissue after salivary glands, while in BT protocols, where the FOV height is larger, the dose to eye lenses increases significantly and is higher than the dose to bone surface, yet still lower than the dose to salivary glands.

In large FOV scans (face and skull), eye lenses, salivary glands and oral mucosa receive the highest doses. The only exception of this trend is again observed for the Promax 3D Max. As already mentioned, the 210° rotation protects the lenses of the eyes. This is also the case in face imaging. However, the largest 26x26 cm^2 skull protocol in Promax 3D Max presents two special features. It does not operate in a symmetrical axial geometry (as all the other protocols), but in an offset acquisition mode. For image reconstruction purposes, an offset acquisition cannot be carried out in partial rotations as the scanning volume - FOV would not be entirely covered. Therefore, the offset skull protocol is performed in a full rotational mode and the lenses are not anymore protected. Furthermore, to achieve an image of the entire skull (26 cm FOV height), the scanner performs two sequential scans via which the lower and the upper head are imaged and then a stitching software is employed to create an image of the full skull. Oesophagus, muscles and RBM are the least irradiated organs.

Calculating the radiation risk in terms of LAR incidence for 5, 10 and 14 years old patients for a typical small FOV protocol (e.g. CUI), we observed an average (in all scanners) 1.78 times higher risk for 5 years old males compared to 10 years old males (1.82 for females) and 2.88 times higher risk when they were compared to 14 years old ones (3.03 for females). When it comes to MFOV protocols, e.g. cleft palate examination, the average LAR incidence for 5 years old males was calculated 2.06 times higher compared to 10 years old ones (2.08 for females), and 4.4 times higher compared to 14 years old ones (4.43 for females). For large FOVs (e.g. face protocol), the average LAR for 5 years old males is 2.05 times higher compared to 10 years old patients (also for females) while it is 4.45 times higher against 15 years old ones (4.27 for females). These figures clarify that while the risk is highly age-dependent, the gender of the patient does not play a significant role on radiation dose.

It must be noted that organ dose (μGy/mAs), E (μSv/mAs) and LAR incidence (#cases/100,000/mAs) values which are derived from tables 3.5 -3.17 for a given age (and gender for LAR estimations), shall not be used for interscanner dose comparison purposes. Interscanner dose comparisons can be performed, if, and only if, the mAs of each exposure is known and is multiplied with the derived normalized values. Each scanner uses completely different mAs exposure settings to provide sufficient images depending on the type of detector, the geometry, the reconstruction voxel size etc. Therefore, comparing mAs normalized values is meaningless without multiplication with the mAs. On the other

hand, when the user wants to compare two protocols and the mAs values are known, interscanner comparison is feasible via the absolute values (μGy, μSv and #cases/100,000). An example of how to use the data is provided in the following section of this chapter.

On the other hand, intrascanner dose comparison between two different protocols is reasonable and can be carried out based on the normalized data in tables, as long as comparison is intended for the same operation mode (and thus for the same mAs exposure settings). This is the case for all scanners which operate with fixed current (mA) during rotation. For scanners using TCM (NewTom 5G and VGI-evo), intrascanner comparison is not feasible with normalized dose values and the table-derived values need again to be compensated with the total mAs. For instance, a normal CUI protocol and a normal face protocol in the two NewTom scanners are not carried out with the same mAs, as the systemrequires different mAs settings for a proper image quality.

In all cases (scanners, protocols), organs follow a dose decreasing pattern with age. This was an expected trend as the older the patient, the larger the organ, and therefore, the lower the irradiated organ fraction for a given FOV, and consequently, the lower the dose. The dose decreasing pattern was verified with the Pearson correlation coefficient which in all cases was ranging between -0.9 and -1.0. Logarithmic and power fitting was attempted for organ doses, E and LAR vs age, yet a logarithmic curve were chosen as they provided a coefficient of determination higher than 0.9 in all cases.

One of the reasons which triggered this project is the large variability in the reported dose values in dental CBCT imaging, especially for paediatric patients. A characteristic example is given in a data meta-analysis review publication by Ludlow et al (2015). The manuscript provided dose values calculated for several dental CBCT protocols with TLDs in an anthropomorphic phantom representing a 10 years old (ATOM, CIRS, USA). Even for a small FOV acquisition (tooth imaging), there is a 5-fold difference in the effective dose estimation between Theodorakou et al (2012) and Ludlow et al (2015). More specifically, Theodorakou et al estimate the effective dose in Accuitomo 170 for a 4x4 cm² FOV (90kV, 87.5mAs) equal to 28 μSv whereas Ludlow et al estimate it to be 150 μSv for a 6x6 cm² under the same acquisition parameters (table 9,10 of that report). This is a characteristic example of the dose variability. Even if the FOV sizes are different, that does not justify such a large variability in risk estimation. Accuitomo 170 uses a symmetrical longitudinal and axial beam and therefore, the 6x6 cm² FOV only exceeds 1 cm beyond the edges of the 4x4 cm². A 1 cm larger FOV cannot provide a 5-fold increase in the E estimation. Furthermore, as E dissolves any organ dose differences, a 5-fold difference in E values implies much larger differences in the estimated organ doses. For an ULJ protocol (14x10 cm²) FOV in Accuitomo 170 (90kV, 87.5 mAs) Theodorakou et al estimate an E of 237 μSv whereas Ludlow et al estimate it equal to 355 μSv (Table 8 of the report). Using the data provided for Accuitomo 170 in table 3.5, the estimated E for a CUI (tooth protocol) at 90kV and 87.5 mAs is 60 μSv which as a figure is closer to Theodorakou et all rather than to Ludlow et al, given that the CUI FOV that was used in this study was 6x6 cm². For the ULJ protocol we used a 10x10 cm² FOV in full accordance with the one used in clinical practice. The data in table 3.9 provides an E of 150 μSv. This value is again closer to Theodorakou et al given the difference in the size of the FOVs.

As mentioned in chapter 2, all the voxel models of our database have been adjusted to have mass values close to the references listed in ICRP Publication 89 (2002) for each specific age and gender category. This is one of the limitations of the study when it comes to NewTom 5G and NewTom VGi-evo dose assessment: while a patient-specific TCM curve can be easily designed based on the data provided after the end of an exam, the TCM curve cannot be applied to the respective patient-specific voxel model; it should be instead be applied to one of our average voxel models. This is due to the fact that a CBCT dataset provides images of the scanning volume and not of the entire head. In all cases where these two scanners were involved, rather than applying patient specific curves, we designed average ones based on data of two or more patients of the same age and gender that have undergone the same study. For tooth imaging, the individual tooth TCM curves didn't differ much, i.e. the AP and LAT prescan mA values were similar, implying that the average TCM curves describe reasonably an

individual patient. However, in cases of medium FOVs, there were large differences between the individual TCM curves. Therefore, the average TCM that we designed to apply to the framework is not optimum for every patient. Finally, due to limited number of patients undergoing face and skull acquisitions in these two scanners, we were not able to retrieve more than one patient. In these two individual cases, a patient specific TCM curve rather than an average one was applied for each age and gender category.

It must be pointed out that radiation risk is always approximated with high uncertainty. The concept of *E* has been strongly criticized, especially when used to estimate the radiation induced risk for paediatric patients, since *E* is a quantity defined for an average population of adult individuals. In paediatric risk assessment *E* can be completely misleading since the proposed radiation tissue weighting factors (ICRP 103, 2007) do not apply for children. While LAR is a better radiation risk metric since it is gender and age at exposure specific, it is still a rough approximation. The BEIR VII report which describes the LAR concept does not provide data for most radiosensitive organs in the head and neck region. To encounter this limitation the average dose of these organs may be calculated and an average LAR can be assessed (as a LAR for 'other organs'), which when added to the LAR for leukemia and for thyroid, provide a rough assessment of the whole body LAR. Alternatively, each individual organ for which data is not provided in the BEIR VII report may be weighted according to each particular radiosensitivity (based on the radiation tissue weighting factors), an individual weighted LAR can be assessed, and their sum when added to leukemia and thyroid LAR provides a rough estimation of the whole body LAR.

The results presented in this study, and especially the data provided in tables 3.5-3.17 can be employed to radiation dose tracking – monitoring software platforms. The only extra information that has to be provided to get absolute organ dose and radiation risk values for any examination carried out in any of the investigated scanners are the x-ray tube mAs, the gender of the patient and the age at exposure. All of them are normally recorded in the DICOM header and hence, they can be easily extracted. To the best of our knowledge, there is no dose monitoring software at this moment that provides organ dose and risk estimations for dental and maxillofacial CBCT exposures.

3.5 Conclusions

An extensive simulation study was carried out to provide organ dose estimations of the most frequent examinations in paediatric dental and maxillofacial radiology. The data provided in the figures and tables of this chapter result in detailed dose assessment for the entire paediatric age range. The only input which is further required to get absolute dose values are the age at exposure and the x-ray tube load. The data can be used for optimization purposes; Intrascanner protocol and operation mode dose comparison and interscanner protocol comparison. For the latter, the x-ray tube load (mAs) for each case is necessary. The E was also calculated and presented in tables based on ICRP 103 (2007) weighting factors. Finally, a software tool was designed to enable the estimation of the gender and age at exposure specific LAR incidence radiation risk metric. The results of this study are readily available for use in dose monitoring software platforms to enable detailed organ dose and risk estimates for paediatric CBCT exposures.

3.6 Roadmap for accurate dose assessment

The aim of this section was to provide guidance on the use of the data presented in this chapter. For three clinical indications which require a small, medium and large FOV, organ doses, E and LAR incidence were calculated. The following dose assessment task was carried out for the three CBCT scanners installed in the Oral and Maxillofacial Surgery – Imaging and Pathology centre of the

University Hospital of Leuven (Campus St. Rafael); the Promax 3D Max, the Accuitomo 170 and the NewTom VGI-evo. The case of a 10 years old who needs to undergo a CUI scan (small-tooth imaging-protocol), an ULJ (Medium, Upper Lower-Jaw protocol) and a face (large) protocol is presented. All selected protocols are among the most frequently applied in the department; a tooth CBCT scan is required for several reasons among which tooth auto transplantation (EzEldeen et al 2017). For trauma patients, an ULJ protocol is usually required whereas facial imaging is performed in cases of craniofacial fractures.

3.6.1 Methods and Materials

The routinely used protocol-specific operation modes for each of the three clinical indications are displayed in tables 3.18-3.20.

Table 3.18 Exposure settings for the clinically applied operation modes for CUI protocols

Scanner	FOV (diameter x height - cm²)	Operation mode	Rotation angle	kV	mAs
Promax 3D Max	5 x 5.5	ULD/NR (S) *	210	96	16
Accuitomo 170	6 x 6	Standard	360	90	87.5
NewTom VGi evo	5 x 5	Normal	360	110	14.4**

*ULD/NR (S) stands for ultra low dose – normal reconstruction – small patient size
**average value of 10 years old males and females (scans performed under TCM)

Table 3.19 Exposure settings for the clinically applied operation modes for ULJ protocols

Scanner	FOV (diameter x height - cm²)	Operation mode	Rotation angle	kV	mAs
Promax 3D Max	10 x 9	ULD/NR (S) *	210	96	16
Accuitomo 170	10 x 10	Standard	360	90	87.5
NewTom VGi evo	10 x 10	Normal	360	110	9.6**

*ULD/NR (S) stands for ultra low dose – normal reconstruction – small patient size
**average value of 10 years old males and females (scans performed under TCM)

Table 3.20 Exposure settings for the clinically applied operation modes for facial protocols

Scanner	FOV (diameter x height - cm²)	Operation mode	Rotation angle	kV	mAs
Promax 3D Max	13 x 13	ULD/NR (S) *	210	96	16
Accuitomo 170	14 x 10	Standard	360	90	87.5
NewTom VGi evo	15 x 12	Normal	360	110	8.9**

*ULD/NR (S) stands for ultra low dose – normal reconstruction – small patient size
**average value of 10 years old males and females (scans performed under TCM)

The equation 3.1 provides the normalized values for organ doses, E and LAR when the appropriate a and b factors are used. To calculate the absolute values the outcome of equation 3.1 was further multiplied with the mAs values in tables 3.18-3.20 (eq 3.2):

Absolute value (di,j, Ej, LARj,k) = [$a * \ln(10) + b$] * (mAs)j (eq 3.2)

where i stands for a specific organ, j for a specific examination and k for a specific gender. Note that x=10 in equation 3.2 (ln(10)), as the study is carried out for a 10 years old child. For CUI calculations we use the scanner-specific a and b values in table 3.5, for ULJ protocol the values in table 3.9 and for facial those illustrated in table 3.14.

3.6.2 Results

Tables 3.21-3.23 present the results of the study. Organ doses are provided for each case along with an estimation of the effective dose and the LAR incidence for a 10 years old male and female. The effective dose has also been converted to number of cases per 100000 persons, such that comparison with LAR is straightforward. The conversion was performed following the statement in ICRP 103 publication (2007) that ''based upon cancer incidence data, the detriment adjusted nominal risk coefficient for cancer is 5.5 10-2 Sv-1 for the whole population'' (page 143, Annex A).

Table 3.21 Organ dose, E and LAR incidence assessment for CUI protocols in three different CBCT scanners

Organs	Scanners		
	Promax 3D Max	Accuitomo 170	NewTom VGi evo
	Absorbed organ doses (μGy)		
Brain	25	41	45
Skin	23	125	45
Oesophagus	10	43	28
Eye lens	48	268	90
Muscle	14	57	33
ET	110	352	245
Thyroid	25	142	76
Salivary glands	432	1537	535
Oral mucosa	650	2190	1509
RBM	15	62	35
bone surface	64	287	161
lymph nodes	39	155	56
E (μSv)	16	60	33
E (# cases/100000)	0.088	0.327	0.182
LAR inc. males (# cases/100000)	0.391	1.422	0.808
LAR inc. females (# cases/100000)	0.555	2.050	1.169

Table 3.22 Organ dose, E and LAR incidence assessment for ULJ protocols in three different CBCT scanners

Organs	Scanners		
	Promax 3D Max	Accuitomo 170	NewTom VGi evo
	Absorbed organ doses (μGy)		
Brain	43	141	103
Skin	62	243	67
Oesophagus	118	265	66
Eye lens	212	1662	186
Muscle	55	171	62
ET	572	1596	539
Thyroid	273	606	246
Salivary glands	1326	3188	1233
Oral mucosa	1311	3724	1790
RBM	49	153	61
bone surface	227	709	281
lymph nodes	115	271	126
E (μSv)	57	150	59
E (# cases/100000)	0.312	0.822	0.325
LAR inc. males (# cases/100000)	1.229	3.256	1.286
LAR inc. females (# cases/100000)	2.058	5.303	2.226

Table 3.23 Organ dose, E and LAR incidence assessment for face protocols in three different CBCT scanners

Organs	Scanners		
	Promax 3D Max	Accuitomo 170	NewTom VGi evo
	Absorbed organ doses (μGy)		
Brain	734	747	1578
Skin	82	289	169
Oesophagus	50	257	83
Eye lens	573	4046	3103
Muscle	61	238	120
ET	664	2055	1147
Thyroid	163	722	131
Salivary glands	1116	4530	2837
Oral mucosa	1082	4189	2181
RBM	95	196	132
bone surface	442	909	613
lymph nodes	73	297	274
E (μSv)	61	187	111
E (# cases/100000)	0.336	1.028	0.609
LAR inc. males (# cases/100000)	1.353	6.704	2.600
LAR inc. females (# cases/100000)	1.931	4.175	3.384

3.6.3 Conclusions

We used the data provided in section 3.3 and the values in the tables in the appendix to calculate each individual organ dose, and assess the E and the LAR incidence for a 10 years old patient for three different clinical cases and scanners. The selected operation modes are those routinely applied in our department: they provide an acceptable balance between image quality and dose and allow the doctors of the department to accomplish their diagnostic task.

CUI imaging is, as expected, the lowest radiation dose protocol due to the smallest FOV. The ULD/NR (S) operation mode in Promax 3D Max is associated with the lowest doses and the lowest risk to the patient. The highest irradiated organs are in all scanners the salivary glands and the oral mucosa. The results show that the Cu-equipped x-ray tube of Promax 3D Max protects the skin of the patient as this scanner always delivers the lowest dose to the skin. It is also worth mentioning the difference in salivary glands to oral mucosa dose ratio. While this ratio is about 0.7 in Promax 3D Max and Accuitomo, it is only 0.35 in NewTom VGi-evo. This is due to the strong current modulation taking place for tooth imaging in NewTom VGi-evo. The AP prescan mA value is much larger compared to the LAT one, as the beam has to cross the entire head to reach the detector in the AP projection, yet only the mouth region has to be traversed in the LAT direction. As a consequence the mA value, and thus the exposure, is much higher when the beam crosses the anterior and posterior part of the head rather than the lateral one. Therefore, the laterally positioned parotid is not that much exposed to primary and scatter compared to the mouth cavity. This is not the case (strong modulation) for ULJ and face protocols; the prescan AP mA value is always higher compared to the LAT one, yet not that considerably different giving rise to weak modulation curve. The modulation in NewTom VGi-evo keeps the doses low in ULJ protocols, and interestingly, it achieves even lower doses to the thyroid and eye lenses compared to Promax 3D Max whose 210° rotation is the strong point towards reducing the dose to the organs anteriorly positioned in the head and neck region. Finally, the results show that Promax 3D Max keeps the radiation detriment in facial scanning at the same levels as the ULJ imaging (LAR

incidence for males and females). The doses to the brain and the lenses are higher due to the increased size of the FOV, yet overall, the risk as provided by the E and the LAR values is similar. This is accomplished due to a change in the SAD in Promax 3D Max. The scanner has three different SAD distances; for every protocol with a diameter less than 13 cm the SAD is 33.3 cm, while it is 43.3 cm for 13cm in diameter protocols and 42.5 cm for 23 cm diameter protocols. This 10 cm transposition of the SAD brings the head in a longer distance from the tube and reduces the absorbed doses at comparable mAs values. It must also be noted that all the protocols in Accuitomo 170 correspond to full 360 rotations. The scanner can carry out the acquisitions in half rotations, yet the image quality is not adequate and half rotational exposures are not applied in the clinic.

Finally, it is important to point out the underestimation of the radiation detriment when E is used as a risk index. When the age and gender independent E value is translated to number of cases per 100000 persons, and compared to LAR incidence, the E underestimates the risk for males about 4.15 times on average (3.94 to 4.44) and 6.3 for females (5.56 to 6.84). Although the absolute risk value is low (maximum 4/100000 for males and 7/100000 for females), the underestimation of the risk when E is used is significant. In all cases, females are more prone to radiation detriment compared to males with an average 1.5 times higher risk for the examined protocols and for the specific age at exposure (10 years old). It must be noted though, that, as already mentioned, the use of E for paediatric patients is problematic and erroneous and hence, so is the detriment assessment when based on E.

3.7 Appendix

Table 3.5 Central Upper Incisors (CUI) logarithmic curve parameters for organ doses, E and LAR incidence (males and females) for all scanners

CS 9300				Accuitomo 170				Promax 3D Max				Scanner
a	b	R^2	r	a	b	R^2	r	a	b	R^2	r	Parameter
-0.055	0.352	0.92	-0.94	-0.257	1.063	0.92	-0.99	-0.548	2.804	0.974	-0.99	Brain
-0.471	1.808	0.90	-0.98	-0.923	3.552	0.96	-0.99	-0.73	3.146	0.991	-0.98	Skin
-0.182	0.570	0.91	-0.98	-0.593	1.852	0.95	-0.97	-1.216	3.452	0.961	-0.98	Oesophagus
-0.918	4.077	0.95	-0.99	-1.522	6.569	0.94	-0.94	-2.082	7.809	0.936	-0.97	Eye lens
-0.173	0.585	0.99	-0.99	-0.712	2.293	0.97	-0.99	-0.923	3.020	0.953	-0.96	Muscles
-1.383	5.036	0.90	-0.98	-3.875	12.941	0.94	-0.94	-6.158	21.042	0.983	-0.99	ET
-0.694	2.384	0.96	-0.99	-1.626	5.362	0.96	-0.99	-1.665	5.423	0.960	-0.97	Thyroid
-1.128	4.717	0.91	-0.96	-12.38	46.074	0.94	-0.93	-16.03	63.886	0.958	-0.95	Salivary glands
-10.14	49.932	0.96	-0.99	-16.41	62.819	0.95	-0.92	-16.82	79.362	0.986	-0.98	Oral mucosa
-0.241	0.845	0.99	-0.99	-0.581	2.044	0.92	-0.98	-0.966	3.139	0.901	-0.89	RBM
-1.119	3.919	0.99	-0.99	-2.958	10.094	0.97	-0.99	-5.009	15.551	0.923	-0.92	Bone surface
-0.556	2.470	0.91	-0.98	-1.129	4.374	0.89	-0.98	-0.079	2.597	0.922	-0.96	Lymph nodes
-0.199	0.850	0.96	-0.99	-0.432	1.675	0.98	-0.99	-0.645	2.486	0.980	-0.96	ED (µSv/mAs)
-0.01	0.033	1.00	-0.99	-0.019	0.060	0.99	-0.99	-0.03	0.094	0.989	-0.97	LAR incidence males
-0.016	0.051	1.00	-0.99	-0.028	0.088	1.00	-0.98	-0.043	0.134	0.991	-0.97	LAR incidence females

Table 3.6 Central Lower Incisors (CLI) logarithmic curve parameters for organ doses, E and LAR incidence (males and females) for all scanners

Promax 3D Max				Scanner
a	b	R^2	r	Parameter
-0.782	2.9806	0.93	-0.93	Brain
-0.948	3.4328	0.97	-0.98	Skin
-0.886	3.0742	0.96	-0.99	Oesophagus
-2.094	7.5981	0.94	-0.98	Eye lens
-1.153	3.5264	0.96	-0.96	Muscles
-5.006	17.645	0.99	-0.98	ET
-2.142	6.8912	0.99	-0.99	Thyroid
-15.65	59.952	0.95	-0.94	Salivary glands
-17.99	83.243	0.98	-0.98	Oral mucosa
-0.766	2.6603	0.98	-0.98	RBM
-3.553	12.344	0.98	-0.98	Bone surface
-0.742	3.3909	0.92	-0.91	Lymph nodes
-0.631	2.4434	0.98	-0.97	ED (µSv/mAs)
-0.03	0.0917	0.99	-0.97	LAR incidence males
-0.044	0.1354	0.98	-0.97	LAR incidence females

NewTom VGi-evo				NewTom 5G			
a	b	R^2	r	a	b	R^2	r
-3.44	11.074	0.97	-0.99	-1.248	4.842	0.94	-0.98
-2.058	7.893	0.99	-0.99	-2.262	9.389	0.91	-0.99
-1.436	5.244	0.94	-0.99	-1.214	4.6036	0.97	-1.00
-7.746	24.102	0.93	-0.97	-5.374	22.483	0.98	-0.99
-2.038	7.005	0.98	-0.99	-1.742	5.9635	0.97	-0.99
-17.66	57.680	0.97	-0.97	-8.728	34.174	0.93	-0.98
-8.453	24.737	0.98	-0.97	-4.006	14.082	0.99	-0.98
-40.39	130.120	0.91	-0.98	-29.47	97.146	0.96	-0.98
-73.73	274.540	0.88	-0.97	-41.58	168.49	0.97	-0.98
-3.041	9.408	0.98	-0.98	-1.385	5.6926	0.93	-0.99
-14.11	43.651	0.98	-0.98	-6.426	26.414	0.93	-0.99
-4.709	14.740	0.97	-0.98	-2.161	9.2017	0.92	-0.98
-2.251	7.478	0.97	-1.00	-1.317	4.9247	0.98	-0.99
-0.084	0.250	0.98	-0.99	-0.055	0.1707	1.00	-0.98
-0.134	0.390	1.00	-1.00	-0.089	0.2681	1.00	-1.00

NewTom VGi-evo				NewTom 5G				CS 9300				Accuitomo 170			
a	b	R^2	r	a	b	R^2	r	a	b	R^2	r	a	b	R^2	r
-2.295	7.303	0.95	-0.97	-0.874	3.438	0.96	-1.00	-0.041	0.311	0.95	-0.99	-0.43	1.544	0.98	-0.87
-2.292	7.701	0.94	-0.93	-2.818	10.213	0.97	-0.98	-0.485	1.844	0.90	-0.98	-0.946	3.585	0.95	-0.99
-1.900	6.693	0.89	-0.97	-1.632	6.120	0.94	-0.99	-0.249	0.747	0.95	-0.98	-0.689	2.107	0.94	-0.95
-5.152	14.631	0.98	-0.96	-4.970	16.422	0.96	-0.95	-0.766	3.393	0.97	-0.99	-1.112	4.796	0.96	-0.95
-1.763	6.130	0.90	-0.91	-1.650	5.820	0.97	-0.96	-0.181	0.599	0.99	-0.99	-0.694	2.222	0.98	-0.99
-20.420	60.767	0.97	-0.97	-11.880	39.659	0.96	-0.99	-1.49	5.365	0.90	-0.98	-3.844	12.712	0.98	-0.97
-10.680	30.231	0.96	-0.96	-5.716	18.769	0.94	-0.96	-0.824	2.740	0.94	-0.98	-1.684	5.472	0.96	-0.96
-19.300	83.827	0.94	-0.99	-14.460	67.235	0.97	-0.94	-0.74	3.903	0.90	-0.89	-9.261	38.170	0.94	-0.97
-73.070	270.830	0.92	-0.98	-45.520	179.250	0.97	-0.99	-9.318	48.890	0.98	-0.99	-14.98	59.881	0.96	-0.94
-2.776	7.870	0.95	-0.93	-1.689	5.642	0.98	-0.96	-0.214	0.776	0.95	-0.99	-0.606	2.076	0.98	-0.99
-12.770	36.209	0.95	-0.93	-7.839	26.180	0.98	-0.96	-1.147	3.958	0.95	-0.97	-2.812	9.635	0.98	-0.99
-3.829	12.005	0.96	-0.98	-1.665	7.629	0.93	-0.99	-0.97	3.420	0.92	-0.99	-0.67	3.492	0.98	-0.99
-2.178	7.137	0.98	-0.99	-1.307	4.941	0.99	-0.99	-0.198	0.855	0.96	-0.99	-0.388	1.566	0.97	-1.00
-0.076	0.224	0.97	-0.99	-0.057	0.175	1.00	-0.98	-0.01	0.033	1.00	-0.99	-0.017	0.055	1.00	-0.99
-0.153	0.440	1.00	-0.98	-0.088	0.270	1.00	-0.98	-0.017	0.053	1.00	-0.98	-0.029	0.089	1.00	-0.99

Table 3.7 Premolar Lower (PL) logarithmic curve parameters for organ doses, E and LAR incidence (males and females) for all scanners

NewTom 5G		CS 9300				Accuitomo 170				Promax 3D Max				Scanner
R^2	r	a	b	R^2	r	a	b	R^2	r	a	b	R^2	r	Parameter
0.97	-0.99	-0.083	0.427	0.99	-0.99	-0.430	1.544	0.98	-0.97	-0.961	3.827	0.96	-0.99	Brain
0.97	-0.98	-0.426	1.811	0.90	-0.98	-0.980	3.883	0.95	-1.00	-0.947	3.733	0.97	-1.00	Skin
0.98	-0.99	-0.231	0.851	0.92	-0.99	-1.117	3.386	0.98	-0.97	-0.660	2.783	0.93	-0.98	Oesophagus
0.96	-0.96	-0.887	3.041	0.91	-0.98	-1.891	5.978	0.97	-0.96	-1.712	5.991	0.96	-0.99	Eye lens
0.99	-0.99	-0.192	0.757	0.98	-0.98	-0.741	2.523	0.99	-0.99	-1.035	3.571	0.97	-0.97	Muscles
0.93	-0.91	-2.667	9.075	0.94	-0.97	-6.110	20.434	0.95	-0.99	-7.996	27.599	0.97	-0.98	ET
0.97	-0.99	-1.352	4.899	0.96	-0.98	-3.581	10.971	0.97	-0.99	-3.568	11.988	0.96	-0.99	Thyroid
0.97	-0.98	-2.995	9.973	1.00	-0.98	-8.740	38.921	0.99	-0.99	-11.490	64.171	0.93	-0.98	Salivary glands
0.95	-0.98	-15.220	64.613	0.99	-0.97	-21.130	76.550	0.93	-0.92	-18.270	90.686	0.94	-0.99	Oral mucosa
0.97	-0.99	-0.329	1.109	0.99	-0.99	-0.373	1.712	0.93	-0.98	-0.523	2.524	0.95	-1.00	RBM
0.97	-0.99	-1.529	5.144	0.99	-0.99	-1.733	7.943	0.93	-0.98	-2.425	11.711	0.95	-1.00	Bone surface
0.94	-0.99	-0.688	2.755	0.97	-0.99	-1.466	5.161	0.94	-0.96	-1.655	5.534	0.96	-0.99	Lymph nodes
0.99	-0.99	-0.325	1.245	0.99	-0.99	-0.595	2.197	0.99	-1.00	-0.636	2.865	0.94	-0.99	ED (μSv/mAs)
1.00	-0.99	-0.015	0.047	1.00	-0.98	-0.025	0.078	0.99	-0.99	-0.031	0.106	1.00	-0.99	LAR incidence males
1.00	-0.98	-0.024	0.075	1.00	-0.98	-0.041	0.124	1.00	-0.98	-0.057	0.178	1.00	-0.99	LAR incidence females

Table 3.8 Premolar Upper (PU) logarithmic curve parameters for organ doses, E and LAR incidence (males and females) for all scanners

Accuitomo 170		Promax 3D Max				Scanner	NewTom VGi-evo					
R^2	r	a	b	R^2	r	Parameter	a	b	R^2	r	a	b
0.92	-0.96	-1.373	5.115	0.95	-1.00	Brain	-2.788	8.647	0.96	-0.98	-1.117	4.143
0.95	-1.00	-0.544	2.521	0.93	-0.95	Skin	-2.174	7.556	0.94	-0.93	-2.633	9.978
0.99	-0.98	-0.708	2.777	0.96	-0.99	Oesophagus	-2.731	9.086	0.97	-0.99	-2.384	8.346
0.93	-0.94	-1.596	5.726	0.96	-0.97	Eye lens	-4.475	13.062	0.98	-0.97	-3.955	14.113
0.99	-0.98	-1.052	3.600	0.98	-0.97	Muscles	-2.556	8.046	0.98	-0.97	-2.364	7.560
0.94	-0.98	-8.706	31.146	0.99	-0.99	ET	-29.040	86.981	0.90	-0.89	-15.880	54.683
0.96	-0.99	-2.956	9.863	0.99	-0.99	Thyroid	-18.950	53.864	0.97	-0.97	-10.170	33.543
0.93	-0.92	-13.850	72.418	0.96	-0.97	Salivary glands	-40.030	144.250	0.90	-0.98	-32.310	118.940
0.93	-0.93	-16.920	87.392	0.95	-0.99	Oral mucosa	-95.440	351.480	0.92	-0.97	-56.010	233.360
0.92	-0.97	-0.602	2.736	0.93	-0.99	RBM	-3.136	9.462	0.98	-0.97	-1.590	6.353
0.92	-0.97	-2.792	12.694	0.93	-0.99	Bone surface	-14.430	43.532	0.98	-0.97	-7.378	29.480
0.99	-0.98	-1.559	5.387	0.97	-0.97	Lymph nodes	-4.457	14.688	0.98	-0.98	-1.372	8.489
0.99	-0.99	-0.620	2.849	0.96	-0.99	ED (µSv/mAs)	-2.988	9.812	0.99	-0.99	-1.840	6.909
0.99	-0.98	-0.032	0.108	1.00	-0.99	LAR incidence males	-0.107	0.313	0.98	-0.99	-0.078	0.242
1.00	-0.98	-0.056	0.177	1.00	-0.99	LAR incidence females	-0.223	0.635	1.00	-0.99	-0.135	0.406

NewTom VGi-evo				NewTom 5G				CS 9300					
a	b	R^2	r	a	b	R^2	r	a	b	R^2	r	a	b
-4.186	13.119	0.97	-0.99	-0.989	4.431	0.96	-0.99	-0.074	0.418	0.95	-0.95	-0.227	1.437
-1.885	7.661	0.98	-0.98	-1.762	8.602	0.93	-0.99	-0.537	2.061	0.92	-0.95	-0.989	3.908
-2.061	7.098	0.98	-1.00	-2.053	7.071	0.99	-0.98	-0.275	0.940	0.93	-0.94	-0.883	2.768
-6.577	21.425	0.87	-0.96	-3.755	18.162	0.95	-0.96	-0.970	3.251	0.96	-0.97	-2.182	6.921
-2.829	8.956	0.97	-0.99	-2.349	7.882	0.98	-0.98	-0.201	0.776	0.98	-0.97	-0.721	2.510
-23.110	79.678	0.92	-0.92	-14.500	54.061	0.97	-0.97	-2.462	8.573	0.92	-0.95	-6.258	21.368
-14.950	44.023	0.97	-0.97	-9.108	28.441	0.98	-0.97	-1.486	4.983	0.95	-0.98	-3.396	10.296
-66.360	201.790	0.95	-0.99	-37.030	121.630	0.99	-0.99	-2.699	9.285	0.96	-0.95	-13.130	50.635
-97.800	356.890	0.95	-0.99	-56.020	225.690	0.90	-0.98	-16.920	67.782	0.99	-0.98	-21.290	76.369
-3.132	10.853	0.90	-0.98	-1.532	6.196	0.95	-0.95	-0.330	1.110	0.98	-0.99	-0.227	1.437
-14.530	50.358	0.90	-0.98	-7.109	28.750	0.95	-0.95	-1.542	5.167	0.98	-0.99	-1.055	6.667
-5.468	17.994	0.97	-0.99	-4.171	13.391	0.95	-0.95	-0.325	2.111	0.84	-0.96	-0.984	4.413
-3.131	10.417	0.97	-1.00	-1.724	6.419	0.98	-1.00	-0.324	1.269	1.00	-0.99	-0.619	2.259
-0.116	0.342	0.99	-0.99	-0.073	0.225	1.00	-0.99	-0.016	0.048	1.00	-0.99	-0.027	0.081
-0.199	0.573	1.00	-0.99	-0.127	0.378	1.00	-0.99	-0.024	0.073	1.00	-0.99	-0.043	0.128

Table 3.9 Upper/Lower Jaw (ULJ) logarithmic curve parameters for organ doses, E and LAR incidence (males and females) for all scanners

CS 9300				Accuitomo 170				Promax 3D Max				Scanner
a	b	R^2	r	a	b	R^2	r	a	b	R^2	r	Parameter
-1.030	4.130	0.98	-0.97	-0.678	3.177	0.98	-0.97	-2.147	7.608	0.93	-0.93	Brain
-1.781	6.745	0.97	-0.99	-1.662	6.600	0.98	-0.98	-2.760	10.221	0.97	-0.98	Skin
-3.566	11.664	0.93	-0.93	-1.776	7.117	0.93	-0.99	-3.446	15.288	0.97	-0.99	Oesophagus
-34.430	97.300	0.94	-0.92	-59.390	155.740	0.93	-0.93	-17.150	52.738	0.98	-0.97	Eye lens
-1.344	4.734	0.97	-0.98	-1.387	5.150	0.96	-0.95	-3.462	11.398	0.97	-0.95	Muscles
-7.203	37.704	0.95	-0.94	-6.535	33.292	0.96	-0.96	-22.010	86.413	0.97	-0.95	ET
-5.808	21.396	0.96	-0.98	-4.749	17.862	0.98	-0.99	-11.550	43.669	0.95	-0.99	Thyroid
-13.330	61.948	0.94	-0.95	-10.440	60.474	0.91	-0.90	-25.270	141.050	0.94	-0.99	Salivary glands
-41.790	163.850	0.99	-0.98	-16.590	80.756	0.92	-0.92	-25.370	140.370	0.94	-0.99	Oral mucosa
-1.350	5.056	0.99	-0.99	-0.949	3.931	0.98	-0.99	-2.503	8.819	0.96	-0.95	RBM
-6.266	23.461	0.99	-0.99	-4.404	18.241	0.98	-0.99	-11.680	41.091	0.96	-0.95	Bone surface
-0.145	6.005	0.94	-0.97	-1.468	6.473	0.88	-0.93	-8.300	26.279	0.91	-0.92	Lymph nodes
-1.238	4.865	0.99	-0.98	-0.744	3.422	0.99	-0.97	-1.495	6.984	0.93	-0.98	ED (µSv/mAs)
-0.055	0.171	0.99	-0.99	-0.034	0.116	0.99	-0.97	-0.074	0.247	0.99	-1.00	LAR incidence males
-0.090	0.280	1.00	-0.98	-0.073	0.229	0.99	-0.97	-0.147	0.467	0.99	-0.99	LAR incidence females

Table 3.10 Lower Jaw (LJ) logarithmic curve parameters for organ doses, E and LAR incidence (males and females) for all scanners

Promax 3D Max			Scanner
b	R^2	r	Parameter
3.163	0.98	-0.97	Brain
6.757	0.99	-0.97	Skin
5.610	0.94	-0.99	Oesophagus
20.444	0.93	-0.97	Eye lens
7.492	0.95	-0.94	Muscles
89.708	0.98	-0.99	ET
34.585	0.97	-0.98	Thyroid
172.280	0.96	-0.95	Salivary glands
131.770	0.98	-0.97	Oral mucosa
5.192	0.97	-0.99	RBM
24.090	0.97	-0.99	Bone surface
11.789	0.96	-0.98	Lymph nodes
6.192	0.99	-0.99	ED (µSv/mAs)
0.211	1.00	-0.98	LAR incidence males
0.382	1.00	-0.99	LAR incidence females

NewTom VGi-evo				NewTom 5G			
a	b	R^2	r	a	b	R^2	r
-8.492	30.330	0.91	-0.96	-2.118	10.139	0.99	-0.99
-4.860	18.210	0.96	-0.99	-6.992	23.645	0.97	-0.95
-3.070	13.915	0.87	-0.96	-5.531	21.517	0.97	-0.96
-17.860	60.510	0.92	-0.91	-23.280	69.492	0.91	-0.90
-7.056	22.739	0.88	-0.95	-3.332	15.632	0.97	-0.98
-46.300	162.760	0.93	-0.98	-46.590	173.240	0.94	-0.93
-20.840	73.576	0.97	-0.99	-21.390	72.584	0.96	-0.95
-113.300	389.350	0.91	-0.90	-67.800	309.070	0.98	-0.99
-77.010	363.820	0.96	-1.00	-45.840	231.870	0.90	-0.96
-5.957	20.036	0.97	-0.96	-2.218	10.047	0.98	-0.99
-27.640	92.966	0.97	-0.96	-10.290	46.620	0.98	-0.99
-6.730	28.607	0.90	-0.98	-4.623	17.704	0.87	-0.89
-4.346	16.169	0.97	-0.96	-3.155	12.937	0.99	-0.98
-0.197	0.588	0.97	-0.99	-0.143	0.455	0.99	-0.97
-0.309	0.943	1.00	-0.97	-0.275	0.840	0.99	-0.97

NewTom VGi-evo		NewTom 5G				CS 9300				Accuitomo 170				
R^2	r	a	b	R^2	r	a	b	R^2	r	a	b	R^2	r	a
0.89	-0.91	-1.825	6.684	0.97	-0.97	-0.259	1.130	0.97	-1.00	-0.199	0.890	0.91	-0.93	-0.810
0.94	-0.93	-3.892	14.550	0.98	-1.00	-0.988	3.675	0.94	-0.93	-0.710	3.301	0.90	-0.91	-1.968
0.91	-0.96	-3.461	14.525	0.94	-0.98	-0.255	1.169	0.92	-0.95	-1.001	3.516	0.93	-0.95	-1.492
0.94	-0.97	-12.150	38.993	0.93	-0.93	-4.109	14.122	0.94	-0.99	-1.301	4.564	0.95	-0.98	-6.595
0.92	-0.98	-4.212	14.375	0.92	-0.99	-0.505	2.416	0.92	-0.96	-0.817	3.035	0.92	-0.92	-2.265
0.93	-0.97	-27.400	100.390	0.92	-0.92	-4.082	15.609	0.97	-0.96	-9.841	33.428	0.92	-0.96	-27.380
0.92	-0.91	-9.813	43.877	0.92	-0.99	-4.633	13.895	1.00	-0.99	-3.526	10.517	0.95	-0.94	-10.780
0.95	-0.95	-51.270	184.340	0.92	-0.99	-8.626	35.399	0.93	-0.97	-9.542	39.746	0.95	-0.98	-55.300
0.91	-0.98	-67.280	265.780	0.96	-0.99	-19.120	98.833	0.98	-0.98	-30.430	96.589	0.93	-0.94	-37.370
0.92	-0.91	-3.056	10.408	0.99	-0.99	-0.704	2.380	0.98	-0.96	-0.582	2.045	0.98	-0.98	-1.394
0.92	-0.91	-14.180	48.291	0.99	-0.99	-3.202	10.872	0.97	-0.95	-2.700	9.486	0.98	-0.98	-6.468
0.91	-0.96	-3.658	15.716	0.97	-0.97	-1.355	5.852	0.98	-0.99	-1.146	5.127	0.96	-0.99	-3.166
1.00	-0.98	-2.716	10.102	0.95	-0.99	-0.625	2.494	0.99	-0.98	-0.687	2.440	0.97	-0.96	-1.813
0.99	-0.96	-0.107	0.331	0.99	-1.00	-0.029	0.092	1.00	-0.98	-0.030	0.088	0.99	-0.96	-0.072
0.98	-1.00	-0.201	0.609	1.00	-1.00	-0.053	0.161	1.00	-0.98	-0.049	0.145	0.98	-0.98	-0.132

CS 9300		Accuitomo 170				Promax 3D Max				Scanner
R^2	r	a	b	R^2	r	a	b	R^2	r	Parameter
0.98	-1.00	-0.365	1.348	0.96	-0.97	-0.837	3.363	0.98	-0.97	Brain
0.95	-0.94	-0.705	3.279	0.93	-0.93	-2.056	6.928	1.00	-0.99	Skin
0.91	-0.98	-0.812	3.005	0.92	-0.97	-1.857	6.230	0.97	-0.99	Oesophagus
0.97	-0.95	-2.224	7.519	0.92	-0.98	-10.560	35.181	0.99	-0.99	Eye lens
0.87	-0.95	-0.711	2.814	0.89	-0.89	-2.208	7.268	0.98	-0.97	Muscles
0.93	-0.93	-9.913	35.043	0.93	-0.99	-25.240	88.520	0.96	-0.99	ET
0.98	-0.97	-3.098	9.294	0.92	-0.92	-9.458	30.995	0.95	-0.95	Thyroid
0.92	-0.95	-10.030	42.875	0.96	-0.97	-53.620	174.140	0.98	-0.98	Salivary glands
0.99	-0.99	-25.390	87.223	0.96	-0.94	-43.530	143.550	0.97	-0.96	Oral mucosa
0.97	-0.95	-0.600	2.113	0.99	-0.98	-1.669	5.883	0.98	-0.98	RBM
0.91	-0.91	-2.786	9.804	0.99	-0.98	-9.727	31.921	0.96	-0.94	Bone surface
0.91	-0.95	-0.744	3.765	0.96	-0.96	-4.586	15.729	0.95	-0.99	Lymph nodes
0.99	-0.98	-0.718	2.522	0.98	-0.96	-1.929	6.492	0.99	-0.99	ED (μSv/mAs)
0.99	-0.98	-0.031	0.090	0.99	-0.95	-0.077	0.222	1.00	-0.98	LAR incidence males
1.00	-0.98	-0.049	0.143	0.97	-0.98	-0.133	0.384	1.00	-0.98	LAR incidence females

Table 3.11 Cleft logarithmic curve parameters for organ doses, E and LAR incidence (males and females) for all scanners

a	b
-7.422	25.866
-4.505	14.639
-5.072	15.542
-3.596	13.777
-3.465	11.462
-60.880	176.770
-11.070	29.780
-79.620	298.160
-143.100	508.080
-4.402	12.866
-20.320	59.387
-2.177	10.620
-4.024	13.451
-0.168	0.489
-0.247	0.715

Table 3.12 Maxillofacial complex curve parameters for organ doses, E and LAR incidence (males and females) for all scanners

Promax 3D Max	Scanner	NewTom VGi-evo				NewTom 5G					
r	Parameter	a	b	R^2	r	a	b	R^2	r	a	b
-0.92	Brain	-9.586	34.228	0.88	-0.90	-2.266	7.903	0.99	-0.98	-0.292	1.263
-0.96	Skin	-4.238	14.861	0.95	-0.94	-4.091	14.976	0.99	-0.99	-0.983	3.683
-0.98	Oesophagus	-4.165	13.194	0.91	-0.98	-4.092	15.285	0.88	-0.96	-0.217	1.030
-0.98	Eye lens	-11.880	40.423	0.89	-0.91	-60.510	166.580	0.93	-0.92	-11.070	32.009
-0.96	Muscles	-3.173	11.276	0.91	-0.96	-4.718	15.237	0.97	-1.00	-0.533	2.480
-0.98	ET	-57.320	173.960	0.89	-0.96	-27.090	99.488	0.95	-0.95	-5.498	19.365
-0.98	Thyroid	-9.667	26.392	0.90	-0.90	-9.281	41.110	0.96	-0.99	-4.325	12.772
-0.98	Salivary glands	-95.410	343.900	0.94	-0.93	-54.880	195.230	0.94	-0.99	-9.642	38.361
-0.97	Oral mucosa	-135.5	496.890	0.93	-0.99	-64.000	255.750	0.96	-0.97	-18.930	97.122
-0.99	RBM	-3.938	13.054	0.89	-0.89	-3.467	11.337	0.98	-0.99	-0.677	2.334
-0.99	Bone surface	-18.270	60.570	0.89	-0.89	-16.090	52.602	0.98	-0.99	-3.231	11.037
-0.95	Lymph nodes	-2.490	11.918	0.90	-0.92	-3.856	16.241	0.97	-0.98	-0.566	4.582
-0.99	ED (μSv/mAs)	-3.955	13.529	0.98	-0.96	-3.021	10.620	0.95	-0.99	-0.624	2.478
-0.99	LAR incidence males	-0.176	0.512	0.98	-0.97	-0.107	0.330	1.00	-1.00	-0.030	0.094
-0.98	LAR incidence females	-0.248	0.721	0.98	-0.98	-0.210	0.621	1.00	-0.99	-0.051	0.156

NewTom 5G				CS 9300				Accuitomo 170						
a	b	R^2	r	a	b	R^2	r	a	b	R^2	r	a	b	R^2
-2.266	7.903	0.99	-0.93	-2.156	9.138	0.94	-0.95	-1.482	6.931	0.93	-0.93	-6.424	25.520	0.93
-0.594	15.774	0.95	-0.98	-1.728	6.879	0.95	-0.96	-1.978	7.716	0.95	-0.97	-3.543	13.642	0.95
-4.348	18.404	0.93	-0.93	-1.496	6.280	0.93	-0.98	-0.992	3.456	0.97	-0.99	-1.932	8.835	0.94
-80.550	404.530	0.97	-0.98	-37.600	192.960	0.93	-0.96	-26.540	147.690	0.95	-0.95	-19.550	119.360	0.98
-2.933	13.458	0.97	-0.96	-0.850	4.130	0.99	-0.98	-1.979	6.641	0.96	-0.95	-4.584	14.518	0.97
-5.118	148.820	0.95	-0.97	-16.390	63.400	0.98	-0.96	-14.800	56.401	0.95	-0.98	-25.560	135.110	0.94
-18.430	58.352	0.96	-0.97	-5.892	18.819	0.97	-0.96	-6.198	17.740	0.99	-0.98	-8.935	28.476	0.97
-104.900	432.190	0.93	-0.93	-30.130	117.550	0.97	-0.98	-32.090	118.310	0.98	-0.98	-37.580	192.440	0.96
-40.940	215.610	0.90	-0.96	-35.280	139.440	0.96	-0.99	-22.180	93.700	0.96	-1.00	-32.390	139.230	0.98
-2.167	10.234	0.97	-0.96	-0.169	4.135	0.99	-0.99	-1.422	5.108	0.90	-0.98	-2.509	10.505	0.99
-10.050	47.487	0.97	-0.96	-6.864	26.875	0.99	-0.99	-6.544	23.484	0.91	-0.97	-11.640	48.745	0.99
-7.295	27.936	0.97	-0.99	-1.978	7.224	0.94	-0.93	-1.567	6.886	0.95	-0.96	-10.420	32.798	0.93
-3.259	13.601	0.97	-0.97	-1.583	5.583	0.97	-0.97	-1.255	4.539	0.99	-1.00	-1.831	8.157	0.98
-0.159	0.506	0.98	-0.97	-0.068	0.199	0.98	-0.99	-0.050	0.155	0.99	-0.99	-0.091	0.300	0.99
-0.273	0.836	0.99	-0.96	-0.101	0.298	1.00	-0.97	-0.086	0.255	1.00	-0.98	-0.149	0.469	1.00

Accuitomo 170			Promax 3D Max				Scanner	NewTom VGi-evo			
b	R^2	r	a	b	R^2	r	Parameter	a	b	R^2	r
12.940	0.95	-0.97	-21.710	79.674	0.97	-0.97	Brain	-11.190	40.286	0.92	-0.94
7.773	0.98	-0.98	-3.613	13.952	0.98	-0.98	Skin	-5.117	20.882	0.93	-0.96
3.627	0.93	-0.99	-1.473	4.812	0.87	-0.91	Oesophagus	-2.191	12.008	0.93	-0.93
126.480	0.93	-0.93	-20.160	122.440	0.96	-0.97	Eye lens	-155.100	616.980	0.91	-0.97
6.341	0.91	-0.95	-4.200	13.487	0.97	-0.97	Muscles	-6.106	19.514	0.92	-0.96
60.039	0.91	-0.96	-35.730	156.730	0.93	-0.99	ET	-49.150	191.400	0.91	-0.99
15.718	0.97	-1.00	-7.429	21.697	0.95	-0.94	Thyroid	-17.560	58.447	0.93	-0.97
88.272	0.92	-0.91	-38.090	184.010	0.95	-0.94	Salivary glands	-144.600	491.200	0.93	-0.92
76.360	0.91	-0.94	-17.480	104.020	0.90	-0.92	Oral mucosa	-69.440	339.050	0.93	-0.98
4.944	0.90	-0.98	-2.605	10.754	0.97	-0.98	RBM	-6.122	20.731	0.95	-0.93
22.938	0.90	-0.98	-12.090	49.897	0.97	-0.98	Bone surface	-28.400	96.472	0.95	-0.93
7.440	0.93	-0.92	-11.060	34.437	0.92	-0.96	Lymph nodes	-15.040	55.532	0.93	-0.99
4.048	0.99	-1.00	-1.928	8.195	0.97	-0.97	ED (µSv/mAs)	-4.668	17.293	0.99	-0.98
0.135	0.99	-0.98	-0.097	0.314	0.98	-0.98	LAR incidence males	-0.208	0.628	1.00	-0.98
0.234	1.00	-0.99	-0.144	0.453	1.00	-0.97	LAR incidence females	-0.321	0.972	0.99	-0.99

Table 3.13 Sinus curve parameters for organ doses, E and LAR incidence (males and females) for all scanners

NewTom VGi-evo				NewTom 5G				CS 9300				
a	b	R^2	r	a	b	R^2	r	a	b	R^2	r	a
-13.950	54.394	0.91	-0.96	-2.807	17.464	0.90	-0.97	-4.193	16.500	0.94	-0.96	-2.726
-5.209	21.083	0.91	-0.95	-5.387	21.987	0.95	-0.97	-1.604	6.647	0.97	-0.99	-2.040
-1.674	9.452	0.84	-0.95	-4.085	16.300	0.96	-0.98	-1.192	3.553	0.93	-0.98	-1.264
-122.300	575.420	0.96	-0.97	-46.800	357.030	0.90	-0.89	-24.680	175.170	0.91	-0.91	-14.120
-6.104	19.581	0.93	-0.97	-2.894	13.461	0.99	-0.98	-0.713	3.297	0.96	-0.99	-1.853
-48.130	191.090	0.90	-0.98	-44.370	199.350	0.94	-0.95	-16.450	62.194	0.93	-0.93	-16.000
-15.940	51.069	0.94	-0.98	-16.180	50.279	0.98	-0.97	-4.467	14.338	0.97	-1.00	-5.600
-203.300	633.080	0.92	-0.91	-146.100	531.450	0.95	-0.96	-28.070	116.790	0.91	-0.98	-21.380
-69.030	316.440	0.91	-0.91	-41.710	202.560	0.90	-0.90	-39.370	147.190	0.95	-0.99	-16.600
-6.325	21.103	0.94	-0.93	-2.349	10.524	0.96	-0.95	-2.134	7.475	0.92	-0.97	-1.351
-29.350	97.916	0.94	-0.93	-10.900	48.833	0.96	-0.95	-9.903	34.685	0.92	-0.97	-6.266
-15.890	56.135	0.90	-0.98	-7.777	28.335	0.89	-0.97	-3.709	11.694	0.91	-0.94	-1.877
-5.273	18.414	0.98	-0.96	-3.592	14.124	0.97	-0.96	-1.356	4.958	0.97	-0.99	-1.082
-0.242	0.695	0.99	-0.98	-0.175	0.536	0.99	-0.98	-0.051	0.160	0.98	-0.99	-0.042
-0.324	0.969	1.00	-0.98	-0.272	0.828	0.99	-0.98	-0.089	0.267	1.00	-0.99	-0.079

Table 3.14 Face curve parameters for organ doses, E and LAR incidence (males and females) for all scanners

CS 9300				Accuitomo 170				Promax 3D Max				Scanner
a	b	R^2	r	a	b	R^2	r	a	b	R^2	r	Parameter
-15.830	47.979	0.93	-0.94	-3.179	15.855	0.96	-0.96	-19.350	90.403	0.97	-0.98	Brain
-5.400	18.859	0.97	-0.97	-3.128	10.508	0.98	-0.99	-4.429	15.314	0.98	-0.98	Skin
-9.323	30.595	0.98	-0.98	-1.923	7.361	0.97	-0.97	-2.398	8.638	0.97	-0.98	Oesophagus
-70.630	313.920	0.97	-0.99	-25.580	105.140	0.94	-0.93	-17.930	77.071	0.95	-0.93	Eye lens
-3.068	10.101	0.92	-0.92	-2.299	8.014	0.96	-0.97	-2.813	10.290	0.95	-0.98	Muscles
-40.570	133.020	0.97	-0.98	-23.720	78.104	0.91	-0.94	-33.180	117.880	0.93	-0.99	ET
-9.872	30.672	0.97	-0.95	-5.191	20.206	0.97	-0.99	-8.509	29.761	0.97	-0.99	Thyroid
-77.900	249.960	0.97	-0.95	-36.420	135.630	0.97	-0.99	-33.150	146.090	0.92	-0.99	Salivary glands
-73.310	237.080	0.98	-0.96	-38.750	137.100	0.94	-0.97	-32.700	142.930	0.93	-0.99	Oral mucosa
-7.145	21.146	0.97	-0.96	-2.149	7.187	0.98	-0.97	-5.035	17.547	0.99	-0.99	RBM
-33.150	98.117	0.97	-0.96	-9.971	33.346	0.98	-0.97	-23.360	81.417	0.99	-0.99	Bone surface
-6.578	20.938	0.96	-0.95	-2.538	9.234	0.99	-0.99	-3.719	13.155	0.91	-0.91	Lymph nodes
-3.621	11.749	0.98	-0.98	-1.763	6.197	0.98	-0.99	-2.530	9.641	0.99	-1.00	ED (µSv/mAs)
-0.132	0.375	0.99	-0.97	-0.072	0.214	0.99	-0.99	-0.102	0.319	1.00	-0.99	LAR incidence males
-0.193	0.555	0.99	-0.98	-0.111	0.3322	0.99	-0.99	-0.163	0.496	1.00	-0.99	LAR incidence females

Table 3.15 Skull curve parameters for organ doses, E and LAR incidence (males and females) for all scanners

Promax 3D Max			Scanner
b	R^2	r	Parameter
94.641	0.97	-0.96	Brain
16.267	0.96	-0.99	Skin
6.846	0.93	-0.94	Oesophagus
72.333	0.96	-0.99	Eye lens
6.433	0.99	-1.00	Muscles
74.344	0.97	-0.99	ET
17.550	0.97	-0.99	Thyroid
106.260	0.91	-0.90	Salivary glands
111.600	0.91	-0.92	Oral mucosa
16.012	0.98	-0.98	RBM
76.252	0.98	-0.98	Bone surface
7.874	0.97	-0.98	Lymph nodes
7.555	0.98	-0.98	ED (µSv/mAs)
0.199	0.98	-0.97	LAR incidence males
0.333	0.99	-0.97	LAR incidence females

NewTom VGi-evo				NewTom 5G			
a	b	R^2	r	a	b	R^2	r
-52.100	297.320	0.95	-0.95	-12.150	44.671	0.98	-0.98
-7.627	36.517	0.81	-0.86	-10.440	38.388	0.97	-1.00
-4.871	20.573	0.97	-0.97	-9.384	32.557	0.94	-0.98
-81.840	537.050	0.96	-0.98	-42.660	276.900	0.98	-0.97
-2.790	19.904	0.86	-0.87	-9.050	30.826	0.96	-0.99
-26.770	190.570	0.96	-0.97	-135.500	421.330	0.94	-0.99
-8.671	34.692	0.86	-0.96	-39.200	123.210	0.99	-0.98
-115.000	583.610	0.97	-0.96	-175.000	592.520	0.97	-0.95
-51.620	363.950	0.74	-0.92	-154.000	537.660	0.95	-0.94
-3.437	22.759	0.91	-0.96	-7.785	27.947	0.94	-0.99
-15.950	105.600	0.91	-0.96	-36.120	129.680	0.94	-0.99
-26.110	90.861	0.99	-0.99	-6.636	29.768	0.95	-0.99
-3.851	21.302	0.98	-0.99	-8.008	26.967	0.99	-0.99
-0.250	0.868	1.00	-0.99	-0.314	0.906	0.99	-0.98
-0.356	1.200	1.00	-0.99	-0.535	1.546	1.00	-0.98

NewTom VGi-evo		NewTom 5G				CS 9300				Accuitomo 170				
R^2	r	a	b	R^2	r	a	b	R^2	r	a	b	R^2	r	a
0.86	-0.88	-33.610	159.720	0.98	-0.97	-9.731	50.956	0.97	-0.98	-4.317	24.843	0.97	-0.98	-20.330
0.92	-0.97	-11.960	46.667	0.97	-0.99	-6.409	22.833	0.99	-0.99	-2.139	10.030	0.98	-0.97	-3.605
0.79	-0.86	-3.861	21.453	0.88	-0.90	-5.405	20.091	0.98	-0.99	-2.331	10.418	0.92	-0.92	-1.223
0.96	-0.96	-31.140	254.380	0.98	-0.97	-22.320	157.980	0.96	-0.99	-13.060	90.360	0.97	-0.98	-5.714
0.95	-1.00	-4.039	18.026	0.92	-0.97	-3.097	11.223	0.94	-0.94	-1.613	7.430	0.92	-0.93	-1.686
0.99	-0.99	-94.360	304.060	0.96	-0.97	-16.580	62.987	0.94	-0.94	-24.750	81.959	0.91	-0.91	-19.250
0.97	-0.97	-33.050	109.030	0.99	-0.98	-4.392	18.901	0.91	-0.97	-4.048	19.784	0.98	-0.97	-3.822
0.97	-0.96	-124.300	482.470	0.95	-0.94	-26.260	139.290	0.92	-0.99	-16.950	99.915	0.93	-0.92	-25.660
0.95	-0.98	-143.300	503.510	0.98	-0.98	-25.750	129.910	0.97	-0.97	-16.660	97.654	0.90	-0.89	-29.450
0.96	-0.99	-10.790	38.682	0.95	-1.00	-3.092	11.037	0.98	-0.99	-2.559	8.417	0.97	-0.95	-4.359
0.96	-0.99	-50.060	179.490	0.95	-1.00	-14.340	51.212	0.98	-0.99	-11.870	39.057	0.97	-0.95	-21.200
0.98	-0.97	-6.858	30.586	0.93	-0.91	-3.481	12.969	0.96	-0.97	-2.248	9.695	0.88	-0.97	-1.489
0.99	-0.98	-7.011	25.942	0.99	-0.99	-1.350	6.863	0.96	-1.00	-1.187	5.416	0.97	-0.95	-1.860
1.00	-0.98	-0.297	0.890	0.99	-0.98	-0.072	0.247	1.00	-0.99	-0.063	0.201	0.98	-0.97	-0.063
0.99	-0.99	-0.498	1.484	0.99	-0.98	-0.121	0.389	1.00	-0.99	-0.103	0.331	0.99	-0.97	-0.108

Table 3.16 Unilateral Temporal bone (UT) curve parameters for organ doses, E and LAR incidence (males and females) for all scanners

NewTom 5G				Scanner
a	b	R^2	r	Parameter
-36.740	168.390	0.95	-0.95	Brain
-7.124	26.170	0.91	-0.93	Skin
-2.060	5.779	0.93	-0.93	Oesophagus
-41.450	195.590	0.94	-0.94	Eye lens
-3.323	16.288	0.95	-0.95	Muscles
-13.500	100.780	0.88	-0.96	ET
-1.625	7.501	0.92	-0.91	Thyroid
-88.380	439.250	0.96	-0.97	Salivary glands
-38.570	187.690	0.97	-0.97	Oral mucosa
-13.580	53.322	0.98	-0.97	RBM
-63.020	247.410	0.98	-0.97	Bone surface
-8.694	24.253	0.91	-0.94	Lymph nodes
-4.324	18.765	0.99	-0.97	ED (µSv/mAs)
-0.201	0.651	0.99	-0.98	LAR incidence males
-0.234	0.767	1.00	-0.98	LAR incidence females

a	b
-48.460	343.460
-11.810	55.511
-6.396	33.249
-130.400	671.960
-9.616	36.952
-63.370	265.310
-32.870	100.480
-178.900	780.410
-46.090	366.040
-7.026	38.654
-32.600	179.360
-22.410	113.910
-6.465	30.860
-0.345	1.150
-0.557	1.770

Table 3.17 Bilateral Temporal bone (BT) curve parameters for organ doses, E and LAR incidence (males and females) for all scanners

Scanner	NewTom 5G			
Parameter	a	b	R^2	r
Brain	-16.830	113.730	0.91	-0.97
Skin	-4.342	18.304	0.91	-0.94
Oesophagus	-1.594	4.398	0.91	-0.91
Eye lens	-50.380	233.680	0.92	-0.92
Muscles	-3.539	14.842	0.93	-0.96
ET	-28.020	143.640	0.99	-0.98
Thyroid	-1.402	5.821	0.89	-0.91
Salivary glands	-63.260	294.880	0.90	-0.91
Oral mucosa	-19.310	95.866	0.98	-0.98
RBM	-6.844	32.134	0.95	-0.93
Bone surface	-31.760	149.100	0.95	-0.93
Lymph nodes	-2.533	10.662	0.89	-0.97
ED (μSv/mAs)	-2.241	11.752	0.97	-0.95
LAR incidence males	-0.121	0.420	0.99	-0.97
LAR incidence females	-0.159	0.536	0.99	-0.99

CHAPTER 4

Radiation dose metrics for dental and maxillofacial CBCT dose monitoring: the CTDI concept

4.1 Introduction

The objective of quality assurance (QA) and quality control (QC) of radiological equipment is to ensure that these systems are safe for use and produce diagnostically acceptable images with reasonably low doses. In this context, radiation dose metrics are essential. They have a double role: to characterize the performance of a system and to allow dose estimates to typical patients by means of appropriate conversion factors. The latter approach is common in Multi Detector CT (MDCT), either via the use of dose length product (DLP) to effective dose conversion factors or via the recently introduced Size Specific Dose Estimate (SSDE) factors applied to $CTDI_{vol}$.

The Computed Tomography Dose Index (CTDI) was first introduced by Shope et al (1981). It aimed to quantify the total dose accumulated by a cylindrical phantom from a single rotation of a fan-shaped X-ray beam. At the time CTDI was introduced there were only head CT scanners, and measurements were performed with TLDs. The slice thicknesses were 7 mm, and the original practical application of the CTDI formula was for +/- 7 T (T = the slice thickness). A pencil ion chamber, 10 cm long, was then developed to meet this criteria, and its active volume was large enough to encompass the primary and the scattered radiation from a narrow, fan-shaped CT beam. CTDI became a standard method for measuring and comparing the radiation output, initially for single-slice CT scanner technology on which the technique was developed, and later for MDCTs and cone beam MDCTs.

Over time, the number of simultaneously captured slices increased from 1 to 320 and as a consequence the x-ray beam shape evolved from fan beam to a wide cone beam geometry (Hu 1999, Kalender 2005, Mori et al 2005, McCollough et al 2007, Takaoka et al 2013). Nowadays, the beam width along the longitudinal z-axis at the axis of rotation can even go beyond 10 cm in recent state of the art MDCT scanners and can be much larger in dental CBCT systems (Mori et al 2005, Rogalla et al 2009, Geleijns et al 2009). While in case of phantom measurements the typical 10 cm long 'pencil' ion chamber is insufficiently long to capture the scatter of narrow beams (e.g. 2cm), for beam widths greater than 10 cm even a part of the primary beam is not collected and the proportion of scatter tail loss gets much higher. A number of studies have since questioned the applicability of CTDI-based metrics for dosimetry of wide cone beam CT systems (Dixon et al 2003, 2006, Boone et al 2007, Perisinakis et al 2007).

Dental CBCT systems are wide cone beam CT scanners which have been routinely used for more than fifteen years for a wide range of applications in oral and maxillofacial imaging. They demonstrate unique geometrical and acquisition features which vary among systems and hence, the establishment of a standardized QA dosimetry method is cumbersome. A wide range of FOVs for different clinical cases are available: the axial diameter of the FOV may vary from about 4 cm for single tooth imaging to more than 25 cm for skull imaging while the longitudinal z-axis beam width may range from 4 to 26 cm for the previously mentioned clinical cases. Some scanners perform a full rotation (360°) around the head of a patient while other systems perform half (180°) or even partial rotations (180°-360°). Such rotations generate asymmetrical and inhomogeneous in-plane dose distributions (Pauwels et al 2012b). Finally, some scanners employ a so-called offset scanning acquisition geometry which enables the acquisition of large scanning volumes with small-sized flat panel detectors (Scarfe and Farman 2008). Consequently, the establishment of a standardized dose index for dental CBCT systems is a complicated task and the relevance of CTDI is questionable.

Several dose indices have been proposed for routine QA measurements on dental CBCTs so far. The SEDENTEXCT consortium suggested two different formulae for a new dental CBCT dose Index (CBCT DI) in which the accumulated dose in a dedicated PMMA phantom for inhomogeneous dose distributions can be approximated by the quantity CBCT DI-1 which corresponds to the average of

seven dose measurements along the diameter of a dedicated PMMA phantom (Pauwels et al 2012b, ICRP 2015, Araki et al 2013). For more homogeneous dose distributions, a CTDIw-adapted formula (CBCT DI-2) is proposed, where the only difference with the standard CTDIw is that CBCT DI-2 weights the central and the average peripheral dose measurements equally. However, to the best of our knowledge, this method does not account for the large z-axis beam widths, especially when a pencil IC replaces a point dose IC. Furthermore, it has not been validated yet whether the two proposed indices can approximate the accumulated dose in the phantom sufficiently.

Two different methodologies were proposed in the early 2010's to tackle the issue of wide z-axis beam widths. AAPM Task Group 111 introduced a methodology applicable to helical and axial operation modes, fan and cone shaped beams of any width, which also covers any table increment, scanning length and any phantom shape (AAPM 2010). For non-stationary table acquisitions, the method suggests the equilibrium dose – pitch product as the most efficient dose metric; this is the upper limiting value of the central cumulative dose, measured at the center of the scanning length of a CT scan with a thimble ion chamber. For stationary acquisitions (like MDCT perfusion scans), the proposed metric is the central cumulative dose f(0). The methodology is easily applicable, well-documented and robust. However, (1) it requires equipment (thimble IC) which is not commonly available in Medical physics departments dealing with diagnostic radiology. (2) The method is not validated for dental CBCT scanners which may be stationary modalities in the sense that there is no patient translation during x-ray tube rotation. (3) Complex non-symmetrical (offset) in-plane and longitudinal beam shapes are used, next to small in-plane diameters.

The International Electrotechnical Commission (IEC) issued in 2010 the IEC 60601-2-44 document (Amendment 1 of version 3), also adopted by the International Atomic Energy Agency (IAEA), aiming to preserve the meaning of the CTDI-based metrics as an integrated index of the entire dose profile representing the total effect of the radiation beam (IEC 2010, IAEA 2011). To cope with the tendency towards wider z-axis collimations, IEC initially superseded the original $CTDI_{w,IEC2.0}$ definition with $CTDI_{w,IEC3.0}$. Instead of dividing the dose integral with the nominal beam width (NxT, N simultaneously captured slices of width T) when assessing the central and peripheral $CTDI_{100}$ values in a standard head or body CTDI phantom (IEC 2.0, equation 4.1), division is made by the 100 mm length or by the nominal z-axis beam width (IEC 3.0, equation 4.2), whichever is the smallest value.

$$CTDI_{100,IEC2.0} = \frac{1}{(NxT)} \int_{-50}^{+50} D(z)dz \quad \text{(eq. 4.1)}$$

$$CTDI_{100,IEC3.0} = \frac{1}{\min\{(NxT),100)\}} \int_{-50}^{+50} D(z)dz \text{ (eq. 4.2)}$$

However, this modification was not sufficient to cope with the very wide z-axis beams of recent state-of-the-art cone beam MDCTs. The new amendment, i.e. $CTDI_{100,IEC3.1}$, employs equation 4.1 for nominal z-axis beam widths up to 40 mm. For nominal beam widths > 40mm, equation 4.3 is used in which a reference beam of approximately 2 cm is defined. The dose integral is subsequently divided by the reference beam width (NxT)ref, and scaled by the ratio of the free in air (scatter free) CTDI measurements of the nominal to the reference beam.

$$CTDI_{100,IEC3.1} = \frac{1}{(NxT)_{ref}} \; x \; \left(\int_{-50mm}^{+50mm} D_{ref} \; (z)dz \right) \; x \; \left(\frac{CTDI_{free-in-air,NxT}}{CTDI_{free-in-air,ref}} \right) \text{(eq. 4.3)}$$

For all methodologies, the $CTDI_w$ values use the same basic formula:

$$CTDI_w = (1/3) * CTDI_{100,c} + (2/3) * CTDI_{100,p} \quad \text{(eq. 4.4)}$$

where $CTDI_{100,c}$ represents the measured CTDI at the central position and $CTDI_{100,p}$ the average CTDI value of the four measurements in the periphery of the CTDI phantom.

The ultimate goal in CT dosimetry has been to include all the effects of primary and scatter radiation in the CTDI metric. This is particularly important in studies where CTDI is used to approximate patient dose; the scatter tails of the single beam profile represent the contribution of the adjacent slices to the central slice of a theoretical multi-rotational acquisition. Theoretically, for very large beam widths, this could be achieved with an infinitely long CTDI phantom and an infinitely long IC, leading to an estimate of the infinite CTDI ($CTDI_{w,\infty}$). In practice, even with extra phantoms that may approximate an 'infinite length', the measurement of $CTDI_{w,\infty}$ is cumbersome. Alternatively, the $CTDI_{efficiency}$ factor has been introduced as the ratio of a measured (practical) CTDI metric ($CTDI_w$) and the $CTDI_{w,\infty}$ (eq.4.5) to describe the error with which the $CTDI_w$ fails to account for the full dose effects. If the ratio is constant for every beam width, the full dose effects can be deduced by applying a simple correction factor ($\frac{1}{CTDI_{efficiency}}$) to $CTDI_w$. Therefore, the utility and relevance of any CTDI-based metric can be checked via the CTDI measurement efficiency that has to be constant for a CTDIw metric to be relevant.

$$CTDI_{efficiency} = \frac{CTDI_w}{CTDI_{w,\infty}} \quad \text{(eq 4.5)}$$

It has been reported that the new IEC 3.1 methodology does indeed give a constant efficiency in modern cone beam MDCTs (IEC 2010, IAEA 2011). Furthermore, it was recently shown that $CTDI_{w,IEC3.1}$ could be efficiently applied to a CBCT system mounted on a linear accelerator (Abuhaimed et al 2014).

The aim of present study was multifold. Initially, our objective was to investigate whether this method leads to robust results when translated to different types of dental CBCT scanners. The decision criterion as to whether the method is applicable employs the $CTDI_{efficiency}$ concept, which requires $CTDI_{efficiency}$ to be constant for the entire range of the available FOVs in a dental CBCT scanner. We investigated the applicability of the method in two scanners with totally different technical specifications and geometry acquisitions; Promax 3D Max and NewTom 5G. Apart from $CTDI_{w,IEC3.1}$, we also assessed the efficiency of $CTDI_{w,IEC2.0}$ and $CTDI_{w,IEC3.0}$. In a second step we aimed to check whether the 1/3 and 2/3 factors for central and peripheral CTDI measurements also apply for dental CBCT scanners by verifying whether the CTDI still represents the average dose in the scanning region. In a third step, we calculated the $CTDI_{w,IEC3.1}$for every clinically applied FOV and for all five scanners involved in the project. Finally, we aimed to provide CTDI to E and LAR conversion factors such that an immediate estimation of organ doses and radiation risk is achieved.

The Monte Carlo (MC)– based simulation approach that was used gave practical solutions for the many practical difficulties in measuring $CTDI_{w,\infty}$. The MC approach enabled the simulation of the 2cm wide reference x-ray beams for free-in-air and phantom measurements, required in the new IEC 3.1 method. Such narrow beam widths are not available on dental CBCT systems and cannot be set manually as there is no manual collimation. A further motivation to use MC methods was the requirement of the IEC 3.1 methodology for a dose integration length that is at least 4 cm larger than the beam width when free in air measurements of beams wider than 6 cm are employed. Practically, this is achievable by stepping the pencil IC through the x-ray beam at intervals equal to its sensitive length and by taking successive measurements at each position. This task is however prone to many errors, especially in

dental CBCTs with a panoramic (patient-sitting-on-a-chair) orientation and was performed with MC. To check the applicability of the three IEC approaches ($CTDI_{w,IEC2.0}$, $CTDI_{w,IEC3.0}$, $CTDI_{w,IEC3.1}$), voxel models of a commercially available pencil IC and the required CTDI phantoms were designed. A novel voxel model was also implemented which allowed the calculation of axial dose distributions and thus an evaluation of whether the 1/3 and 2/3 factors for central and peripheral CTDI measurements also apply for dental CBCT scanners.

4.2 Methods and Materials

4.2.1 Investigation of the applicability of $CTDI_{w,IEC2.0}$, $CTDI_{w,IEC3.0}$ and $CTDI_{w,IEC3.1}$ method for different scanners, technical specifications and investigated clinical protocols

Two dental CBCT scanners with different geometric and technical specifications were employed: the Newtom 5G and the Promax 3D Max. The Newtom 5G system is oriented horizontally (as in conventional CT), whereas the Promax 3D Max has a vertical, panoramic-like orientation. The x-ray tube – detector system In Newtom 5G, always performs a full rotation around the head of the patient while the Promax 3D Max makes a partial 210° rotation for each protocol, except for full skull imaging where a full rotation is employed. The beam shape in the axial plane is asymmetrical in the Newtom 5G due to offset scanning in all cases (except the 6x6 and 8x8 cm² FOVs), while the Promax 3D Max employs a symmetrical radiation field, with the exception of the skull protocol which is also performed with an offset configuration (figure 4.1).

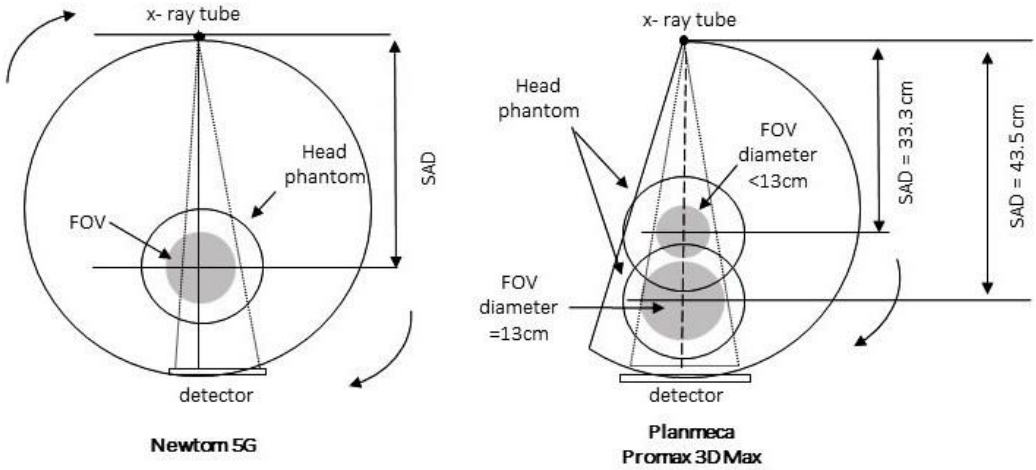

Figure 4.1. Geometric specifications of the two models. The Newtom 5G employs a beam offset and a full rotation (except for the smallest FOVs); the Planmeca Promax 3D Max employs a symmetrical beam and a 210° rotation (except for the largest FOV). In Promax 3D Max there is a change in the SAD according to the diameter of the FOV.

The Source to Axis of rotation distance (SAD) is fixed for the Newtom 5G, but for Promax 3D Max, the SAD changes depending on the protocol and the associated FOV. Other differences between these scanners are related to their energy spectra. In the Newtom 5G, each clinical protocol operates at 110 kV whereas the Promax 3D Max operates at 96 kV. An additional Aluminum (Al) x-ray tube filter is used

in the Newtom 5G while a combined Cu (Copper)/Al filter is used in the Promax 3D Max; both are flat filters without any beam shaping-bowtie structure. Table 4.1 summarizes the technical specifications of both scanners.

Table 4.1 Technical specifications of the two scanners

Specifications	Newtom 5G	Promax 3D Max
Total filtration *	4.4 mmAl @70 kV	> 0.5 mmCu + 2.5 mmAl
Operating voltage (kV)	110	96
Measured HVL at the operating voltage (mmAl)	4.75	9.00
SDD (cm)**	97	60
SAD (cm) ***	66.4	33.3 / 43.5 / 42.6 ***
Rotation	360°	210° / 360° ****

*Based on the specifications provided by the manufacturer

**SDD stands for Source to Detector Distance and SAD for Source to Axis of Rotation distance

***The SAD changes according to the diameter of the FOV; for a diameter d<13cm, the SAD=33.3 cm, for d=13cm the SAD = 43.5 cm and for d=23cm the SAD = 42.6 cm

****Full rotation (360°) applies only for skull protocols having a FOV diameter of 23 cm

Table 4.2 presents the protocols studied. For both scanners, six protocols were investigated: 6x6, 8x8, 12x8,15x5,15x12, 18x16 cm² and 5x5.5, 8.5x7.5, 10x5.5, 10x9, 13x16 and 23x16 cm² for the NewTom 5G and the Promax 3D Max respectively (FOV expressed as diameter x height cm2). They were selected to cover the entire range of the available FOV sizes.

In present study, the CTDI results were normalized to the tube load, i.e. they were expressed in mGy/mAs to get the results applicable for every operation mode (low dose, normal or high dose) which uses different mAs settings. Normalization to mAs is allowed since there is no change in SAD/SDD ratio, in filtration, in the rotation geometry or the operating voltage among the different operation modes which could influence the output of the scanner.

4.2.2 Implementation of the IEC methods through voxel modeling

A head CTDI voxel model, resembling a typical head CTDI phantom, was designed for future MC simulations of CTDI related concepts. The phantom/voxel model material was Polymethyl Methacrylate (PMMA), with a diameter of 16 cm and a height of 15 cm (figure 4.2). Assessment of $CTDI_{w,IEC2.0}$ and $CTDI_{w,IEC3.0}$ was straightforward: the dose was estimated using MC simulation at the central and peripheral holes of the standard head CTDI voxel model (equations 1 and 2) followed by calculation of $CTDI_{w,IEC2.0}$ and $CTDI_{w,IEC3.0}$ via equation 4.4.

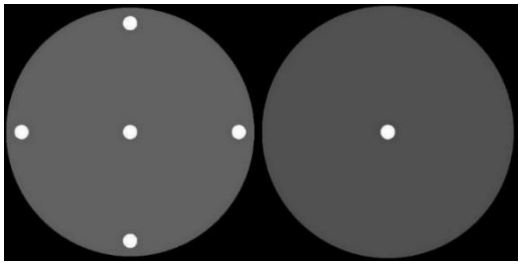

Figure 4.2 The head CTDI voxel model. When the dose is calculated in one of the holes (central hole on the right hand image), the other holes are simulated to consist of PMMA, representing good practice in CTDI measurements, i.e. using PMMA plugs in the remainder holes

The calculation of $CTDI_{w,IEC3.1}$ requires $CTDI_{free-in-air}$ MC dose simulations for every nominal beam and each respective reference beam in order to calculate the ratio ($\frac{CTDI_{free-in-air,NxT}}{CTDI_{free-in-air,ref}}$) (equation 4.3). MC dose simulations in the head CTDI voxel model then gave an estimate of $CTDI_{100,\mathrm{ref}}$, or, more precisely, the factor $\frac{1}{(NxT)_{ref}}\ x\ \left(\int_{-50mm}^{+50mm} D_{ref}\ (z)dz\right)$.

To carry out the $CTDI_{free-in-air}$ simulations, a voxel model of a typical 10 cm long pencil IC was designed. The voxel model was built in Matlab (version 7.12.0.635, R2011a, MathWorks Inc.) according to the DCT10 Pencil IC specifications (RTI Electronics, Molndal, SE). The outer diameter was 0.92 cm with a 0.06 cm thick graphite equivalent wall. Air equivalent plastic 'C-552' with density 1.76 g/cm³ was used for this wall (http://physics.nist.gov/cgi-bin/Star/compos.pl?refer=ap&matno=126). In the center of the IC, a 0.2 cm diameter inner Al electrode was simulated. The in-plane voxel dimension was 0.01cm (figure 4.3). According to the IEC3.1 methodology, the requested dose integration length for free in air measurements has to extend at least 4 cm beyond the nominal beam width (2cm at each side of the beam). Therefore, the active length of the IC voxel model was set to 10cm for the simulations of the 6x6 and 15x5 cm² protocols in the NewTom 5G and the 5x5.5 and 10x5.5 cm² protocols in the Promax 3D Max. For the other protocols the active length was set at 20 cm to simulate two consecutive measurements with a 10 cm long IC. The pencil IC voxel model was positioned in the MC framework with its long axis parallel to the axis of rotation at the SAD for every FOV.

To calculate the factor $\frac{1}{(NxT)_{ref}}\ x\ \left(\int_{-50mm}^{+50mm} D_{ref}\ (z)dz\right)$, the standard head CTDI voxel model was employed and virtual reference FOVs, having a beam width of 2cm and a diameter equal to the diameter of each investigated nominal FOV, were designed (figure 4.4, table 4.2). The reference beam width was in all cases 2 cm, and hence, the dose integration length was set to 10 cm. The head CTDI voxel phantom was positioned with its axis parallel to the rotation axis at the SAD.

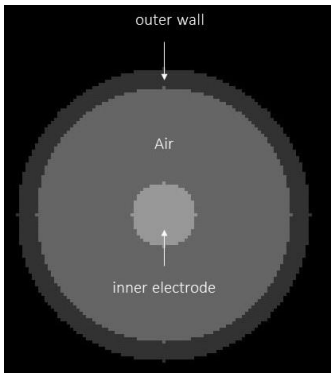

Figure 4.3 Axial cross section of a voxelized pencil IC

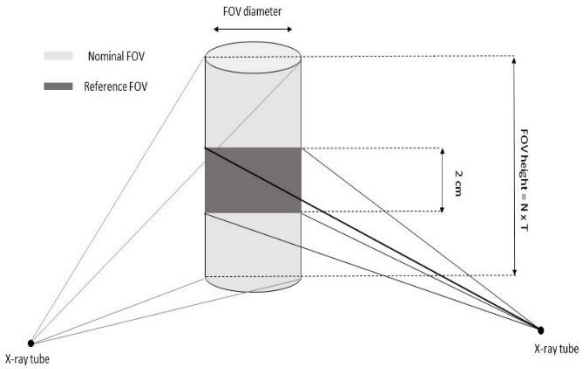

Figure 4.4 Reference and nominal FOV

To calculate the CTDI measurement efficiency, $CTDI_{w,\infty}$ MC calculations were performed. Mori et al (2005) showed that phantom and dose integration length should be greater than 30 cm to capture more than 90% of the full dose profile (Mori et al 2005, Perisinakis et al 2007). Therefore, a 50 cm long head CTDI voxel phantom with a typical 16 cm diameter was designed to approximate the infinite length, along with a dose integration length of 50 cm. IEC (2010) and IAEA (2011) reported CTDI efficiency curves generated with a 50 cm long phantom to simulate the infinite length.

For CTDI simulations in the head phantoms (standard and infinitely long), instead of directly simulating the IC at each position inside the phantom, the PMMA voxels which corresponded to the IC position were specified and dose in PMMA calculated. Subsequently, dose in air was obtained by multiplying by the ratio of the mass energy absorption coefficient in air to that in PMMA. This method reduces the large simulation uncertainties due to the limited number of photon interactions in air (active volume of the ion chamber).

To obtain the dose values in mGy, the MC calculated value in mGy*cm (dose x integration length) was either divided by the z-axis beam width for the typical $CTDI_{w,IEC2.0}$ estimation or by the minimum value of the beam width and the active IC length for the $CTDI_{w,IEC3.0}$ estimation. For MC validation purposes, the MC calculated $CTDI_{w,IEC3.0}$ values were compared against real measurements for four different protocols in NewTom 5G (6x6, 15x5, 15x12 and 18x16 cm²). A standard head CTDI phantom was positioned in such a way that its central longitudinal axis coincided with the axis of rotation of the scanner and dose measurements were carried out at the operating voltage of each protocol (110 kV) with a calibrated pencil IC (DCT10, RTI Electronics, Molndal, SE).The geometry validation process, which was designed to test the accurate reproduction of the phantom set-up, was carried out only for the IEC 3.0 methodology. The reason IEC 3.0 was selected for validation of the geometry over IEC 3.1 was (1) to overcome practical complexities which could have introduced uncertainties in IEC 3.1 CTDI real dose measurements; (2) the accurate stepping of the IC for consecutive free-in-air measurements and (3) the lack of reference beams (as there was no manual collimation in both scanners).

The clinical relevance of the new CTDI metric (IEC 3.1) was tested by verifying whether the ratio of $CTDI_{w,IEC3.1}$to $CTDI_{w,\infty}$ (equation 4.5) was constant.

We designed a “spider” voxel model which enabled us to visualize the in-plane dose distribution and calculate directly the absorbed dose in PMMA (figure 4.5). This directly calculated absorbed dose was subsequently compared to that one deduced from $CTDI_{w,IEC3.1}$ This comparison aimed to (1) investigate whether $CTDI_{w,IEC3.1}$ manages to represent the dose accumulated in the scan volume in dental CBCT exposures (as it should do according to the historical definition of CTDI) and (2) check the relevance of the center (1/3) versus peripheral (2/3) weighting factors in the CTDI definition. To this

end, The spider phantom had the typical dimensions and composition of a PMMA – standard head CTDI phantom, yet with an axial configuration that allowed dose calculations in 160 different sectors.

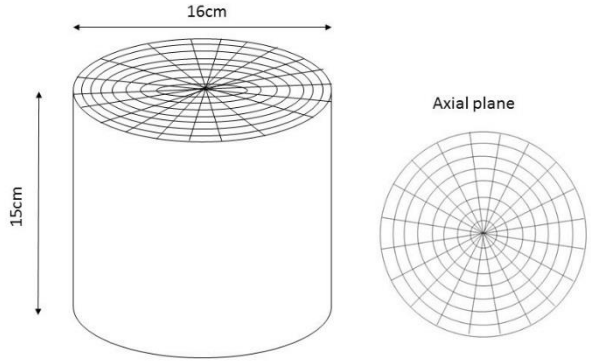

Figure 4.5 The spider-like voxel model employed to illustrate the axial dose distribution and calculate the average dose in the scan plane.

4.2.3 Calculation of $CTDI_{w,IEC3.1}$ for every FOV and scanner involved in the study and proposal of conversion factors

We assessed the $CTDI_{w,IEC3.1}$ for every FOV which has been clinically applied in this project (table 3.4). In conjunction with the dose calculations in chapter 3, we provide a straightforward way to assess age-specific organ dose and risk assessment for every clinical protocol via scanner-specific conversion factors.

4.3 Results

4.3.1 Investigation of the applicability of $CTDI_{w,IEC2.0}$, $CTDI_{w,IEC3.0}$ and $CTDI_{w,IEC3.1}$ methods for different scanners, technical specifications and investigated clinical protocols

The MC simulation uncertainty was calculated in terms of % CV (Coefficient of Variance) of the calculated dose values. The average %CV on $CTDI_{free-in-air}$ calculations was 4% whereas for CTD100 calculations in the head phantom, the average statistical uncertainty was less than 0.5%. For dose calculations in PMMA in the spider-phantom, the average uncertainty was less than 0.2%. In all cases, 10 million histories per projection were simulated for a total number of 360 and 210 projections in Newtom 5G and Promax 3D Max respectively. In the case of the largest 23 x16 cm² FOV in Promax 3D Max, namely is a full rotation protocol, 360 projections were simulated. The overall uncertainty in the calculations is estimated to be around 6%, including a 2% measurement uncertainty for the IC used in the MC framework customization procedure, and provided by the calibration lab.

The protocols for both scanners and the respective calibration factors (histories/mAs) are presented in table 4.2. When the calibration factors of all FOVs are plotted against the field area at each projection, i.e. the product diameter x height, a linear relationship is observed as illustrated in figure 4.6. This allows calculation of calibration factors for the virtual, 2cm wide, reference beams. It should be noted that the field size calculations were based on the collimation openings that were provided by the manufacturers and not from any measured or even indicated diameter.

Table 4.2 Calibration factors for each scanner

FOV (cm²) (diameter x height)	Clinical indication	diameter (cm)	height (cm)	type	field area (cm²)	histories/mAs
NewTom 5G						
6 x 6	Tooth	6.5	6.3	Nominal beams	40.6	4.103E+10
8 x 8	Upper/lower jaw	8.6	7.9		67.8	6.921E+10
12 x 8	Sinus	9.9	7.9		77.9	8.584E+10
15 x 5	Temporal bone	11.6	5.5		63.4	6.458E+10
15 x 12	Face	11.6	13.4		155.7	1.572E+11
18 x 16	Face / Skull	13.4	16.7		223.9	2.296E+11
6 x 2	/	6.5	2	Reference beams	13.0	1.232E+10
8 x 2		8.6	2		17.2	1.663E+10
12 x 2		9.9	2		19.7	1.925E+10
15 x 2		11.6	2		23.3	2.286E+10
18 x 2		13.4	2		26.8	2.649E+10
Promax 3D Max						
5 x 5.5	Tooth	5	5.5	Nominal beams	27.5	2.03E+10
8.5 x 7.5	Teeth	8.5	7.5		63.8	4.62E+10
10 x 5.5	Cleft palate	10	5.5		55.0	3.97E+10
10 x 9	Upper/lower jaw	10	9		90.0	6.70E+10
13 x 16	Face	13	16		208.0	8.78E+10
23 x 16	Skull	13.6	16		217.6	1.00E+11
5 x 2	/	5	2	Reference beams	10.0	7.76E+09
8.5 x 2		8.5	2		17.0	1.28E+10
10 x 2		10	2		20.0	1.50E+10
13 x 2		13	2		26.0	1.14E+10
23 x 2		13.6	2		27.2	1.20E+10

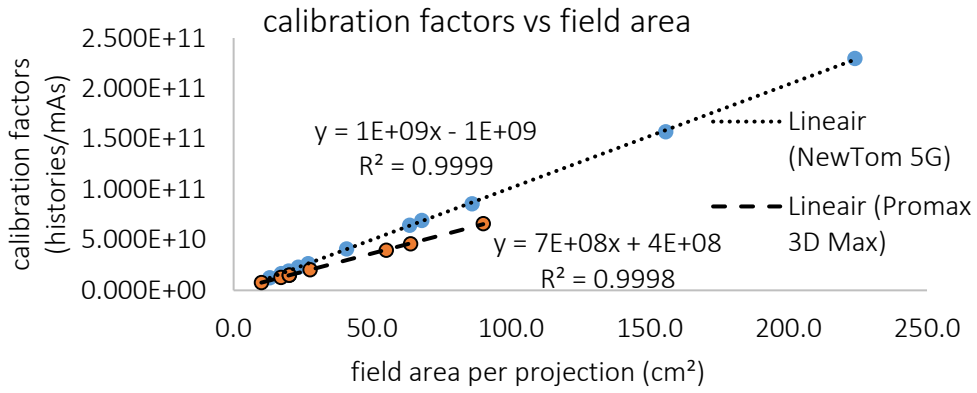

Figure 4.6. Linear relationship between calibration factors and the field area of the FOV per projection

The MC calculated $CTDI_{w,IEC3.1}$ values along with the MC calculated $CTDI_{w,IEC3.0}$ and $CTDI_{w,IEC2.0}$ values are presented in Table 4.3 for the two systems.

Table 4.3. $CTDI_{w,IEC2.0}$, $CTDI_{w,IEC3.0}$ and $CTDI_{w,IEC3.1}$ MC calculated values for both scanners

NewTom 5G			
FOV (cm²) (diameter x height)	$CTDI_{w,IEC2.0}$ (mGy/mAs)	$CTDI_{w,IEC3.0}$ (mGy/mAs)	$CTDI_{w,IEC3.1}$ (mGy/mAs)
6 x 6	0.123	0.123	0.124
8 x 8	0.152	0.152	0.162
12 x 8	0.187	0.187	0.189
15 x 5	0.202	0.202	0.203
15 x 12	0.160	0.215	0.208
18 x 16	0.135	0.225	0.211
Promax 3D Max			
5 x 5.5	0.057	0.057	0.057
8.5 x 7.5	0.079	0.079	0.082
10 x 5.5	0.090	0.090	0.091
10 x 9	0.088	0.088	0.089
13 x 16	0.048	0.076	0.070
23 x 16	0.037	0.059	0.054

Table 4.4 presents the % difference between the simulated and the measured $CTDI_{w,IEC3.0}$ values in the NewTom 5G scanner for the geometry validation purposes.

Table 4.4. Validation of the MC method via $CTDI_{w,IEC3.0}$ comparison

FOV (cm²) (diameter x height)	Monte Carlo $CTDI_{w,IEC3.0}$ (mGy/mAs)	Measured $CTDI_{w,IEC3.0}$ (mGy/mAs)	% difference
6 x 6	0.123	0.116	5.7
15 x 5	0.202	0.195	3.5
15 x 12	0.215	0.212	1.4
18 x 16	0.225	0.228	-1.3

The $CTDI_{w,\infty}$ values and the $CTDI_{efficiency}$ of the three methods (IEC 2.0, IEC 3.0 and IEC 3.1) are presented in tables 4.5 and 4.6 for the NewTom 5G and the Promax 3D Max respectively.

Table 4.5. $CTDI_{w,\infty}$ and measurement efficiency in NewTom 5G

FOV (cm²) (diameter x height)	$CTDI_{w,\infty}$ (mGy/mAs)	$CTDI_{efficiency}$ (IEC 2.0)	$CTDI_{efficiency}$ (IEC 3.0)	$CTDI_{efficiency}$ (IEC 3.1)
6 x 6	0.147	0.84	0.84	0.85
8 x 8	0.185	0.82	0.82	0.88
12 x 8	0.223	0.84	0.84	0.85
15 x 5	0.233	0.87	0.87	0.87
15 x 12	0.235	0.68	0.91	0.89
18 x 16	0.237	0.57	0.95	0.89

Table 4.6. $CTDI_{w,\infty}$ and measurement efficiency in Promax 3D Max

FOV (cm²) (diameter x height)	$CTDI_{w,\infty}$ (mGy/mAs)	$CTDI_{efficiency}$ (IEC 2.0)	$CTDI_{efficiency}$ (IEC 3.0)	$CTDI_{efficiency}$ (IEC 3.1)
5 x 5.5	0.068	0.84	0.84	0.83
8.5 x 7.5	0.097	0.81	0.81	0.85
10 x 5.5	0.109	0.83	0.83	0.83
10 x 9	0.111	0.79	0.79	0.80
13 x 16	0.081	0.59	0.94	0.86
23 x 16	0.064	0.58	0.92	0.84

The PMMA voxel model in figure 4.5 was designed to visualize the dose distributions in the axial plane and to directly calculate the absorbed dose in PMMA for every investigated protocol. These dose distributions are shown in figures 4.7 and 4.8 for the two systems. For each protocol, the absorbed dose in each of the 160 sectors of the phantom was calculated and was normalized to the highest absorbed dose. The highest dose sectors, receiving 95-100% of the maximum absorbed dose, are illustrated in black, with each grey level step from black to white corresponding to a 5% dose decrease from the preceding value. The outer lines indicate the border of the 16 cm-diameter phantom and the dotted lines show the borders of the FOV diameter.

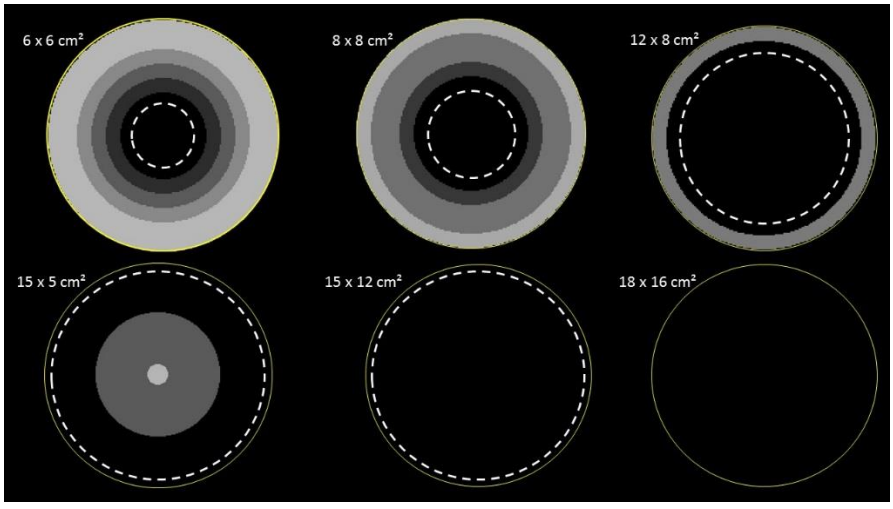

Figure 4.7. In-plane dose distribution for each protocol in NewTom 5G. Dose decreases in 5% steps (grey levels) from black (highest dose) to white (lowest dose)

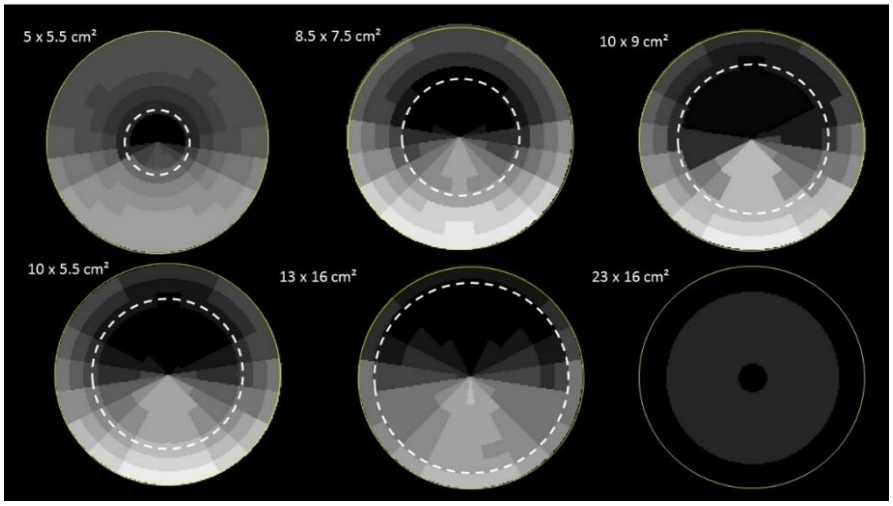

Figure 4.8. In-plane dose distribution for each protocol in Promax 3D Max. Dose decreases in 5% steps (grey levels) from black (highest dose) to white (lowest dose)

In tables 4.7 and 4.8, $D_{PMMA,CTDI}$ represents the absorbed dose in PMMA as deduced from $CTDI_{w,IEC3.1}$ simulations and based on the 1/3 and 2/3 weighting for the central and peripheral dose estimates. D_{PMMA} represents the absorbed dose in PMMA as directly calculated with the spider phantom. Considering the D_{PMMA} as the gold standard, the relevance of the 1/3 and 2/3 weighting factors can be evaluated by comparing D_{PMMA} to $D_{PMMA,CTDI}$ for each FOV.

Table 4.7 $D_{PMMA,CTDI}$ vs D_{PMMA} values for the NewTom 5G

FOV (cm²) (diameter x height)	$D_{PMMA,CTDI}$ (mGy/mAs)	D_{PMMA} (mGy/mAs)	$\frac{D_{PMMA,CTDI}}{D_{PMMA}}$
6 x 6	0.096	0.098	0.99
8 x 8	0.126	0.134	0.94
12 x 8	0.146	0.157	0.93
15 x 5	0.157	0.168	0.94
15 x 12	0.161	0.174	0.90
18 x 16	0.163	0.175	0.93

Table 4.8 $D_{PMMA,CTDI}$ vs D_{PMMA} values for the Promax 3D Max

FOV (cm²) (diameter x height)	$D_{PMMA,CTDI}$ (mGy/mAs)	D_{PMMA} (mGy/mAs)	$\frac{D_{PMMA,CTDI}}{D_{PMMA}}$
5 x 5.5	0.048	0.054	0.89
8.5 x 7.5	0.070	0.078	0.91
10 x 5.5	0.077	0.085	0.89
10 x 9	0.075	0.090	0.83
13 x 16	0.059	0.068	0.87
23 x 16	0.045	0.052	0.87

4.3.2 Calculation of $CTDI_{w,IEC3.1}$ for every FOV and scanner involved in the study and proposal of conversion factors

Tables 4.9 presents the $CTDI_{w,IEC3.1}$ asestimated with MC for every clinically applied FOV for each scanner.

Table 4.9 $CTDI_{w,IEC3.1}$ MC calculated values for every clinically applied protocol in every scanner

FOV (diameter x height – cm^2)	CTDIw,IEC3.1 (mGy/mAs)
NewTom 5G	
6 x 6	0.124
8 x 8	0.162
12 x 8	0.189
15 x 5	0.203
15 x 12	0.208
18 x 16	0.211
Promax 3D Max	
5 x 5.5	0.057
8.5 x 4.8	0.07
8.5 x 7.5	0.082
10 x 5.5	0.091
10 x 9	0.089
10 x 13	0.092
13 x 13	0.068
13 x 16	0.07
23 x 16	0.054
23x26 *	0.054
Accuitomo 170	
6 x 6	0.052
8 x 8	0.057
10 x 5	0.066
10 x 10	0.067
14 x 10	0.078
17 x 12	0.081
CS 9300	
5 x 5 (80 kV)	0.034
8 x 8 (85 kV)	0.062
10 x 5 (85 kV)	0.067
10 x 10 (85 kV)	0.068
17 x 11 (85 kV)	0.11
17 x 13.5 (85 kV)	0.111
NewTom VGi evo	
5 x 5	0.136

8 x 5	0.197
8 x 8	0.195
10 x 5	0.263
10 x 10	0.216
12 x 8	0.247
15 x 12	0.287
16 x 16	0.273
24 x 19	0.293

*The 23 x 26 cm² protocol is carried out in a stitching mode of two sequential 23 x 16 cm². Therefore, it was considered as a sequential acquisition equivalent to axial scanning in MDCTs

The $CTDI_{w,IEC3.1}$ values presented in table 4.9 and the results of the dose study in chapter 3 enable the assessment of task-based, scanner and age-specific CTDIw,IEC3.1 to organ dose, E and LAR conversion factors. More specifically conversion factors are given by the following equations:

CF ($CTDI_{w,IEC3.1}$ to organ dose d_i) = $\frac{d_{ijkl}}{(CTDI_{w,IEC3.1})ij}$ (μGy/mGy) (eq.4.6)

CF ($CTDI_{w,IEC3.1}$ to E) = $\frac{E_{ijl}}{(CTDI_{w,IEC3.1})ij}$ (μSv/mGy) (eq.4.7)

CF ($CTDI_{w,IEC3.1}$ to LAR incidence) = $\frac{LAR_{ijlm}}{(CTDI_{w,IEC3.1})ij}$ (#cases/100,000/mGy) (eq.4.8)

where i is the scanner model, j the protocol, k the organ, l the age and m the gender of the patient. In parentheses the units of each conversion factors are displayed. The values of $d_{ijkl}, E_{ijl}, LAR_{ijlm}$ can be deduced from the tables 3.5-3.17 for each desirable clinical case, scanner, organ, age and gender while the respective $(CTDI_{w,IEC3.1})ij$ can be retrieved from table 4.9.

4.4 Discussion

The aim of this work was to investigate the applicability of the CTDI-based metrics given in IEC 60601-2-44 to wide dental cone beam CT dosimetry. We investigated CTDI as a potential metric for CBCT scanners because it is a method that requires equipment which is available in Medical Physics QA groups in diagnostic radiology and furthermore, is a dose metric which Medical Physicists are familiar with, and is displayed in most dental CBCTs. The study uses MC simulations as a solution for measurements that would be very difficult, time consuming or cumbersome in practice. The applied MC framework was used to simulate two scanners selected for their different geometries and technical specifications.

The key parameter used to evaluate the applicability of CTDI-based metrics was CTDI measurement efficiency. A stable efficiency over the entire range of longitudinal beam widths indicates that the metric is capable of estimating the total primary and scatter radiation dose in a phantom for a broad range of protocols. The results of this study showed that the IEC 3.1 approach results in a constant efficiency, whereas $CTDI_{w,IEC3.0}$ or the $CTDI_{w,IEC2.0}$ do not. The results suggest that $CTDI_{w,IEC3.1}$ should be used, consistent with the conclusions of the IAEA report for the wide cone beam CT systems. One of the main reasons which triggered the implementation of a simulation study was the requirement of the IEC 3.1 methodology for a reference, 2cm z-axis beam width. Such beams do not exist in dental CBCT systems since this width is too small to be a relevant clinical setting for a single rotation. Furthermore, to the best of our knowledge, most dental CBCTs are not equipped with manual collimation for setting the volume of interest. In the light of this study, manufacturers should be urged

to include a reference beam, at least in service mode. Monte Carlo simulations are an alternative solution, yet this is obviously not a tool for routine quality assurance practice, although It could perhaps be part of a commissioning report. Although IEC 2.0 and IEC 3.0 methods have been superseded by IEC 3.1, present work has investigated all IEC versions since many (if not all) CBCT manufacturers still employ the CTDI IEC 2.0 version for their displayed values. The study proves that vendors should comply with the IEC 3.1. The study proves that older IEC versions are definitely not applicable to CBCTs. Six protocols in the NewTom 5G and in the Promax 3D Max, covering a wide range of beam widths and clinical applications, from single tooth to full skull imaging, were investigated for the relevance of the new CTDI metric. Differences in $CTDI_{w,IEC3.1}$ (tables 4.3 and 4.9) result from scanner design characteristics. The NewTom 5G scanner operates at 110kV and has an inherent filtration of 4.4 mmAl corresponding to a measured HVL of 4.75 mmAl, whereas the combined Cu and Al filtration of the Promax 3D Max results in a measured HVL of 9.00 mmAl at an operating voltage of 96 kV. Furthermore, NewTom 5G performs a full rotation compared to the partial rotation of the Promax 3D Max. All this accounts for the higher CTDI values of the Newtom 5G scanner, when expressed per mAs, yet clinical protocols are performed at lower mAs values on this scanner. As shown in the tables, the normalized CTDI values (mGy/mAs) in the Promax 3D Max are lower in the larger FOV compared to the smaller FOV protocols. This is due to the smaller magnification factors for the larger FOV protocols, which are performed at increased SAD (table 4.1).

The aim of the IEC 3.1 method is to provide a robust methodology that accounts for the long scatter tails of wide cone beams in CTDI measurements. Literature shows that the method provides a consistent weighted CTDI measurement efficiency of around 75% for every beam width in a body CTDI phantom (IEC 2010, IAEA 2011). In another study, the IEC proposed methodology was found to result in $CTDI_{w,IEC3.1}$ values which underestimate the $CTDI_{w,\infty}$ by 18% and 24% in a head and body phantom respectively; the latter study being conducted on a CBCT mounted on a linear accelerator (Abuhaimed et al 2014). In our study, the $CTDI_{w,IEC3.1}$ was found to underestimate the $CTDI_{w,\infty}$ by 13% (NewTom 5G) and 16% (Promax 3D Max) (tables 4.5 and 4.6). Although the efficiency is not the same for the two systems, it remains stable per scanner. The method provides a consistent efficiency over the entire range of protocols, which is independent of system operation mode (symmetric or an offset scanning mode), rotation angle (partial or full rotation) and FOV (0.87 ± 0.02 for NewTom 5G and 0.84 ± 0.02 for Promax 3D Max). On the contrary, the average efficiency values with the IEC 3.0 approach were 0.87 ± 0.05 for NewTom 5G and 0.86 ± 0.02 for Promax 3D Max. However, the main limitation of the IEC 3.0 method was that despite the relatively constant efficiency values for beam widths ≤ 10 cm, there was an increasing efficiency trend for wider beams. Finally, the IEC 2.0 method resulted in high standard deviation values on the CTDI efficiency: 0.77 ± 0.12 for NewTom 5G and 0.74 ± 0.12 for Promax 3D Max. It shall be emphasized that the absolute value of the efficiency is not the primary factor of concern. A stable efficiency rather than an efficiency close to 1 is the major requirement for a robust CTDI metric. A better performance is a more stable average efficiency over the entire range of FOVs with a low SD rather than a higher average efficiency with a higher SD. The lower efficiency in periphery compared to that in the centre is definitely a reason why partial rotation CBCT systems (Promax 3D Max) exhibit a lower efficiency compared to the full rotation beam geometry (NewTom 5G).

An essential difference between dental CBCT scanners and other wide Cone Beam CT system, either a state-of-the-art cone beam MDCT scanner or a CBCT scanner mounted on a radiotherapy system, is the size of the beam in the axial plane, i.e. the diameter of the FOV. In dental CBCTs, protocols for a single tooth, multiple teeth and jaw imaging comprise the majority of the predefined protocols in any system. They have diameters that are considerably smaller than 16cm, which is the diameter of a head CTDI phantom. The in-plane dose distribution was evaluated using a spider-like voxel model (figure 4.5). In addition to visualizing the dose distribution, the phantom enables the comparison between the $CTDI_{w,IEC3.1}$ value and the accumulated dose over the scan volume. The highest dose areas were

always towards the center of the phantom, indicated in figures 4.7 and 4.8 by the black regions, as opposed to MDCTs where the highest dose is observed around the periphery of the phantom and the lowest dose in the center. This is because the small diameter FOVs in dental CBCT scanners restrict the beam to a small area around the center of the phantom; it is only the center of the phantom which is continuously exposed by the x-ray beam at each projection and hence receives the highest dose in a rotation. When the diameter of the FOV approaches the diameter of the phantom, the dose distribution is inverted with the highest dose being observed around the periphery and the lowest towards the center. This is the case for the 15x5, 15x12 and 18x16 cm² protocols in the NewTom 5G and for the 23x16 cm² protocol in the Promax 3D Max. The Newtom 5G presents a concentric dose distribution which is attributed to the 360° rotation of the paired x-ray tube–detector system. In the Promax 3D Max there is a large dose inhomogeneity, due in part attributed to the size of the FOVs, although the 210° rotation angle has a larger influence. The beam-on and beam off angles are obvious in figure 8: the x-ray tube makes a 210° rotation, starting from a right lateral position, crossing the phantom posteriorly and stopping in the opposite left lateral position.

The $CTDI_w$ is an estimate of the accumulated dose from a single beam profile and is calculated from a combination of $CTDI_{100}$ measurements, i.e. 1/3 of a central measurement and 2/3 of the average of 4 $CTDI_{100}$ measurements around the periphery. To test whether $CTDI_{w,IEC3.1}$ still gives an accurate estimate of the accumulated dose for wide and inhomogeneous dental CBCT beam profiles, D_{PMMA} was calculated with the spider-like phantom (tables 4.7 and 4.8). The results showed that $CTDI_{w,IEC3.1}$ underestimates the accumulated dose in the scan volume. The average ratio of $\frac{D_{PMMA,CTDI}}{D_{PMMA}}$ for all protocols was 0.94 ± 0.03 for the NewTom 5G and 0.88 ± 0.03 for the Promax 3D Max. The minimum permissible ratio to consider $CTDI_{w,IEC3.1}$ an accurate estimate of the accumulated dose in the scan plane is 0.915: given that the uncertainty in the dose calculations is 6% and according to the error propagation theory, the Coefficient of Variance of the ratio ($\frac{D_{PMMA,CTDI}}{D_{PMMA}}$) is 0.085 (or 8.5%). Therefore, the maximum permissible ratio, such that the $CTDI_{w,IEC3.1}$ approximates the accumulated dose sufficiently closely should not be lower than 0.915 The full rotation NewTom 5G scanner fulfills this requirement whereas the partial rotational Promax 3D Max provides a slightly lower ratio. It can therefore be concluded that $CTDI_{w,IEC3.1}$ approximates accumulated dose sufficiently closely for full rotation systems, yet care should be taken when using this approximation for partial rotation systems. It must be noted however, that this underestimation concerns the comparison of two phantom-based dose values; one indirectly assessed via CTDI and the other directly via MC simulations in the PMMA volume. However, if CTDI had to be used as an estimate of patient dose, it would provide an overestimated dose value. This is due to the fact that the concept of CTDI was introduced based on the theoretical proof that the scatter tails of a single dose profile in a single axial acquisition compensate for the contribution of the adjacent slices to a specific slice in a multi-rotational acquisition (either axial or helical). In other words the scatter tails when included in the calculation of CTDI bring the dose in the scan volume to the Multi Scan Average Dose level of a helical or axial multi scan acquisition (Shope et al 1981, IAEA 2011). In dental CBCT scanners there is no translation, and hence, the $CTDI_{w,IEC3.1}$ value offers an overrated value of the dose. In CBCTs there is only one rotation without translation. The integrated dose (including the scatter tails) is divided by the beam width to provide the CTDI. This means that the scatter tails are inherently included in the calculated dose to the scanned volume. This extra dose due to scatter would bring the dose level to the MSAD if there were multiple rotations. However, since there are no multiple rotations but just one rotation without translation, the added scatter overestimates the dose to the scanned volume.

However, in a single, no translational acquisition, and especially in head and neck imaging, it is essential to know the effect of the scatter tails as they correspond to the extra dose in critical organs like the thyroid. More importantly, It should be pointed out that CTDI-based metrics are neither intended for nor should be used as an indication of patient dose (McNitt-Gray 2002, McCollough et al 2011). CTDI is a well-defined procedure to measure the x-ray tube output, to compare the output of different protocols and to optimize protocols. In the context of a Quality Assurance programme, the CTDI phantom is positioned with its axis along the center of rotation, as was the case in this study.

The positioning of all the phantoms in the center of the beam rather than in the axis of rotation, may not resemble a clinical case, where the head of a patient may be off center positioned, especially in cases of small FOV-protocols for single tooth or teeth imaging. However, as stated in the literature, the CTDI is a dose index of the x-ray tube output and should not be related to patient dose (McCollough et al 2011). Positioning the CTDI phantom off-center to mimic a clinical situation, deviates from established methodology and is time consuming, given the numerous different positions of the same FOV in the head to image different clinical volumes. In this study, we investigated the use of CTDI as an output dose index. In this context, all IEC and IAEA suggested CTDI versions were checked against infinite CTDI to investigate which methodology provided a robust metric, i.e. a constant CTDI efficiency over the entire range of the clinically available FOVs.

The investigated CTDI IEC 3.1 approach has been shown to be relevant for dental CBCT scanners. However, the application of the method could prove cumbersome in daily routine Quality Assurance / Quality Control measurements. As most current systems have a vertical (panoramic) orientation, the positioning of the phantoms and dosemeters at the center of rotation is practically difficult. Even $CTDI_{free-in-air}$ measurements are difficult as displacement of the IC in well - defined increments is required. On many systems, repeated measurements are time consuming while another difficulty arises from the requirement of the IEC 3.1 approach for reference 2cm beam widths: in most dental CBCT scanners, it is not possible to manually collimate the beam width to 2 cm in order to create reference beams. Furthermore, compared to MDCTs where the axial FOV is fixed and thus a single reference beam is adequate for every nominal collimation-beam thickness, in CBCTs, the reference beam should have the same diameter with each nominal FOV. It follows that this generates a large series of measurements. Notwithstanding these difficulties, the use of $CTDI_{w,IEC3.1}$ can be recommended, given the stability of this metric. We suggest that manufacturers display the $CTDI_{w,IEC3.1}$ and provide practical help during acceptance tests of CBCT modalities by creating reference beams and providing all the necessary information to fully understand the dose distributions.

The conversion factor equations presented in equations 4.6-4.8 can be immediately used and applied from the manufacturers and from any user. They provide a straightforward and immediate way to assess organ dose, E and LAR once CTDIw,IEC3.1 is displayed on the monitor of the scanner.

4.5 Conclusions

The current study has investigated the applicability of the IEC 60601-2-44-(Amendment 1 of version 3, IEC 3.1), and the IAEA health series report N.5 method for wide cone beam dosimetry, to dental CBCT scanners. MC methods were employed as a means of overcoming practical limitations such as the use of infinitely long phantoms and the absence of small 2cm thick reference x-ray beams. The methodology was tested on two dental CBCT systems with different geometries and acquisition properties. The results suggest that the new approach is relevant and feasible for such different

systems. CTDI comparisons between dental CBCTs and MDCTs should be based on the new method, as this provides a robust estimate of $CTDI_{w,\infty}$ which is an index of the full dose effects of a wide beam in a phantom. The in-plane dose distributions can be notably different from those in MDCT due to partial rotations and/or small axial FOVs.

CHAPTER 5

General Discussion and Conclusions

Imaging is the most important diagnostic tool in dentistry with more than a quarter of all radiographs in Europe being accomplished by dentists. While 2D imaging has been taken up since the discovery of x-rays, the advent of SSCTs in 1970s brought initially a new perspective in dental cross sectional imaging. Since then, around 2000, smaller-in-size and lower-in-cost dental CBCT scanners have been brought into the market. Initially as an emerging technology, nowadays dental CBCTs play a key role in many fields of dentistry and maxillofacial radiology. However, their widespread use has raised radiation protection concerns. CBCTs have not only replaced higher dose MDCT modalities, but also 2D panoramic and intraoral scans which are among the lowest dose techniques in radiography. Besides, the evolution of CBCT technology is not as fast as in MDCT imaging: recent advancements in MDCTs include dose reduction techniques (TCM, adaptive collimation), new (iterative) reconstruction methods and the development of dual energy and spectral MDCTs. All these new features reduce dose or increase information content. It can therefore be questioned whether CBCTs are a (relatively) low dose imaging solution (Stratis et al 2017a). Radiation protection concerns become even more important due to the increasing use of CBCTs in paediatric patients. Being more radiosensitive and with a longer life expectancy compared to adults, paediatric dental CBCT acquisitions are not anymore a matter to disregard.

Dosimetry in paediatric CBCT imaging is a complex task. First, it is the unavailability of dosimetric tools. Traditional methods with anthropomorphic phantoms and TLDs have a limited value; it is not only the unavailability of phantoms that cover the entire paediatric age range but also the fact that the available ones do not provide detailed organ segmentation in the head and neck region. Besides, CBCTs exhibit large in-plane and longitudinal dose inhomogeneity due to their complex acquisition geometry which in turn requires dose assessment in the entire organ and not in restricted organ–specific locations as TLDs offer. These two reasons also explain the large variability in reported dental CBCT doses.

The objective of this study was to provide a roadmap towards radiation dose and risk assessment in paediatric dental CBCT imaging. The project focused on the development of a flexible MC dose platform that can be easily adjusted to any dental CBCT scanner and aims to provide an extensive dosimetric assessment for the most frequent CBCT exams with the use of an in-house built family of paediatric head and neck voxel models.

Chapter 1 deals with the development of the dosimetric MC framework. It is based on an existing hybrid tool developed in our group (Zhang 2011, 2013a) and employs the EGSnrc simulation code. The motivation for modifying the tool was mainly to obviate limitations in acquiring data from vendors which are considered proprietary and hence, they are difficult to obtain. More specifically, to explicitly simulate the x-ray tube in a part by part basis, specific details such as the orientation, the composition and the dimensions of the anode, the composition and the shape of the added filtration, and the design of the tube housing which influences the inherent filtration are required. The modification was based on a methodology proposed by Turner et al (2009) for MDCT simulation studies. Instead of simulating the tube and storing the x-ray output in phase-space files which are subsequently directed to voxel models for dose assessment, the current version of the MC tool is based on real measurements performed with an ion chamber. These measurements aim to determine the energy spectrum at the operating x-ray tube voltage (kV), to specify the total filtration, and, are employed to a scanner specific input file to the code.

The MC framework was customized for five different CBCT scanners, each presenting unique features. Promax 3D Max (Planmeca, FI) employs partial 210° rotations and has a combined Al / Cu added filtration. Accuitomo 170 (Morita JP) is the only non-pulsed exposure scanner (among the ones in the study) and employs a bowtie filter. NewTom VGi-evo (QR srl, IT) employs a TCM dose reduction technique while NewTom 5G (QR srl, IT) presents a MDCT orientation (patient in a supine position laying on a table). Finally, CS 9300 (Carestream USA) employs a bowtie Cu/Al filtration and partial rotations of 200°. After calibrating the framework for each scanner and protocol to enable conversion of simulated to absolute dose values, we validated it against dose measurements in a homogeneous

water phantom obtained with an IC and against TLD measured doses in a non-homogeneous paediatric anthropomorphic model (ATOM 5 years old, CIRS, USA). The validation results proved that the framework is reliable for accurate dose assessment calculations (6% maximum percent difference between measured and simulated dose values). With the use of the MC framework we investigated the influence of several CBCT technical specifications on patient dose. In a first study, we showed that the use of Cu filtration results in dose reductions to skin and to those organs which are inside the primary radiation field. This is mainly the case for salivary glands and oral mucosa (the two highest irradiated organs in dental CBCT imaging). On the other hand, for those organs which are exposed only to scatter, such as brain and thyroid for small and medium FOV imaging), the dose can even increase as Cu makes the energy spectrum stronger which in turn increases the amount of scatter. In a second study, we concluded that bowtie filters offer an average 15% organ dose reduction compared to flat filters of thickness equal to the central bowtie one, with the highest dose reduction being for peripheral organs and for the skin. Finally, we investigated the influence of TCM. The implementation of TCM in MC frameworks is a complicated task as it requires projection data that is usually not available in rotational TCM systems. For MDCT systems, the simulation of rotational TCM is mainly accomplished by downsampling the longitudinal TCM on an image by image basis. In CBCTs, such a technique is not feasible since there is no patient translation and the acquisition is carried out in a single rotation. Our study showed that in case projection data is not available to deduce the modulation curve, organ dose and risk estimation is still reliable with a tolerance of about 10%. This is mainly due to the fact that the anatomy and the shape of the head is such that it does not induce strong current modulations. Therefore, dose assessment is reliable when the average mAs / rotation is used. On the other hand, when TCM is compared to fixed current acquisitions, it was shown to provide high organ dose reductions (about 40% and 20% in standard and high resolution protocols respectively) to achieve the same level of image noise. This conclusion was drawn for a preprogrammed TCM technique, i.e. 'Safebeam' employed in the two NewTom scanners. However, this scheme is not a patient-specific and attenuation-based one since it takes into account a software-employed mathematical formula. We conducted a study in which we compared such a preprogrammed modulation scheme to a fully attenuation-based one. We showed that the attenuation-based one is capable of achieving higher dose reductions, especially when the modulation strength increases. This is however difficult to achieve given the low generator capacities of current CBCT scanners.

The MC framework, as developed from a basic toolbox to a more dedicated framework, is now easily adjustable to any scanner and can be easily modified to investigate new system specifications. Scanner details are managed through a scanner-specific input file where the technical and geometric details are controlled. Typical further applications could include the design or testing of any other geometry (rotational angle, dose in emergency beam-off cases where acquisition is stopped due to patient motion, new filters, TCM etc).

Chapter 2 presents the development of a software database of head and neck paediatric voxel models. All the models have been segmented in detail for head and neck dose assessment studies. Each model represents a full head and consists of twenty two organs, all radiosensitive ones included, apart from RBM and lymph nodes. This is due to the resolution limits of the existing 3D scanners: it is not possible to accurately segment RBM and lymph nodes at present. However, RBM dose calculation can be carried out following the 3 Factor approach, a method which is based on the energy dependent assessment of the attenuation ratio of RBM to the segmented skeletal mixture, the RBM mass fraction in the skeletal mixture and an energy enhancement factor to compensate for the different absorption properties of the high dense skeleton and the low dense RBM (Caracappa et al 2009, Kramer et al 1982). For the dose to lymph nodes, a mathematical formula weighting dose to substitute organs can be used (Tapiovaara and Siiskonen 2008).

The models were created from MDCT images rather than from CBCT datasets. This is due to the fact that accurate dose assessment in CBCT imaging requires dose mapping in the complete head: while the reconstructed CBCT image datasets display only the truncated FOV region, the entire head is though exposed to radiation during rotation. The fact that the dental CBCT dataset cannot be used to reconstruct the entire head made our project more challenging: the available number of pediatric scans of head & neck was very limited. The voxel data base that was created during our project is considered to be sufficiently complete and is now available for more applications. It includes seventeen models, both males and females from 2 months to 14 years old.

For personalized dosimetry, a voxel model as close as possible to the patient under study should be used. It is not that difficult to achieve this for adult heads. However, children are not adults. There is a steep growth in anatomical development in paediatric ages. As the size of each individual organ and the size of the head play a primary role in the dose received by a fixed FOV exposure, it is of great importance to have age-specific voxel models for carrying out dosimetric tasks.

Our hypothesis was that the ICRP mass (and other) data (ICRP 89, 2002) are gold standard and representative for the population. Therefore, each voxel model has been compared to and adjusted to the reference age-specific mass values. This is an alternative to what is often used in other domains (example: fMRI data processing), where real patient data are mapped to an anatomical atlas.

This action to adjust organ masses to reference values was further inspired by the ICRP 110 publication on the creation of the two reference adult (male/female) models which are widely used for Monte Carlo dose calculations. The models are widely accepted to represent the 'average' male and female person.

The fact that our models are based on CT datasets triggered a study to propose a correction method for the head orientation. The head is inclined to the front due to the head-support-feature of the CT scanner. As voxel models preserve the geometric characteristics of the initial CT scanning geometry, the head orientation has to be corrected, i.e. Frankfort plane needs to get horizontal, as this is the proper geometry in a dental CBCT exposure. A detailed, protocol and model-specific method for applying rotational and translational corrections was also proposed. A dose study revealed that such corrections are required for accurate dose assessment since a mere application of a CT-based model (or MRI) for dental CBCT MC studies can lead to large (up to 45% for the investigated protocols) organ dose miscalculated values. Finally, a study was carried out to show the implementation of voxel models in a MC framework. The study compared organ doses between males and females in three different age categories for a common CBCT exam, i.e. the cleft protocol. The study revealed that there are not considerable organ dose differences between males and females of the same age. Apart from some exceptional cases, most organ dose differences were within 10%.

Although designed for dedicated dental CBCT MC studies, the presented database can be used for dose assessment in the head and neck region for any radiologic, nuclear medicine and radiotherapy modality. Each model is provided in a file which includes the entire stack of the segmented tiff images, an excel file of the organ IDs and their elemental composition. A matlab code creates the proper text file for the EGS code, yet it can be easily adjusted to the required format of other MC family codes. Finally, a Matlab code which enables the rotation correction is also provided.

Chapter 3 is the core chapter of the project. It presents the results of an extensive simulation study for the most common CBCT exams, carried out with twelve models, both males and females, covering the entire paediatric age range (5 – 14 years old), in all five scanners for which the MC platform was customized, calibrated and validated. The results are presented in protocol-specific tables which include the logarithmic fit data of organ doses, Effective dose and LAR incidence (all normalized to mAs) as a function of age, for every scanner. The results show a dose decreasing pattern with age. This is somewhat expected given that a fixed in size radiation field can entirely expose a small organ, yet as the size increases with age, the field may partially irradiate it as the age of the patient increases. The best fit that was constantly providing a coefficient of determination in the dose response relationship

with age higher than 0.9 was the logarithmic (table 3.5 – 3.17). The investigated clinical cases included SFOV tooth imaging protocols (Central Upper Incisors (CUI), Central Lower Incisors (CLI), Premolar Upper (PU) and lower (PL)), medium MFOV protocols (Upper and Lower Jaw imaging (ULJ), Lower Jaw (LJ), cleft palate imaging, unilateral (UT) and bilateral (BT) temporal bone) and large LFOV protocols (sinus, dentomaxillofacial complex, face and skull imaging). The highest doses were observed for the youngest patients and the highest resolution operation modes.

However, high resolution operation modes are not frequently applied in dental CBCT imaging. In most dental CBCT scanners the x-ray tube load (mAs) and the voltage (kV) are automatically adjusted when the voxel size, which defines the resolution level of the dataset, is selected. The reconstruction voxel size primarily depends on the dimensions of the FPD pixel size. In most cases these fine pixel elements have very small dimensions which allow a relatively large reconstruction voxel size to be selected and provide sufficient resolution for the diagnostic task. A large voxel size – low resolution mode operates with low mAs settings and, as a consequence, doses are relatively low for a 3D imaging modality. In some cases increased noise may be encountered, yet diagnostic tasks in dental CBCT scanners do not require soft tissue differentiation (low contrast) that could be influence by image noise.

Nevertheless, in cases where resolution has to be further improved compared to standard CBCT imaging, organ dose and radiation risk may increase significantly. The highest doses among all cases have been encountered in a high resolution mode of a skull protocol in Accuitomo 170. This mode operates with 5 mA and 30.8 sec continuous exposure (154 mAs) in a full rotational acquisition. In that case the effective dose is as high as 0.53 mSv, while the LAR incidence for males is 15 cases / 100,000 persons and for females is 25 cases / 100,000 persons. The dose to thyroid is close to 2 mGy while there is an almost 10.5 mGy dose to the lenses of the eyes. Even under these extreme circumstances, the dose to the eye lenses is well below the radiation induced cataract limit (500 mGy). In such high dose cases, even if they are rare, a thyroid collar is recommended for younger patients, as the absence of manual collimation can partially bring the thyroid inside the primary field. Even when this is not the case, a thyroid collar offers protection against scatter radiation out of the mouth cavity towards the thyroid region.

A comparison with background cancer incidence rate data is necessary to understand the magnitude of the risk from dental CBCT imaging. According to Cancer Research UK (https://www.cancerresearchuk.org/home), it is estimated that 1 child per 500 in Great Britain will be diagnosed with cancer by the age of 14. This is about 200 cases/100,000 persons, which means that a high resolution full-face CBCT exposure adds about 10% to the total background risk. In another publication, Isaevska et al (2017) reported a total cancer incidence rate of 157 per million persons per year for ages up to 14 years old while Ward (Ward et al 2014) published an annual incidence rate of 178 cases per million for boys and 160 per million for girls from birth to 14 years old. These figures correspond to accumulated values of 157, 178 and 160 cases / 100000 over a period of 10 years which clarifies that a high resolution CBCT exposure may add considerably to the background risk. However, this is an extreme case and most protocols operate in operation modes which provide LAR values less than 5 cases / 100,000 (1-2 cases/ 100,000 for small FOVs, 2-5 for medium and large FOVs for males and females).

Chapter 4 addresses the need to have radiation dose metrics that quantify the radiation output of a scanner and provide rough dose estimations for dose monitoring purposes. We investigated the relevance of a recently proposed (by IEC and IAEA) version of CTDI for wide cone beam CT dosimetry. We have proven this so-called CTDIw,IEC3.1 metric to be a robust dose assessment approach which manages to account for the full dose effects of wide beams and their wide scatter tails in CBCTs, providing a constant CTDI measuring efficiency, i.e. it underestimates the ideal CTDIw,∞ by a constant amount over the entire range of z-collimations. We investigated the applicability of the methodology in two scanners which exhibit most of the special technical and geometric specifications of CBCT scanners. NewTom 5G operates with a preprogrammed TCM system, uses offset scanning geometry

for most FOVs, and employs full rotational acquisitions in a unique, for CBCTs, orientation which resembles a MDCT geometry rather than a CBCT one. On the other hand, Promax 3D Max has a special Cu/Al flat filter mounted inside the x-ray tube, performs partial rotations of 210° (apart from the largest skull FOV) with a symmetrical axial geometry. The study concluded that the investigated CTDIw,IEC3.1 approach results in a constant CTDI efficiencyfor both CBCT scanners. It could now be adopted by CBCT vendors for dose monitoring purposes. However, it shall be mentioned that CTDIw,IEC3.1 is just a dose metric of the radiation output of the scanner and must not be mistakenly interpreted as patient dose. In MDCT, this happens sometimes, though. In CBCT, approximating locally absorbed dose by the CTDI is even more problematic. Dental CBCTs carry out a full exam in a single partial, half or full rotation. Therefore, there is an intrinsic, formalism-related, misconception; CTDI was established in CT dosimetry due to the fact that the scatter tails of a single dose profile can equally contribute to the dose at each axial slice with the extra dose of the adjacent slices in a multirotational acquisition. This means that the scatter tails bring the dose magnitude of a single axial dose profile to the Multi Scan Average Dose level which is the average dose in the scanning region of a CT exam. This is never the case in CBCTs where there is just a single rotation acquisition. Another issue which makes CTDI problematic in CBCT dosimetry is that while CTDI phantoms are always positioned with their central axis along the centre of rotation, in clinical CBCT cases, and especially in small and medium FOV imaging, the head of the patient is always off-center positioned. Therefore the measuring geometry of CTDI does not mimic a real clinical scenario in CBCT.

However, these issues would be a matter of concern if CTDI was used as a patient dose index rather than a scanner output index. The fact that CTDI produces a constant measuring efficiency provides a robust way to quantify the output and can be efficiently used for comparing doses between protocols, to quantify dose differences between operation modes and to optimize exposures.

This project provides the tools to carry out accurate, scanner- and patient-specific dose simulations for every clinical task in dentomaxillofacial CBCT imaging: a MC framework which is easily customized towards different models and already calibrated and validated for different systems and a database of paediatric head and neck voxel models. The results presented in the tables of this manuscript allow accurate organ dose and risk estimations: the user just needs to apply the scanner and protocol specific normalized dose value for a specific age at exposure (tables in the appendix of chapter 3) and multiply with the mAs of the exposure to get the absolute dose or risk value. It is also straightforward to estimate organ doses and the radiation risk from CTDI by making use of the conversion factors in chapter 4.

The present study is an extensive dose assessment work dedicated to dental CBCT imaging. The acquired knowledge and the tools that have been developed during this project can be employed in future applications, not only in CBCT imaging but in a wide range of modalities in diagnostic radiology. The developed MC framework can cope with the rotation of the paired x-ray tube – detector system around the patient and deal with multiple projections involved in a CBCT exposure. Besides, it can be easily adjusted to work in conjunction with potential patient translation which makes it ideal for MDCT simulation studies. It can be also tuned to work for a single projection which is the case in simple radiography acquisitions. It is also feasible to extend its use in interventional radiology and cardiology systems as the basic features of such systems are similar with CBCTs, i.e. x-ray exposures from different projections. As long as detailed technical and x-ray acquisition parameters at each projection are provided in a radiation dose structure report (kV, mA, pulse length, field size, filtration), the framework can be adjusted for interventional MC dose calculations. In the same way, the MC framework can be customized for advanced x-ray modalities like dedicated CBCTs for orthopedic applications, breast CTs, and robotic advanced x-ray systems. The establishment of a toolbox that enables calculations of these modalities requiring minimum user input is a future project based on the current work.

The current work is also considered a detailed guide for optimizing exposures in CBCT systems. However, optimization of exposures requires image quality (IQ) assessment which was not the scope

of this study. Future work involves image quality measurements with a dedicated phantom that was developed during a previous doctoral project in our department (Pauwels et al 2012b). While IQ assessment with such a phantom is objective, subjective assessment can also be performed via our framework. The initial form of the framework as originally developed by Zhang et al (2013), before modifying it to make it more flexible and to overcome the difficulties regarding vendor proprietary data, was capable of simulating the entire imaging CBCT chain from x-ray production to image formation. Future work includes relinking the imaging chain to the modified version of the MC framework to enable image production with simulation techniques. Such a tool will allow the optimization of exposures to be performed in a comprehensive way, will enable intermodality dose and IQ comparison, will facilitate the monitoring of exposures and the possibility to assess the performance of a system before employed in a clinical environment.

BIBLIOGRAPHY

AAPM Report No. 111. Comprehensive Methodology for the Evaluation of Radiation Dose in X-Ray Computed Tomography. American Association of Physicists in Medicine, College Park, MD: One Physics Ellipse, 2010

AAPM 2015 http://www.aapm.org/pubs/CTProtocols/documents/PediatricRoutineHeadCT.pdf

AAPM 2016 http://www.aapm.org/pubs/CTProtocols/documents/AdultRoutineHeadCT.pdf

Abuhaimed A, Martin CJ, Sankaralingam M, Gentle DJ and Mercury M 2014 An assessment of the efficiency of methods for measurement of the computed tomography dose index(CTDI) for cone beam (CBCT) dosimetry by Monte Carlo simulation Phys Med Biol 59 6307-6326

Agostinelli S et al 2003 GEANT4—a simulation toolkit Nucl. Instrum. Methods Phys. Res. A 506:250–303

Al Najjar A, Colosi D, Dauer LT, Prins R, Patchell G, Branets I, et al. 2013 Comparison of adult and child equivalent doses from 2 dental cone-beam computed tomography units. Am J Orthod Dentofacial Orthop 143:784–92.

American Dental Association Council on Scientific Affairs (2012) The use of cone-beam tomography in dentistry. An advisory statement from the American Dental Association Council on Scientific Affairs. J Am Dent Assoc 143:899–902

Andreo P 1991 Monte Carlo techniques in medical radiation physics Phys. Med. Biol. 36:861-920

Araki K, Patil S, Endo A and Okano T 2013 Dose indices in dental cone beam CT and correlation with dose-area product Dentomaxillofac Rad 42 20120362

Boone JM 2007 The trouble with CTDI 100 Med Phys 34 1364-1371

Bozkurt A, Chao TC and Xu XG 2000 Fluence-to-dose conversion coefficients from monoenergetic neutron beams below 20 MeV based on the VIP-Man anatomical model. Phys. Med. Biol. 45: 3059-79

Brenner DJ 2008 Effective dose: a flawed concept that could and should be replaced Br J Radiol 81 (967) 521-3

Brown FB (ed) 2003 MCNP—A general Monte Carlo N-particle transport code (version 5) Report LA UR-03-1987 (Los Alamos National Laboratory, Los Alamos, NM)

Buzug TM 2008 Computed Tomography-From Photon Statistics to Modern Cone-Beam CT. Springer-Verlag, Berlin Heidelberg, Germany

Calabrese EJ and O'Connor MK 2014 Estimating Risk of Low Radiation Doses – A Critical Review of the BEIR VII Report and its Use of the Linear No-Threshold (LNT) Hypothesis Radiat Res 182 463-474

Caon M, Bibbo G and Pattison J. 1999 An EGS4-ready tomographic computational model of a 14-year-old female torso for calculating organ doses from CT examinations. Phys. Med. Biol. 44 2213–25

Caracappa PF, Chao ETC, Xu G 2009 A study of predicted bone marrow distribution on calculated marrow dose from external radiation exposures using two sets of image data for the same individual Health Phys 96 (6) 661-674

Chen J 2004 Mathematical models of the embryo and fetus for use in radiological protection Health Phys. 86 285–95

Christ A, Kainz W, Hahn E, Honegger K, Zefferer M, Neufeld E et al 2010 The Virtual Family—development of surface-based anatomical models of two adults and two children for dosimetric simulations. Phys. Med. Biol. 55: N23–38

Cristy M and Eckerman K F 1987 Specific absorbed fractions of energy at various ages from internal photon sources I: methods Oak Ridge National Laboratory Report ORNL/TM-8381/V1 (Oak Ridge, TN: Oak Ridge National Laboratory) http://ordose.ornl.gov/documents/tm8381V1.pdf

De Vos W., Casselman J., Swennen G.R.J 2009 Cone beam computerized tomography (CBCT) imaging of the oral and maxillofacial region: A systematic review of the literature Int. J. Oral Maxillofac. Surg. 38 609-625

Dixon RL 2003 A new look at CT dose measurement: Beyond CTDI Med Phys 30, 1272-1280

Dixon RL 2006 Reconstructing CT dosimetry-A realistic strategy for the future Requiem for the pencil chamber Med Phys 33 3973-3976
Eckhardt R 1987 Stan Ulam John Van Neumann and the Monte Carlo Method Los Alamos Science Special Issue 131-141
Edwards AA and Lloyd D C 1998 J. Radiol. Prot. 18 175
Endo M, Mori S, Tsunoo T, Miyazaki H 2006 Magnitude and effects of x-ray scatter in a 256-slice CT scanner Med Phys 33 (9): 3359-68
European Commission 2004 European guidelines on radiation protection in dental radiology - The safe use of radiographs in dental practice, Luxembourg, Publications office of the European Union
European Commission 2012 Cone Beam CT for Dental and Maxillofacial Radiology: Evidence Based Guidelines, Radiation Protection Publication 172.
European Commission 2014 Radiation Protection No180: Medical Radiation Exposure of the European Population Part ½, Luxembourg, Publications office of the European Union
EzEldeen M, Stratis A, Coucke W, Codari M and Jacobs R 2017 As Low Dose As Sufficient Quality: Optimization of Cone-Beam Computed Tomography Scanning Protocol for Tooth Autotransplantation Planning and Follow-up in Children J Endod 43 (2) 210-7
Ferrari P, Gualdrini G. 2005 An improved MCNP version of the NORMAN voxel phantom for dosimetry studies. Phys. Med. Biol. 50: 4299–4316.
Fisher H L J and Snyder W S 1966 Variation of dose delivered by 137Cs as a function of body size from infancy to adulthood Health Physics Division Annual Progress Report for Period Ending July 31, 1966 Report ORNL-4007 (Oak Ridge, TN: Oak Ridge National Laboratory) 221–28
Fisher H L J and Snyder W S 1967 Distribution of dose in the body from a source of gamma rays distributed uniformly in an organ Health Physics Division Annual Progress Report for Period Ending July 31, 1967 Report ORNL-4168 (Oak Ridge, TN: Oak Ridge National Laboratory)
Fishman GS 1995 Monte Carlo: concepts, algorithms, and applications. (New York: Springer)
Flohr T, Stierstorfer K, Bruder H, Simon J, Schaller S 2002a New technical developments in multislice CT, part 1: Approaching isotropic resolution with sub-millimeter 16-slice scanning. Röfo Fortschr Geb Rontgenstr Neuen Bildgeb Verfahr 174 839-845
Flohr T, Bruder H, Stierstorfer K, Simon J, Schaller S, Ohnesorge B 2002b New technical developments in multislice CT, part 2: sub-millimeter 16-slice scanning and increased gantry rotation speed for cardiac imaging. Röfo Fortschr Geb Rontgenstr Neuen Bildgeb Verfahr 174 1022-1027
Geleijns J, Salvado Artells M, de Bruin PW, Mather R, Muramatsu Y and McNitt-Gray MF 2009 Computed Tomography dose assessment for a 160mm wide, 320 detector row, cone beam CT scanner Phys Med Biol 54, 3141-3159
Gies M, Kalender WA, Wolf H, Suess C. 1999 Dose reduction in CT by anatomically adapted tube current modulation. I. Simulation studies. Med Phys 26:2235-47
Gijbels F, Sanderink G, Wyatt J, Van Dam J, Nowak B and Jacobs R 2004 Radiation doses of indirect and direct digital cephalometric radiography Br Dent J 197 149-152
Goldman LW. Principles of CT and CT technology 2007 J. Nucl. Med. Technol. 35 (3) 115–128
Gosselin MC, Neufeld E, Moser H, Huber E, Farcito S, Gerber L et al. 2014 Development of a new generation of high-resolution anatomical models for medical device evaluation: the virtual population 3.0. Phys. Med. Biol. 59 5287–303
Granlund C, Thilander-Klang A, Ylhan B, Lofthag-Hansen S, Ekestubbe A. 2016 Absorbed organ and effective doses from digital intra-oral and panoramic radiography applying the ICRP 103 recommendations for effective dose estimations. Br J Radiol 89: 20151052
Hart D and Wall BF 2002 Radiation Exposure of the UK population from medical and dental x-ray exposures. Chilton, NRPB-W4
Hart D, Hillier MC and Wall BF 2002 Doses to patients from medical x-ray examinations in the UK – 2000 Review. Chilton, NRPB-W14

Hart D, Wall BF, Hillier MC, Shrimpton PC 2010 Frequency and Collective dose form medical and dental x-ray examinations in the UK, 2008. HPA-CRCE-012, Chilton, UK, Health Protection Agency
Haycock GB, Schwartz GJ, Wisotsky DH 1978 Geometric method for measuring body surface area: A height-weight formula validated in infants, children, and adults. J Pediatr 93 (1): 62-66
Hirata A, Ito N, Fujiwara O, Nagaoka T and Watanabe S 2008 Conservative estimation of whole-bodyaveraged SARs in infants with a homogeneous and simple-shaped phantom in the GHz region Phys. Med. Biol. 53 7215–23
Holroyd JR and Gulson AD 2009 The Radiation Protection Implications of the Use of Cone Beam Computed Tomography (CBCT) in Dentistry – What You Need To Know. Chilton, UK, Health Protection Agency
Horner K, Islam M, Flygare L, Tsiklakis K and Whaites E 2009 Basic principles for use of dental cone beam computed tomography: consensus guidelines of the European Academy of Dental and Maxillofacial Radiology Dentomaxillofac Radiol 38 187-195
HPA 2010 Guidance on the safe use of Dental Cone Beam CT (Computed Tomography) Equipment HPA-CRCE-010, Chilton, Health Protection Agency
Hu H 1999 Multi-slice helical CT: Scan and reconstruction Med Phys 26 5-18
International Atomic Energy Agency 2011, "Status of computed tomography dosimetry for wide cone beam scanners," IAEA Human Health Reports No. 5
International Electrotechnical Commission 2010, Medical Electrical Equipment - Part 2-44 Edition 3, Amendment 1: Particular requirements for basic safety and essential performance of X-ray equipment for computed tomography, IEC-60601-2-44-Edition 3, Amendment 1; 62B/804/CD, Committee Draft (CD), IEC Geneva
ICRP, 1975 Report of the Task Group on Reference Man ICRP Publication 23 (Oxford, UK: Pergamon)
ICRP, 1977. Recommendations of the ICRP. ICRP Publication 26. Ann. ICRP 1 (3).
ICRP, 1991. 1990 Recommendations of the International Commission on Radiological Protection. ICRP Publication 60. Ann. ICRP 21 (1-3).
ICRP, 2002. Basic Anatomical and Physiological Data for Use in Radiological Protection Reference Values. ICRP Publication 89. Ann. ICRP 32 (3-4).
ICRP, 2003. Relative Biological Effectiveness (RBE), Quality Factor (Q), and Radiation Weighting Factor (w_R). ICRP Publication 92. Ann. ICRP 33 (4).
ICRP, 2007. The 2007 Recommendations of the International Commission on Radiological Protection. ICRP Publication 103. Ann. ICRP 37 (2-4).
ICRP, 2009. Adult Reference Computational Phantoms. ICRP Publication 110. Ann. ICRP 39 (2)
ICRP, 2012 ICRP Statement on Tissue Reactions / Early and Late Effects of Radiation in Normal Tissues and Organs – Threshold Doses for Tissue Reactions in a Radiation Protection Context. ICRP Publication 118. Ann. ICRP 41(1/2).
ICRP, 2015. Radiological Protection in Cone Beam Computed Tomography (CBCT). ICRP Publication 129. Ann. ICRP 44(1)
Isaevska E, Manasievska M, Alessi D, Mosso ML, Magnani C, Sacerdote C et al 2017 Cancer incidence rates and trends among children and adolescents in Piedmont, 1967-2011 Plos One 12(7): e0181805
Jacobs, R. 2011 Dental cone beam CT and its justified use in oral health care. Journal of the Belgian Society of Radiology. 94(5), pp.254–265. DOI:http://doi.org/10.5334/jbr-btr.662
Jacobs R and Quirynen M 2014 Dental cone beam computed tomography: justification for use in oral implant placement Periodontology 2000 66 203-213
Kalender WA 2005 CT: the unexpected evolution of an imaging modality Eur Radiol Suppl 15 (Suppl 4), D21-D24
Kawrakow I, Mainegra - Hing E, Rogers DWO, Tessier F and Walters BRB 2009 The EGSnrc Code System: Monte Carlo Simulation of Electron and Photon Transport NRCC Report PIRS-701, NRC Canada, http://irs.inms.nrc.ca/software/egsnrc/documentation.html

Keat N. Report 05016 2005 CT scanner automatic exposure control systems. ImPACT; London, England: [Accessed March 2014]. 2005. http://www.impactscan.org/reports/Report05016.htm.
Khatonabadi M, Zhang D, Mathieu K, Kim JH, Lu P, Cody D et al. 2012 A comparison of methods to estimate organ doses in CT when utilizing approximations to the tube current modulation function. Med Phys 39(8):5212–5228
Kiljunen T, Kaasalainen T, Suomalainen A, Kortesniemi M. 2015 Dental cone beam CT: A review. Phys Med 31 844-860
Kim J H, Kim C S and Whang J H 2010a Assessment of radiation dose for surrounding organs and persons approaching implanted patients upon brachytherapy of prostate cancer with Iridium-192 Radiat. Prot. Dosim. 141 283–8
Kim S, Song H, Movsas B, Chetty IJ 2012 Characteristics of x-ray beams in two commercial multidetector computed tomography simulators: Monte Carlo simulations. Med Phys 39 (1): 320-9
Koedooder K, Venema HW 1986 Filter materials for dose reduction in screen-film radiography. Phys Med Biol. 31(6):585–600
Kramer R, Zankl M, Williams G and Drexler G 1982 The calculation of dose from external photon exposures using reference human phantoms and Monte Carlo methods: Part I. The male (ADAM) and female (EVA) adult mathematical phantoms GSF-Report S-885 (Neuherberg: Institut fuer Strahlenschutz, GSF-Forschungszentrum fuer Umwelt und Gesundheit)
Langland OE, Langlais RP 1985 Early pioneers of oral and maxillofacial radiology. Oral Surg Oral Med Oral Pathol Oral Radiol Endod 80 496–511.
Lee C and Bolch WE. 2003 Construction of a tomographic computational model of a 9-mo-old and its Monte Carlo calculation time comparison between the MCNP4C and MCNPX codes. Health Phys. 84 (Suppl), S259
Lee C, Williams JL, Lee C and Bolch WE. 2005 The UF series of tomographic computational phantoms for paediatric patients. Med.Phys. 32 (12): 3537-3548
Lee C, Lee C, Shah AP and Bolch WE 2006 An assessment of bone marrow and bone endosteum dosimetry methods for photon sources. Phys. Med. Biol. 51 5391-5407
Lee C, Han EY, Bolch WE. 2007 Consideration of the ICRP 2006 revised tissue weighting factors on age-dependent values of the effective dose for external photons. Phys. Med. Biol. 52 41–58
Lee GS, Kim JS, Seo YS, Kim JD 2013 Effective dose from direct and indirect digital panoramic units Imaging Sci Dent 43: 77-84)
Li X, Samei E, Segars WP, Sturgeon GM, Colsher JG, and Frush DP 2011 Patient-specific radiation dose and cancer risk for pediatric chest ct. Radiology 259(3):862–874
Li X, Segars WP, Samei E 2014 The impact on CT dose of the variability in tube current modulation technology: a theoretical investigation. Phys Med Biol 59 4525-4548
Long DJ, Lee C, Tien C, Fisher R, Hoerner MR, Hintenlang D and Bolch WE 2013 Monte carlo simulations of adult and pediatric computed tomography exams: validation studies of organ doses with physical phantoms Medical physics 40(1):013901
Looe HK, Eenboom F, Chofor N, Pfaffenberger A, Steinhoff M, Ruhmann A et al. 2008 Conversion coefficients for the estimation of effective doses in intraoral and panoramic dental radiology from dose area product values Radiat Prot Dosimetry 131 (3) 365 – 373
Lopez-Rendon X, Zhang G, Oyen R, Bosmans H, Zanca F 2014 Implementing the complete beam hardening effect of the bowtie filter versus scaling beam intensities: effects on dosimetric applications in computed tomography J. Med. Imag. 1(3) 033507
Lopez-Rendon X, Walgraeve MS, Woussen S, Dedulle A, Zhang G, Bosmans H et al 2017a Comparing different methods for estimating radiation dose to the conceptus Eur. Radiol. 27(2):851-858
Lopez-Rendon X, Zhang G, Coudyzer W, Develter W, Bosmans H and Zanca F 2017b Do we need tube current modulation information for accurate organ dosimetry in chest CT? Protocols dose comparison Eur Radiol 27 4490–4497

Ludlow JB, Davies-Ludlow LE, White SC. 2008a Patient risk related to common dental radiographic examinations: the impact of 2007 International Commission on Radiological Protection recommendations regarding dose calculation. J Am Dent Assoc 139:1237-1243.
Ludlow JB and Ivanovic M 2008 b Comparative dosimetry of dental CBCT devices and 64-slice CT for oral and maxillofacial radiology. Oral Surg. Oral Med. Oral Pathol. Oral Radiol. Endod. 106 106–114
Ludlow JB, Timothy R, Walker C, Hunter R, Benavides E Samuelson DB et al.2015 Effective dose of dental CBCT – a meta analysis of published data and additional data for nine CBCT units Dentomaxillofac Radiol 44 20140197
Loubele M, Jacobs R, Maes F, Schutyser F, Debaveye D, Bogaerts R et al 2005 Radiation Dose Vs Image Quality for Low-Dose CT Protocols Of The Head For Maxillofacial Surgery And Oral Implant Planning Radiat Prot Dosimetry 117 (1-3) 211-216
Mah JK, Huang JC, Choo H 2010 Practical applications of cone-beam computed tomography in orthodontics J. Am. Dent. Assoc. 141 7S-13S
Marcu M, Hedesiu M, Salmon B, Pauwels R, Stratis A, Oenning ACC et al 2018 Estimation of the radiation dose for pediatric CBCT indications: a prospective study on Promax 3D Int J Paediatr Dent (accepted for publication), doi: 10.1111/ipd.12355
Martin CJ. 2007 Effective dose: how should it be applied to medical exposures? Br J Radiol 80 639–47
Martin CJ. 2008 The application of effective dose to medical exposures. Radiat Prot Dosimetry 128 1 (1-4)
McCollough C, Bruesewitz M, Kofler J. 2006 CT Dose Reduction and Dose Management Tools: Overview of available options. Radiographics 26 503-512
McCollough CH, Primak AN, Saba O, Bruder H, Stierstorfer K, Raupach R, Suess S, Schmidt B, Ohnesorge BM and Flohr TG 2007 Dose performance of a 64-channel dual-source CT scanner Radiology 243 775-84
McCollough CH, Leng S, Yu L, Cody DD, Boone JM and McNitt-Gray MF 2011 CT Dose Index and Patient Dose: They Are Not the Same Thing Radiology 259, 311-316
McNitt-Gray MF 2002 AAPM/RSNA Physics Tutorial for Residents: Topics in CT- Radiation Dose in CT Radiographics 22, 1541-1553
Miracle A.C and Mukherji S.K 2009a Cone beam CT of the head and neck, Part 2: Clinical applications. Am. J. Neuroradiol. 30 1285-92
Miracle A C and Mukherji S K 2009b Cone beam CT of the head and neck: part 1. Physical principles Am. J. Neuroradiol. 30 1088–95
Mori S, Endo M, Nishizawa K, Tsunoo T, Aoyama T, Fujiwara H and Murase K 2005 Enlarged longitudinal dose profiles in cone-beam CT and the need for modified dosimetry Med Phys 32 1061-1069
Nagaoka T, Kunieda E and Watanabe S. 2008 Proportion-corrected scaled voxel models for Japanese children and their application to the numerical dosimetry of specific absorption rate for frequencies from 30 MHz to 3GHz. Phys. Med. Biol. 53: 6695
National Research Council of the National Academies 2006 Health Risks from Exposure to Low Levels of Ionizing Radiation - BEIR VII. Washington, DC: The National Academies Press
Nicholson RA, Thornton A, Akpan M 1995 Radiation dose reduction in paediatric fluoroscopy using added filtration. Br J Radiol 68(807):296–300.
Nipper C, Williams JL, and Bolch WE. 2002 Creation of two tomographic voxel models of pediatric patients in the first year of life. Phys. Med. Biol. 47 3143–3164
Oenning AC, Jacobs R, Pauwels R, Stratis A, Hedesiu M Salmon B 2017 Cone-Beam CT in paediatric dentistry: DIMITRA project position statement Pediatr Radiol https://doi.org/10.1007/s00247-017-4012-9
Okano Tomohiro and Jaideep Sur 2010 Radiation dose and protection in dentistry Japanese Dental Science Review 46, 112—121

Park S, Lee J K and Lee C 2006 Development of a Korean adult male computational phantom for internal dosimetry calculation Radiat. Prot. Dosim. 121 257–64
Pauwels R. et al. and The SEDENTEXCT Project Consortium 2012a Effective dose range for dental cone beam computed tomography scanners. Eur. J. Radiol. 81, 267–271
Pauwels et al and the SEDENTEXCT Project Consortium 2012b Dose distribution for dental cone beam CT and its implication for defining a dose index Dentomaxillofac Radiol 41 583-593
Pauwels R, Cockmartin L, Ivanauskaité D, Urbonienė A, Gavala S, Donta C, et al. 2014 Estimating cancer risk from dental cone-beam CT exposure based on skin dosimetry. Phys Med Biol 59:3877–91
Pauwels R 2015a Cone Beam CT for dental and maxillofacial imaging: dose matters Radiat Prot Dosimetry 165 (1-4) 156-61
Pauwels R, Araki K, Siewerdsen JH, Thongvigitmanee SS 2015b Technical aspects of dental CBCT: state of the art. Dentomaxillofac Radiol 44 20140224
Perisinakis K, Damilakis J, Tzedakis A, Papadakis A, Theocharopoulos N, Gourtsoyiannis N 2007 Determination of the weighted CT dose index in modern multi-detector CT scanners. Phys. Med. Biol. 52 (21) 6485-95
Petoussi-Hens N, Schlattl H, Zankl M, Endo A, Saito K. 2012 Organ doses from environmental exposures calculated using voxel phantoms of adults and children. Phys. Med. Biol. 57 5679–5713.
Puthenpurayil JG, Elenjickal JT, Mathew J, Kumar VRB 2015 Fundamentals of cone beam computed tomography for a prosthodontist The Journal of Indian Prosthodontic Society 15 (1) 8-13
Rogalla P 2009 Dynamic Volume CT with 320-Detector rows: Technology and Clinical Applications: in Multislice CT edited by M.F. Reiser, C.R. Becker, K. Nikolaou and G. Glazer (Medical Radiology, Diagnostic Imaging, Springer-Verlag, Berlin Heidelberg), pp 25-320
Rogers DWO and Bielajew AF 1990 Monte Carlo techniques of electron and photon transport for radiation dosimetry, The dosimetry of ionizing radiation, Chapter 5
Rogers DWO 2006 Fifty years of Monte Carlo simulations for medical physics Phys. Med. Biol 51:R287-301
Rogers, D.W.O et al. 2011 BEAMnrc users manual, NRCC Report PIRS-0509(A) revK, (Ottawa: National Research Council)
Rollins JD, Collins JS, Holden KR. 2010 United States Head Circumference Growth Reference Charts: Birth to 21 Years. J Pediatr 156 (6) 907-913
Rottke D, Patzelt S, Poxleitner P and Schulze, D 2013 Effective dose span of ten different cone beam CT devices. Dentomaxillofac. Radiol. 42 20120417
Salvadó M, Cros M, Joemai RMS, Calzado A, and Geleijns J 2015 Monte carlo simulation of the dose distribution of icrp adult reference computational phantoms for acquisitions with a 320 detector-row cone-beam ct scanner Physica Medica 31(5):452–462, 2015
Salvat F et al 2003 PENELOPE, A Code System for Monte Carlo Simulation of Electron and Photon Transport (Issy-les-Moulineaux, France: OECD Nuclear Energy Agency)
Salvat F 2015 Penelope-2014: A Code System for Monte Carlo Simulation of Electron and Photon Transport OECD Nuclear Energy Agency (NEA)
Scarfe W.C, Farman A.G, Sukovic P. 2006 Clinical applications of cone beam computed tomography in dental practice. JCDA 72 75-80
Scarfe WC, Farman AG. 2008 What is cone-beam CT and how does it work? Dent Clin North Am 52 707–30
SEDENTEXCT Project (2011) Chapter 4, Justification and referral criteria. Surgical applications. Implant dentistry. In: Radiation protection: Cone Beam CT for Dental and Maxillofacial Radiology. Evidence based guidelines 2011 (v2.0 Final). http://www.eadmfr.info/ sites/default/files/guidelines_final.pdf
Sempau J, Sanchez-Reyes A, Salvat F, Oulad ben Tahar B, Jiang SB and Fernandez-Varea JM 2001 Monte Carlo simulation of electron beams from an accelerator head using PENELOPE Phys Med Biol 46, 1163-1186

Shope TB, Gagne RM and Johnson GC 1981 A method for describing the doses delivered by transmission x-ray computed tomography Med Phys 8, 488-495
Shrimpton PC, Jones DG, Wall BF 1988 The influence of tube filtration and potential on patient dose during x-ray examinations. Phys Med Biol. 33(10):1205–12
Siewerdsen JH, Waese AM, Moseley DJ, Richard S, and Jaffray DA 2004 Spektr: a computational tool for x-ray spectral analysis and imaging system optimization. Med Phys 31(11):3057–3067, doi: 10.1118/1.1758350. URL http://dx.doi.org/10.1118/1.1758350.
Smans K, Tapiovaara M, Cannie M, Struelens L, Vanhavere F, Smet M et al. 2008 Calculation of organ doses in x-ray examinations of premature babies. Med. Phys. 35 556–68
Snyder W S, Ford M R Warner G G, Fisher H L Jr 1969 Estimates of absorbed fractions for monoenergetic photon sources uniformly distributed in various organs of a heterogeneous phantom J. Nucl. Med. 10 5–52 (Suppl 3)
Stratis A, Zhang G, Lopez-Rendon X, Jacobs R, Bogaerts R, Bosmans H. 2016a Customization of a Monte Carlo dosimetry tool for dental Cone Beam CT systems. Radiat Prot Dosim 169 (1-4): 378-385
Stratis A., Zhang G., Jacobs R, Bogaerts R, Bosmans H. 2016b Rotating and translating anthropomorphic head voxel models to establish an horizontal Frankfort plane for dental CBCT Monte Carlo simulations: a dose comparison study. Phys Med Biol. 61(24):N681-N696.
Stratis A, Zhang G, Lopez-Rendon X, Politis C, Hermans R, Jacobs R et al 2017a Two examples of indication specific radiation dose calculations in dental CBCT and Multidetector CBCT scanners Phys Med 41 71-77
Stratis A., Touyz N, Zhang G., Jacobs R, Bogaerts R, Bosmans H and DIMITRA project partners 2017b Development of a paediatric head voxel model database for dosimetric applications. Br J Radiol. 90 (1078):20170051. doi: 10.1259/bjr.20170051. Epub 2017 Jul 27
Tack D and Gevenois PA 2007 Radiation Dose from Adult and Pediatric Multidetector Computed Tomography. Springer-Verlag, Berlin Heidelberg, Germany
Takaoka H, Funabashi N, Uehara M, Fujimoto Y and Kobayashi Y 2013 Diagnostic accuracy of coronary 320 slice CT angiography using retrospective electrocardiogram gated acquisition compared with virtual prospective electrocardiogram gated acquisition with and without padding Int J Cardiol 168 2811-5
Tanner RJ, Shrimpton PC, Hart D et al. 2000 Frequency of medical and dental x-ray examinations in the UK – 1997/98. Chilton, NRPB – R 320
Tapiovaara M, Siiskonen T. 2008 PCXMC A Monte Carlo program for calculating patient doses in medical x-ray examinations (2nd edition) STUK-A231, Edita Prima Oy, Helsinki, Finland
Theodorakou C, Walker A, Horner K, Pauwels R, Bogaerts R, Jacobs R, et al. The SEDENTEXT Project consortium 2102 Estimation of paediatric organ and effective doses from dental cone beam ct using anthropomorphic phantoms. Br J Radiol 85:153–60.
Tian X, Li X, Segars WP, Paulson EK, Frush DP, Samei E. 2014 Pediatric chest and abdominopelvic CT: Organ Dose Estimation Based on 42 Patient Models. Radiology 270 (2) 535-547
Turner AC, Zhang D, Kim HJ, DeMarco JJ, Cagnon CH, Angel E et al 2009 A method to generate equivalent energy spectra and filtration models based on measurement for multidetector CT Monte Carlo simulations Med Phys 36, 2154-2164
Visser H, Rödig T, Hermann K-P. 2001 Dose reduction by direct-digital cephalometric radiography. Angle Orthod 71 159–163.
Walters BRB, Kawrakow I and Rogers DWO 2012 History by history statistical estimators in the Beam code system Med Phys 29, 2745-2752
Wandl-Vergesslich KA. 2000 Guidelines on Best Practice in the X-Ray Imaging of Children, By J.V. Cook, K. Shah, S. Pablot, K. Kyriou, A. Pettet, M. Fitzgerald, Queen Mary's Hospital for Children. Eur J Radiol. 33(1):67.

Ward E, DeSantis C, Robbins A, Kohler B, Jemal A 2014 Childhood and Adolescent Cancer Statistics 2014 CA CANCER J CLIN 64 83-103
White SC, Pharoah MJ. 2009 Oral radiology: principles and interpretation, 6th ed., St. Louis: Mosby Elsevier
WHO, World Health Organization 2007 Development of a WHO growth reference for school-aged children and adolescents Department of Nutrition, World Health Organization, Geneva 27, Switzerland. doi: 10.2471/BLT.07.043497
Woodard HQ, White DR 1986 The composition of body tissues Br J Radiol 59 1209-1219
Woussen S, Lopez-Rendon X, Vanbeckevoort D, Bosmans H, Oyen R, Zanca F 2015 Clinical indications and radiation doses to the conceptus associated with CT scanning in pregnancy: a retrospective study Eur Radiol 26(4):979-85
Xu XG and Eckerman KF 2010 “Handbook of anatomical models for radiation dosimetry”, Boca Raton, USA: CRC Press
Xu XG. 2014 An exponential growth of computational phantom research in radiation protection, imaging and radiotherapy : a review of the fifty-year history. Phys. Med. Biol 59: R233-R302.
Yu L, Vrieze TJ, Bruesewitz MR, Kofler JM, DeLone DR, Pallanch JF, Lindell P, McCollough CH 2010 Dose and image quality evaluation of a dedicated cone-beam CT system for high contrast neurologic applications Am. J. Roentgenol. 194 W193-201
Zhang G, Pauwels R, Marshall N, Shaheen E, Nuyts J, Jacobs R, Bosmans H 2011 Development and validation of a hybrid simulation technique for cone beam CT: application to an oral imaging system Phys.Med.Biol 56 5823-5843
Zhang G, Marshall N, Bogaerts R, Jacobs R, Bosmans H 2013a Monte Carlo modeling for dose assessment in cone beam CT for oral and maxillofacial applications Med Phys 40 072103
Zhang G, Marshall N, Jacobs R, Liu Q, Bosmans H. 2013 b Bowtie filtration for dedicated cone beam CT of the head and neck: a simulation study. Br J Radiol 86:20130002.
Zhou H, keall PJ, Graves EE 2009 A bone composition model for Monte Carlo x-ray transport simulations Med. Phys 36 (3) 1008-1018
Zubal IG, Harrell CR, Smith EO, Rattner Z, Gindi GR, Hoffer PB 1994 Computerized Three-dimensional Segmented Human Anatomy Med. Phys. 21(2) p.299-302

SUMMARY

CBCT scanners have been introduced in dental and maxillofacial radiology in the early 2000s, and since then they have been developed into the most important diagnostic tool with a wide range of applications in orthodontics, endodontics, periodontics, implantology and orthognathic surgery. Being reportedly associated with lower doses compared to imaging, yet higher doses compared to conventional intraoral and panoramic modalities, their extensive use especially in paediatric imaging raised radiation protection concerns.

This project focuses on organ dose and radiation risk assessment using a Monte Carlo (MC) simulation approach and a newly developed database of voxel models. The simulation platform was built in EGSnrc and has been customized, calibrated and validated for various CBCT scanner models. The simulation tool takes into account all geometric and technical specifications of current CBCT technology and manages to obviate any requirement for details which are proprietary data and vendors are reluctant to share. The framework was applied to investigate the influence of filter shape and composition on patient dose and the impact and effectiveness of a preprogrammed dose reduction Tube Current Modulation (TCM) system.

Chapter 2 describes the creation of a pediatric head and neck voxel model database. The selection process of the qualified MDCT datasets, the voxelisation methodology and the development of the appropriate format for MC simulations is described. A methodology to apply geometric corrections for converting an inclined Frankfort plane to a horizontal one is also described.

In chapter 3, voxel models are employed to each scanner specific MC framework and an extensive simulation study is performed to assess organ doses for the most common dental CBCT examinations; for single tooth imaging, upper/lower jaw and cleft imaging, sinus and maxillofacial complex imaging, temporal bone, face and skull imaging. Apart from organ doses, the radiation induced risk was also assessed via Effective Dose (E) and the age and gender dependent Life Attributable Risk (LAR). Logarithmic curves were fitted to provide a handful tool for (future) age specific dose assessment.

Chapter 4 deals with metrics for radiation dose monitoring purposes. The relevance and role of the recently proposed $CTDI_{w,IEC3.1}$ in dental CBCT imaging is investigated. Once it was proved that it is applicable to dental CBCT scanners, $CTDI_{w,IEC3.1}$ was assessed for every investigated protocol in this study. Finally, combining the results of chapter 3 and 4, scanner, protocol and age specific conversion factors of CTDI to organ doses, E and LAR have been proposed.

SAMENVATTING

CBCT scanners werden begin de jaren 2000 voor het eerst geïntroduceerd in dentale en maxillofaciale radiologie. Sindsdien zijn deze scanners onmisbaar geworden voor het overgrote deel van de applicaties in de orthodontie, endodontie, parodontologie, implantologie en orthognatische chirugie. Ondanks de lagere dosissen vergeleken met MDCT imaging, zijn de dosissen nog steeds hoger dan bij conventionele intra-orale en panoramische modaliteiten. Hierdoor, en door het veelvuldig gebruik van CBCT scanners, wordt veel aandacht besteed aan radioprotectie, vooral bij pediatrische patiënten.

Dit project focust op het berekenen van orgaandosissen en de risicobeoordeling voor bestraling aan de hand van een Monte Carlo (MC) simulatieplatform en een nieuwe database met voxelmodellen. Een EGSnrc MC simulatieplatform werd aangepast, gekalibreerd en gevalideerd voor verschillende modellen van CBCT scanners. Het houdt rekening met alle geometrische en technische specificaties van de huidige CBCT technologie en biedt een alternatieve manier aan om vertrouwelijke data die de fabrikanten niet willen delen, te berekenen. Dit platform werd gebruikt om de invloed van de vorm en compositie van de filter op de patiëntendosis te onderzoeken en om de impact en effectieve werking van een voorgeprogrammeerd buisstroommodulatie (TCM) systeem voor dosisreductie te bestuderen.

Hoofdstuk 2 beschrijft het ontwerpen van de database voor hoofd- en nek voxelmodellen van pediatrische patiënten. Het selectieproces van de geschikte MDCT datasets, de voxelisatie methodologie en de ontwikkeling van het juiste formaat voor de MC simulaties werd in detail gedocumenteerd. Ook een methode voor het toepassen van geometrische correcties bij het omzetten van het Frankfort vlak in een horizontaal vlak is hier beschreven.

In hoofdstuk 3 worden deze voxelmodellen geïmplementeerd in de scanner-specifieke MC simulatieplatformen. Een extensieve simulatiestudie is uitgevoerd voor het evalueren van orgaandosissen voor de meest voorkomende dentale CBCT onderzoeken. Deze onderzoeken zijn het beeldvormen van een enkele tand, de boven- en/of onderkaak, schisis, de sinussen, complexe maxillo faciale aandoeningen, temporaal bot en onderzoeken van het aangezicht en de schedel. Naast deze orgaandosissen werd ook het risico geïnduceerd door straling onderzocht aan de hand van de Life Attributable Risk (LAR), die de afhankelijk van leeftijd en geslacht incorporeert, en de effectieve dosis. Via het fitten van logaritmische curves werd een uitgebreide tool ontwikkeld voor verdere leeftijdsafhankelijke dosisbepalingen.

In hoofdstuk 4 worden de grootheden voor het controleren van de stralingsdosissen onderzocht, en meer bepaald de relevantie en de rol van de recent voorgestelde grootheid $CTDI_{w,IEC3.1}$ in dentale CBCT beeldvorming. Na het bewijs dat deze grootheid inderdaad relevant en toepasbaarheid is voor dentale CBCT scanners werd de $CTDI_{w,IEC3.1}$ voor elk reeds nader bekeken protocol in deze studie onderzocht. Door het combineren van de resultaten van hoofdstuk 3 en 4 werden scanner-, protocol- en leeftijdsspecifieke conversiefactoren van CTDI naar orgaandosissen, E en LAR gerealiseerd.

ACKNOWLEDGMENT

"As you set out for Ithaka, hope your road is a long one, full of adventure, full of discovery. Laistrygonians, Cyclops, angry Poseidon—don't be afraid of them: you'll never find things like that on your way as long as you keep your thoughts raised high, as long as a rare excitement stirs your spirit and your body. Laistrygonians, Cyclops, wild Poseidon—you won't encounter them unless you bring them along inside your soul, unless your soul sets them up in front of you.
Hope your road is a long one. May there be many summer mornings when, with what pleasure, what joy, you enter harbors you're seeing for the first time; may you stop at Phoenician trading stations to buy fine things, mother of pearl and coral, amber and ebony, sensual perfume of every kind—as many sensual perfumes as you can; and may you visit many Egyptian cities to learn and go on learning from their scholars.
Keep Ithaka always in your mind. Arriving there is what you're destined for. But don't hurry the journey at all. Better if it lasts for years, so you're old by the time you reach the island, wealthy with all you've gained on the way, not expecting Ithaka to make you rich.
Ithaka gave you the marvelous journey. Without her you wouldn't have set out. She has nothing left to give you now. And if you find her poor, Ithaka won't have fooled you. Wise as you will have become, so full of experience, you'll have understood by then what these Ithakas mean."

Konstantinos Kavafis

Ithaka is the poem that Prof. Nicholas M Spyrou was using to motivate his students. He was Professor of Radiation and Medical Physics, Chairman of Medical Physics and Director for the MSc Course in Medical Physics and the BSc course in Physics with Medical Physics at the University of Surrey, Guildford, UK. He passed away in March 2018. Professor, I am honored to have been one of your students. This thesis is dedicated to you.

It is sometimes amazing how nicely a poem can describe a period in your life. This was my PhD period over the last four years… a journey. It all started four years ago. Memories are still strong. A car full of stuff, and me and my wife driving about 2,500 km to get here in Belgium from Greece. I didn't expect Ithaka to make me rich…I gained a lot on my way. This poem was continuously coming in my mind in hard moments. As a source of inspiration to move on. But also in happy moments, as a reminder that Ithaka is offering me the marvelous journey.

This thesis is respectfully presented to Prof. Luc Sels, rector of KU Leuven, to Prof. Dr. Paul Herijgers, dean of the Faculty of Medicine, to Prof. Dr. Raymond Oyen, head of the department of Radiology at UZ Leuven.

I would like to express my gratitude to my PhD committee. To Prof. Tania Roskams for chairing the public defense. To Prof. Steven Dymarkowski for coordinating the reading committee and to the members of my jury committee: Prof. Dr. Constantinus Politis, Prof. Dr. Gerda Neyens, Prof. Dr. Jan Casselman, Prof. Dr. Kostas Perisinakis and Dr. Sue Edyvean for spending their valuable time to read this thesis, to make comments and suggestions that increased the level of this thesis.

To Prof. Dr. ir. Hilde Bosmans. Sometimes words are just not enough. You have been much more than a supervisor and boss. Your door has always been open to discuss, to support, to motivate, to encourage, to inspire. Thank you very much for everything. Thank you for trusting me twice. Initially to work as a Medical Physicist with a short-term contract in your team, and then to carry out this PhD project. Thank you very much for our long discussions either in the office, where a five-minute discussion could end up in a three-hour constructive conversation (and for sure, that could be the beginning of a potential project), or in the car while driving for project meetings. For every problem, minor or major, professional or personal, there was only one solution… talk to Hilde. *You gave me the*

marvelous journey. Without you I wouldn't have set out. Thank you so much Hilde, I am so grateful, proud and happy to know you and to have worked with you.
To Prof. Dr. Reinhilde Jacobs. Working with you was a great pleasure. Your unique way to motivate your people and your leadership skills are invaluable supplies for my future career. Your way to transmit your passion for work in a clinical and academic level will follow me hereafter.
To Prof. Dr. Ria Bogaerts. You welcomed me very warmly, you were always there and you were always willing to help me. Always in a positive attitude and with a smile, you made every problem seem simple. Thank you very much.
Financial and administrative issues…solved. Thank you very much Mr. Peter Vermaelen. I would also like to acknowledge KU Leuven for the financial support via the OT Research fund (OT 13/109). To Ingrid Fruyt and Linda Meersman. I really appreciate your help. I traveled to many places worldwide over the last four years to give presentations, to attend conferences and courses. I appreciate so much the fact that I didn't have to worry about flight tickets, cars, expenses, hotels, etc. Everything was solved well in advance. Thank you very much. You are the best secretaries in the world.
To Dr. Guozhi Zhang. Guozhi my friend, you are a Chinese machine. It is unbelievable how efficiently you can work and solve things. I sometimes have the impression that if you had to compete with a computer you would always be the winner. Thank you very much for your robust platform, for your help to guide me especially in the beginning, and for saving a lot of my time by offering me solutions to difficult problems. I got to know you during my first semester when you came back from the Mayo Clinics. After four years that we know each other I am convinced that what you told me back then is true (about the 97%). Thanks a lot Guozhi.
To Xochitl, my Mexican colleague, office mate and friend. You had already been a PhD researcher for two years when I started. At that time you were still exploring software and Monte Carlo options. You shared everything with me and made my start easy and smooth. Then we had the same office. We had been changing ideas on professional, personal and even political matters. We accomplished together so many RSNA and ECR conferences, supporting each other on high-pressure moments. Thanks a lot Xoch.
To all my colleagues. To Lesley and Elena, my first office mates. Thank you very much for your tips, especially in the beginning when one can easily get lost. To Joke, Kim and Annelies my QA colleagues. To Nick for his clever ideas and his British sense of humor (I will never forget the Scottish mode that you were desperately looking for in the train on our way to Vienna). To Michiel, Liesbeth, Mitco, Janne, An, Stoyko, Gati and Frédéric. We may not have spent much time together but I will always remember you guys. Go on with the great work. To Mostafa, my Egyptian friend and colleague in St Rafael. I am very lucky to know you, my friend. Apart from being a great scientist you are one of the kindest people I have ever met. Many thanks to the group in St Rafael for the collaboration.
To my students, Nathan, Brecht, Joeri and Laura for putting so much effort in their MSc dissertation projects and for helping me a lot with, their ideas and their tools. To Joris Awouters. You will be a great radiologist Joris. The voxel model database started with your hard work. Thank you very much. To Cedric Vanmarcke and Robbert Struyven who worked with me for their summer projects. Thanks a lot guys I really appreciate your help.
To Spyros a.k.a Dejan, my best friend and brother since childhood. We may not have been talking too much since I arrived in Belgium but I know that you will be there for me and I will be there for you. I am coming back, my friend. To Irene, Yiannis, Natasa and Stelios, my Greek colleagues and friends. Thank you very much for the stress-relieving discussions, for the new horizons that you opened to me, for your understanding and belief in me. To the 'AMMAN PIA' brothers Angelos, Kostas, Marios,

Dimitris and Nikos. All of them physicists, each working in a different field. Guys you were an oasis in difficult moments.

To Michael Molfetas and Nikos Panagiotakis, my former bosses and mentors. I am so lucky and thankful to both of you because I had the unique chance to learn the job from the best. This project is also dedicated to both of you. Thank you very much.

To my sister Evi and my nieces Viktoria and Aspasia. I love you so much. Your skype calls were so much precious, and your encouragement and support so much important to me. Especially to you Viktorako. You visited us in a very difficult moment and you were like an angel at home. It gave me so much strength that you cannot imagine. You were just two years old back then, and probably, you won't remember it; but believe me, you made a great job with your presence and your smile. And to you my little Rambo – Aspasia. You were born at the second best day of my life. A continuous source of joy. What a kid…

To my mom Viktoria. There are no words to express my gratitude. You have done so much over the last five years. You visited us so many times without counting any cost, any difficulty. You were there whenever I was asking your help. You annihilated time and distance. You are the best. To my dad Yiannis. You taught me to be proud and humble, to keep going even when things don't work out as expected, to be patient, and that there is always a purpose for everything even if I cannot see what this is all about. This journey actually started in 2004 in a small apartment in Southgate where we were staying together. You are my dad but you are also my best friend.

To my wife Dimitra. Oh captain my captain…you fought so hard. Especially for you, nothing was easy when we arrived. *Laistrygonians, Cyclops, angry Poseidon—don't be afraid of them: you'll never find things like that on your way as long as you keep your thoughts raised high, as long as a rare excitement stirs your spirit and your body. Laistrygonians, Cyclops, wild Poseidon—you won't encounter them unless you bring them along inside your soul, unless your soul sets them up in front of you.* You beat them all my dear. You didn't let me fall in the hardest period of my life; and only you know which period that was. You offered me the safest trip. I still remember that frightening silence in the car and the tears in your eyes when we left our home and our families to come over here. And since then, you were putting a stone on a pile each day, you built a rock, and I am so proud of you and of what you have achieved over these years. I love you so much. That car on our way here was full of stuff. Now on our way back, it is going to be full with the toys of our little princess.

To Lina, my lovely daughter, my treasure, my princess. You were born here, honey, in Leuven, and that day is the best of my life. You came into our lives in our third year here, and you filled the house with your smile, your cheerful voice, your energy. You made your first steps and you said your first words here in Leuven. We are the most happy parents in the world Linako mou. I will tell you a little secret. Papa had to give so many oral presentations during his PhD. Just a few seconds before his presentations, he was always checking your photos in his mobile, and this was so much stress-relieving. I adore you my darling.

Andreas

DISCLOSURE OF CONFLICT OF INTEREST

The author declares that he has no relevant financial interests that relate to the research described in this PhD thesis.

CURRICULUM VITAE

Andreas Stratis was born in February 1981 in Larissa, Greece. He obtain his BSc degree in Physics from the Aristotle University of Thessaloniki, Greece, in 2004, and his MSc degree in Medical Physics from the University of Surrey at Guildford, UK, in 2005. After gradualting, he followed a Medical Physics training scheme in Radiology, Nuclear Medicine and Radiotherapy at the 'Evangelismos' General Hospital of Athens and at the 'Aretaieio' University Hospital of Athens in Greece. Since 2008 he is officially licensed to work as a Medical Physicist on the fields of ionizing and non-ionizing radiations. From 2008 to 2013, he had been working as a Medical Physicist in Radiology and Nuclear Medicine in public and private hospitals in Greece. He has been Public Relations director (2010-2012) and Secretary Assistant (2012-2014) of the Hellenic Association of Medical Physicists. In 2013 he joined the Medical Physics team of the University Hospital of Leuven, Belgium, and in January 2014 he started his PhD at the Faculty of Medicine of the KU Leuven with a main aim to assess organ doses and radiation risk for paediatric patients in dental and maxillofacial Cone Beam CT imaging.

PUBLICATIONS

- **Stratis A. et al.** Development of a paediatric head voxel model database for dosimetric applications. Br J Radiol. 2017 Oct;90(1078):20170051. doi: 10.1259/bjr.20170051. Epub 2017 Jul 27.
- **Stratis A. et al.** Two examples of indication specific radiation dose calculations in dental CBCT and Multidetector CT scanners. Phys Med. 2017 Sep;41:71-77. doi: 10.1016/j.ejmp.2017.03.027. Epub 2017 Apr 6.
- Oenning A, Jacobs R, Pauwels R**, Stratis A**, Hedesiu M, Salmon B, Dimitra Research Group. Cone-Beam CT in paediatric dentistry: DIMITRA project position statement. Pediatr Radiol doi: 10.1007/s00247-017-4012-9
- EzEldeen M, **Stratis A**, Coucke W, Codari M, Politis C, Jacobs R. As Low Dose as Sufficient Quality: Optimization of Cone-beam Computed Tomographic Scanning Protocol for Tooth Autotransplantation Planning and Follow-up in Children. J Endod. 2017 Feb;43(2):210-217. doi: 10.1016/j.joen.2016.10.022
- Widmann G, Bischel A, **Stratis A**, Bosmans H, Jacobs R, Gassner EM, Puelacher W, Pauwels R. Spatial and contrast resolution of ultralow dose dentomaxillofacial CT imaging using iterative reconstruction technology. Dentomaxillofac Radiol. 2017 Apr;46(4):20160452. doi: 10.1259/dmfr.20160452. Epub 2017 Feb 17
- **Stratis A. et al.** Rotating and translating anthropomorphic head voxel models to establish an horizontal Frankfort plane for dental CBCT Monte Carlo simulations: a dose comparison study. Phys Med Biol. 2016 Dec 21;61(24):N681-N696.
- **Stratis A. et al.** Customization of a Monte Carlo dosimetry tool for dental Cone Beam CT systems. Radiat Prot Dosim (2016), 169 (1-4): 378-385
- Widmann G., Bischel A., **Stratis A..,** Kakar A, Bosmans H., Jacobs R., Gassner EM., Puelacher W., Pauwels R. Ultralow dose dentomaxillofacial CT imaging and iterative reconstruction techniques: variability of Hounsfield units and contrast to noise ratio. Br J Radiol (2016), 89 (1060): 20151055

- **Stratis A. et al**. A Monte Carlo study on the effect of the orbital bone to the radiation dose delivered to the eye lens. Proc. SPIE 9412, Medical Imaging 2015: Physics of Medical Imaging, 941231 (18 March 2015); doi:10.1117/12.2082029SPIE
- **Stratis A. et al.** Accuracy of CT dose monitor values-a multicentric study. Radiat Prot Dosimetry (2014), 158 (3): 285-289
- **Stratis A. et al.** The effect of a combined tube current modulation system on dose delivered to patients undergoing thoracic and abdominal CT with a 128 slice scanner. Radiat Prot Dosim (2013) 153(2):206-211.
- J. Koutsikos, G. Misichronis, I.Xirafi, H.Tourkohoriti, **A. Stratis**, F. Chroni, A. Velidaki. Thyroglossal duct cyst: a significant pitfall on I-131 follow- up whole-body scintigraphy. Eur J Nucl Med Mol Imaging (2011) 38 (Suppl 2): S229-S259

PRESENTATIONS

Belgian Hospital Physicists Association, Annual meeting, Antwerp, Belgium (2017)

- **Stratis A. et al**. A dose comparison study between CBCT and MSCT scanners for two clinical cases via Monte Carlo simulations: orthognathic treatment planning and temporal bone acquisitions.

Radiological Society of North America, RSNA 2017, Chicago, IL, USA (2017)

- **Stratis A. et al**. Preprogrammed Tube Current Modulation vs Attenuation-based Tube Current Modulation vs fixed current acquisitions: which technique delivers the lowest doses in dental CBCT scanners?

Radiological Society of North America, RSNA 2015, Chicago, IL, USA (2016)

- **Stratis A. et al.** Organ dose and radiation risk assessment for orthognathic patients in large FOV dental CBCT and head MSCT imaging. Radiological Society of North America, November 2016, Chicago, USA (SSE21)
- **Stratis A. et al.** Does rotational tube current modulation have significant impact on organ doses in dental CBCT to impose its implementation in dose calculating software tools?. Radiological Society of North America, November 2016, Chicago, USA (SSK16)

1st European Congress of Medical Physics, Athens, Greece (2016)

- **Stratis A. et al.** Head CBCT vs head MSCT imaging; comparing organ doses and radiation risks for a cohort of orthognathic patients
- N. Touyz**, A. Stratis**, G Zhang, R Jacobs, R Bogaerts and H Bosmans, Creation of a paediatric head voxel model database for dosimetric applications

Belgian Hospital Physicists Association, Annual meeting, Antwerp, Belgium (2016)

- **Stratis A. et al.** Employing CTDI to dental CBCT scanners – A Monte Carlo study, oral presentation

European Congress of Dentomaxillofacial Radiology, Cardiff, Wales (2016)

- **Stratis A. et al.** Age-dependent organ dose calculations in dental CBCT imaging for a cohort of cleft palate patients, poster presentation

European Congress of Radiology, European Society of Radiology (ECR), Vienna, Austria (2016)

- **Stratis A. et al.** Patient – specific organ dose assessment in a dental cone beam CT scanner with tube current modulation. "European Congress of Radiology (DOI link: http://dx.doi.org/10.1594/ecr2016/C-1145), EPOS (electronic poster)

Radiological Society of North America, RSNA 2015, Chicago, IL, USA (2015)

- **Stratis A. et al.** Should dental CBCT scanners be equipped with Cu filters? A Monte Carlo organ dose comparison study, oral presentation
- **Stratis A. et al.** A Monte Carlo dosimetry comparison study of two different paediatric protocols for teeth auto transplantation planning and follow up, oral presentation
- **Stratis A. et al.** Quantifying uncertainties in absorbed organ dose calculations in Monte Carlo simulations of dental Cone Beam CT applications, oral presentation

European Diagnostic Reference Levels for Paediatric Imaging, PiDRL workshop, Lisbon Portugal (2015)

- **Stratis A. et al.** Patient specific paediatric dose assessment in dental Cone Beam Computed Tomography via Monte Carlo calculations, oral presentation

Optimisation in X-ray and Molecular Imaging 2015, Fourth Malmö Conference on Medical Imaging, Gothenburg, Sweden (2015)

- **Stratis A. et al.** Customization of a Monte Carlo dosimetry tool for dental Cone Beam CT systems, oral presentation.

European Congress of Radiology, European Society of Radiology (ECR), Vienna, Austria (2015)

- **Stratis A. et al.** The influence of the orbital bone density on the eye-lens dose in dental CBCT, (SS 7 13), B-0680 , oral presentation (Best on site scientific presentation, Physics in Radiology, Innovations in CT technology).
- Bosmans H., **Stratis A**., Zhang G. Cone-beam CT: C. 3D dentomaxillofacial imaging (RC 113), A-014

SPIE Medical Imaging 2015, Orlando, FL, USA (2015)

- **Stratis A. et al.** A Monte Carlo study on the effect of the orbital bone to the radiation dose delivered to the eye lens, poster presentation.

European Academy of Dentomaxillofacial Radiology, 2nd Junior meeting, Freiburg, Germany (2015)

- **Stratis A. et al.** Patient-specific approach of CBCT imaging in children: custom-made Monte Carlo simulations, oral presentation.

Belgian Hospital Physicists Association, Annual meeting, Antwerp, Belgium (2015)

- **Stratis A. et al.** A Monte Carlo dental Cone Beam CT dosimetry tool based on measured energy spectra and filtration, oral presentation.

European Conference on Medical Physics, September 2014, Athens, Greece (2014)

- **Stratis A. et al.** Energy and angular dependence of thermoluminescent detectors in the dental CBCT energy range, poster presentation

European Medical Physics and Engineering Conference, incorporating the VIth European Conference of Medical Physics, 18-20 , Sofia, Bulgaria (2012)

- **Stratis A. et al.** Accuracy of CT dose monitor values- a multicentric study, electronic poster presentation

European Workshop to Introduce Radiation Protection 162. Dublin, Ireland (2011)

- **Stratis A. et al.** The effect of a combined tube current modulation system on dose delivered to patients undergoing thoracic and abdominal CT with a 128 slice scanner

European Congress of Radiology (ECR), European Society of Radiology, Vienna, Austria (2010)

- **Stratis A. et al.** Radiation doses from CT Coronary Angiography versus Interventional Coronary Angiography, Electronic Poster

International Conference on Radiation Protection in Medicine, Varna, Bulgaria (2010)

- **Stratis A. et al.** A multicentric study on patient dose in multislice CT, Electronic Poster Presentation, Roentgenologia and Radiologia Suppl. 10: 65, S5.P1.

12th Congress of the International Radiation Protection Association (IRPA12), Buenos Aires, Argentina (2008)

- S. Kottou, V. Tsapaki, M. Molfetas, **A. Stratis**, A. Louizi, I. Mavrikou, V. Neofotistou: Radiation doses in flat detector digital systems in interventional cardiology procedures